Universitá degli Studi di Ferrara

PhD Degree in Physics
CYCLE XXIX
COORDINATOR Prof. Vincenzo Guidi

PROGRESS TOWARDS A FIRST MEASUREMENT OF THE MAGNETIC BIREFRINGENCE OF VACUUM WITH A POLARIMETER BASED ON A FABRY-PEROT CAVITY

S.S.D. FIS/01

Supervisor:

Prof. Zavattini Guido

Dott. Della Valle Federico

PhD student:

Ejlli Aldo

Years 2014/2016

The work described in this thesis was carried out within the PVLAS experiment. I was greeted by the PVLAS team, which I had already met during my Master Degree thesis. First of all, I would like to thank my supervisor, Guido Zavattini who gave me confidence and guided me during these three years of the thesis work. Thank you, Guido, in particular, for patiently answering my questions. Thanks also for guiding me through all the topics we discussed together, from which I have learned a lot, and which brought us to face the main problems regarding the experiment. I appreciated your daily availability, your frankness and your dedication to research. These led to a constructive collaboration and to significant progress towards the detection of the quantum vacuum. My special thanks go to Federico Della Valle, my thesis co-supervisor. Thank you, Federico, for these three years during which you have always been available to guide me and answer my questions with great rigour. Thanks for always encouraging me to get to the bottom of things and to the confidence you have given me during our daily work. Thank you for your patience which you have dedicated to organising the material of this thesis and for discussing all the arguments step by step. Finally, thank you very much for your optimism, your skills and your enthusiasm that makes it a pleasure to work with you. I would also like to thank Ugo Gastaldi for having been present throughout my thesis period. I thank you for having read this manuscript and for having actively helped me prepare for the defence. Thank you, Giuseppe Ruoso, for your kindness, for your valuable advice during our discussions in these three years and for reading the thesis. Of course, I cannot forget Edoardo Milotti, Ruggero Pengo and Giuseppe Messineo. Thank you all for the months of work together during my PhD internship and for all the wise advice you have given me during these three years.

A special thanks goes to my wife Antonela and my two children Matias and Erik who gave me the strength to face and solve all difficulties. A big thanks goes to my father Broz who left us towards the end of my PhD: I will never forget your motivations and your determination in looking forwards. I also want to finally thank the rest of my family who patiently waited for this moment.

Table of contents

Abstract

This dissertation work was carried out in the context of the PVLAS experiment, financed by INFN and MIUR, which has the ultimate goal of measuring the magnetic birefringence of vacuum. Photon-photon interaction and therefore magnetic birefringence of vacuum anticipated Quantum Electrodynamics (QED): these effects, already studied since 1936 by Euler, Heisenberg and Weisskopf, are associated with the fluctuations of electron-positron pairs in vacuum. The effective Lagrangian density derived by these scientists was later confirmed by Schwinger in 1951 within the QED formalism. For a 2.5 T magnetic field it is found that the induced vacuum magnetic birefringence is:

$$\Delta n^{\mathrm{EHW}} = 2.47 \times 10^{-23} \qquad @\ 2.5\ \mathrm{T}.$$

This birefringence is extremely small and is still waiting for a direct experimental confirmation.

This thesis mainly concerns the new high sensitive polarimeter of the PVLAS experiment. The polarimeter consists of a pair of crossed polarisers, a Fabry-Perot cavity with a high finesse ($\mathscr{F} = 7 \times 10^5$) and uses the heterodyne technique to minimise the noise and the systematic effects. The anisotropy of vacuum with respect to electromagnetic radiation is produced using two rotating dipole permanent magnets characterised globally by the parameter $\int B^2 dl = 10.25\ \mathrm{T}^2\mathrm{m}$.

In this thesis work, the experimental apparatus is characterised and the sources of spurious signals and excess wide band noise are studied. As the principal source of spurious signals, we have identified diffused light modulated by a mechanical coupling between the tube and the magnet. A detailed description of the methods used to minimise this magneto-mechanical coupling, as well as other noises and systematic effects, is given. The improvements thus obtained have allowed acquiring data for rather extended periods of time - of a few weeks - and this has allowed the improvement of the existing current limits on magnetic vacuum birefringence, reaching a noise floor (1σ c.l.)

$$\Delta n^{(\mathrm{PVLAS})} = (12 \pm 17) \times 10^{-23} \qquad @\ B = 2.5\ \mathrm{T},$$

a factor 7 above the predicted QED value.

To reach the predicted QED value a ten fold improvement in sensitivity is necessary. The cause of the excess wide band noise, which is more than a factor 50 above the expected budget, is still unknown. Experimentally it is observed that the noise has a trend $\approx 1/f^{\alpha}$ with α between 0.5 and 1. The problem of the excess wide band noise is common to all the experimental efforts, past and present, intended to measure the vacuum magnetic birefringence. The sensitivity of these experiments and the slope of the spectral noise seem to suggest that the limit may be due to the thermal noise of the mirrors. These remarks, to which this thesis work has also contributed, perhaps will lead to a new understanding of the residual noise of such devices and to the development of useful new experimental methods.

Introduction

The PVLAS experiment in Ferrara, funded by the Minister of Research in the context of the Projects of Relevant National Interest (PRIN), and the National Institute of Nuclear Physics (INFN), involves researchers from the Universities of Trieste, Ferrara, and the INFN National Laboratories of Legnaro. This ambitious project aims at a first measurement of the magnetic birefringence of vacuum (MBV). The birefringence induced by an external field is predicted by Quantum Electrodynamics (QED) and is a direct consequence of the $\gamma\gamma$ interactions. One must note that the most precise particle physics theory that has been ever devised is the QED theory: experiments measuring the $g-2$ of the muon and of the electron give a perception of that. It must be noted though that such precise verifications of QED always regard the presence of a charged particle. A direct verification of the theory in the case in which only photons are involved is still missing. The sensitivity of experiments today is still not good enough to measure MBV: with currently available magnetic fields the induced MBV is $\Delta n \approx 4\times 10^{-24}$ @ 1 T. This exceedingly small and fine prediction explains why this phenomenon has not been observed so far.

In MBV experiments it is necessary to measure a difference of the speeds of light with polarisation perpendicular and parallel to the traverse magnetic field which, for $B = 1$ T, is of the order of $\Delta v/c = 4\times 10^{-24}$. At present this extremely small speed difference is not directly observable by measuring the speed of light separately for the two polarisations. Rather, it is conceivable to measure the ellipticity ψ induced on a linearly polarised beam of light which traverses a magnetic field in vacuum. If L is the length of the light path in the magnetic field B, ϑ is the angle between the polarisation vector of the light and the magnetic field direction, the induced ellipticity is

$$\psi = 4\times 10^{-24} \times \left(\frac{\pi L}{\lambda} B^2 \sin 2\vartheta\right) \tag{1}$$

with B measured in tesla. To get a feeling of the difficulty of these measurements notice that for $B = 1$ T, $L = 1$ m, $\lambda = 1$ μm, $\vartheta = 45°$: $\psi = 5\times 10^{-17}$. The calculation of the magnetic birefringence and of other effects generating ellipticity and/or dichroism in vacuum are presented in Chapter 1.

The method chosen in the PVLAS experiment is to measure the ellipticity of a linearly polarised laser beam passing through a region of transverse magnetic field. This is an intrinsically differential measurement of the difference in the speed of light for the two polarisations. The magnetic region is provided by two permanent magnets of maximum field 2.5 T and 0.82 m in length, arranged horizontally and rotating around their axis at a frequency ν_B up to 23 Hz. A rotating magnetic field induces a modulated ellipticity on the laser beam at a twice the rotation frequency.

To measure the ellipticity acquired by the beam a polarimeter is employed composed of two crossed polarisers, a high finesse Fabry-Perot cavity and an ellipticity modulator.

Using the Fabry-Perot optical cavity one obtains an amplification factor of $N = \frac{2\mathscr{F}}{\pi}$, where $\mathscr{F}$ is the finesse of the cavity. As we will see in this thesis, we have reached a finesse of $\mathscr{F} = 770\,000$. The difficulty in using such high finesse cavities is that the resonance FWHM is extremely small: ≈ 60 Hz compared to the laser light frequency of $\nu_{\text{laser}} = 2.8 \times 10^{14}$ Hz. To maintain resonance, the light source must be frequency locked to the cavity to obtain a constant laser-cavity coupling.

Finally, since the intensity at the output of the crossed polarisers alone is quadratic in ellipticity, we get a linearisation of the effect using the heterodyne technique which requires the implementation of an ellipticity modulator. The detailed description of the experimental method is given in Chapter 2

My thesis work started in January 2014, when the complete apparatus had just begun to be optimised. The first few months were devoted to the characterisation of the apparatus and to some test measurements. The characterisation and the method used to analyse the data is described in Chapter 3.

After the detailed characterisation of the polarimeter, spurious signals were present in phase with the rotating magnets. At this stage, we had identified the diffused light as a source of spurious signals. It will be shown how the mechanical coupling of tube and magnet induces spurious signals and how we proceeded to solve this problem.

We then dealt with an important feature of the Fabry-Perot cavity which is the intrinsic birefringence of the two cavity mirrors. The effect of the intrinsic birefringence of the mirrors was immediately observed during the calibration of the apparatus when measuring the magnetic birefringence of gases. Firstly we noted an attenuation of the ellipticity signal with respect to the predicted one. This is due to the fact that the eigenstates of the two polarisations of light in the cavity have different resonance frequencies, separated by a few hertz. A second effect of the birefringence of the cavity is a cross-talk between the ellipticity and the rotation signals. Finally, with the frequency of the ellipticity signal being close to the frequency cutoff of the cavity, the signals are filtered by the Fabry-Perot cavity which acts as a low-pass filter. A more detailed study of the dynamic response of the cavity, also considering the mirror birefringence, brought to the result that the behaviour of a birefringent Fabry-Perot cavity deviates from a simple first order filter. For a correct calibration of the apparatus these effects must all be taken into account.

A critical attention has also been paid to the wide-band noise. This noise has no phase relation with the rotating magnets. At present, this noise remains the only obstacle to measuring the magnetic birefringence of vacuum. With respect to the calculated noise budget due to known sources, the polarimeter shows a noise about a factor 50 above the expected one. To understand the source of this excess noise we tried changing a number of elements: different polarisers, further reduction of the diffused light, redesigning of the feedback circuit. We also performed several tests modifying the locking parameters and other experimental parameters (modulation amplitude, laser power, environmental noise). These experimental tests put constraints on the origin of the excess noise. We believe that the source of this excess noise is an intrinsic thermal noise of the mirrors. In Chapter 4 all the material regarding the hunting for wide-band noise and systematics will be presented.

Finally, a lot of effort has been also addressed to the analysis of the data collected during these years. The data, acquired after the improvements of the polarimeter, consisted mainly in ellipticity data but a part was also dedicated to rotation data. The analysis presented in this thesis has set the best laboratory limits on the magnetic birefringence of vacuum and on the existence of axion-like particles with masses above 1 meV and of millicharged particles. All the collected data are presented in Chapter 5.

0.1 Publications

The work done during the three years of my thesis has given rise to the following publications:

F. Della Valle, A. Ejlli, U. Gastaldi, G. Messineo, E. Milotti, R. Pengo, L. Piemontese, G. Ruoso, G. Zavattini, “Measurement of the Cotton Mouton effect of water vapour”, Chemical Physics Letters **592**, 288 (2014).

F. Della Valle, A. Ejlli, U. Gastaldi, G. Messineo, E. Milotti, R. Pengo, L. Piemontese, G. Ruoso, S. Sabotig, G. Zavattini, “Experimental perspectives in (low-energy) photon-photon scattering”, Journal of Physics: Conference Series **490**, 012153 (2014).

F. Della Valle, E. Milotti, A. Ejlli, U. Gastaldi, G. Messineo, L. Piemontese, G. Zavattini, R. Pengo, G. Ruoso, “Extremely long decay long decay time optical cavity”, Optics Express **22**, 11570 (2014).

F. Della Valle, E. Milotti, A. Ejlli, G. Messineo, L. Piemontese, G. Zavattini, U. Gastaldi, R. Pengo, G. Ruoso, “First results from the new PVLAS apparatus: a new limit on vacuum magnetic birefringence”, Physical Review D **90**, 092003 (2014)

A. Ejlli, F. Della Valle, U. Gastaldi, G. Messineo, E. Milotti, R. Pengo, G. Ruoso, G. Zavattini, “Progress toward a direct experimental detection of gamma-gamma interactions”, Nuclear and Particle Physics Proceedings **270-272**, 67 (2016).

F. Della Valle, A. Ejlli, U. Gastaldi, G. Messineo, E. Milotti, R. Pengo, G. Ruoso, G. Zavattini, “The PVLAS experiment: measuring vacuum magnetic birefringence and dichroism with a birefringent Fabry-Perot”, European Physics Journal C **76**, 24 (2016).

G. Zavattini, F. Della Valle, A. Ejlli, G. Ruoso, “A polarisation modulation scheme for measuring vacuum magnetic birefringence with static fields”, European Physics Journal C **76**, 294 (2016).

A. Ejlli, F. Della Valle, G. Zavattini, “Polarisation dynamics of a birefringent Fabry-Perot cavity”, arXiv:1707.02967v1.

Chapter 1

Quantum vacuum

This thesis describes the last three years of the experimental effort in progress within the PVLAS collaboration to perform the first observation of the Magnetic Birefringence of Vacuum (MBV). MBV is expected as a consequence of the existence of the antiparticle of the electron and of the possibility of the virtual creation of particle-antiparticle pairs in vacuum. Together with the Casimir effect, MBV represents a macroscopic evidence of quantum vacuum. The PVLAS experiment intends to observe the ellipticity induced in vacuum on a linearly polarised beam of light passing through a transverse magnetic field. The speed of light results from virtual microscopic processes involving photons in the quantum vacuum. The presence of an external (magnetic/electric) field, which acts on the charged particle-antiparticle pairs and polarises the vacuum, results, at the macroscopic level, in a variation of the speed of light. Furthermore, the speed of light depends on the polarisation: the speeds of light polarised parallel and orthogonal to the direction of the external (magnetic/electric) field are different.

The consequences on Electrodynamics of the existence of electron-positron virtual pairs were derived already in 1936 (shortly after the introduction of the Dirac equation – 1928 – and the observation of the positron – 1932). With the Heisenberg-Euler effective Lagrangian, new terms have to be added to Maxwell's equations, which make the new equations no longer linear in the electric and magnetic fields. In section 1.1 we present the mathematical formulation of the electromagnetic quantum vacuum and the Heisenberg-Euler effective Lagrangian. The electric permittivities and the magnetic permeabilities $\varepsilon_\perp$, $\varepsilon_\|$, $\mu_\perp$, $\mu_\|$ are also derived.

In a more general framework, vacuum effects are described by means of Feynman graphs, and quantum field theory takes into account other hypothetical effects such as the vacuum fluctuations of particles with fractional charge and bosonic axion-like particles. All of them are predicted to give place to observable magneto-optical effects. Normally, scattering experiments in particle physics have featured the observation of the interaction of beams with targets when matter particles (fermions) are present either as the beam or the target. Considered as a scattering experiment, PVLAS represents one of the rare cases in which both the beam and the target are composed of bosons (photons of the laser beam and virtual photons of the magnetic field).

1.1 Heisenberg-Euler effective Lagrangian

The electromagnetic classical vacuum

Classically the electromagnetic field in vacuum is described by Maxwell's equations (1861-1862), which allow wave propagation. The electromagnetic properties of vacuum, in classical electrodynamics, are represented by two fundamental constants: the vacuum permittivity ε_0 and the vacuum permeability μ_0, with the speed of light given by $c = \frac{1}{\sqrt{\varepsilon_0\mu_0}}$. The two constants describe, respectively, the proportionality factor between $\mathbf{D}$ and $\mathbf{E}$ and between $\mathbf{B}$ and $\mathbf{H}$ in vacuum. The field $\mathbf{D} = \varepsilon_0\mathbf{E}$ is the electric displacement vector, $\mathbf{E}$ is the electric field vector, $\mathbf{B} = \mu_0\mathbf{H}$ is the magnetic induction vector, and $\mathbf{H}$ is the magnetic field vector. Any variation of the speed of light compared to c is attributed to the fact that the light propagates in a medium, that is, not in vacuum. To describe the electromagnetic properties of matter, one introduces the tensors $[\varepsilon]$ and $[\mu]$ characterising the medium itself: $\mathbf{D} = [\varepsilon]\mathbf{E}$ and $\mathbf{B} = [\mu]\mathbf{H}$. The speed of light in a medium is smaller than the speed of light in vacuum by a factor n, called the index of refraction, equal to (in an isotropic medium for which $[\varepsilon] = \varepsilon$ and $[\mu] = \mu$)

$$n = \frac{\sqrt{\varepsilon\mu}}{\sqrt{\varepsilon_0\mu_0}} \tag{1.1}$$

Vacuum is therefore the medium to which one associates, in classical electrodynamics, a refractive index n exactly equal to 1. Classically there is no polarisation or magnetisation of vacuum in the presence of a magnetic or electric field. In contrast a medium, in the presence of an electric and/or magnetic field, may exhibit a birefringence, i.e. the medium may have different indices of refraction for two orthogonal polarisations. Two effects that generate birefringence are the Cotton-Mouton effect (CME) [1, 2] and the Kerr effect [3, 4]. In the CME, a birefringence proportional to the square of an external magnetic field is induced, whereas in the Kerr effect the birefringence is proportional to the square of an electric field. In both cases, a linearly polarised beam of light traversing a medium perpendicularly to an external field will become elliptically polarised if the polarisation is not aligned with one of the birefringence axes. Therefore the optical response of the medium depends on the external field strength. This correlation means that ε and μ are not constants but functions of the external fields. So in general n depends on $\mathbf{E}$ and $\mathbf{B}$: $n = n(\mathbf{E},\mathbf{B})$.

To describe this nonlinear interaction, one uses the constitutive equations of the medium giving the relation between the polarisation $\mathbf{P}$ and $\mathbf{E}$, the relation between the magnetisation $\mathbf{M}$ and $\mathbf{B}$ and the Maxwell's equations [5]. When no charge density or current density is present, Maxwell's equations in SI units [6] are

$$\begin{aligned} \nabla \times \mathbf{E} &= -\frac{\partial \mathbf{B}}{\partial t} & \qquad \nabla \cdot \mathbf{D} = 0 \\ \nabla \times \mathbf{H} &= \frac{\partial \mathbf{D}}{\partial t} & \qquad \nabla \cdot \mathbf{B} = 0 \end{aligned}$$

with

$$\mathbf{H} = \frac{1}{\mu_0}\mathbf{B} - \mathbf{M} \qquad \mathbf{D} = \varepsilon_0 \mathbf{E} + \mathbf{P}. \tag{1.2}$$

Considering the propagation of light in a medium, both the external field and the light fields produce a polarisation $\mathbf{P}$ and a magnetisation $\mathbf{M}$. Instead, in vacuum, the two vectors, magnetisation and polarisation, are zero ($\mathbf{P}_{\text{vac}} = 0$ and $\mathbf{M}_{\text{vac}} = 0$).

	C	P	T	CPT
E	-	-	+	+
B	-	+	-	+
F	+	+	+	+
G	+	-	-	+

Table 1.1: Symmetry properties of the electromagnetic fields and of the invariants F and G with respect to C, P and T.

Classically, the electromagnetic interaction is described by a Lagrangian density $\mathscr{L}$, which is a function of the fields in the system and their derivatives [7]. The mathematical expression of the Lagrangian density $\mathscr{L}$ is mainly determined by the fact that it must be relativistically invariant, and therefore must be a function of the Lorentz invariants [7]:

$$F = \left(\varepsilon_0 E^2 - \frac{B^2}{\mu_0}\right) \qquad \text{and} \qquad G = \sqrt{\frac{\varepsilon_0}{\mu_0}}(\mathbf{E}\cdot\mathbf{B}). \tag{1.3}$$

The general expression of a relativistically invariant Lagrangian density can be written in terms of Lorentz invariants,

$$\mathscr{L} = \sum_{i=0}^{\infty}\sum_{j=0}^{\infty} c_{i,j} F^i G^j. \tag{1.4}$$

Thanks to the symmetry properties of the **E** and **B** fields (see table 1), F and G are also CPT invariant, but while F is C, P, and T invariant, G violates P and T. Since classical vacuum is separately invariant for each of the C, P, and T symmetries, all the coefficients $c_{i,j}$ with odd j are null, and in particular $c_{0,1} = 0$. The lowest order term, with $c_{0,0} = 0$ and $c_{1,0} = \frac{1}{2}$ corresponds to the classical Maxwell Lagrangian density

$$\mathscr{L}_0 = \frac{1}{2}\left(\varepsilon_0 E^2 - \frac{B^2}{\mu_0}\right) = \frac{F}{2}. \tag{1.5}$$

Now we can derive the constitutive equations for **D** and **H** from the Lagrangian [7]:

$$\mathbf{D} = \frac{\partial \mathscr{L}}{\partial \mathbf{E}} \qquad \text{and} \qquad \mathbf{H} = -\frac{\partial \mathscr{L}}{\partial \mathbf{B}}, \tag{1.6}$$

For a plane wave propagating in vacuum, both F and G are equal to zero and therefore $\mathscr{L}_0 = 0$. This statement means that, due to the Lorentz invariance, the propagation of a plane wave in vacuum cannot be affected by any nonlinear interaction.

We can draw some conclusions concerning classical electrodynamics: the difference between vacuum and matter due to electromagnetic properties are that

- in classical vacuum the magnetic permeability μ_0 and the electric permittivity ε_0 are not functions of the fields, but are constants. In matter, this is not the case;
- classical vacuum does not allow a polarisation **P** or a magnetisation **M**;
- classical vacuum does not exhibit nonlinear interactions as in matter.

The electromagnetic quantum vacuum

The idea of the classical vacuum changed when Heisenberg [8] and Dirac [9] introduced the Uncertainty Principle and the theory of the positron, respectively. The Uncertainty Principle, first proposed in 1927 by Heisenberg, states that the time interval Δt during which an energy measurement is performed is related to the energy uncertainty $\Delta\mathscr{E}$ by:

$$\Delta\mathscr{E}\Delta t \geq \frac{\hbar}{2} \tag{1.7}$$

A year later, in 1928, Dirac introduced the wave equation for the electron, which implied the existence of antiparticles. A few years later, the anti-electron was experimentally observed, and it became evident that an important consequence of the Uncertainty Principle and of the Dirac theory was the existence of $\gamma\gamma$ interactions [10, 11]. Citing from Halpern's 1933 letter:

.... Here purely radiation phenomena are of particular interest inasmuch as they might serve in an attempt to formulate observed effects as consequences of hitherto unknown properties of corrected electromagnetic equations. We are seeking, then, scattering properties of the "vacuum".

This prediction has so far not yet been confirmed experimentally by a direct observation in a laboratory experiment.

The first mathematical formulation of electromagnetic nonlinearities in vacuum was published in 1935 by Euler and Kockel [12]. Details on their estimation can be found in Ref. [13]. In an article published in 1936 by Heisenberg and Euler [14], a complete theoretical study of the effects related to the fact that electromagnetic radiation can be transformed into matter and *vice-versa* was made. The starting point of the authors was that it was no longer possible to separate processes in a vacuum from those involving matter, since electromagnetic fields can create matter if they are strong enough. Moreover, even if they are not strong enough to create matter, they can polarise the vacuum because of the creation of virtual matter, dominantly electron-positron pairs, and thus the result of applying the constitutive equations changes [14]. The resulting effective Lagrangian density for electromagnetic fields in the absence of matter is [14]:

$$\begin{aligned}\mathscr{L}_{HE} &= \frac{1}{2}\left(\varepsilon_0 E^2 - \frac{B^2}{\mu_0}\right) + \alpha \int_0^\infty e^{-\eta}\frac{d\eta}{\eta^3} \\ &\times \left\{ i\eta^2 \sqrt{\frac{\varepsilon_0}{\mu_0}}(\mathbf{E}\cdot\mathbf{B}) \frac{\cos\left[\frac{\eta}{\sqrt{\varepsilon_0}E_{cr}}\sqrt{C}\right] + \text{conj.}}{\cos\left[\frac{\eta}{\sqrt{\varepsilon_0}E_{cr}}\sqrt{C}\right] - \text{conj.}} + \varepsilon_0 E_{cr}^2 + \frac{\eta^2}{3}\left(\varepsilon_0 E^2 - \frac{B^2}{\mu_0}\right)\right\},\end{aligned} \tag{1.8}$$

with

$$C = \left(\varepsilon_0 E^2 - \frac{B^2}{\mu_0}\right) + 2i\frac{\varepsilon_0}{\mu_0}(\mathbf{E}\cdot\mathbf{B}), \tag{1.9}$$

and where $\alpha = \frac{e^2}{4\pi\varepsilon_0\hbar c}$ is the fine structure constant, e the charge of the electron, $\hbar$ the Planck's constant h divided by 2π, and η the integration variable. The quantity $E_{cr} = \frac{m_e^2 c^3}{e\hbar}$ has the dimensions of an electric field and it is called the critical electric field corresponding to a value:

$$E_{cr} = 1.3 \times 10^{18}\ \text{V/m}. \tag{1.10}$$

It corresponds to the electric field needed to create an electron mass m_e at rest over a distance equal to the length of reduced electron Compton wavelength $\lambdabar = \frac{\lambda_e}{2\pi} = \frac{\hbar}{m_e c}$. In the same way one can define a critical magnetic field such as: $B_{cr} = \frac{E_{cr}}{c} = \frac{m_e^2 c^2}{e\hbar}$:

$$B_{cr} = 4.4 \times 10^9 \text{ T}. \tag{1.11}$$

The authors derived the Lagrangian $\mathscr{L}_{HE}$ in the following approximations:

- Slowly varying fields:

$$\frac{\hbar}{m_e c}|\nabla E| \ll E, \qquad \frac{\hbar}{m_e c^2}\left|\frac{\partial E}{\partial t}\right| \ll E \tag{1.12}$$

$$\frac{\hbar}{m_e c}|\nabla B| \ll B, \qquad \frac{\hbar}{m_e c^2}\left|\frac{\partial B}{\partial t}\right| \ll B \tag{1.13}$$

- Fields much smaller than their critical values:

$$B \ll B_{cr} = \frac{m^2 c^2}{e\hbar} = 4.4 \times 10^9 \quad \text{T}, \qquad E \ll E_{cr} = \frac{m^2 c^3}{e\hbar} = 1.3 \times 10^{18} \quad \text{V/m} \tag{1.14}$$

- Only virtual electron-positron pairs are exchanged.

In general, the QED Lagrangian $\mathscr{L}_{HE}$ can be expanded as indicated in Eq. (1.4). Reminding that symmetry requires that $c_{1,1} = 0$, at the lowest order one has

$$\mathscr{L}_{HE} = c_{1,0}F + c_{2,0}F^2 + c_{0,2}G^2. \tag{1.15}$$

The values of $c_{2,0}$ and $c_{0,2}$ can be written following the Euler-Kockel result [12] as:

$$c_{2,0} = \frac{2\alpha^2\hbar^3}{45 m_e^4 c^5} \simeq 1.67 \times 10^{-30} \text{ m}^3/\text{J}, \qquad \text{and} \qquad c_{0,2} = 7c_{2,0}, \tag{1.16}$$

and therefore

$$\mathscr{L}_{HE} = \frac{1}{2\mu_0}\left(\frac{E^2}{c^2} - B^2\right) + \frac{2\alpha^2}{45\mu_0^2}\frac{\hbar^3}{m_e^4}\left[\left(\frac{E^2}{c^2} - B^2\right)^2 + 7(\mathbf{E}\cdot\mathbf{B})^2\right]. \tag{1.17}$$

Note that this result is prior to the formulation of QED but was verified later by Schwinger [15]. Next term coefficients can be found in Refs. [14, 16, 17]. Each term can be represented as a Feynman graph, as in Fig. 1.1. The first term in the Equation (1.17), quadratic in the fields, is the classical electromagnetic Lagrangian leading to Maxwell's equations in vacuum, for which the superposition principle holds and no light-by-light interaction is possible. The other term, instead, implies that Electrodynamics is nonlinear in vacuum, giving rise to a new

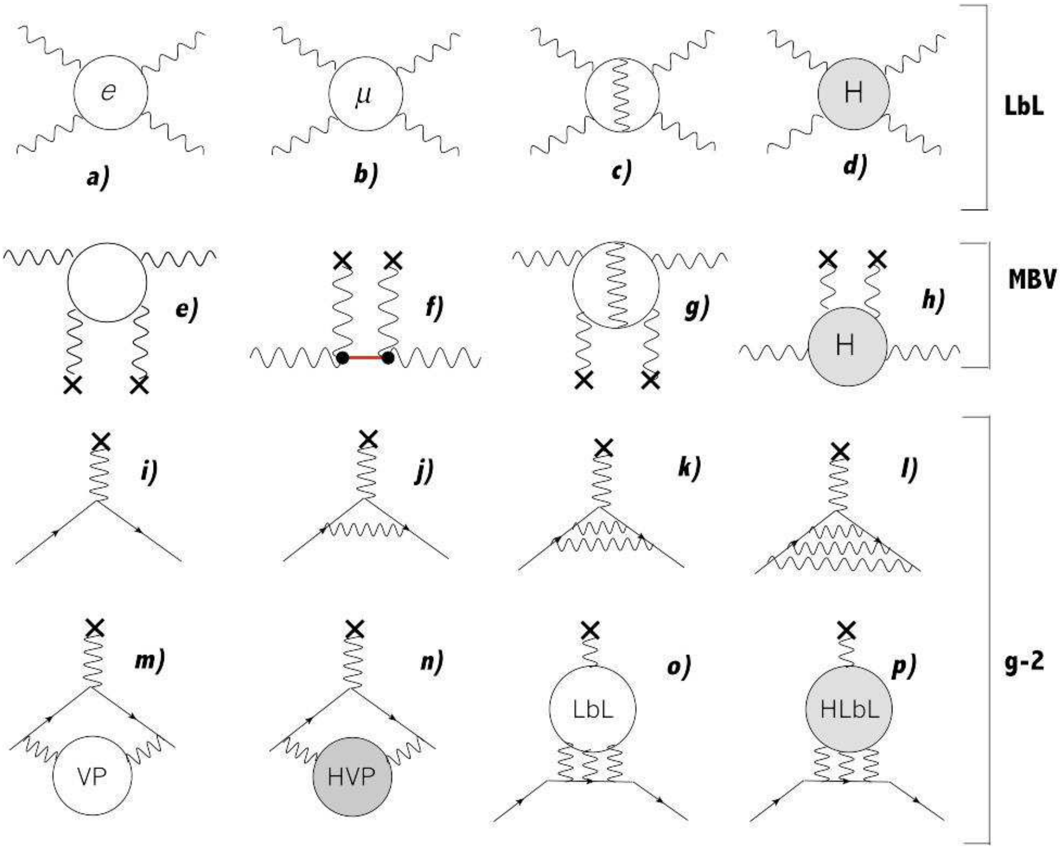

Figure 1.1: Contributions to Light by Light scattering, *a)* to *d)*, Magnetic Birefringence of Vacuum, *e)* to *h)* and $g-2$, *i)* to *p)*.

class of observable effects. The higher order terms of the free Lagrangian are proportional to $1/m^4$. If, instead of electron-positron pairs, we considered the contribution of other pairs of charged particles like lepton-antilepton such as $\mu^+\mu^-$ and $\tau^+\tau^-$ the effect would be negligible compared to the contribution due to e^-e^+. The Feynman graphs of Figs. 1.1*a)* and 1.1*e)* are the simplest ones giving rise to non-zero matrix elements with e^-e^+ pairs. Note that a graph with only three external photons has a null matrix element according to the Furry theorem [18]. This statement implies that no term proportional to a product of three electromagnetic fields like E^3, E^2B, EB^2 and B^3 can be present in $\mathscr{L}_{\mathrm{HE}}$, and indeed this is the case in equation (1.17). In the particular case in which photons propagate in an external magnetic field, the leading Feynman diagram is shown in figure 1.1*e)*. Today it is thought that the interaction between two photons, mediated by loops of electron-positron pairs and (with remarkably weaker effects) by loops of muons, hadrons etc., could also be mediated by hypothetical very light particles which couple to two photons [see fig. 1.1*f)*].

1.2 QED vacuum magnetic birefringence

In this section we deal with the estimation of the linear birefringence induced in vacuum by an electric or magnetic field. The field equations are determined by the energy density U, which is a function of the field intensities. The following relation exists between the energy density U and the Lagrangian density $\mathscr{L}$ [16],

$$U = \mathbf{E}\cdot\frac{\partial\mathscr{L}}{\partial\mathbf{E}} - \mathscr{L}. \tag{1.18}$$

Using the general expression of the Lagrangian density (1.4) the energy density is:

$$U = \sum_{i=0}^{\infty}\sum_{j=0}^{\infty} c_{i,j}\left(2\varepsilon_0 i F^{(i-1)} G^j E^2 + (j-1)F^i G^j\right). \tag{1.19}$$

Considering the case in which the fields vary slowly over the length $\frac{\hbar}{mc}$ and the time $\frac{\hbar}{mc^2}$ [see Eqs. (1.12) and (1.13)], the Lagrangian expression can be expanded in powers of the invariants F and G [16]. Expanding in series of powers in the invariants up to the third order, we obtain:

$$\mathscr{L} = c_{1,0}F + \mathscr{L}' = c_{1,0}F + c_{2,0}F^2 + c_{0,2}G^2 + c_{3,0}F^3 + c_{1,2}FG^2 + ... \tag{1.20}$$

Using equation (1.19) we obtain the energy density of vacuum in the presence of an electromagnetic field:

$$\begin{aligned} U &= c_{1,0}\left(\varepsilon_0 E^2 + \frac{B^2}{\mu_0}\right) + c_{2,0}F\left(3\varepsilon_0 E^2 + \frac{B^2}{\mu_0}\right) + c_{0,2}G^2 + \\ &+ c_{3,0}F^2\left(5\varepsilon_0 E^2 + \frac{B^2}{\mu_0}\right) + c_{1,2}G^2\left(3\varepsilon_0 E^2 - \frac{B^2}{\mu_0}\right)... \end{aligned} \tag{1.21}$$

where the coefficients are:

$$c_{1,0} = 1/2,\ c_{2,0} = \frac{\alpha}{90\pi}\frac{1}{\varepsilon_0 E_{cr}^2},\ c_{0,2} = 7c_{2,0},\ c_{3,0} = \frac{2\alpha}{315\pi}\frac{1}{\varepsilon_0^2 E_{cr}^4},\ c_{1,2} = \frac{13}{2}c_{3,0}. \tag{1.22}$$

Using relations (1.2) and (1.6) the polarisation and the magnetisation vectors are:

$$\mathbf{P} = \frac{\partial\mathscr{L}}{\partial\mathbf{E}} - \varepsilon_0\mathbf{E} \qquad \text{and} \qquad \mathbf{M} = \frac{\partial\mathscr{L}}{\partial\mathbf{B}} + \frac{\mathbf{B}}{\mu_0}. \tag{1.23}$$

Using the Lagrangian expansion (1.20), we obtain the expression for the magnetisation and polarisation of vacuum at the lowest order in the fields:

$$\mathbf{P} = 4c_{2,0}\varepsilon_0\mathbf{E}F + 2c_{0,2}\sqrt{\frac{\varepsilon_0}{\mu_0}}\mathbf{B}G, \tag{1.24}$$

$$\mathbf{M} = -4c_{2,0}\frac{\mathbf{B}}{\mu_0}F + 2c_{0,2}\sqrt{\frac{\varepsilon_0}{\mu_0}}\mathbf{E}G.\mathrm{vac} \tag{1.25}$$

Now we discuss the two particular cases in which a polarised electromagnetic wave passes through a region of vacuum in the presence of a transverse electric or magnetic field. In a medium, linear birefringence in the presence of an electric field was discovered by John Kerr in 1875 and is called the Kerr effect [3, 4]. A linearly polarised electromagnetic plane wave passing through a medium in the presence of an orthogonal electric field experiences a different index of refraction according to whether the polarisation is parallel or orthogonal to the electric field: $n_{\parallel} \neq n_{\perp}$. The difference $n_{\parallel} - n_{\perp} = \Delta n_K$ is proportional to the square of the electric field:

$$\Delta n_K = k_K E^2_{\mathrm{ext}}. \tag{1.26}$$

The same happens in the presence of a magnetic field. This effect was investigated in detail by A. Cotton and H. Mouton in 1905 [1, 2] in liquids and by W. Voigt in gases 30 years after the Kerr effect was discovered. Similarly to the Kerr effect, when a magnetic field is applied to a medium, the difference in the indices of refraction, $n_{\parallel}$ and $n_{\perp}$, is proportional to the square of the magnetic field:

$$\Delta n_{CM} = k_{CM} B^2_{\mathrm{ext}}. \tag{1.27}$$

We will see that due to Eqs. (1.24) and (1.25) the same effects are expected in vacuum. Let us concentrate on the Cotton-Mouton effect in vacuum whose detection is the aim of our experiment. Consider a homogeneous static magnetic field $\mathbf{B}_{\mathrm{ext}}$ in vacuum. When a polarised plane wave traverses an orthogonal static magnetic field, equations (1.24) and (1.25) give the following expressions for the magnetisation **M** and polarisation **P**:

$$\mathbf{P}_{\mathrm{vac}} = -4c_{2,0}\varepsilon_0\frac{B_0^2}{\mu_0}\mathbf{E}_\gamma + 2c_{0,2}\frac{\varepsilon_0}{\mu_0}\mathbf{B}_{\mathrm{ext}}(\mathbf{E}_\gamma\cdot\mathbf{B}_{\mathrm{ext}}), \tag{1.28}$$

$$\mathbf{M}_{\mathrm{vac}} = 4c_{2,0}\frac{B_0^2}{\mu_0^2}\mathbf{B}_\gamma + 8c_{2,0}\frac{\mathbf{B}_{\mathrm{ext}}}{\mu_0^2}(\mathbf{B}_\gamma\cdot\mathbf{B}_{\mathrm{ext}}) \tag{1.29}$$

where $\mathbf{E}_\gamma$ and $\mathbf{B}_\gamma$ are the electric and magnetic fields of the incident wave.

The tensorial electric permittivity $[\varepsilon]$ and tensorial magnetic permeability $[\mu]$ are defined as $\mathbf{D} = [\varepsilon]\mathbf{E}$ and $\mathbf{B} = [\mu]\mathbf{H}$. Using expressions (1.2) for **H** and **D** one finds the following equations:

$$\begin{aligned}
\mathbf{D}_{\text{vac}} &= \left(\varepsilon_0 - 4c_{2,0}\varepsilon_0\frac{B_0^2}{\mu_0}\right)\mathbf{E}_\gamma + 2c_{0,2}\frac{\varepsilon_0}{\mu_0}\mathbf{B}_{\text{ext}}(\mathbf{E}_\gamma\cdot\mathbf{B}_{\text{ext}}) \\
\mathbf{H}_{\text{vac}} &= \left(\frac{1}{\mu_0} + 4c_{2,0}\frac{B_0^2}{\mu_0^2}\right)\mathbf{B}_\gamma + 8c_{2,0}\frac{\mathbf{B}_{\text{ext}}}{\mu_0^2}(\mathbf{B}_\gamma\cdot\mathbf{B}_{\text{ext}}).
\end{aligned} \tag{1.30}$$

The terms $(\mathbf{E}_\gamma\cdot\mathbf{B}_{\text{ext}})$ and $(\mathbf{B}_\gamma\cdot\mathbf{B}_{\text{ext}})$ depend on the polarisation of the incident wave. When the polarisation direction is parallel ($\|$) to or perpendicular ($\perp$) to the external field we have that:

$$\begin{aligned}
\varepsilon_\| &= \varepsilon_0\left(1 - 4c_{2,0}\frac{1}{\mu_0}B_{\text{ext}}^2 + 2c_{0,2}\frac{1}{\mu_0}B_{\text{ext}}^2\right) \\
\varepsilon_\perp &= \varepsilon_0\left(1 - 4c_{2,0}\frac{1}{\mu_0}B_{\text{ext}}^2\right) \\
\Delta\varepsilon &= \varepsilon_\| - \varepsilon_\perp = 2c_{0,2}\frac{\varepsilon_0}{\mu_0}B_{\text{ext}}^2
\end{aligned} \tag{1.31}$$

and

$$\begin{aligned}
\mu_\| &= \mu_0\left(1 + 4c_{2,0}\frac{1}{\mu_0^2}B_{\text{ext}}^2\right) \\
\mu_\perp &= \mu_0\left(1 + 12c_{2,0}\frac{1}{\mu_0^2}B_{\text{ext}}^2\right) \\
\Delta\mu &= \mu_\| - \mu_\perp = -8c_{2,0}\frac{1}{\mu_0}B_{\text{ext}}^2.
\end{aligned} \tag{1.32}$$

One can therefore calculate the refractive index using the definition (1.1),

$$\begin{aligned}
n_\| &= 1 + c_{0,2}\frac{B_{\text{ext}}^2}{\mu_0} \\
n_\perp &= 1 + 4c_{2,0}\frac{B_{\text{ext}}^2}{\mu_0}.
\end{aligned} \tag{1.33}$$

From the last two equations, one sees that the velocity of the light is less than c even in vacuum. Furthermore, there is a birefringence given by:

$$\Delta n_{\text{vac}} = n_\| - n_\perp = (c_{0,2} - 4c_{2,0})\frac{B_{\text{ext}}^2}{\mu_0} \tag{1.34}$$

Recalling that $c_{0,2} = 7c_{2,0}$ one can write

$$\Delta n_{\text{vac}} = 3A_e B_{\text{ext}}^2 \tag{1.35}$$

where

$$A_e = \frac{2\alpha^2}{45\mu_0}\frac{(\hbar/m_e c)^3}{m_e c^2} = 1.32 \times 10^{-24}\ \text{T}^{-2}. \tag{1.36}$$

For example, with a laboratory magnetic field intensity of 2.5 T the value of the anisotropy Δn_{vac} is:

$$\Delta n_{\text{vac}} \approx 2.5 \cdot 10^{-23} \quad @ \quad 2.5\ \text{T}. \tag{1.37}$$

At the same order of approximation, we can calculate the Kerr effect in vacuum, Δn_K, in the presence of a static electric field $\mathbf{E}_{\text{ext}}$. The result is that Δn_K has an expression analogous to Δn_{vac}, but with opposite sign and the field B_{ext} substituted with E_{ext}/c:

$$\Delta n_{K,\text{vac}} = -\frac{3A_e}{c^2}E_{\text{ext}}^2. \tag{1.38}$$

Let's note that, due to the factor $1/c^2$, the effect of a 1 T magnetic field is obtained with a 300 MV/m electric field.

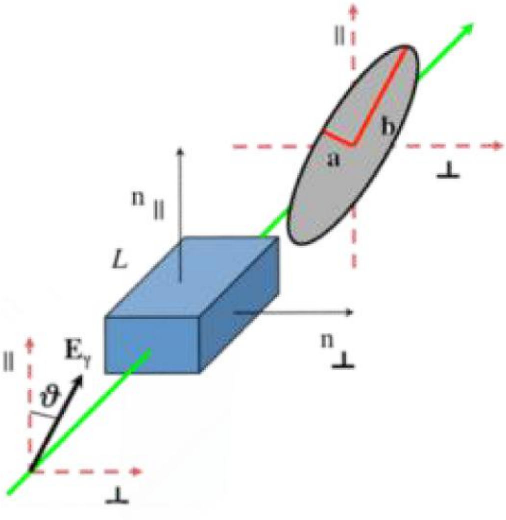

Figure 1.2: Linearly polarised light traversing a birefringent medium acquires an ellipticity ψ.

A direct measurement of the anisotropy Δn_{vac} can be made by measuring the ellipticity acquired by a linearly polarised laser beam passing through the birefringent vacuum. The two components of a linearly polarised beam of light passing through a birefringent region of length L in the direction orthogonal to the direction of the magnetic field acquire a small phase difference $\delta\phi$:

$$\delta\phi = 2\pi\frac{L}{\lambda}(n_{\parallel} - n_{\perp})\sin 2\vartheta \tag{1.39}$$

where λ is the wavelength of the light and ϑ is the angle between the direction of the electric field of the linearly polarised beam and the direction of the external magnetic field. At the output of the birefringent region the beam acquires an ellipticity ψ (see figure 1.2) given by:

$$\psi_{\mathrm{vac}} = \frac{\delta\phi}{2} = \pi\frac{L}{\lambda}\Delta n_{\mathrm{vac}}\sin 2\vartheta \tag{1.40}$$

which is the ratio of the minor axis to the major axis of the ellipse described by the electric field of the wave.

In general, also absorption can be described using the complex index of refraction:

$$\widehat{n} = n + i\kappa. \tag{1.41}$$

If the absorption is anisotropic, the medium is said to be dichroic. The relationship between the extinction coefficient κ and the absorption coefficient μ is given by $\mu = \frac{4\pi\kappa}{\lambda}$. It has been shown that the dichroism generated by a magnetic field due to e^+e^- pairs is negligible [19]: no significant imaginary part κ of the index of refraction is predicted in QED.

1.2.1 Higher order QED corrections

Figure 1.1*g)* shows one of the Feynman diagrams for the α^3 contribution to vacuum magnetic birefringence (radiative corrections to the 1.1*e)* diagram). The effective Lagrangian density for this correction has been evaluated [20] and can be expressed as

$$\mathscr{L}_{\mathrm{rad}} = \frac{A_e}{\mu_0}\left(\frac{\alpha}{\pi}\right)\frac{10}{72}\left[32\left(\frac{E^2}{c^2} - B^2\right)^2 + 263\left(\frac{\mathbf{E}}{c}\cdot\mathbf{B}\right)^2\right]. \tag{1.42}$$

This Lagrangian leads to a 1.45% extra contribution Δn_{rad} to the vacuum magnetic birefringence given in equation (1.35):

$$\Delta n_{\mathrm{rad}} = \frac{25\alpha}{4\pi}3A_e B_{\mathrm{ext}}^2 = 0.0145\cdot\Delta n_{\mathrm{vac}}. \tag{1.43}$$

1.3 Other effects generating magnetic birefringence in vacuum

Looking over the e^+e^- loop [Figs. 1.1*e)* and 1.1*g)*], let us consider other contributions to MBV. As already mentioned, contributions of muon loops are estimated to be depressed with respect to those of the electron loops by a factor $(m_e/m_\mu)^4 \approx 5.5 \times 10^{-10}$ and so to be negligible. For the same reason, contributions from $q\bar{q}$ charged hadron loops [Fig. 1.1*h)*] are expected to be depressed by a factor between $(m_e/m_q)^4$ and $(m_e/m_\pi)^4$ [21]. However, the hadronic contributions are not completely under control because of the difficulties of QCD calculations in the low energy regime [21].

Coming to the realm of speculations, the very same diagram of Fig. 1.1*e)* might apply to so far hypothetical light particles with fractional charge (milli-charged particles, MCP) [22, 23]. The diagram of Fig. 1.1*f)* applies instead to a neutral boson weakly coupled to two photons and called Axion-like particle (ALP) [24–26]. In the presence of an external transverse field, both can give place to magneto-optical effects.

1.3.1 Axion Like Particles

Weak experimental limits exist for the contribution of axion-like particles (ALPs) [see fig.1*f)*]. The best model independent experimental limits on the mass and the coupling constant of ALPs with mass $m > 10^{-3}$ eV are due to limits on the observed ellipticity in experiments aiming at detecting MBV induced ellipticity. The limits obtained by the PVLAS collaboration will be presented in this thesis as ellipticity noise. MBV experiments could become appealing in searches for ALPs if and when their sensitivity would become competitive with regeneration experiments like CAST [27, 28].

The measurement of the ellipticity and the rotation (due to a dichroism), induced by ALPs can in principle fully characterise the pseudoscalar or scalar nature of the hypothetical boson particle, its mass $m_{a,s}$ and its coupling constant $g_{a,s}$. In their paper, in which polarimetry for the detection of ALPs is proposed for the first time, L. Maiani, R. Petronzio and E. Zavattini were motivated by the search for axions [24] related to QCD. These particles are pseudoscalar, neutral, and spinless bosons introduced [29–32] to solve the *strong CP problem*, namely the fact that there is no experimentally observed CP violation in quantum chromodynamics, even if there is no known reason for CP to be conserved in QCD. A discussion of non-Standard Model physics in external fields can be found in ref. [33]. Magnetic birefringence accompanied by magnetic dichroism may, however, be generated in a vacuum by the hypothetical light bosonic spin zero ALP, in analogy with the Primakoff effect [34]. The processes causing birefringence are shown in Fig. 1.1*f)*. The Lagrangian density describing the interaction of a pseudoscalar field ϕ_a and scalar field ϕ_s with two photons can be expressed as (for convenience, we use the natural Heavyside-Lorentz units, so that $1\ \mathrm{T} = \sqrt{\frac{\hbar^3 c^3}{e^4 \mu_0}} = 195\ \mathrm{eV}^2$ and $1\ \mathrm{m} = \frac{\mathrm{e}}{\hbar\mathrm{c}} = 5.06 \times 10^6\ \mathrm{eV}^{-1}$)

$$\begin{aligned} \mathscr{L}_a &= g_a \phi_a \mathbf{E} \cdot \mathbf{B} \\ \mathscr{L}_s &= g_s \phi_s \left(E^2 - B^2\right) \end{aligned} \qquad (1.44)$$

where g_a and g_s are the coupling constants of a pseudoscalar field ϕ_a and of a scalar field ϕ_s, respectively. Considering the pseudoscalar case, it is clear from these expressions that in the presence of an external uniform magnetic field $\mathbf{B}_{\mathrm{ext}}$, a photon with electric field $\mathbf{E}_\gamma$ parallel to $\mathbf{B}_{\mathrm{ext}}$ will interact with the pseudoscalar field whereas for electric fields perpendicular to $\mathbf{B}_{\mathrm{ext}}$ there is no such interaction. For the scalar case the opposite is true: an interaction will exist if $\mathbf{E}_\gamma \perp \mathbf{B}_{\mathrm{ext}}$ and does not if $\mathbf{E}_\gamma \parallel \mathbf{B}_{\mathrm{ext}}$. When an interaction is present, the photon oscillates into the pseudoscalar/scalar particle. For photon energies above the mass $m_{a,s}$ of such particle candidates, a real production can follow. On the other hand, even if the photon energy is smaller than the mass of the particles, virtual production is possible, therefore causing a phase delay to the photons with a direction of the electric field that allows an interaction. The net result is that the presence of these particles causes a vacuum dichroism (selective absorption in function of the photon's polarisation state) and vacuum birefringence. The measurable effects of these two properties is an apparent rotation of the polarisation plane θ (apparent because there is a net loss in photons) and an ellipticity ψ due to the phase delay between the two polarisation directions. The ellipticity ψ is related to the birefringence $\Delta n^{(\mathrm{ALP})}$ and the rotation θ is related to the extinction coefficient $\Delta\kappa^{(\mathrm{ALP})}$ by

$$\begin{aligned} \psi &= \pi \frac{\Delta n^{(\mathrm{ALP})} L}{\lambda} \\ \theta &= \pi \frac{\Delta \kappa^{(\mathrm{ALP})} L}{\lambda} \end{aligned} \qquad (1.45)$$

The ellipticity ψ and the rotation θ of the polarisation of an electromagnetic wave, with polarisation allowing an interaction according to the Lagrangian densities (1.44), can be expressed, for both the scalar and pseudoscalar cases, as [24, 25, 35]:

$$\psi = \frac{\omega L g_{a,s}^2 B_{\mathrm{ext}}^2}{4 m_{a,s}^2} \left(1 - \frac{\sin 2x}{2x}\right) \qquad (1.46)$$

$$\theta = \left(\frac{g_{a,s} B_{\mathrm{ext}} L}{4}\right)^2 \left(\frac{\sin x}{x}\right)^2 \qquad (1.47)$$

where, in vacuum, $x = \frac{Lm_{a,s}^2}{4\omega}$, ω is the photon energy and L is the magnetic field length. Therefore in the pseudoscalar case, where ($n_\parallel^a > 1$, $\kappa_\parallel^a \neq 0$) and ($n_\perp^a = 1$, $\kappa_\perp^a = 0$) and in the scalar case, where ($n_\perp^s > 1$, $\kappa_\perp^s \neq 0$) and ($n_\parallel^s = 1$, $\kappa_\parallel^s = 0$), one also has [32]

$$
\begin{aligned}
|\Delta n^{(\mathrm{ALP})}| &= n_\parallel^a - 1 = n_\perp^s - 1 = \frac{g_{a,s}^2 B_{\mathrm{ext}}^2}{2m_{a,s}^2}\left(1 - \frac{\sin 2x}{2x}\right), \\
|\Delta\kappa^{(\mathrm{ALP})}| &= \kappa_\parallel^a = \kappa_\perp^s = \frac{2}{\omega L}\left(\frac{g_{a,s}B_{\mathrm{ext}}L}{4}\right)^2\left(\frac{\sin x}{x}\right)^2.
\end{aligned}
\tag{1.48}
$$

1.3.2 Millicharged particles

Let us consider the interactions between the laser beam and the magnetic field mediated by vacuum fluctuations of hypothetical particles with fractional charge $\pm\varepsilon e$ and mass m_ε as discussed in references [22, 23]. The photons passing through a uniform magnetic field can interact with such fluctuations. If the photon energy ω is $\omega > 2m_\varepsilon$, this results in the production of real pairs accompanied by an amplitude depletion of the incident photon. If the photon energy is $\omega < 2m_\varepsilon$, only a phase delay will result. This situation applies to both fermions or bosons with spin-0. Now we will discuss birefringence effects (real part) and dichroism (imaginary part) of the complex refraction index (1.41) due to these hypothetical particles.

- Dirac fermions

Consider the case in which the particles are millicharged Dirac fermions (DF). As derived in Refs [36, 37], the indices of refraction of photons with polarisation parallel and perpendicular to the external magnetic field have two different regimes of mass defined by the value of a dimensionless parameter χ (S.I. units):

$$
\chi \equiv \frac{3}{2}\frac{\hbar\omega}{m_\varepsilon c^2}\frac{\varepsilon e B_{\mathrm{ext}}\hbar}{m_\varepsilon^2 c^2}
\tag{1.49}
$$

It can be shown that [22, 23]

$$
n_{\parallel,\perp}^{(\mathrm{Df})} = 1 + I_{\parallel,\perp}^{(\mathrm{Df})}(\chi) A_\varepsilon B_{\mathrm{ext}}^2
\tag{1.50}
$$

with

$$
I_{\parallel,\perp}^{(\mathrm{Df})}(\chi) = \begin{cases} \left[(7)_\parallel, (4)_\perp\right] & \text{for } \chi \ll 1 \\ -\frac{9}{7}\frac{45}{2}\frac{\pi^{1/2}2^{1/3}\left(\Gamma(\frac{2}{3})\right)^2}{\Gamma(\frac{1}{6})}\chi^{-4/3}\left[(3)_\parallel, (2)_\perp\right] & \text{for } \chi \gg 1 \end{cases}
$$

and

$$A_\varepsilon = \frac{2}{45\mu_0}\frac{\varepsilon^4\alpha^2\bar{\lambda}_\varepsilon^3}{m_\varepsilon c^2} \tag{1.51}$$

in analogy to equation (1.36), and where Γ is the Euler gamma function.

In the limit of large masses ($\chi \ll 1$) these expressions reduce to the QED case with the substitution of εe with e and m_ε with m_e in equation (1.50). The dependence on B_ext remains the same as for the well known QED prediction. For small masses ($\chi \gg 1$) the index of refraction now also depends on the parameter $\chi^{-4/3}$ resulting in a net dependence of Δn on $B_\mathrm{ext}^{2/3}$ rather than B_ext^2. The induced birefringence is in both mass regimes

$$\Delta n^{(\mathrm{Df})} = A_\varepsilon B_\mathrm{ext}^2 \begin{cases} 3 & \text{for } \chi \ll 1 \\ -\frac{9}{7}\frac{45}{2}\frac{\pi^{1/2}2^{1/3}\left[\Gamma\left(\frac{2}{3}\right)\right]^2}{\Gamma\left(\frac{1}{6}\right)}\chi^{-4/3} & \text{for } \chi \gg 1. \end{cases} \tag{1.52}$$

For the dichroism one finds [23, 36, 37],

$$\Delta\kappa^{(\mathrm{Df})} = \frac{1}{8\pi}\frac{\varepsilon^3 e\alpha\lambda B_\mathrm{ext}}{m_\varepsilon c} \begin{cases} \sqrt{\frac{3}{32}}\,e^{-4/\chi} & \text{for } \chi \ll 1 \\ \frac{2\pi}{3\Gamma(\frac{1}{6})\Gamma(\frac{13}{6})}\chi^{-1/3} & \text{for } \chi \gg 1. \end{cases} \tag{1.53}$$

- Spin-0 charged bosons

We obtain very similar expressions to the Dirac fermion case also for the spin-0 (s0) charged particle case [23, 37]. We define two mass regimes by the same parameter χ of expression (1.49). In this case, the indices of refraction for the two polarisation states on the magnetic field direction are

$$n^{s0}_{\parallel,\perp} = 1 + I^{s0}_{\parallel,\perp}(\chi) A_\varepsilon B_\mathrm{ext}^2 \tag{1.54}$$

with

$$I^{s0}_{\parallel,\perp}(\chi) = \begin{cases} \left[\left(\frac{1}{4}\right)_\parallel, \left(\frac{7}{4}\right)_\perp\right] & \text{for } \chi \ll 1 \\ -\frac{9}{14}\frac{45}{2}\frac{\pi^{1/2}2^{1/3}(\Gamma(\frac{2}{3}))^2}{\Gamma(\frac{1}{6})}\chi^{-4/3}\left[\left(\frac{1}{2}\right)_\parallel, \left(\frac{3}{2}\right)_\perp\right] & \text{for } \chi \gg 1. \end{cases}$$

Vacuum magnetic birefringence is therefore

$$\begin{aligned} \Delta n^{s0} &= A_\varepsilon B_\mathrm{ext}^2 \left[I^{s0}_\parallel(\chi) - I^{s0}_\perp(\chi)\right] = \qquad (1.55) \\ &= A_\varepsilon B_\mathrm{ext}^2 \begin{cases} -\frac{6}{4} & \text{for } \chi \ll 1 \\ \frac{9}{14}\frac{45}{2}\frac{\pi^{1/2}2^{1/3}(\Gamma(\frac{2}{3}))^2}{\Gamma(\frac{1}{6})}\chi^{-4/3} & \text{for } \chi \gg 1 \end{cases} \end{aligned}$$

and vacuum dichroism is given by

$$\Delta\kappa^{(\mathrm{s0})} = \frac{1}{8\pi}\frac{\varepsilon^3 e\alpha\lambda B_{\mathrm{ext}}}{m_\varepsilon c}\begin{cases} -\sqrt{\frac{3}{8}}\,e^{-4/\chi} & \text{for } \chi \ll 1 \\ -\dfrac{\pi}{3\Gamma(\frac{1}{6})\Gamma(\frac{13}{6})}\chi^{-1/3} & \text{for } \chi \gg 1. \end{cases} \tag{1.56}$$

Note that there is a difference in sign, in both the birefringence Δn and in the dichroism $\Delta\kappa$ induced by an external magnetic field in the presence of Dirac fermions compared to the case where there are spin-0 particles.

Chapter 2

Experimental method

This chapter presents the experimental method followed by the PVLAS experiment to detect the magnetic birefringence of vacuum. This matter is treated here only in principle; a characterisation of the actual apparatus is found in Chapter 3. The first idea is due to E. Iacopini and E. Zavattini [38]. The innovative strategy is still essentially the same as of 1979, while many significant improvements have been devised. The main building blocks of the scheme are a magnetic field region, a pair of crossed polarisers, heterodyne detection, and an optical path multiplier. A few technical issues necessary for the comprehension and the auto-consistency of the presentation have been added; I tried to keep their treatment as concise as possible.

2.1 Magnetic polarimetry

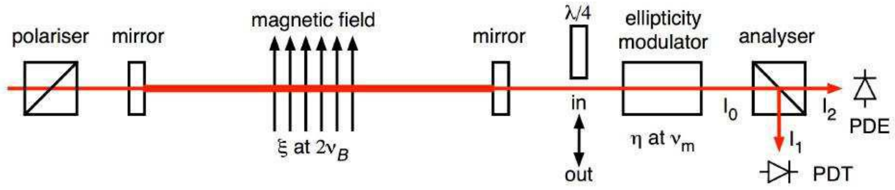

Figure 2.1: Principle scheme of the PVLAS polarimeter. PDE: Extinction Photodiode; PDT: Transmission Photodiode.

Figure 2.1 shows a principle scheme of the PVLAS polarimeter. A linearly polarised light beam (wavelength λ) is fed to a Fabry-Perot optical cavity, consisting of two mirrors. The beam in the Fabry-Perot cavity traverses the bore of a dipole magnet, with the magnetic field direction orthogonal to the light propagation direction and making an angle $\phi(t)$, variable in time, with respect to the polarisation direction. The birefringence and/or dichroism induced in the medium by the magnetic field generates a time dependent effect: an ellipticity, a rotation or both. An ellipticity modulator adds then a small variable ellipticity $\eta(t) \ll 1$ to the polarisation of the beam transmitted by the cavity. The ellipticity $\eta(t)$ will beat with the ellipticity generated by the magnetic field but not with the rotation. For rotation measurements, a quarter-wave-plate (QWP) is inserted at the exit of the cavity with one of its axes aligned to the input polarisation, converting the electric field rotation acquired by the beam in the magnetic field region into an ellipticity (and, at the same time, the ellipticity into a rotation). Finally, a polariser, crossed with respect to the input prism, extinguishes the polarisation component of the beam parallel to the input polarisation. The residual intensity is collected by a light detector, and then Fourier analysed. In the present set-up, the complete polarimeter depicted in Fig. 2.1 is kept under pneumatic vacuum.

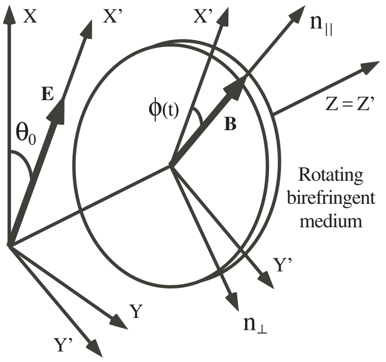

Figure 2.2: Reference frame for the calculations. XY: laboratory coordinates; X': the direction of the electric field as defined by the polariser; $n_{\|}$: the direction of the magnetic field, rotating around the beam path Z at a frequency ν_B.

To calculate the effect, we use the Jones matrices [39] to describe the beam and the optical elements. This technique ignores beam divergence which generates, through the Fresnel formulas, a polarisation pattern across the surface of the beam. For simplicity, the optical components are also considered ideal, namely not affecting intensity, and the extinction factor of the polarisers σ^2 is assumed negligible. In these approximations, the ellipticity modulator is described by the matrix

$$\mathbf{H} = \begin{pmatrix} 1 & i\eta \\ i\eta & 1 \end{pmatrix},$$

the quarter wave-plate is given by

$$\mathbf{Q} = \begin{pmatrix} q & 0 \\ 0 & q^* \end{pmatrix},$$

where $q = 1$ for ellipticity measurements, when the wave-plate is out of the optical path and $\mathbf{Q}$ therefore coincides with the identity matrix $\mathbf{I}$, whereas $q = (1+i)/\sqrt{2}$ for rotation measurements. The general optical element representing a linear magnetic birefringence and a dichroism can be written, in its axes and neglecting an overall attenuation factor, as

$$\mathbf{X}_0 = \begin{pmatrix} e^{\xi} & 0 \\ 0 & 1 \end{pmatrix},$$

where ξ is a small complex number that we write as $\xi = i2\psi - 2\theta$ $(\theta, \psi \ll \eta \ll 1)$. The quantity 2ψ is the phase difference between the two polarisation directions acquired in the birefringent medium and $1 - e^{-2\theta}$ is the fraction of the electric field absorbed in the dichroic medium. Without loss of generality, we consider the x direction (X' direction of Figure 2.2) as the absorbing as well as the slow axis. The quantity ψ is the maximum ellipticity[1] that the light can acquire due to $\mathbf{X}_0$, while θ is the maximum rotation. Both correspond to an angle $\phi = 45^\circ$ between the polarisation direction and the magnetic field direction. In the case of the vacuum birefringence of equation (1.40), for a length $L = 1.64$ m of a magnetic field $B_{\text{ext}} = 2.5$ T and light wavelength $\lambda = 1.064$ μm, the ellipticity ψ due to the vacuum magnetic birefringence is

$$\psi_{\text{vac}} = \pi \frac{\Delta n_{\text{vac}} L}{\lambda} = 1.2\ 10^{-16}. \tag{2.1}$$

In the particular case of QED, dichroism is unmeasurably small.

Placing $\mathbf{X}_0$ at an angle ϕ with respect to the polarisation direction, one finds

$$\mathbf{X}(\phi) = \frac{1}{2} \begin{pmatrix} 1 - \cos 2\phi + e^{\xi}(1 + \cos 2\phi) & -\left(1 - e^{\xi}\right) \sin 2\phi \\ -\left(1 - e^{\xi}\right) \sin 2\phi & 1 + \cos 2\phi + e^{\xi}(1 - \cos 2\phi) \end{pmatrix}.$$

To show the salient features of our polarimetric method, we begin with neglecting the effect of the Fabry-Perot cavity. The electric field at the analyser is then represented by

$$\mathbf{E}(\phi) = \begin{pmatrix} E_1 \\ E_2 \end{pmatrix} = E_0 \mathbf{H} \cdot \mathbf{Q} \cdot \mathbf{X}(\phi) \cdot \begin{pmatrix} 1 \\ 0 \end{pmatrix}. \tag{2.2}$$

---

[1] The ellipticity is the ratio of the minor to the major axis of the ellipse described by the electric field vector of the light.

Components	Frequency	Amplitude (in units of I_0)
I_{DC}	DC	$\eta_0^2/2$
I_-	$\nu_\mathrm{m} - 2\nu_B$	$\eta_0 \psi$
I_+	$\nu_\mathrm{m} + 2\nu_B$	$\eta_0 \psi$
$I_{2\nu_\mathrm{m}}$	$2\nu_\mathrm{m}$	$\eta_0^2/2$

Table 2.1: Fourier components of the extinguished intensity signal.

The two polarisation states are spatially separated by the analyser and collected by two photodiodes. For ellipticity measurements (quarter-wave-plate not inserted), the intensity collected at the photodiode PDE is

$$I_2^{\mathrm{ell}}(\phi) = I_0 \left(\eta^2 + 2\eta\,\psi \sin 2\phi\right) + \text{higher order terms}. \tag{2.3}$$

For rotation measurements, with the quarter-wave-plate inserted,

$$I_2^{\mathrm{rot}}(\phi) = I_0 \left(\eta^2 + 2\eta\,\theta \sin 2\phi\right) + \text{higher order terms}. \tag{2.4}$$

The light having the same polarisation as the input is collected at the photodiode PDT and has intensity

$$I_1 \approx I_0 = \varepsilon_0 c \frac{E_0^2}{2}.$$

We employ the heterodyne method to measure ψ and θ: the angle ϕ is varied linearly as a function of time as $\phi(t) = 2\pi\nu_B t + \phi_B$ and η as $\eta(t) = \eta_0 \cos(2\pi\nu_\mathrm{m} t + \phi_\mathrm{m})$, with $\nu_B \ll \nu_\mathrm{m}$. The sought for values of each of the quantities ψ and θ are extracted from the measurement of I_1 and from the amplitude and phase of three components in a Fourier transform of the extinguished intensity I_2: the component $I_{2\nu_\mathrm{m}}$ at $2\nu_\mathrm{m}$ and the components $I_\pm$ at $\nu_\mathrm{m} \pm 2\nu_B$. The main signal components in the frequency range from 0 to $2\nu_\mathrm{m}$ are shown in table 2.1 in the case of an ellipticity measurement. Similar expressions hold in the case of a rotation measurement, with ψ replaced by θ. Note that in our approximations no first harmonic of the modulator (I_{ν_m}) should be seen at frequency ν_m. This frequency component appears in the spectrum due to the presence of static birefringences on all the optical elements. However, as will be seen in the next chapter, this component is stably maintained at zero in the normal functioning of the polarimeter. The ellipticity and rotation values are then obtained as

$$\psi, \theta = \frac{I_- + I_+}{2\sqrt{2 I_0 I_{2\nu_\mathrm{m}}}} = \frac{\eta_0}{4} \frac{I_- + I_+}{I_{2\nu_\mathrm{m}}}. \tag{2.5}$$

If a lock-in amplifier is used to demodulate the residual intensity at the frequency $\nu_{\rm m}$, instead of I_+ and I_- one finds a single component at $2\nu_B$, and the resulting ellipticity and rotation signals are

$$\psi,\theta = \frac{I_{2\nu_B}}{2\sqrt{2I_0 I_{2\nu_{\rm m}}}} = \frac{\eta_0}{4}\frac{I_{2\nu_B}}{I_{2\nu_{\rm m}}}. \tag{2.6}$$

The ellipticity and rotation signals come with a distinct phase that, in the case a lock-in amplifier is employed, is $2\phi_B$. With reference to the Figure 2.2, one can observe that the value of ϕ_B is $-\theta_0$, with θ_0 the angle between a reference direction X and the polarisation direction. With this position, the axes of $\mathbf{X}_0$ coincide with the laboratory axes (XY) and the ellipticity is maximum at the time $t_0 = (\theta_0 + \pi/4)/(2\pi\nu_B)$. We will return to this point in the calibration section.

2.2 Optical path multiplier

Given the smallness of the sought for optical effects, an amplification scheme is necessary. In the PVLAS experiment, this is obtained by the use of a Fabry-Perot (FP) cavity. This choice came into the project of the experiment at the beginning of the '90s [40] to overcome the limitations of the multi-pass cavities that were used before as optical path multipliers [35]. In fact, multi-pass cavities require large mirrors and hence a large volume of magnetic field; moreover, the path multiplication factor is limited to $\approx 10^3$ at most [35]. The FP was employed for the first time in 1994 by the PVLAS group for a measurement of the Faraday effect of air [41]. The first published data came only in 1995 [42]. In this section, we make a broad presentation of the Fabry-Perot cavity. For the purpose of completeness, a brief account is given in appendix of the topic of dielectric mirrors.

2.2.1 Fabry-Perot cavity

The FP interferometric cavity consists of two aligned mirrors separated by a distance d. Although interferometers make use of spherical mirrors and Gaussian beams, we analyse the case of a plane wave of amplitude E_0 and frequency ν incident on two plane and parallel mirrors. This approach is justified as the wavelength is much smaller than the diameter of the beam; in an appendix we will tackle the argument of the Gaussian beams. In this section, the optical response of the interferometer is analysed in terms of the multiple interference of the beams produced by partial reflections on the mirrors (see Fig. 2.3). Let $r_{1,2}$ and $t_{1,2}$ be the reflection and transmission coefficients of the reflecting surfaces of the two mirrors. The back surfaces are assumed to have $t = 1$ and $r = 0$. It must be noted that, following the

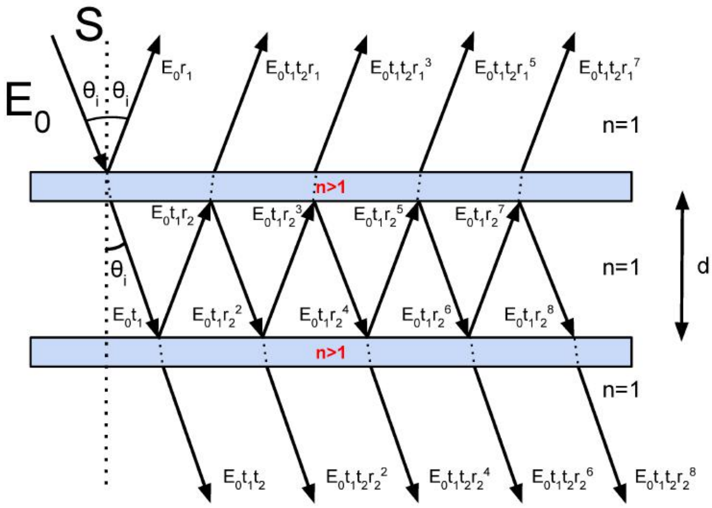

Figure 2.3: Multiple interference between two plane parallel mirrors.

Fresnel formulae [43], to r_1 and r_2 a 180° phase change is associated, whereas t_1 and t_2 are positive. Mirror reflection is always characterised by some small absorption and scattering, diffraction losses being negligible, as negligible is the absorption due to the medium between the mirrors (low pressure gas or vacuum). The analysis is carried out at an incident angle θ_i and the limit $\theta_i \to 0$ is then taken. The electric field transmitted through the cavity can be written by summing the amplitudes of all the partial rays:

$$\begin{aligned} E_{\mathrm{T}} &= t_1t_2E_0 + t_1t_2r_1r_2e^{i\delta}E_0 + t_1t_2(r_1r_2e^{i\delta})^2E_0 + \ldots = \\ &= t_1t_2E_0\sum_{n=0}^{\infty}(r_1r_2e^{i\delta})^n = E_0\frac{t_1t_2}{1-r_1r_2e^{i\delta}}. \end{aligned} \tag{2.7}$$

In the first row of this equation, the first term, with the phase arbitrarily set to zero, represents the amplitude of the first ray that has passed the slab without reflections; the second term describes the second ray that has reflected twice before exiting; and so on. Relative to the previous one, each term has a phase difference δ given by the optical path difference $2d\cos\theta_i$. The limit $\theta_i \to 0$ simply corresponds to $\cos\theta_i \to 1$. The phase difference corresponding to this optical path difference is then:

$$\delta = \frac{4\pi d}{\lambda} = \frac{4\pi d\,\nu}{c}, \tag{2.8}$$

where $\lambda = c/\nu$ is the wavelength of the light in vacuum. The phase δ can equally well be considered a function of the distance d between mirrors, of the wavelength λ or of the frequency of the light ν.

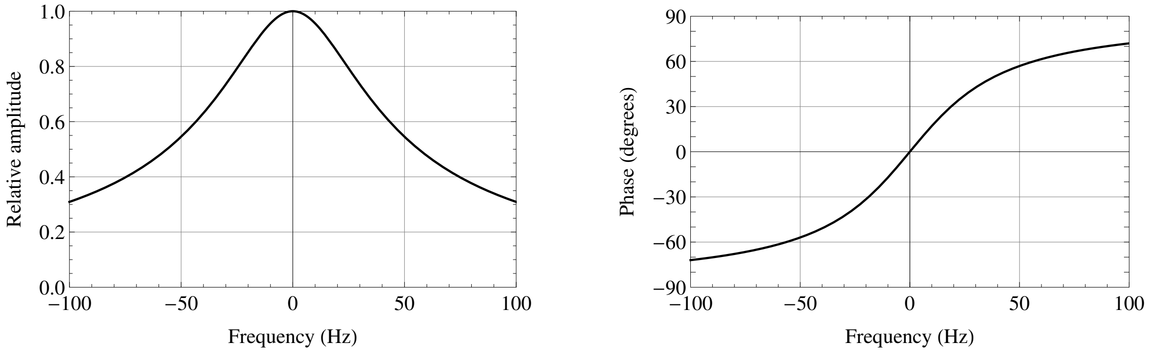

Figure 2.4: Left: normalised amplitude of the electric field transmitted by a FP cavity with $d = 3.303$ m, $r_1 r_2 = 0.9999955$ and $t_1 t_2 = 2.4 \times 10^{-6}$ as a function of the frequency difference from the maximum. Right: phase ϕ_T of the transmitted electric field.

The transmitted electric field is maximum for $\cos\delta = 1$, namely for

$$d = m\frac{\lambda}{2} \qquad \text{or} \qquad \nu = m\frac{c}{2d}$$

where m, the *order of interference*, is any integer. In other words, maximum transmission occurs when the distance between the two reflecting surfaces is an integer multiple of the half wavelength, or if the frequency of the light is a multiple of the *free spectral range* frequency

$$\nu_{\text{fsr}} = \frac{c}{2d} \tag{2.9}$$

Figure 2.4 shows the relative amplitude and the phase of the transmitted electric field

$$|E_{\text{T}}(\delta)| = E_0 \frac{t_1 t_2}{\sqrt{1 + r_1^2 r_2^2 - 2 r_1 r_2 \cos\delta}} \tag{2.10}$$

$$\phi_T = \arctan\frac{r_1 r_2 \sin\delta}{1 - r_1 r_2 \cos\delta}. \tag{2.11}$$

Coming to intensities, we assume for simplicity that the two reflecting surfaces have the same transmittance and reflectance:

$$t_1^2 = t_2^2 = T \qquad r_1^2 = r_2^2 = R;$$

hence

$$I_{\mathrm{T}}(\delta) = I_0 \frac{T^2}{1+R^2-2R\cos\delta}, \tag{2.12}$$

where $I_0 = c\varepsilon_0 E_0^2/2$. The maximum transmitted intensity is

$$I_{\mathrm{T,max}} = I_0 \frac{T^2}{(1-R)^2},$$

The transmitted intensity can be cast in the canonical Airy form

$$I_{\mathrm{T}} = I_{\mathrm{T,max}} \frac{1}{\left(1+F\sin^2\frac{\delta}{2}\right)}, \tag{2.13}$$

having defined the coefficient F as

$$F = \frac{4R}{(1-R)^2}.$$

As a function of δ, the transmitted intensity appears as a series of equispaced interference peaks separated by large dark regions. For high reflectance, the peaks are very narrow, and their frequency full-width at half-maximum ν_{c} can be calculated as

$$\frac{1}{2} = \frac{1}{1+F\sin^2(\pi\nu_{\mathrm{c}}/2\nu_{\mathrm{fsr}})} \qquad \text{or} \qquad \nu_{\mathrm{c}} = \frac{\nu_{\mathrm{fsr}}(1-R)}{\pi\sqrt{R}}.$$

The quantity

$$\mathscr{F} = \frac{\nu_{\mathrm{fsr}}}{\nu_{\mathrm{c}}} = \frac{\pi\sqrt{R}}{1-R} \tag{2.14}$$

is called the *finesse* of the interferometer. It depends only on the reflectance of the mirrors.

The field inside the cavity is a quasi-stationary wave, whose amplitude can be calculated by summing the contributions of all the partial wavelets. On top of the resonance

$$E_{\mathrm{inside}} = \frac{E_T}{t_2} = E_0 \frac{t_1}{1-r_1 r_2}.$$

The Fabry-Perot cavity is thus an electric field intensifier. In the absence of an input wave, the internal field decays with a time constant dictated by the reflectance of the mirrors: in a complete round trip, corresponding to a time interval $\Delta t = 2d/c = 1/\nu_{\mathrm{fsr}}$, the amplitude decays as $E'_{\mathrm{inside}} = r_1 r_2 E_{\mathrm{inside}}$ or

$$E_{\mathrm{inside}}(t) = E_{\mathrm{inside}}(0)\, e^{-t/\tau_E},$$

where

$$\tau_E = -\frac{1}{\nu_{\rm fsr}}\frac{1}{\ln r_1 r_2} \approx \frac{1}{\nu_{\rm fsr}}\frac{1}{1-R} \approx \frac{1}{\nu_{\rm fsr}}\frac{\mathscr{F}}{\pi}.$$

Reminding that light intensity is the square of the electric field, one has that the decay time of the intensity is $\tau = \tau_E/2$ and hence

$$\mathscr{F} = 2\pi\nu_{\rm fsr}\tau = \frac{\pi c \tau}{d}.$$

For the light reflected from the cavity we have

$$\begin{aligned} E_{\rm R} &= -r_1E_0 + t_1^2 r_2 e^{i\delta}E_0 + t_1^2 r_2 e^{i\delta} r_1 r_2 e^{i\delta} E_0 + t_1^2 r_2 e^{i\delta}(r_1 r_2 e^{i\delta})^2 E_0 + \ldots = \\ &= -r_1 E_0 + t_1^2 r_2 e^{i\delta} E_0 \sum_{n=0}^{\infty} (r_1 r_2 e^{i\delta})^n = -E_0 \frac{r_1 - r_2(r_1^2 + t_1^2)e^{i\delta}}{1 - r_1 r_2 e^{i\delta}} \end{aligned}$$

that with our assumptions can be written as

$$E_{\rm R} = rE_0 \frac{1 + R(R+T) - (T+2R)\cos\delta - iT\sin\delta}{1 + R^2 - 2R\cos\delta}.$$

Note that the quantity $A = 1 - R - T$ is the fraction of the intensity absorbed or scattered in a round trip in the cavity. The electric field reflected from the FP bears a phase difference with respect to the incident light:

$$\phi_{\rm R}(\delta) = -\arctan\left[\frac{(1-A-R)\sin\delta}{1 + R(1-A) - (1-A+R)\cos\delta}\right]. \tag{2.15}$$

As for the reflected intensity:

$$I_{\rm R}(\delta) = I_0 \frac{R[1 - 2(1-A)\cos\delta + (1-A)^2]}{1 + R^2 - 2R\cos\delta}. \tag{2.16}$$

In terms of R, T and A, the expression of the transmitted electric field is:

$$E_T = E_0 \frac{T[(1 - R\cos\delta) + iR\sin\delta]}{1 + R^2 - 2R\cos\delta} \tag{2.17}$$

with phase

$$\phi_T(\delta) = \arctan\frac{R\sin\delta}{1 - R\cos\delta}. \tag{2.18}$$

2.2.2 Polarimetry with a FP

We now show that the FP cavity amplifies the signals observed in our scheme of measurement of magneto-optical effects. To this end we write the electric field entering the analyser, taking into account Eq. (2.7) and in analogy with equation (2.2), as

$$\begin{aligned}\mathbf{E}(\delta,\phi) &= \begin{pmatrix} E_1 \\ E_2 \end{pmatrix} = E_0\,\mathbf{H}\cdot\mathbf{Q}\cdot\sum_{n=0}^{\infty}\left[Re^{i\delta}\mathbf{X}^2(\phi)\right]^n\cdot Te^{i\delta/2}\mathbf{X}(\phi)\cdot\begin{pmatrix}1\\0\end{pmatrix} = \\ &= E_0\,\mathbf{H}\cdot\mathbf{Q}\cdot\left[\mathbf{I}-Re^{i\delta}\mathbf{X}^2(\phi)\right]^{-1}\cdot Te^{i\delta/2}\mathbf{X}(\phi)\cdot\begin{pmatrix}1\\0\end{pmatrix}. \qquad (2.19)\end{aligned}$$

In the case of ellipticity measurements, since at resonance $\delta = 0$ (mod 2π), and given that $R \approx 1$, the intensity collected by photodiode PDE, at the lowest order, is

$$I_2^{\rm ell}(\phi) \simeq I_0\left[\eta^2 + \frac{4\eta\psi}{1-R}\sin 2\phi\right]. \qquad (2.20)$$

Analogously, in the case of rotation measurements, one has

$$I_2^{\rm rot}(\phi) \simeq I_0\left[\eta^2 + \frac{4\eta\theta}{1-R}\sin 2\phi\right], \qquad (2.21)$$

while

$$I_1 \approx I_{\rm T,max} = \varepsilon_0 c\frac{E_0^2}{2}\frac{T^2}{(T+A)^2}. \qquad (2.22)$$

Comparing these formulas with the corresponding ones calculated above without the Fabry-Perot cavity Equations (2.3) and (2.4), one sees that the expressions are very similar, with the latter ones having the signals ψ and θ of Equation (2.5) amplified by a factor

$$N = \frac{2}{1-R} \approx \frac{2\mathscr{F}}{\pi},$$

where $\mathscr{F}$ is the *finesse* of the cavity, that can be up to $\sim 10^6$ [44]. This amplification factor N is a *lengthening* of the optical path, as the very form of Equation (2.19) suggests.

The dynamical character of the polarimetric method presented here brings in a frequency response of the measurement: the measured values of rotation and ellipticity are filtered by the cavity at the frequency $2\nu_B$ according to equations (2.7) and (2.11). In fact, in the polarimetric method presented above, the magnetic birefringence modulates the optical length of the cavity at twice the rotation frequency of the magnets as $d' = d + L\Delta n\cos 2\omega_B t$, where L is the length of the magnetic region. As a consequence, the resonance frequency of the cavity is modulated:

$$\frac{\Delta\nu}{\nu} = \Delta n \frac{L}{d} \cos 2\omega_B t.$$

As the electric field inside the cavity responds with a time constant τ_E, the same applies to the ellipticity signal.

Besides heterodyne detection, high amplification is another important feature of the polarimetric technique adopted by the PVLAS experiment. In this way, the ellipticity of Equation (2.1) becomes of order 10^{-10}.

2.2.3 Intrinsic noise of the polarimeter

We now want to calculate the limit sensitivity of the apparatus in the case a lock-in amplifier is used to demodulate the signal. Starting from Equation (2.5), if the noise at the frequency $\nu_\mathrm{m} - 2\nu_B$ is uncorrelated to the noise at $\nu_\mathrm{m} + 2\nu_B$, one must take into account a factor $\sqrt{2}$ due to the folding of the spectrum around ν_m. If $I_\mathrm{noise}(2\nu_B)$ is the rms noise spectral density of the demodulated light intensity at the frequency of the signal, the expected peak sensitivity of the polarimeter is

$$S_{2\nu_B} = \frac{I_\mathrm{noise}(2\nu_B)}{I_1 \eta_0}.$$

Several intrinsic effects contribute to $S_{2\nu_B}$, all of which can be expressed as a noise in the light intensity impinging on the detector. We consider first the intrinsic rms shot noise due to the direct current i_dc in the detector in a frequency band $\Delta\nu$

$$i_\mathrm{shot} = \sqrt{2e\, i_\mathrm{dc} \Delta\nu}.$$

According to Equations (2.3) or (2.4), the direct current inside the photodiode is given by $qI_1\eta_0^2/2$, where q is the efficiency of the detection process. However, any pair of crossed polarising prisms has a nonzero minimum extinction coefficient for intensity. For the best polarisers, the extinction coefficient can be as low as $\sigma^2 \approx 10^{-8}$. This effect introduces an additional term in the detected intensity which is written as $I_1\sigma^2$. This leads to

$$I_\mathrm{shot} = \sqrt{\frac{2eI_1}{q}\left(\sigma^2 + \frac{\eta_0^2}{2}\right)} \qquad \text{and} \qquad S_\mathrm{shot} = \sqrt{\frac{2e}{qI_1}\left(\frac{\sigma^2 + \eta_0^2/2}{\eta_0^2}\right)}.$$

This represents the ultimate sensitivity of the present polarimetric method.

Other effects contributing to the noise are the Johnson noise of the transimpedance G of the photodiode

$$I_J = \sqrt{\frac{4k_BT}{G}}, \qquad \text{giving} \qquad S_J = \sqrt{\frac{4k_BT}{G}}\frac{1}{qI_1\eta_0},$$

the photodiode dark noise

$$I_{\text{dark}} = \frac{i_{\text{dark}}}{q}, \qquad \text{with} \qquad S_{\text{dark}} = \frac{i_{\text{dark}}}{qI_1\eta_0},$$

and the relative intensity noise (RIN) of the light emerging from the cavity

$$I_{\text{RIN}}(\nu) = I_1 N_{\text{RIN}}(\nu),$$

giving

$$S_{\text{RIN}}(2\nu_B) \approx N_{\text{RIN}}(\nu_{\text{m}})\frac{\sqrt{(\sigma^2+\eta_0^2/2)^2+(\eta_0^2/2)^2}}{\eta_0}, \tag{2.23}$$

where in the last equation we consider that the contributions of all the peaks in the Fourier spectrum add incoherently to the intensity noise at ν_{m}, and that $\nu_B \ll \nu_{\text{m}}$.

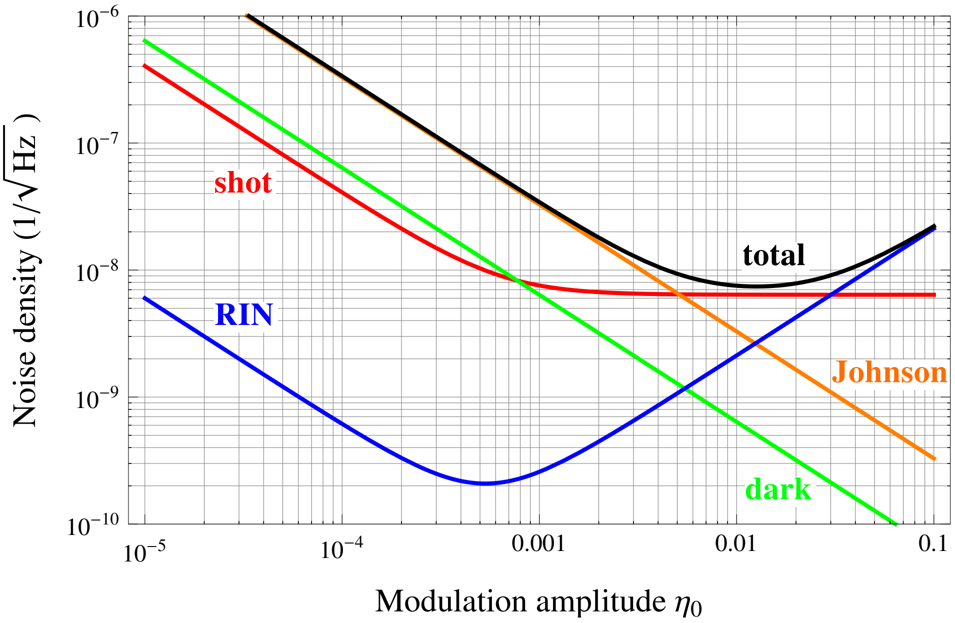

Figure 2.5: Intrinsic peak noise components of the polarimeter as a function of the ellipticity modulation amplitude η_0 in typical operating conditions, with $q \approx 0.7$ A/W, $I_1 = 8$ mW, $\sigma^2 = 2\times10^{-7}$, $G = 10^6\ \Omega$, $i_{\text{dark}} = 25\ \text{fA}_{\text{rms}}/\sqrt{\text{Hz}}$, and $N_{\text{RIN}}(\nu_{\text{m}}) \approx 3\times10^{-7}/\sqrt{\text{Hz}}$.

Figure 2.5 shows all the intrinsic contributions as functions of η_0 in typical operating conditions. The figure shows that the expected noise

$$S_{\text{tot}} = \sqrt{S_{\text{shot}}^2 + S_J^2 + S_{\text{dark}}^2 + S_{\text{RIN}}^2} \tag{2.24}$$

has a minimum for a modulation amplitude $\eta_0 \approx 10^{-2}$.

2.3 Laser-cavity locking

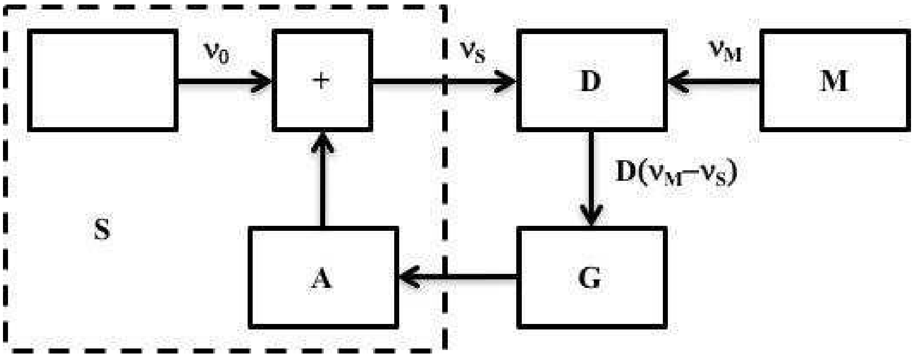

Figure 2.6: General scheme of a feedback system locking the slave frequency ν_0 to a master frequency ν_{M}. The symbol “+" indicates sum, D the discriminator, G the amplifier, A the actuator. The actuator is incorporated in the slave system.

The use of a Fabry-Perot cavity for polarimetric measurements requires that the frequency ν_{L} of the laser light that enters the cavity coincide with one of the frequencies $m\nu_{\text{fsr}}$ for which the cavity resonates, and that this situation remains stable for the time necessary to perform the measurement. In other words, the resonance condition must be maintained stable in a dynamic equilibrium that contrasts thermal drifts and longitudinal mechanical vibrations of the mirrors. It is therefore necessary to have a “frequency coupling” between the laser light source and the FP cavity. This frequency coupling cannot be obtained without an active feedback system. The general scheme of the feedback system is shown in Fig. 2.6. In the figure, the two systems are represented as a master and a slave. The symbol “+" indicates sum, D the discriminator, G the amplifier, A the actuator. The actuator is incorporated in the slave system. For the output of the slave system, one has

$$\nu_{\text{S}} = \nu_0 + \text{AGD}(\nu_{\text{M}} - \nu_{\text{S}}) \qquad \text{or} \qquad \nu_{\text{S}} = \frac{\nu_0 + \text{AGD}\nu_{\text{M}}}{1 + \text{AGD}} \tag{2.25}$$

In the limit in which the *open loop gain* $G_{\text{open loop}} = \text{AGD} \to \infty$, $\nu_{\text{S}} = \nu_{\text{M}}$, and the noise in the frequency difference is strongly suppressed. The coefficients D, G and A are complex functions of the frequency difference $\nu_\mathrm{M} - \nu_\mathrm{S}$. Bandpass and stability of the locking system are determined by the frequency response of its components. Control theory describes the stability of linear systems with reference to the position of the poles of the transfer functions [45].

The locking scheme adopted in the PVLAS experiment follows the Pound-Drever-Hall (PDH) technique [46, 47], which features a fast frequency discrimination. To this end, a sinusoidal frequency modulation of the laser light is used at an RF frequency ν_PDH, and the reflected intensity is an input for the discriminator D. In this way, the limitation imposed by the bandwidth of the FP cavity, which affects the transmitted intensity, is bypassed. This is mandatory in the case of very high finesse cavities with long lifetimes. Moreover, as it will be shown below, this locking scheme is relatively insensitive to intensity noise coming both from the laser source and from the cavity.

For the actuation, one possibility is to modify the instantaneous position of the mirrors of the cavity, for example by making use of piezoelectric actuators; another option is to adjust the frequency of the laser. This second possibility, which has a larger frequency bandwidth, can, in turn, be implemented in two different ways. The traditional technique consists in adding a frequency modulator to the optical set-up; a simpler solution is to resort to tuneable laser sources, like for example diode lasers or Nd:Yag NPRO ones [48–50].

As far as the frequency modulation is concerned, the PVLAS experiment has developed an original method which consists in acting at a single frequency on the very same frequency control of a solid state laser outside its linear range [48]. A phase modulation introduces an unwanted noise called residual amplitude modulation (RAM) that can significantly limit the overall performance of the system. The adopted frequency modulation scheme optimises the RAM and reaches better results than in the case of a phase modulator [48, 49]. We will now describe in detail the discriminator of the PDH method. The amplification and actuation sections will be described in the next chapter.

The principle setup of the PDH frequency locking system is given in Fig. 2.7. With reference to this figure we analyse the electric field of the light at the sections A, B and C. At section A the electric field is

$$E_\mathrm{A} = E_0 e^{i2\pi(m\nu_\mathrm{fsr}+\Delta\nu)t} \tag{2.26}$$

where $\Delta\nu = \nu_\mathrm{L} - m\nu_\mathrm{fsr}$ is the difference between the laser frequency and the resonance frequency of the cavity. The electric field after the phase modulator, i.e at section B, is

$$\begin{aligned} E_\mathrm{B} &= E_0 e^{i[2\pi(m\nu_\mathrm{fsr}+\Delta\nu)t+\beta\sin(\Omega_\mathrm{PDH}t)]} = \\ &\approx E_0 e^{i2\pi(m\nu_\mathrm{fsr}+\Delta\nu)t}\left[J_0(\beta)+J_1(\beta)\left(e^{i\Omega_\mathrm{PDH}t} - e^{-i\Omega_\mathrm{PDH}t}\right)\right] \end{aligned} \tag{2.27}$$

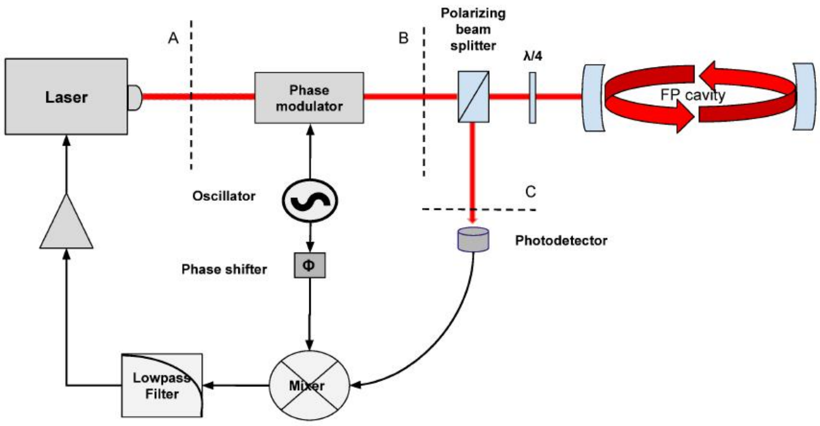

Figure 2.7: Frequency coupling scheme between laser and cavity according to the Pound-Drever-Hall technique. For the sake of clarity, a phase modulator is employed for the frequency modulation of the laser light.

where $\Omega_{\mathrm{PDH}} = 2\pi\nu_{\mathrm{PDH}}$ is the modulation angular frequency of the oscillator and J_0, J_1 are the Bessel functions of the first kind, and β is the *modulation depth*. To first order, the electric field of the laser light features three frequency components: the carrier ν_{L} and two sidebands with frequencies $\nu_{\mathrm{L}} \pm \nu_{\mathrm{PDH}}$. The sidebands must be kept far enough from the central frequency to be totally reflected by the FP when the central frequency is in resonance. The modulation frequency ν_{PDH} must then be comprised between the line-width ν_{c} and the free spectral range of the cavity ν_{fsr}:

$$\nu_{\mathrm{c}} \ll \nu_{\mathrm{PDH}} \ll \nu_{\mathrm{fsr}}. \tag{2.28}$$

To write the electric field at section C we treat each frequency component independently. The transfer function of the reflected field is

$$h_R(\Delta\nu) \equiv \frac{E_R}{E_0} = r\frac{1+R(1-A)-(1-A+R)\cos\delta - i(1-A-R)\sin\delta}{1+R^2-2R\cos\delta} \tag{2.29}$$

where $\delta = 4\pi d(\nu_{\mathrm{L}} - m\nu_{\mathrm{fsr}})/c = 2\pi\Delta\nu/\nu_{\mathrm{fsr}}$. The phase ϕ_R of h_R with respect to the incident field is given by equation (2.15). In figure 2.8 this phase is plotted as a function of the frequency difference $\Delta\nu$ for the cavity used in this thesis. For small δ, ϕ_R becomes

$$\phi_R(\Delta\nu) \simeq -\delta\,\frac{1-A-R}{A(1-R)} \approx -\delta\,\frac{\mathscr{F}T}{\pi A} \tag{2.30}$$

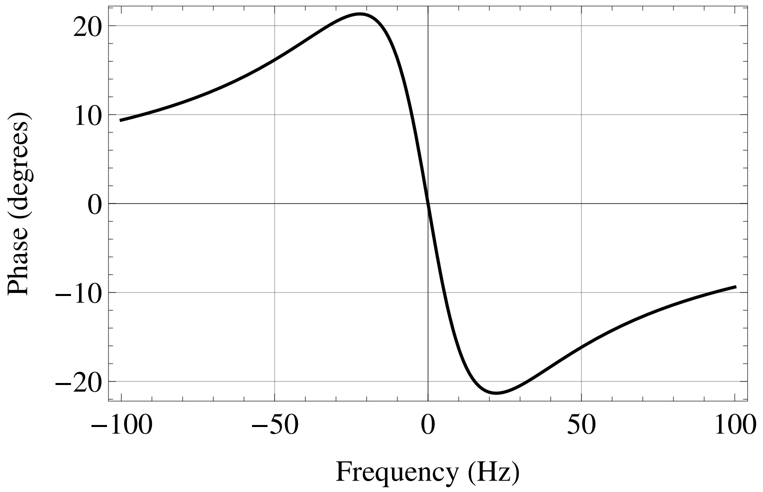

Figure 2.8: Phase ϕ_R of the reflected electric field for a cavity with $d = 3.303$ m, $R = 0.9999955$ and $A = 2.1 \times 10^{-6}$ as a function of the frequency difference between laser and cavity.

In principle, the PDH system keeps the cavity in the maximum transmission condition. The electric field E_{C} of the light reflected from the FP in correspondence of section C is

$$\begin{aligned} E_{\mathrm{C}}(t) \simeq E_0\, e^{i2\pi(m\nu_{\mathrm{fsr}}+\Delta\nu)t}\, \Big[& J_0(\beta)\, h_R(\Delta\nu) + \\ & + J_1(\beta) e^{i\Omega_{\mathrm{PDH}}t}\, h_R(\Delta\nu + \nu_{\mathrm{PDH}}) - J_1(\beta) e^{-i\Omega_{\mathrm{PDH}}t}\, h_R(\Delta\nu - \nu_{\mathrm{PDH}}) \Big] . \end{aligned} \tag{2.31}$$

Near the resonance condition, the sidebands are in practice completely reflected by the cavity with small phases $\pm\phi_{\mathrm{PDH}}$:

$$h_R(\Delta\nu + \nu_{\mathrm{PDH}}) = h_R^*(\Delta\nu - \nu_{\mathrm{PDH}})| \simeq e^{i\phi_{\mathrm{PDH}}} \tag{2.32}$$

The reflected electric field near the resonance condition becomes then

$$E_{\mathrm{C}}(t) \simeq E_0\, e^{i2\pi(m\nu_{\mathrm{fsr}}+\Delta\nu)t} \left[J_0(\beta)\, h_R(\Delta\nu) + 2iJ_1(\beta)\, \sin(\Omega_{\mathrm{PDH}}t + \phi_{\mathrm{PDH}}) \right] \tag{2.33}$$

After point C, the beam is focused on the photodiode PDR which generates a voltage signal $V_R(t)$ proportional to $P_{\mathrm{C}} \propto |E_{\mathrm{C}}|^2$:

$$V_R(t) = qGP_{\mathrm{C}}(t)$$

where q is the efficiency of the photodiode (at $\lambda = 1064$ nm, an InGaAs photodiode has $q \approx 0.7$ A/W), G is the transimpedance of the photodiode and P_{C} the light power at point C. The signal V_R from the photodiode contains terms at frequencies 0, ν_{PDH} and $2\nu_{\mathrm{PDH}}$. The

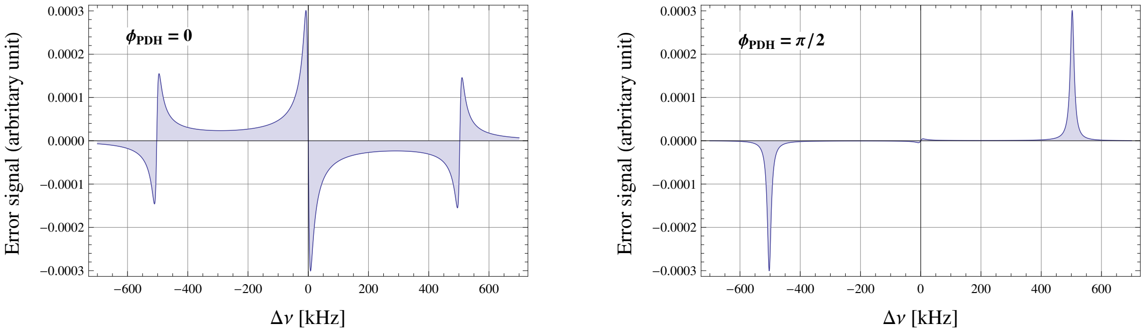

Figure 2.9: Calculation of the DC component of the signal from the PDR photodiode demodulated at the frequency ν_{PDH} of the phase modulation as a function of frequency. Left: in-phase component; right, quadrature component. This plot does not represent the small-frequency approximation of equation (2.33); it stems instead from equation (2.31). The cavity simulated in these plots has a finesse $\mathscr{F} = 3000$, $L = 3.303$ m, $\nu_{\mathrm{fsr}} = 45$ MHz, modulation frequency $\nu_{\mathrm{PDH}} = 503$ kHz.

ν_{PDH} component is:

$$V_{R,\nu_{\mathrm{PDH}}}(t) = 4P_0 q G J_0(\beta) J_1(\beta) h_R(0) \sin\left[\phi_R(\Delta\nu)\right] \sin\left(\Omega_{\mathrm{PDH}} t + \phi_{\mathrm{PDH}}\right) \tag{2.34}$$

where P_0 is the laser power at section A. This signal is then fed to a mixer, together with the signal from a local oscillator at the frequency ν_{PDH} with an adjustable phase ϕ_0 (see Fig. 2.7). At the output of the mixer, the product

$$V_{\mathrm{mixer}}(t) = \chi V_{R,\Omega_{\mathrm{PDH}}}(t) \sin(\Omega_{\mathrm{PDH}} t + \phi_0) \tag{2.35}$$

is obtained, where χ (≈ 0.5) is the efficiency factor of the mixer.

The DC component of this product represents an error signal V_E for the difference in frequency $\Delta\nu$ between laser and cavity. The DC component can in fact be written as

$$V_{\mathrm{mixer,DC}} = 2P_0 \chi q G J_0(\beta) J_1(\beta) h_R(0) \cos(\phi_{\mathrm{PDH}} - \phi_0) \sin\left[\phi_R(\Delta\nu)\right] \tag{2.36}$$

which is a maximum for $\phi_0 = \phi_{\mathrm{PDH}}$ (mod π) (*in-phase* component) and is zero for $\phi_0 = \phi_{\mathrm{PDH}} \pm \pi/2$ (*quadrature* component). Graphs of the two components are shown in figure 2.9. Near the resonance ($\phi_R \approx 0$), the in-phase component is

$$V_E(\Delta\nu) = 4P_0 \chi q G J_0(\beta) J_1(\beta) h_R(0) \frac{\mathscr{F} T}{A} \frac{\Delta\nu}{\nu_{\mathrm{fsr}}} \tag{2.37}$$

The slope of V_E at $\Delta\nu = 0$ is

$$D_0 = \left.\frac{\partial V_E}{\partial(\Delta\nu)}\right|_{\Delta\nu=0} = 4\chi q G \frac{T\mathscr{F}^2}{\pi\nu_{\rm fsr}} J_0(\beta) J_1(\beta) P_0 \tag{2.38}$$

The product $J_0 J_1$ has a maximum value ≈ 0.34 for a modulation depth $\beta \approx 1.1$. The maximum slope of the error signal is then ($q = 0.7$ A/W)

$$D_0 \approx 12 \frac{T\mathscr{F}^2}{\nu_{\rm fsr}} G[\Omega]\, P_0[\mathrm{W}]\ \mathrm{mV/Hz}. \tag{2.39}$$

2.4 Calibration of the apparatus: the Cotton-Mouton effect

The main characteristic of the PVLAS technique is an extraordinary sensitivity to birefringence. On the contrary, the accuracy that can be reached could be questioned. Even if the response of the polarimeter, whose mathematics has been treated so far only in principle, is fully traceable, and prescinding from the systematic effects that will be described in a following chapter, the complexity of the apparatus strongly suggests the need for a calibration measurement. This is obtained with the so-called Cotton-Mouton (or Voigt) effect, namely the magnetic birefringence of pure transparent materials observed for the first time by A. Cotton and H. Mouton [1, 2] in liquids, and predicted by Voigt [51] in gases. Given the sensitivity of the apparatus, the calibration measurements can be performed with a very low gas pressure, namely in a condition very similar to vacuum measurements. Moreover, along the years, the measurements have produced data of interest for the atomic physics research field [52–59]. A small amount of pure gas ($P \sim 1$ mbar) is introduced into the vacuum vessel hosting the polarimeter through a leak valve. The gas fills the magnetic region and the cavity. In order not to disturb the light beam, the gas must have negligible absorption at the laser wavelength. With the Cotton-Mouton effect, a calibration of both the amplitude and the phase of the effect is obtained.

The theoretical treatment of the CME is due to Langevin (1910) and Buckingham and Pople (1956) [60]. The macroscopic anisotropy $\Delta n_{CM} = (n_\parallel - n_\perp)$ is related to anisotropies in the microscopic molecular hyperpolarisability tensor of the medium. A temperature dependence of the effect derives from the general energy-dependent molecular orientation effect [61]. All the PVLAS measurements reported in this thesis have been taken at a single temperature near the NTP standard of 20°C: the temperature of the gas is assumed to be that of the laboratory room. From the calculations as well as from the experiments it comes out that Δn_{CM} is proportional to the square of the magnetic field and varies linearly with the gas pressure:

$$\Delta n_{CM} \propto B^2 P$$

Following Rizzo, Rizzo and Bishop [62], the results of the measurements are given making reference to the unitary birefringence Δn_u, namely scaling the measured Δn_{CM} at $B = 1$ T and $P = 1$ atm:

$$\Delta n_u = \frac{\Delta n_{CM}}{B^2 P}$$

Species	Δn_u (T^{-2}atm^{-1})	λ (nm)	Ref.
H_2	$(8.28 \pm 0.57) \times 10^{-15}$	514	[62]
	$(8.82 \pm 0.25) \times 10^{-15}$	633	[62]
He	$(2.08 \pm 0.14) \times 10^{-16}$	1064	[56]
	$(2.19 \pm 0.12) \times 10^{-16}$	1064	[63]
	$(2.20 \pm 0.14) \times 10^{-16}$	1064	[58]
H_2O	$(6.67 \pm 0.21) \times 10^{-15}$	1064	[57]
Ne	$(6.9 \pm 0.2) \times 10^{-16}$	1064	[54, 55]
CO	$(-2.24 \pm 0.45) \times 10^{-13}$	546	[62]
	$(-1.90 \pm 0.12) \times 10^{-13}$	633	[62]
	$(-1.80 \pm 0.06) \times 10^{-13}$	633	[62]
CH_4	$(1.59 \pm 0.21) \times 10^{-14}$	633	[62]
N_2	$(-2.66 \pm 0.42) \times 10^{-13}$	1064	[64, 65]
	$(-2.02 \pm 0.18) \times 10^{-13}$	1064	[65]
O_2	$(-2.29 \pm 0.08) \times 10^{-12}$	1064	[52]
	$(-1.79 \pm 0.35) \times 10^{-12}$	1064	[65]
Ar	$(7.5 \pm 0.5) \times 10^{-15}$	1064	[59]
	$(4.31 \pm 0.38) \times 10^{-15}$	1064	[65]
CO_2	$(-4.22 \pm 0.31) \times 10^{-13}$	1064	[65]
Kr	$(9.98 \pm 0.40) \times 10^{-15}$	1064	[53, 55]
	$(8.28 \pm 1.30) \times 10^{-15}$	1064	[65]
Xe	$(2.85 \pm 0.25) \times 10^{-14}$	1064	[53, 55]
	$(2.59 \pm 0.40) \times 10^{-14}$	1064	[66]

Table 2.2: Unitary magnetic birefringence of important inorganic gaseous species. Other molecules and older values for the species listed here are found in Ref. [62].

An important point to note is that the residual atmosphere in the vacuum system can contribute to the magnetic birefringence. The knowledge of the Cotton-Mouton effect for the residual molecular species in the vacuum is thus essential to guarantee that the effect due to the partial pressure of each and all the residual gases be much smaller than the effect of the MBV. A list of recent measurements of the unitary magnetic birefringence of a few inorganic gaseous species at room temperature is shown in Table 2.2. The molecules listed in the table are either natural residual gases in the vacuum chamber or are gases that can be used for calibration. The reported values span four orders of magnitude, from He ($\Delta n_u \sim 10^{-16}\,\mathrm{T}^{-2}\mathrm{atm}^{-1}$) to O_2 ($\Delta n_u \sim 10^{-12}\,\mathrm{T}^{-2}\mathrm{atm}^{-1}$), the vacuum magnetic birefringence being equivalent to that of 20 nbar of Helium or 2 pbar of Oxygen. If the direction of $\mathbf{B}$ corresponds to the slow axis of birefringence ($n_\parallel > n_\perp$, the case of the noble gases and the vacuum), $\Delta n > 0$. In the case $\Delta n < 0$ (O_2 and N_2) the direction of $\mathbf{B}$ corresponds to the fast axis.

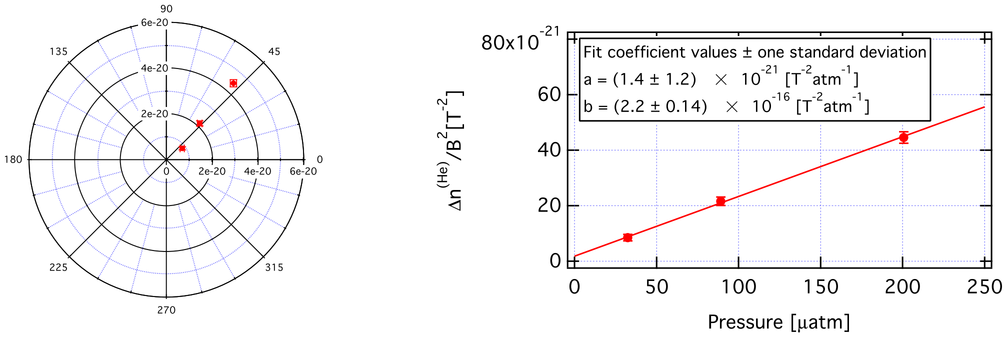

Figure 2.10: Left: polar plot of Cotton-Mouton measurements of He at three different pressures. Right: the amplitude of the measurements as a function of the pressure.

The magnetic birefringence of gases is analysed with the same mathematics presented in the first sections of the chapter. Hence the measurement of the Cotton-Mouton effect of a gas of known unitary magnetic birefringence represents an absolute calibration of the apparatus or a verification of its status. For the calibration measurements, the gas pressure is kept low enough so that the apparatus is in a condition near to that of vacuum (e.g., in Ref. [58], $P_{\mathrm{He}} = 32\ \mu$bar), while the signal is large enough not to require a too long integration. The phase and amplitude of the detected signal represent the sought for calibration of the apparatus. An example is shown in Fig. 2.10. In particular, the oriented direction defined by the result of the measurement displayed on a polar plane defines what in the following will be called the "physical axis" of the polarimeter: the result of any measurement of birefringence must fall on this axis (if performed at the same frequency as the calibration).

.1 Appendix 2.I: Forerunners

The modern history of the measurement of the magnetic birefringence of vacuum begins in 1979 with the seminal paper by Iacopini and Zavattini [38]. In that article the authors proposed an experimental scheme for the measurement that is substantially the one adopted by the PVLAS experiment. The first experiment realised using their technique [67] did not have the sensitivity for measuring the MBV [68] and produced Cotton-Mouton data [69–71] in simplified apparatuses with no path multiplier.

The second attempt to make a direct measurement of the vacuum birefringence was in the framework of an international collaboration between Brookhaven National Laboratory (BNL), Fermi National Accelerator Laboratory, and Rochester and Trieste Universities (BFRT collaboration). The experiment was funded for axion search under the name of Experiment 840 of BNL [72, 35]. Its name in the INFN was LAS (Laser Axion Search). In this experiment, two superconducting magnets provided a 4 T magnetic field on a length of 8.8 meters. The light source was an argon laser ($\lambda = 514$ nm). The magnetic field was modulated by pulsing the current of the magnets to give an oscillating component of amplitude $\int B^2 dl = 7.1$ T^{2}m at the maximum frequency of about 80 mHz. The cavity was constituted by a multi-pass cavity that gave the best results amplifying the optical path of a factor thirtyfour. As a modulator, a Faraday rotator was used. The experiment has put limits on the existence of axion-like particles.

LNL apparatus

The PVLAS set-up in Legnaro had a long development starting in 1992 [73]. It featured an ellipsometer with a vertical Fabry-Perot (FP) cavity with the two mirrors spaced 6 m apart. A superconductive dipole magnet about 1 m long rotated around the FP axis and was operated with field intensities up to 5.5 T. Running periods after a fill of the magnet cryostat with liquid He lasted up to 4 hrs. The optical set-up extended vertically about 8 m and included two black granite optical benches (one above and the second below the magnet) supported by the same floor (see Fig. 11). The lower optical bench was in a pit whose floor is a thick concrete slab resting on four 14 m high pillars buried in the ground. The slab and the pillars are therefore seismically isolated from the surrounding hall floor and the building. Four granite pillars supported the top optical bench. A quartz tube of 2.5 cm diameter passing through the warm bore of the cryostat containing the magnet connected an upper and a lower vacuum chamber. The optical components installed directly onto the optical benches were exposed to ambient air. Instead, the polariser and the first mirror of the FP, as well as the second mirror and the analyser plus the ellipticity modulator, were installed inside

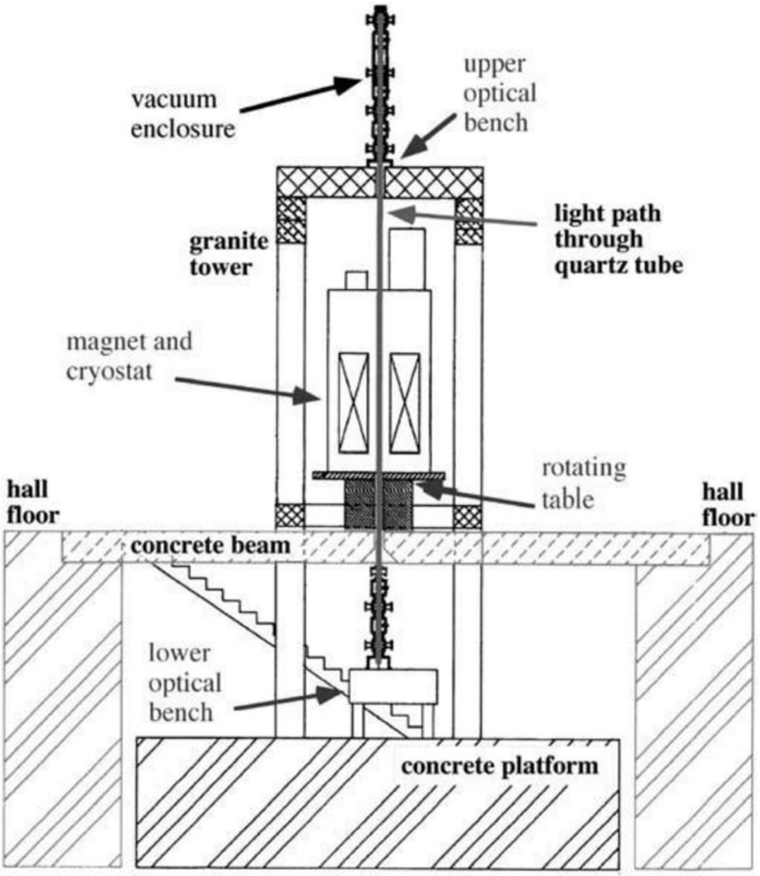

Figure 11: Schematic layout of the LNL apparatus: the ellipsometer develops vertically: the polariser and the first cavity mirror are supported by the lower optical bench, whereas the second cavity mirror, the modulator and the analyser are in a vacuum chamber on the upper optical bench.

the high vacuum enclosure. The turntable holding the cryostat with the superconducting dipole magnet was supported by a concrete beam crossing over the pit and resting on the hall floor. The magnet stayed upright and rotated around its axis at a characteristic frequency of 0.3 Hz. The magnetic field lines were therefore in the horizontal plane. The pressure during measurement was kept at the level of $P = 10^{-8}$ mbar, value for which the contribution to the ellipticity of the Cotton-Mouton effect is smaller than the magnetic birefringence of vacuum. Two types of laser sources were used in turn: an infrared Nd:YAG laser emitting 0.8 W at 1064 nm coupled to a FP with finesse $\mathscr{F} = 70\,000$, and a green laser emitting 0.08 W at 532 nm coupled to a FP with a finesse $\mathscr{F} = 37\,000$.

The operational sensitivity of the LNL polarimeter over long runs was 10^{-6} rad$/\sqrt{\text{Hz}}$ for rotation and $10^{-6}/\sqrt{\text{Hz}}$ for ellipticity. Before 2007, the data featured persistent signals that could be interpreted as an apparent rotation due to a differential absorption [74, 29] and as an ellipticity [75]. The rotation signals generated quite an interest since, if authentic, would have been the signature of new physics. After an extensive upgrade, the rotation signals disappeared [76, 77]. Also, the ellipticity signal disappeared at a lower field (2.3 T), while it was still present at high fields albeit not well reproducible and not compatible with the upper limit derived from the 2.3 T data and the B^2 scaling law [76, 77]. These signals were therefore considered as systematics. The 2.3 T ellipticity data have provided the best limits for the total cross section of low energy $\gamma\gamma$ interactions [76, 77]. Limits on the vacuum birefringence and dichroism were also derived as

$$\Delta n \leq 1.1 \times 10^{-19} \qquad \text{and} \qquad \Delta\kappa \leq 0.9 \times 10^{-19}.$$

Calibrations of the ellipsometer have repeatedly been made. They have provided the most accurate measurements of the CM parameters for noble gases [53–56]. Runs with He have been made at pressures as low as 0.04 mbar [56].

The experience with the LNL apparatus has demonstrated that two main features are necessary for a reliable observation of MBV: that the signal is independent of the rotation frequency of the magnet and that the phase of the ellipticity signal must be aligned with the physical axis determined during calibrations with gases. A further requirement would be the ability to verify that the signal depends on B^2.

Ferrara test set-up

Between 2008 and 2012, a prototype polarimeter featuring a 140 cm long FP coupled with two rotating permanent dipole magnets has been in operation as the Ferrara test set-up [78]. This set-up has been a model for the apparatus described in this thesis. Fig. 12a shows the scheme of the test apparatus and Fig. 12b a picture of it. At the centre one can see the two permanent dipole magnets, each 20 cm long, with external diameter 19 cm and 15 mm bore, generating a magnetic field of maximum intensity $B = 2.3$ T. For these magnets, the measured $\int B^2 dl$ is 1.85 $\mathrm{T^2m}$. The finesse of the cavity was $\mathscr{F} = 240000$. All the optical components were either fixed directly onto a seismically isolated optical bench $2.4 \times 1.2\ \mathrm{m}^2$ or were fixed inside two rigidly connected and communicating vacuum chambers, which in turn rest on the optical bench. The magnets are supported by a sturdy aluminum structure which is disconnected from the seismically isolated optical bench and resting on the lab floor. Ball bearings support the two magnets at their extremities. The magnet on the analyser side is equipped with a coaxial electric motor which puts the magnet in rotation around the axis of its bore. The magnet on the polariser side can be connected mechanically to the other magnet by a home-made mechanical piece so that the two magnets rotate at the same angular velocity

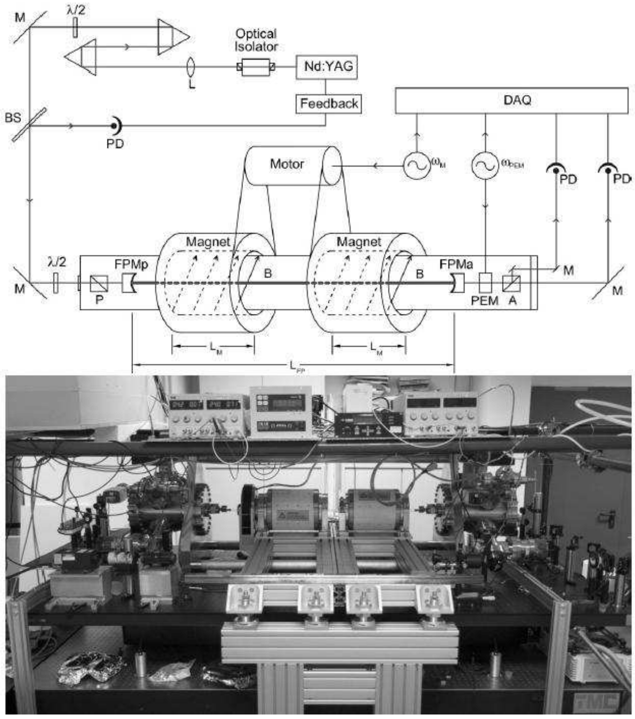

Figure 12: An optical scheme (upper panel) and photograph (lower panel) of Ferrara test set-up. At the center, one can see the two dipole permanent magnets. The optics are supported by a seismically isolated optical bench whereas the magnet supports rest on the floor.

with fixed relative phases equal to 0°, 90°, 180° or 270°. The reason for having two magnets is that the rotating magnets can act on the optics and fake ellipticity signals. It is therefore desirable to perform measurements of the zero of the ellipticity scale in conditions as close as possible to those in which an authentic signal is expected. This cannot be obtained with a single superconducting magnet, because when there is no field in the magnet bore, also the stray field is absent. With two identical magnets with orthogonal fields, the net ellipticity generated by a magnetic birefringence is zero. Running the two magnets with the fields parallel and perpendicular allows to distinguish a real physical signal from spurious signals due to the stray field.

In the LNL experiment it was observed that mechanical and ellipticity spectra were very similar. The test set-up in Ferrara, using a seismically isolated optical table, demonstrated a clear correlation between the seismic noise on the optical components and the ellipticity noise [79]. As one can see in Fig. 13, the spectral noise density was better with the seismically isolated optical table. It was not investigated which direction of the seismic noise mostly influenced the ellipticity spectrum.

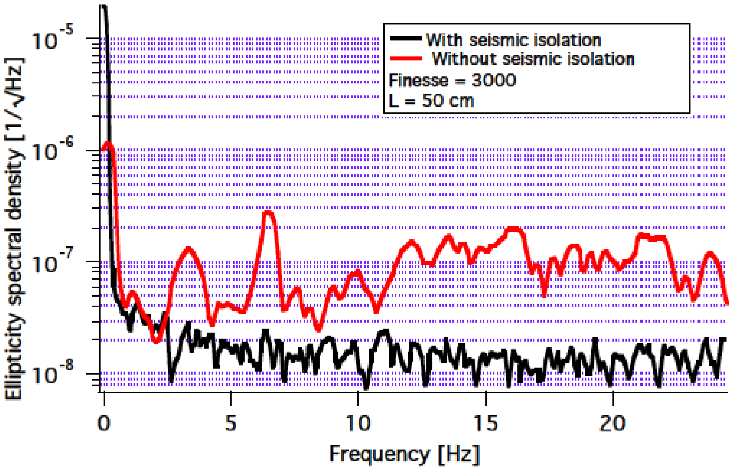

Figure 13: Plot of the ellipticity as a function of frequency measured from the modulator carrier frequency. The red curve is obtained with the seismic isolation turned off.

The sensitivity of the Ferrara test set-up was $S^{\text{meas}}_{2\nu_{\text{B}}} = 3 \times 10^{-7}\ \text{Hz}^{-1/2}$ at 6 Hz. With the test apparatus in a condition in which spurious peaks were not present, a measurement of a few hours has been done. The measurement led to an upper bound on the magnetic vacuum birefringence Δn measured with a magnetic field $B = 2.3$ T:

$$\Delta n \leq 4.6 \times 10^{-20} \qquad \text{at } 95\% \text{ c.l.}$$

Putting out from the polarimeter the two FP mirrors, a sensitivity $S^{\text{meas}}_{\text{No-FP}} = 6 \times 10^{-9}\ \text{Hz}^{-1/2}$ was instead measured.

.2 Appendix 2.II: Competing approaches

The Q&A project (Quantum electrodynamics test & search for Axion like particles), started in 1996 [80], makes use of a permanent dipole magnet 60 cm long with a magnetic field of 2.3 T. The magnet rotates around its axis. A Fabry-Perot of finesse $\mathscr{F} = 30\,000$ increases the optical path through the magnetic field.The two mirrors are suspended with vibrations attenuators of the type developed for the interferometric gravitational wave detectors. The experiment has measured the Cotton-Mouton of several gases [65]. A limit on the vacuum dichroism has been also obtained as

$$\Delta\kappa^{(\text{Q\&A})} \leq 1.5 \times 10^{-19}.$$

	BFRT [35]	PVLAS-LNL [76]	PVLAS-FE [59]	Q & A [64]	BMV [82]	OVAL [83]
Magnet	superconductor	superconductor	permanent	permanent	electromagnet	electromagnet
B modulation	current	rotating	rotating	rotating	pulsing	pulsing
B_{ext} (T)	3.25 ± 0.62	2.3	2.5	2.3	6.5	11.4
Effective $2\nu_B$ (Hz)	0.032	0.6	10	13.5	80	130
$\int B^2\, dL$ (T^2 m)	40	5.3	10.25	3.2	5.8	13.8
λ (nm)	514	1064/532	1064	1064/532	1064	1064
Path amplifier	Multipass	FP	FP	FP	FP	FP
N	34	4.5×10^4	4.5×10^5	1.9×10^4	3×10^5	2×10^5
Effective $N\psi_{\text{QED}}$	3.3×10^{-14}	2.8×10^{-12}	5.4×10^{-11}	7.1×10^{-13}	9.6×10^{-12}	9.7×10^{-12}
Detection scheme	heterodyne	heterodyne	heterodyne	heterodyne	homodyne	homodyne
S_ψ $(1/\sqrt{\text{Hz}})$	7.9×10^{-8}	1.8×10^{-6}	5×10^{-7}	1×10^{-6}	$\approx 10^{-7}$	$\approx 2 \times 10^{-7}$
$S_{\Delta n_u}$ $(\text{T}^{-2}/\sqrt{\text{Hz}})$	9.5×10^{-18}	2.6×10^{-18}	3.7×10^{-20}	5.7×10^{-18}	4.2×10^{-20}	8.3×10^{-20}
Duty cycle D_{c}	1	~ 0.01	$\lesssim 1$	≈ 0.78	5.2×10^{-6}	2.5×10^{-4}
Integration time T_{int} (s)	1.6×10^4	6.5×10^4	2.7×10^6	3.6×10^4	≈ 0.15	0.12
Integrated Δn_u (T^{-2})	7.5×10^{-20}	2.0×10^{-20}	4.8×10^{-23}	3.0×10^{-20}	2.5×10^{-21}	1.1×10^{-18}
$T_{\text{SNR}=1}$ (yr)	1.8×10^5	1.3×10^6	2.7	7.1×10^4	6.7×10^5	5.3×10^4

Table 3: A synoptic table for the experiments aiming at the magnetic birefringence of vacuum. For the experiments employing pulsed magnets, the maximum magnetic field is reported; for them, the effective frequency is $1/2\pi\tau_{\text{FWHM}}$. In these experiments, moreover, the cavity filters the ellipticity generated by the magnetic field, hence the "effective" $N\psi_{QED}$. The value of S_ψ of the BMV experiment has been read from the ellipticity spectral density graph of their work; this sensitivity is at least an order of magnitude too high to be consistent with the integrated Δn_u. The values reported for the integrated Δn_u correspond to the noise values; the BFRT and BMV experiments have also a central value not compatible with zero at 1σ. As the Q & A experiment has not measured birefringence, their value of $\Delta\kappa_u$ is reported. The time required to reach SNR $= 1$ is given by $\left(S_\psi/N\psi_{\text{QED}}\right)^2/D_c$.

The OSQAR (Optical Search for QED Vacuum Birefringence, Axions, and Photon Regeneration) experiment [81] is based on a 15 m long LHC dipole magnet that can reach a 9 T field. The experiment uses Fabry-Perot cavities but has not yet chosen a strategy to modulate the effect. The set-up has only produced limits on the existence of axion-like particles by studying the graph of Fig. 1.1*f)* with the Light Shining through a Wall technique [35].

The BMV (Biréfringence Magnétique du Vide) project [66] began in 2000 at the Laboratoire National des Champs Magnétiques Intenses of Toulouse. The vacuum magnetic birefringence is induced by a pulsed magnet capable of 5 pulses per hour with a maximum field of 14 T with an effective length of 13.7 cm. The coils are immersed in liquid nitrogen, and a hole of diameter of 12 mm extends along the cryostat to let the laser light pass through the magnetic field region. The laser light is locked to the cavity with the Pound-Drever-Hall technique. The amplification of the light path in the magnetic region is realised using a 2.3 m long Fabry-Perot cavity with a finesse $\mathscr{F} = 481\,000$. The homodyne technique is employed for the linearisation of the ellipticity in the extinguished intensity: a known static ellipticity is added to the polarisation exploiting the intrinsic birefringence of the cavity. The calibration is made by measuring the Cotton-Mouton effect in gas. The experiment has measured the Cotton-Mouton effect of several gases, among them Helium at low-pressure [63]. The best limit for the magnetic birefringence of vacuum is reported in Ref. [82] at a 3σ c.l. as

$$\Delta n^{(\mathrm{BMV})}/B^2 = (6.1 \pm 7.5) \times 10^{-21}\ \mathrm{T}^{-2}.$$

While the sensitivity of the apparatus is not sufficient to measure the magnetic birefringence in a reasonable time, an upgrade is underway to increase the signal of a factor 50.

OVAL [83] (Observing VAcuum with Laser) is a recent experimental effort in Japan that has developed an original pulsed magnet with a high repetition rate of 0.2 Hz. The magnet is cooled down with liquid nitrogen, and a maximum magnetic field of 11.4 T has been obtained over a length $L = 17$ cm. The Fabry-Perot cavity has a length of 1.38 m and a finesse $\mathscr{F} = 320000$. Given the pulse width of ≈ 1 ms, an effective $\int B^2 dL = 3.4\ \mathrm{T}^2\mathrm{m}$ is obtained. A static ellipticity is added for homodyne detection as in the BMV experiment. The measured limit on the magnetic birefringence of vacuum is

$$\Delta n^{(\mathrm{OVAL})}/B^2 \leq 1.1 \times 10^{-18}\ \mathrm{T}^{-2}.$$

Another proposal aiming at a first measure of the vacuum magnetic birefringence is the experimental proposal Hera-X (**H**eisenberg-**E**uler-bi**R**efringent-**A**LPS-e**X**periment) announced in a workshop at DESY in Nov 2015 [84]. The Hera-X proposal plans to make use of a 177 m long array of HERA superconducting magnets with 5.3 T with a resulting $\int B^2 dL = 5 \times 10^{-3}$ T^{2}m. The cavity length is estimated to be 200 m. The modulation of the effect is obtained by ramping the magnetic field with a frequency up to 7 mHz. Another possibility to modulate the effect without ramping the amplitude of the magnetic field has been proposed in [59].

At present, the best performances are still those achieved by the PVLAS apparatus installed at Ferrara [59]. In Tab. 3, the characteristics of the experiments are summarised and compared.

.3 Appendix 2.III: Multilayer dielectric coating

The reflecting surface of the mirrors of the Fabry-Perot cavity is a multi-layer stack of dielectric films of calibrated thickness deposited onto a transparent substrate. The deposition is usually obtained by ion sputtering or evaporation As the PVLAS experiment aims at high finesse, it is not possible to use mirrors made with metal layers, that have a too large absorption $(5-10\%)$ in the near infrared to ultraviolet region. One must note that higher reflectivity also provides higher damage threshold.

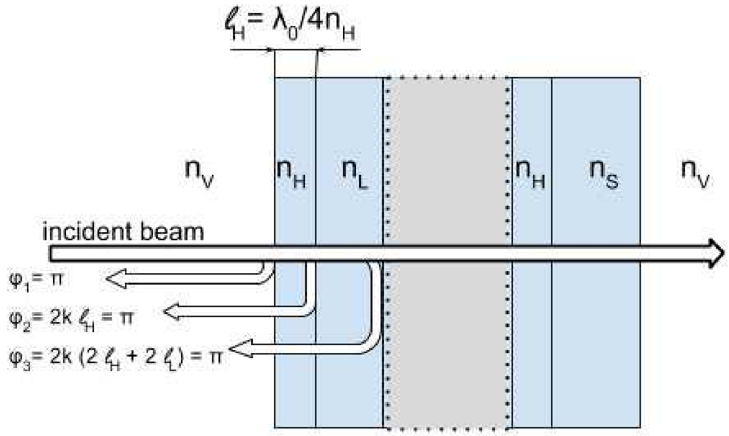

Figure 14: A light beam impinging on the multi-layer coating of the reflecting surface of a dielectric mirror, alternating high (n_H) and low (n_L) indices of refraction of thicknesses ℓ_H and ℓ_L, respectively. The multi-layer stack begins and ends with the material with a high index of refraction. The φ's are the phases of the reflected partial waves.

Fig. 14, shows a scheme of a multilayer dielectric mirror. According to the Fresnel formulas, the reflection and transmission coefficients for the electric field of light impinging normally on the interface between two media of refractive indices n_1 and n_2 are

$$r_{12} = \frac{(n_1 - n_2)}{(n_1 + n_2)} \qquad t_{12} = \frac{2n_1}{(n_1 + n_2)}.$$

In the case $n_1 < n_2$, the reflection coefficient is $r_{12} < 0$, and the reflected field has a π phase shift with respect to the incident field. The transmitted field is instead always in phase with the incident one. Consider now an optical substrate with an index of refraction n_S coated with many layers having alternately high ($n_H > n_S$) and low (n_L) index of refraction. In this system, if the thicknesses ℓ_H and ℓ_L of the layers are such that $n_H \ell_H = n_L \ell_L = \lambda/4$, the electric fields reflected at all the interfaces add in phase. In fact, considering the two surfaces of the first high-index layer of Fig. 14, one can see that the Fresnel formulas assign the field reflected at the first (low-to-high index) interface a negative sign. The wave reflected at the second (high-to-low index) interface suffers no phase shift upon reflection, but before reaching the first surface, it has traveled a total optical path corresponding to a phase shift of π. This phase difference implies that the two reflected partial waves have the same phase. The same conclusion applies to the two surfaces of a low-index layer. It follows then that all the reflected beams in a multilayer dielectric coating, as well as their multiple reflections, add in phase. The complementary process happens to the transmitted field: all the partial waves at the second interface of each layer have opposite phase, and destructive interference occurs. If a large number of ($\lambda/4$) layers of alternating low and high indices are deposited on a substrate, the overall reflectivity can reach a very high value. The intensity reflectivity of a dielectric mirror made with a stack of $2N_L + 1$ layers turns out to be [43]

$$R = \left[\frac{1 - \frac{n_H^2}{n_S} \left(\frac{n_H}{n_L} \right)^{2N_L}}{1 + \frac{n_H^2}{n_S} \left(\frac{n_H}{n_L} \right)^{2N_L}} \right]^2 . \qquad (40)$$

Fig. 15 shows the predicted value of $1 - R$ as a function of the number N_L of layer pairs. One must note that what limits the performance of a dielectric mirror are the losses inside the bulk of the material of the layers [85].

.4 Appendix 2.IV: Gaussian beams

In a previous section, we described the characteristics of the Fabry-Perot cavity that could be deduced from the approximation of the light beam as a plane wave. However, laser beams are not plane waves, but Gaussian beams and optical elements have finite dimensions. This fact

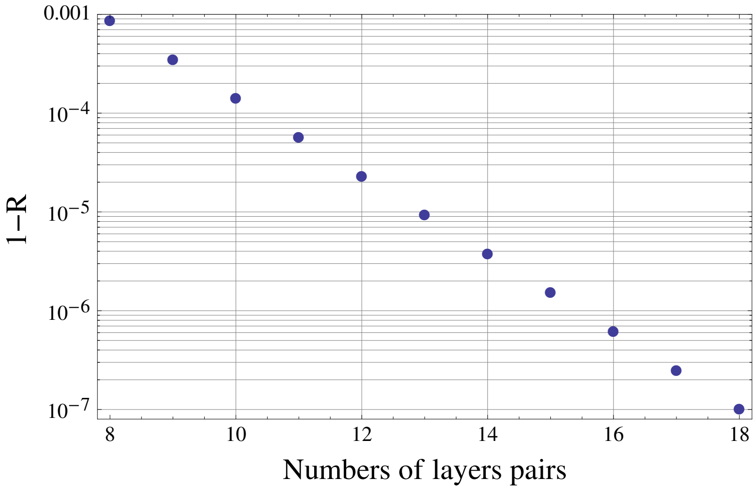

Figure 15: Logarithmic plot of the coefficient $(1-R)$ as a function of the number of layer pairs with index of refraction $n_H = 2.28$ (TiO_2) and $n_L = 1.45$ (SiO_2). The substrate has $n_S = 1.54$ (BK7 glass).

brings in a specific discipline of optics, that is worthwhile to resume here [86]. One needs to search for a solution of the wave equation with no translational symmetry. The Helmholtz equation in an isotropic dissipative medium is

$$\nabla^2 \mathbf{E} + k^2 \mathbf{E} = 0,$$

where

$$k^2 = \omega^2 \mu \varepsilon \left[1 + \frac{i\sigma}{\omega\varepsilon} \right]$$

and σ is the conductivity of the medium. Let us indicate with z the coordinate along the beam axis. One looks for a solution in the form

$$\mathbf{E}(\mathbf{r}) = \mathbf{A}(\mathbf{r})\, e^{ikz},$$

where the wave amplitude $\mathbf{A}$ is not a constant but instead a function of the position $\mathbf{r}$ satisfying

$$\nabla^2 \mathbf{A} + 2ik \frac{\partial \mathbf{A}}{\partial z} = 0. \tag{41}$$

.4.1 Fundamental mode

To solve this equation, one assumes that the second derivative of $\mathbf{A}$ with respect to z can be neglected. For the moment, we limit to solutions with azimuthal symmetry. With these hypotheses the equation becomes, in the cylindrical coordinates (ρ, ϕ, z),

$$\frac{1}{\rho}\frac{\partial}{\partial\rho}\left(\rho\frac{\partial A_0}{\partial\rho}\right)+2ik\frac{\partial A_0}{\partial z}=0. \tag{42}$$

An approximate solution to the above equation can be written as

$$A_0=\exp\left\{i\left[P(z)+\frac{k}{2q(z)}\rho^2\right]\right\},$$

where $P(z)$ and $q(z)$ are complex functions. The latter one is responsible for the behaviour of the electric field as a function of the distance ρ from the beam axis; the shape of the wavefront is encoded in there. Substituting this expression in the equation above and equating terms with the same powers of ρ one finds:

$$\frac{dq}{dz}=1 \qquad \text{and} \qquad \frac{dP}{dz}=\frac{i}{q}.$$

Integrating these equations one gets

$$q(z)=z+q_0 \qquad \text{and} \qquad P(z)=i\ln\frac{z+q_0}{q_0},$$

where $P(0)=0$.

To make clear the meaning of the q function, one has to rewrite it in terms of the two real parameters $R(z)$ e $w(z)$:

$$\frac{1}{q(z)}=\frac{z+q_0^*}{z^2+2z\Re(q_0)+|q_0|^2}=\frac{1}{R(z)}+i\frac{\lambda}{\pi w^2(z)}.$$

The parameter R is interpreted as the curvature radius of the wavefront. In fact, for large z, it grows as z, and the surfaces of constant phase are almost exactly spherical. The w parameter describes the confinement of the wave amplitude in the vicinity of the beam axis according to a Gaussian function with standard deviation depending on z; the quantity w is the *waist* of the beam; $2w$ plays the role of beam diameter at position z. We put the origin of the coordinates where the wavefront is plane $[R(z=0)=\infty]$. In $z=0$, q is purely imaginary:

$$q_0=-i\frac{\pi w_0^2}{\lambda}\equiv -iz_0,$$

where z_0 is the *Rayleigh range*; we have then

$$q(z) = z + q_0 = z - i\frac{\pi w_0^2}{\lambda} = z - iz_0,$$

and hence

$$\frac{1}{q(z)} = \frac{z}{z^2 + \pi^2 w_0^4/\lambda^2} + i\frac{\pi w_0^2/\lambda}{z^2 + \pi^2 w_0^4/\lambda^2} = \frac{z}{z^2 + z_0^2} + i\frac{z_0}{z^2 + z_0^2},$$

$$\begin{aligned} R(z) &= z\left[1 + \left(\frac{\pi w_0^2}{z\lambda}\right)^2\right] = z\left[1 + \left(\frac{z_0}{z}\right)^2\right], \\ w^2(z) &= w_0^2\left[1 + \left(\frac{z\lambda}{\pi w_0^2}\right)^2\right] = w_0^2\left[1 + \left(\frac{z}{z_0}\right)^2\right]. \end{aligned}$$

The curvature radius is thus infinite at $z = 0$ and at $z = \pm\infty$; its minimum absolute value is $|R(z_0)| = 2z_0$. The beam diameter is minimum at $z = 0$ and grows with a hyperbolic law with an asymptote of slope

$$\theta_0 = \frac{\lambda}{\pi w_0}.$$

This diameter growth is the same of the theory of the diffraction of a plane wave from a circular hole of diameter $2w_0$. For this reason, Gaussian beams are said to be *diffraction limited* even if they usually do not emerge from a pinhole. Dividing the expressions of $R(z)$ and $w^2(z)$ one obtains

$$\frac{\lambda z}{\pi w_0^2} = \frac{z}{z_0} = \frac{\pi w^2}{\lambda R},$$

from which we obtain the expressions of w_0 and z as functions of R and w:

$$w_0^2 = \frac{w^2}{1 + \left(\frac{\pi w^2}{\lambda R}\right)^2} \qquad \text{and} \qquad z = \frac{R}{1 + \left(\frac{\lambda R}{\pi w^2}\right)^2}.$$

We explicitly note that while a spherical wave is completely characterised by total power and center of curvature, and a plane wave by intensity and propagation direction, to characterise a Gaussian beam two more parameters are needed. They can be the minimum waist w_0 and its position along the beam path or, in an alternative, the curvature radius and the waist at any point along z.

As for the function $P(z)$,

$$iP(z) = -\ln\left[1 + i\frac{z\lambda}{\pi w_0^2}\right] = -\ln\sqrt{1 + \left(\frac{z\lambda}{\pi w_0^2}\right)^2} - i\arctan\left[\frac{z\lambda}{\pi w_0^2}\right].$$

The real part of P is the *Gouy phase correction* $\Phi_G(z)$ of the Gaussian beam with respect to the phase of the plane wave

$$\Phi_G(z) = -\arctan\left[\frac{z\lambda}{\pi w_0^2}\right],$$

which is zero for $z = 0$, and tends to $\pm\pi/2$ for $z = \mp\infty$. The imaginary part is instead responsible for an amplitude decrease with the widening of the wavefront, with a factor $w_0/w(z)$.

In conclusion, the electric field is written as

$$E_0(\mathbf{r}) \propto \frac{w_0}{w}\exp\left[-\frac{\rho^2}{w^2}\right]\exp\left\{i\left[k\left(z + \frac{\rho^2}{2R}\right) + \Phi\right]\right\},$$

this equation is called the “fundamental mode". In any plane orthogonal to the z axis, the intensity profile of the beam is Gaussian:

$$I(\rho,z) = I_0\frac{w_0^2}{w^2}\exp\left[-\frac{2\rho^2}{w^2}\right] = I_0\frac{1}{1+(z/z_0)^2}\exp\left[-\frac{2\rho^2}{w^2}\right].$$

The wave has its the maximum intensity at $z = 0$, where a wavefront is a plane and $w = w_0$; this value halves at $z = \pm z_0$ due to the coefficient $(w_0/w)^2$. The power passing through a pinhole of diameter $2\rho_0$ is given by

$$P_{\rho_0}(z) = \int_0^{\rho_0} I(\rho,z)\,2\pi\rho\,d\rho = I_0\frac{\pi w_0^2}{4\sqrt{w_0^2\left(1+\frac{z^2}{z_0^2}\right)}}\left[1 - e^{-\frac{4\rho_0^2}{\sqrt{w_0^2\left(1+\frac{z^2}{z_0^2}\right)}}}\right] \tag{43}$$

The total power of a Gaussian beam is

$$P_0 = \int_0^{\infty} I(\rho,z)\,2\pi\rho\,d\rho = \frac{1}{2}I_0\,\pi w_0^2.$$

.4.2 Higher order modes

The expression found above for $E_0(\mathbf{r})$ is called the “fundamental mode". Other solutions to the equation (41) for A do not enjoy azimuthal symmetry. It can be shown [86] that these functions can be written as

$$E_{lm}(\mathbf{r}) \propto \frac{w_0}{w} H_l\left(\frac{\sqrt{2}\rho\cos\phi}{w}\right) H_m\left(\frac{\sqrt{2}\rho\sin\phi}{w}\right) \exp\left[-\frac{\rho^2}{w^2}\right] \exp\left\{i\left[k\left(z+\frac{\rho^2}{2R}\right)+\Phi_{lm}\right]\right\},$$

where the phase of the wave is

$$\Phi_{lm}(z) = -(l+m+1)\arctan\left[\frac{z\lambda}{\pi w_0^2}\right].$$

For higher order modes, the larger the mode number, the larger the phase velocity. Modes with the same phase velocity are said to be degenerate; degenerate modes have $l+m = l'+m'$. The function H_n is the Hermite polynomial of order n. We determine the Hermite polynomials from the recursive formula

$$H_{n+1}(x) = 2xH_n(x) - 2nH_{n-1}(x).$$

The first polynomials are

$$\begin{aligned} H_0(x) &= 1, \\ H_1(x) &= x, \\ H_2(x) &= 4x^2-2, \\ H_3(x) &= 8x^3-12x. \end{aligned}$$

The index n is the number of nodes of the polynomial: the (l,m) mode consists of $(l+1)\times(m+1)$ lobes. For the same w_0 and z, the transverse dimension of the mode grows with indexes l and m. The curvature radius evolves in the same way for all the optical modes.

.5 Appendix 2.V: Gaussian beams and optical resonators

.5.1 Matrix formulation of geometrical optics: the *ABCD* law

In the passage through a centered optical system, namely one in which all the surfaces have rotational symmetry around an optical axis, the mode of a paraxial Gaussian beam is conserved. The curvature radius of the wavefront and the minimum waist are instead altered.

In this section, we apply the matrix formulation of geometrical optics [87] to the propagation of a Gaussian beam to derive the so-called *ABCD* law.

If a ray is coplanar with the optical axis, one can use a single transverse coordinate in this plane. In the following we limit to a treatment with a single transverse coordinate. In a section (x,z) of a centred optical system, a paraxial ray at z is completely characterised by its transverse position x and its slope with respect to the optical axis $\dot{x} = dx/dz$. In the paraxial approximation, the slopes are approximately the sine of the angle or even the angle. In a homogeneous medium, from the initial conditions, x_0 and $\dot{x}_0$ one has, at position z,

$$x(z) = x_0 + \dot{x}_0\,(z - z_0); \qquad \dot{x}(z) = \dot{x}_0.$$

This can be written in a compact form as

$$\begin{bmatrix} x(z) \\ \dot{x}(z) \end{bmatrix} = \begin{bmatrix} 1 & z - z_0 \\ 0 & 1 \end{bmatrix} \begin{bmatrix} x_0 \\ \dot{x}_0 \end{bmatrix}.$$

Passing from a medium with index of refraction n_1 to a medium with index of refraction n_2

$$x_+ = x_- \qquad \text{and} \qquad \dot{x}_+ = \frac{n_1}{n_2}\dot{x}_-$$

or

$$\begin{bmatrix} x_+ \\ \dot{x}_+ \end{bmatrix} = \begin{bmatrix} 1 & 0 \\ 0 & n_1/n_2 \end{bmatrix} \begin{bmatrix} x_- \\ \dot{x}_- \end{bmatrix}.$$

A spherical diopter at z does not change the distance of the ray from optical axis ($x_+ = x_-$); the position of the object z_1 and of the imagine z_2 are given by the equation

$$x_+ = x_- \qquad \text{and} \qquad \frac{n_1}{z - z_1} + \frac{n_2}{z_2 - z} = \frac{n_1 - n_2}{R}$$

(R is positive if concavity looks into objects space). Substituting in the last one $z - z_1 = x_-/\dot{x}_-$ and $z_2 - z = -x_+/\dot{x}_+ = -x_-/\dot{x}_+$ and solving for $\dot{x}_+$ one finds

$$\dot{x}_+ = -\frac{n_1 - n_2}{n_2 R} x_- + \frac{n_1}{n_2}\dot{x}_-$$

or

$$\begin{bmatrix} x_+ \\ \dot{x}_+ \end{bmatrix} = \begin{bmatrix} 1 & 0 \\ (1 - n_{12})/R & n_{12} \end{bmatrix} \begin{bmatrix} x_- \\ \dot{x}_- \end{bmatrix}$$

A spherical mirror is described by

$$x_+ = x_- \qquad \text{and} \qquad \frac{1}{z-z_1} + \frac{1}{z_2 - z} = \frac{2}{R}.$$

Substituting again $z - z_1 = x_-/\dot{x}_-$ and $z_2 - z = -x_-/\dot{x}_+$ and solving for $\dot{x}_+$, one obtains

$$\dot{x}_+ = -\frac{2}{R}x_- + \dot{x}_-$$

and the matrix of a spherical mirror is thus

$$\begin{bmatrix} 1 & 0 \\ -2/R & 1 \end{bmatrix}$$

A thin lens of focal length f is described by

$$x_+ = x_- \qquad \text{and} \qquad \frac{1}{z-z_1} + \frac{1}{z_2 - z} = \frac{1}{f}$$

and hence, for a thin lens,

$$\dot{x}_+ = -\frac{1}{f}x_- + \dot{x}_-$$

and

$$\begin{bmatrix} x_+ \\ \dot{x}_+ \end{bmatrix} = \begin{bmatrix} 1 & 0 \\ -1/f & 1 \end{bmatrix} \begin{bmatrix} x_- \\ \dot{x}_- \end{bmatrix}$$

A thin lens of focal length f has the same matrix of a spherical mirror with curvature radius $R = 2f$.

The equations derived above can be interpreted in terms of the propagation of spherical waves. Let us consider a spherical wave originating in a point P_1 at a distance R_1 from the first principal plane of an optical system forming a real image in a point P_2 at a distance R_2 from the second principal plane. One has

$$\frac{1}{R_2} = \frac{1}{R_1} - \frac{1}{f}$$

The quantities R_1 and R_2 are the curvature radiuses of the wavefronts at the input and the output of the optical system. The following equations hold:

$$x_2 = Ax_1 + B\dot{x}_1; \qquad \dot{x}_2 = Cx_1 + D\dot{x}_1; \qquad R_1 = x_1/\dot{x}_1; \qquad R_2 = x_2/\dot{x}_2.$$

By eliminating $x_1, x_2, \dot{x}_1$ and $\dot{x}_2$, the so called *ABCD* is obtained:

$$R_2 = \frac{AR_1 + B}{CR_1 + D}$$

Let us list a few properties of the matrices:

1. The determinant of the matrix is the ratio of the indices of refraction of the first and the last media; this means that in a matrix there can be at most two vanishing elements, that are found along a diagonal;
2. if $B = 0$, the coordinates z_- and z_+ are conjugated and the magnification of the optical system is A;
3. if $C = 0$, the system transforms a parallel beam in an other parallel beam (telescopic system), with angular magnification given by D;
4. if $A = 0$, a beam parallel to the optical axis ($\dot{x}_- = 0$) has focus in z_+ ($x_+ = 0$);
5. analogously, if $D = 0$, the light coming from z_- emerges as a parallel beam.

.5.2 Matrix optics and Gaussian beams

In the previous section we noted that, in the free propagation of a Gaussian beam, the complex parameter q evolves like

$$q = q' + (z - z')$$

exactly the same as the curvature radius of a spherical wave. The equation of a thin lens of focal length f can then be generalised as

$$\frac{1}{q'_2} = \frac{1}{q'_1} - \frac{1}{f}$$

where q'_1 and q'_2 are given at the position of the lens. Combining the two relations, one obtains, for the parameters q_1 and q_2 respectively measured at the distances d_1 and d_2 before and after the lens,

$$q_2 = \frac{(1 - d_2/f)\,q_1 + (d_1 + d_2 - d_1 d_2/f)}{-q_1/f + (1 - d_1/f)}$$

As seen before, the matrix of the optical system is given by

$$\begin{bmatrix} 1 & d_2 \\ 0 & 1 \end{bmatrix} \begin{bmatrix} 1 & 0 \\ -\frac{1}{f} & 1 \end{bmatrix} \begin{bmatrix} 1 & d_1 \\ 0 & 1 \end{bmatrix} = \begin{bmatrix} 1 - \frac{d_2}{f} & d_1 + d_2 - \frac{d_1 d_2}{f} \\ -\frac{1}{f} & 1 - \frac{d_1}{f} \end{bmatrix}$$

Hence, in the case of a thin lens, for the parameter q, the same “*ABCD* law" describing the transformation of the curvature radius of the wavefront of a spherical wave traversing an optical system holds:

$$q_2 = \frac{A\, q_1 + B}{C\, q_1 + D}$$

As a consequence, a thin lens of focal length f can be used to transforms a Gaussian beam characterized by a minimum waist w_{01} at position $z_0 = 0$ in a beam with a specified minimum waist w_{02}. This waist is found at a position z_2 that we now want to calculate. Let us remember that the q's are in this case purely imaginary:

$$q_1 = -i\frac{\pi w_{01}^2}{\lambda} \qquad \text{and} \qquad q_2 = -i\frac{\pi w_{02}^2}{\lambda}$$

The imaginary part of the *ABCD* law is written as

$$Dq_2 = Aq_1 \qquad \text{namely} \qquad \frac{d_1 - f}{d_2 - f} = \frac{w_{01}^2}{w_{02}^2}$$

while the real part is

$$Cq_1q_2 = B \qquad \text{namely} \qquad (d_1 - f)(d_2 - f) = f^2 - f_0^2$$

where

$$f_0 = \frac{\pi w_{01} w_{02}}{\lambda}$$

solving the two equations for d_1 and d_2 one gets

$$d_1 = f \pm \frac{w_{01}}{w_{02}}\sqrt{f^2 - f_0^2} \qquad d_2 = f \pm \frac{w_{02}}{w_{01}}\sqrt{f^2 - f_0^2}$$

A plane mirror simply folds the propagation diagram of the beam. A spherical mirror with a curvature radius R has the same effect as a lens with $f = R/2$. If the surface of the mirror coincides with the shape of the of the incident wavefront, the beam propagation after the mirror traces back the evolution of the beam before the mirror.

.5.3 Cavity stability

In this section, we describe the geometrical constraint a cavity must satisfy to be employed as an optical path multiplier. We start considering a system made up of a periodical succession of thin lenses with alternate focal lengths f_1 and f_2, separated by a distance d. This system is the unfolding of the propagation of a paraxial beam between two mirrors of curvature radius $R_1 = 2f_1$ and $R_2 = 2f_2$ separated by the distance d. A curvature radius is positive if the concavity of the mirror points inside the cavity; this corresponds to a converging lens. Convex mirrors, with a negative focal length, are instead diverging. The propagation of the beam is obtained by the infinite repetition of a basic matrix describing the propagation of the beam for a length d, through the first lens f_1, again for d and through the second lens f_2. We note that this is the correct description of a multi-pass cavity, while generally in a Fabry-Perot the first mirror is itself a lens that must be taken into account.

The basic matrix is given by

$$\begin{bmatrix} 1 & 0 \\ -\dfrac{1}{f_2} & 1 \end{bmatrix} \begin{bmatrix} 1 & d \\ 0 & 1 \end{bmatrix} \begin{bmatrix} 1 & 0 \\ -\dfrac{1}{f_1} & 1 \end{bmatrix} \begin{bmatrix} 1 & d \\ 0 & 1 \end{bmatrix} =$$

$$\begin{bmatrix} 1-\dfrac{d}{f_1} & d\left(2-\dfrac{d}{f_1}\right) \\ -\dfrac{1}{f_1}-\dfrac{1}{f_2}+\dfrac{d}{f_1 f_2} & -\dfrac{d}{f_2}+\left(1-\dfrac{d}{f_1}\right)\left(1-\dfrac{d}{f_2}\right) \end{bmatrix}$$

Passing from step n to $n+1$

$$x_{n+1} = A\,x_n + B\,\dot{x}_n; \qquad \dot{x}_{n+1} = C\,x_n + D\,\dot{x}_n$$

From the two equations one obtains the expressions

$$\dot{x}_n = (x_{n+1} - A\,x_n)/B \qquad \text{and} \qquad \dot{x}_{n+1} = (x_{n+2} - A\,x_{n+1})/B$$

that, substituted into the second (the determinant $AD - BC$ is unitary), give

$$x_{n+2} - (A+D)\,x_{n+1} + x_n = 0$$

This equations has a solution

$$x_n = x_0\,e^{in\theta}$$

which, substituted in the preceding equation gives

$$e^{i2\theta} - (A+D)\,e^{i\theta} + 1 = 0$$

which results in

$$e^{\pm i\theta} = \frac{A+D}{2} \pm i\sqrt{1 - \frac{(A+D)^2}{4}}$$

and

$$\cos\theta = \frac{A+D}{2} = 1 - \frac{d}{f_1} - \frac{d}{f_2} + \frac{d^2}{2f_1 f_1}$$

The angle θ is thus determined only by the geometry of the system. A general solution can thus be written as

$$x_n = a\cos n\theta + b\sin n\theta = x_{\max}\,\sin(n\theta + \theta_0)$$

Obviously $x_0 = a$, while the value of b is obtained by

$$x_1 = A\,x_0 + B\dot{x}_0 = a\cos\theta + b\sin\theta$$

The condition $-1 \leq \cos\theta \leq 1$ can be put as

$$0 \leq \left(1 - \frac{d}{2f_1}\right)\left(1 - \frac{d}{2f_2}\right) \leq 1$$

or, in terms of the curvature radiuses of the mirrors

$$0 \leq \left(1 - \frac{d}{R_1}\right)\left(1 - \frac{d}{R_2}\right) \leq 1$$

When this condition is not satisfied, the exponential becomes real and the solution diverges. The stability condition can be represented graphically. With $g_i = 1 - d/R_i$, stability is ensured by

$$0 \leq g_1 g_2 \leq 1$$

If g_1 and g_2 are orthogonal coordinates in a Cartesian plane, stable regions are found in the first and the third quadrants between the coordinate axes and the equilateral hyperbola of equation $g_1 g_2 = 1$. To values $g < 1$ concave mirrors correspond, with $0 < R < d/2$ for $g < -1, D/2 < R < d$ for $-1 < g < 0$, $d < R$ for $0 < g < 1$. One has convex mirrors ($R < 0$) for $g > 1$.

In the case the mirrors are identical, the elemental matrix is simplified. The finite difference equation is instead the same and one has

$$\cos\theta = \frac{A+D}{2} = 1 - \frac{d}{2f} = 1 - \frac{d}{R}$$

The stability equation becomes

$$0 \leq \frac{d}{R} \leq 2$$

Chapter 3

The PVLAS experimental set-up in Ferrara.

3.1 Clean room

Figure 3.1: Two views of the PVLAS clean room and monitoring area station.

The PVLAS experiment is located in an industrial building of the Department of Physics of Ferrara/INFN Ferrara together with other experiments and the mechanical workshop (see Figure 3.1). The experiment is hosted in a 6.4×8.9 m^2 ISO-4 class clean room (the maximum number of particles per cubic meter with dimension ≥ 0.1 μm is $10,000$). The structure was previously used for the assembly of LHCb detectors. A schematic layout of the clean room is shown in Figure 3.2. The large equipment necessary for air conditioning is located outside the building.

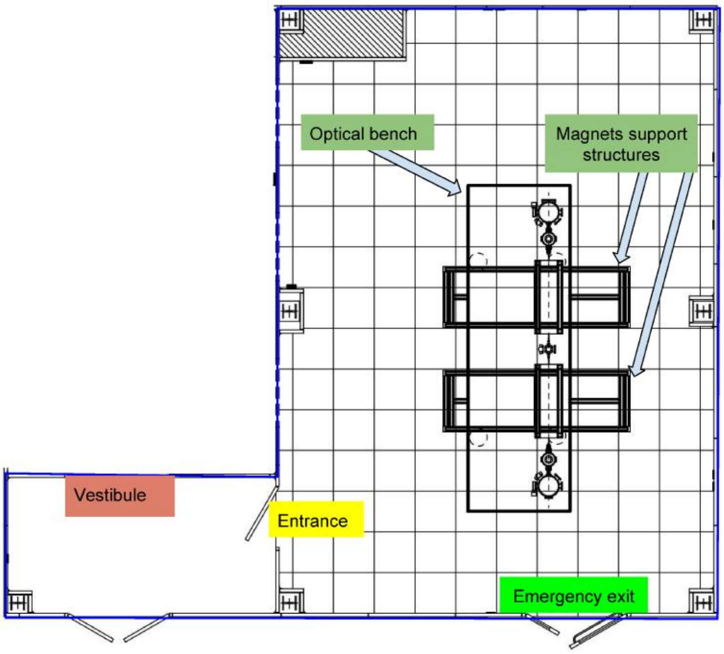

Figure 3.2: Layout of the PVLAS experiment inside the clean room.

The clean room has controlled temperature, humidity (necessary to prevent electrostatic problems) and pressure and is under operation 24h/24. It is kept at 56% relative humidity, and at 23°C temperature. The measured temperature shows an oscillation of 0.1° with a period of ~ 10 min. The air pressure inside the clean room is slightly higher than the atmospheric pressure to prevent the entrance of unfiltered air. Three pumpable gas lines are available inside the clean room, coming from cylinders of pure gases placed outside the building. Access to the clean room is restricted when the class IV laser is on.

To minimise environmental noise, the PVLAS apparatus is normally monitored and handled from a control zone located outside the clean room. Human presence inside the clean room is only needed during tuning or calibrations.

3.2 Optical bench and seismic noise isolation

The optical bench consists of a granite table and a mechanically isolated support system. The main characteristics of the are listed in table 3.2. The granite optical table, manufactured by Microplan, Quarona (VC), Italy, has dimensions $4.8 \times 1.5 \times 0.5$ m^3 and a weight of ≈ 4 tons. The main characteristics of the granite table are high internal stability, good thermal stability due to the large mass, a linear expansion coefficient smaller than steel, hardness comparable

Material	Granite with honeycomb structure
Mass	4 tons
Dimensions	$480 \times 150 \times 50$ cm^3
Position stability	± 0.01 mm
Attenuation of seismic noise	See Figure 3.4

Table 3.1: Main characteristics of the optical table (see also Figs. 3.2 and 3.25).

to good-quality tempered steel, excellent flatness of the surfaces, nonmagnetic nor conductive material.

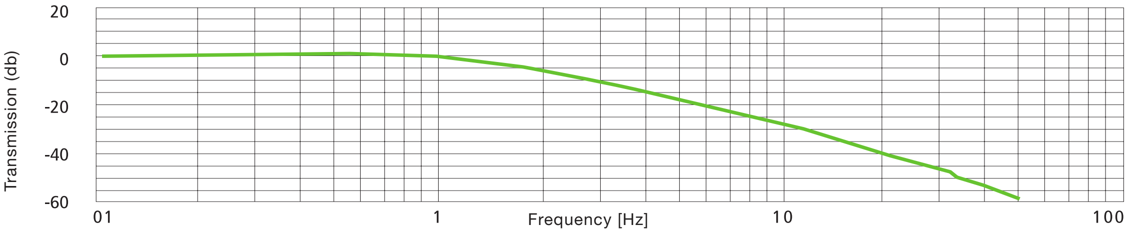

Figure 3.3: The transmission function of the membrane air spring BiAir declared by the manufacturer.

The bench is sustained by four pneumatic air springs produced by Bilz Vibration Technology AG. These legs are part of the 6 degrees of freedom AIS$^{\text{TM}}$-Active Isolation System, which is based on programmable logic controllers (PLC), high-speed electro-pneumatic servo-valves and membrane vertical and horizontal air springs. The typical frequency response of one of the degrees of freedom is shown in figure 3.3. As one can see, the cut-off frequency of the insulation system is about 1 Hz. The whole AIS system is insensitive to magnetic fields. Besides vibration isolation, the system controls the absolute value of all the six degrees of freedom of the position of the bench. This accurate position control is reached using position sensors (resolution 0.2 μm), acceleration sensors (resolution 8 μg), air-pressure sensors (resolution 0.2 mbar) and electro-valves. The overall repeatability of the feedback system at each of the six position monitors is within ± 0.01 mm.

After installation and optimization of the vibration isolation system by the manufacturer, a measurement of the vertical component of the acceleration of the floor and of the optical table was acquired. The Fourier spectra of the two measurements are shown in Figure 3.4. The attenuation of the ambient seismic noise was found compatible with the characteristics claimed by the manufacturer.

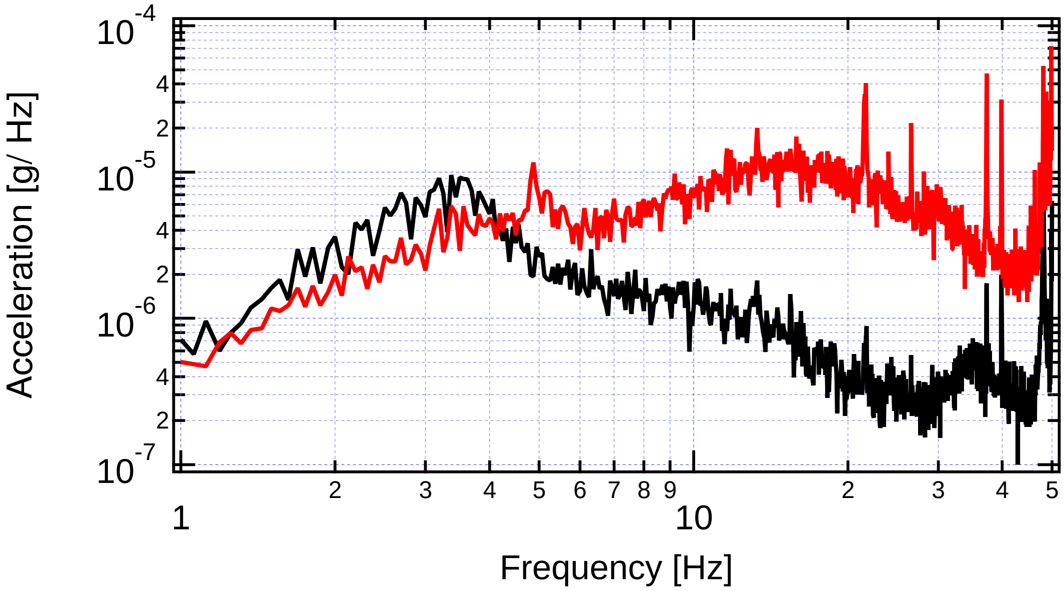

Figure 3.4: Fourier spectrum of the vertical component of the acceleration on the floor of the clean room (red curve) and on the seismically isolated optical bench (black curve).

3.3 The two rotating magnets

Magnetic field region

External diameter ϕ_{ext}	280 mm
Internal free bore diameter ϕ_{in}	20 mm
Overall length	938 mm
Magnetic field in the center of the bore	2.5 T
Magnetic stray field on axis 20 cm outside	10^{-4} T
Mass	450 kg
Maximum tested rotation frequency	23 Hz
Magnetic material	$Nd_2Fe_{14}B$
Longitudinal sectors	12
Number of wedges per sector	16
Magnetic field profile on axis	see Figure 3.9

Table 3.2: Characteristics of the twin permanent magnets.

In the PVLAS apparatus two high-field dipole permanent magnets are installed; their characteristics are listed in table 3.3. They are 0.94 cm long cylinders of external radius $r_{\mathrm{ext}} = 14$ cm with a clear bore of radius $r_{\mathrm{in}} = 10$ mm. The magnets can rotate around their axes at a frequency higher than 20 Hz. The magnetic field vectors of the two magnets rotate

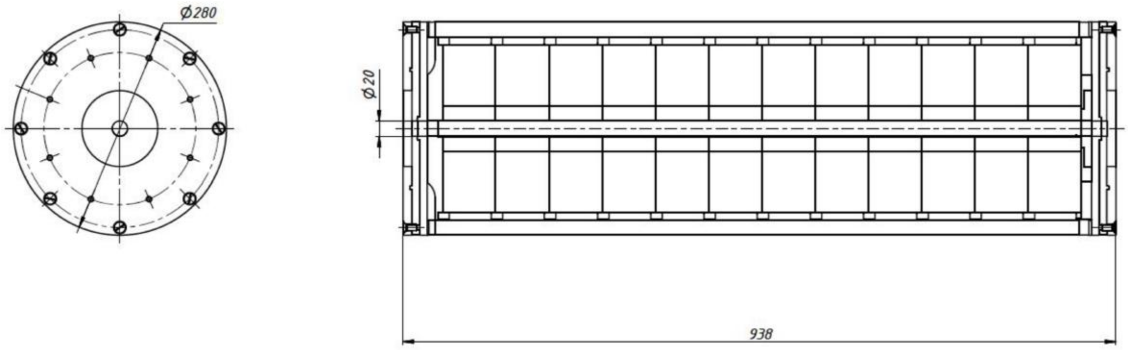

Figure 3.5: Technical drawing of a magnet.

in planes normal to the path of the light stored in the cavity. The central bore of each magnet is traversed by a dielectric vacuum tube to allow the passage of the laser light in vacuum. The diameter of each tube is smaller than the diameter of the bore of the magnets: no contact is allowed between the magnet and the tube. The two magnets have been designed and realised by Advanced Magnetic Technology & Consulting (Troitsk, Moscow, Russia) which has also balanced them for rotation up to 6 Hz. The magnets are housed in a 1 cm thick iron cylindrical casing ending on both sides with flanges orthogonal to the axis of the cylinder. The parallelism of the two flanges is better than 0.1 mrad. The magnetic material of the magnets is an alloy of neodymium, iron and boron with chemical formula $Nd_2Fe_{14}B$ of the crystalline tetragonal system. Developed in 1982 by General Motors and Sumitomo Special Metals, “Neodymium” magnets are the strongest permanent magnets available on the market.

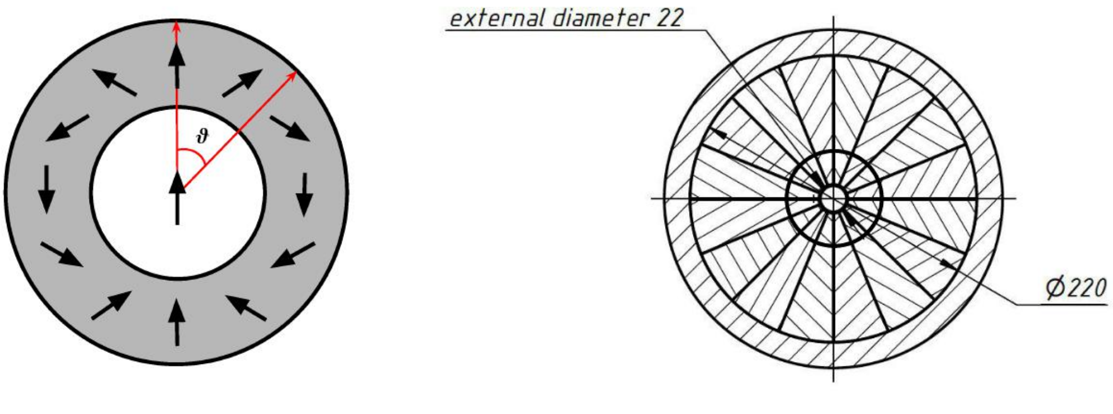

Figure 3.6: On the left, the principle scheme of the cylindrical Halbach geometry: as a function of the polar angle ϑ, the direction α of polarisation inside the cylindrical corona continuously rotates as $\alpha = 2\vartheta$. On the right the practical realisation of the scheme for the PVLAS magnets: the i-th sector of the corona is magnetised along $\alpha_i = 2\langle\vartheta\rangle_i$.

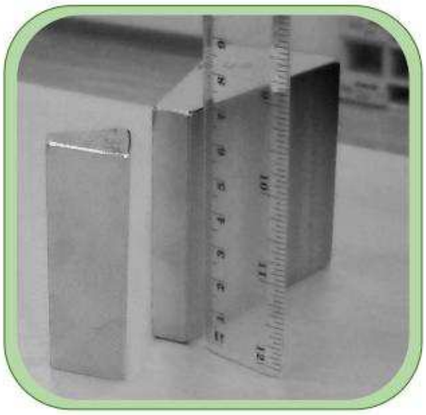

Figure 3.7: Picture of the two types of magnetic elements used for the realisation of the PVLAS permanent magnets according to the Halbach scheme.

The magnetic structure of the magnets follows the Halbach cylindrical scheme (see Figure 3.6) generating an intense fairly homogeneous magnetic field in the central bore, with the return field well confined within the cylinder with, ideally, a zero field outside. To this end, the magnetisation direction inside the cylindrical corona should continuously rotate as a function of the polar angle as $\alpha = 2\vartheta$. In the practical realisation of this scheme, the number and shape of the magnetic elements may vary: a general rule is to rotate the magnetisation direction while going from one element to the other. The more smoothly the magnetisation direction turns along the ring, the larger the number of sectors the ring is divided into and the closer is the field pattern to the ideal one. A picture of the two types of magnetic elements used during the fabrication of the PVLAS magnets is shown in Fig. 3.7. The field in the center of a finite length Halbach cylinder is given analytically by the following expression [88]

$$B_{\text{centre}} = B_{\text{rem}} \left[\ln\left(\frac{r_{\text{ext}}}{r_{\text{in}}}\right) + \frac{z_0}{2\sqrt{r_{\text{in}}^2 + z_0^2}} - \frac{z_0}{2\sqrt{r_{\text{ext}}^2 + z_0^2}} - \ln\left(\frac{\sqrt{r_{\text{ext}}^2 + z_0^2} + z_0}{\sqrt{r_{\text{in}}^2 + z_0^2} + z_0}\right)\right] \tag{3.1}$$

where r_{ext} is the outer radius of the cylinder, r_{in} is the inner radius and $z_0 = L/2$, where L is the length of the cylinder and B_{rem} is the remanent flux density of the magnetic material. For Neodymium magnets, $B_{\text{rem}} = 1.1 - 1.5$ T. A plot of B_{centre} as a function of the internal radius r_{in} is shown in Figure 3.8.

The longitudinal profile of the magnetic field of one PVLAS magnetic is shown in Fig. 3.9. The magnetic profiles show a maximum field value of 2.5 T for a total $\int B^2 dL = (5.12 \pm 0.04)$ T^{2}m. This value corresponds to an effective length $L = 0.82$ m for a nominal value of the field $B = 2.5$ T. The stray field along the axis 20 cm outside the each magnet is less than 1 G.

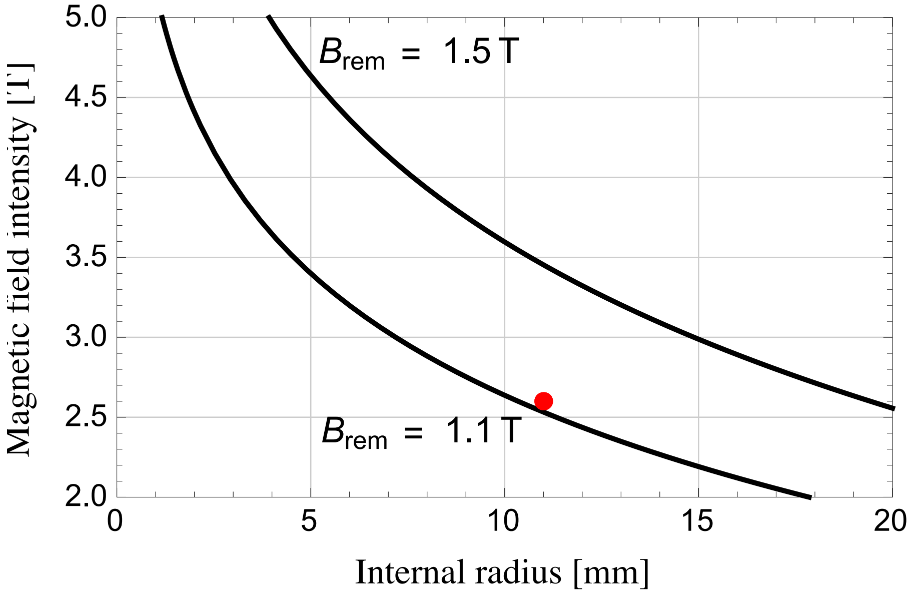

Figure 3.8: Calculated magnetic field intensity in the centre of a Halbach cylinder [eq. (3.1)] as a function of the internal radius for $B_{\text{rem}} = 1.1$ T and $B_{\text{rem}} = 1.5$ T, for fixed external radius $r_{\text{ext}} = 110$ mm and length $L = 838$ mm. The red dot indicates the PVLAS magnets.

Support, alignment and rotation of the magnets

Each magnet is suspended using ball bearings to allow rotation. It is held in an aluminum cart hanging from an aluminum structure standing on the floor (see Fig. 3.10; the diagonal bars and the triangular plates stiffening the structures are not displayed). The two support structures are aligned so that the axis of rotation of each magnet coincides with the path of the laser light in the FP cavity. The centres of the two magnetic regions are separated by ≈ 150 cm (see Figure 3.25). Each of the supports of the ball bearings can be adjusted continuously in the vertical direction to align each magnet along the optical axis of the FP cavity. The carts with the magnets can slide in the transverse horizontal direction along rails fixed to the top of the frames supporting the magnets to allow the insertion and the removal of the vacuum tubes passing through the bores. A fine adjustment of the position of the tubes is done using the tube holders to better than 0.01 mm. The two support structures have been recently coupled by horizontal girders not displayed in the figure. The ensemble of the two structures is supported by four pneumatic feet to reduce the transmission to the floor of the vibrations generated by the two rotating magnets.

The rotating magnets induces mechanical vibrations in the supporting structure. It has to be noted that the factory balancing was performed with a different mechanical assembly with respect to the magnet suspension in the experiment. To reduce the vibrations a balancing

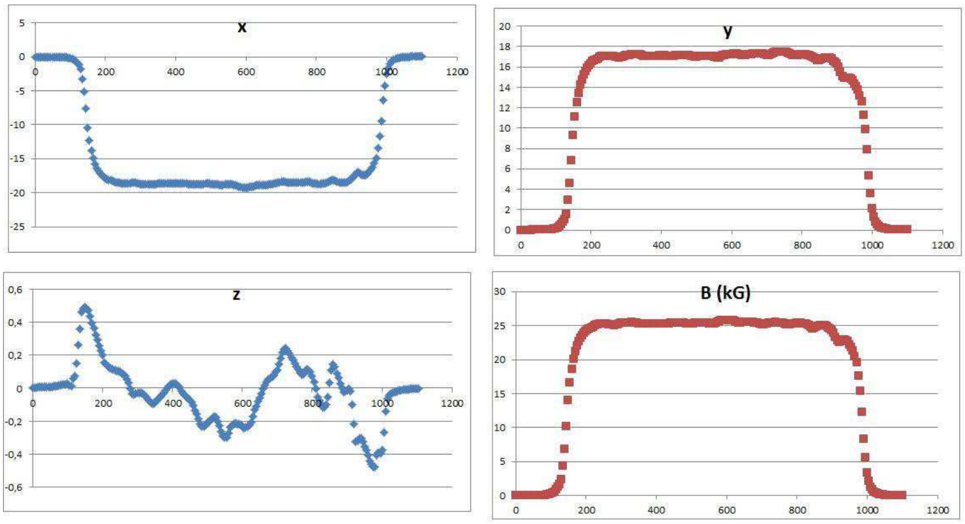

Figure 3.9: The measured intensity of the magnetic field along the bore for the three axes x, y and z, and the total transverse magnetic field.

procedure at $\nu_B = 4$ Hz was done. To balance a magnet two accelerometers (labeled 1 and 2) are mounted to sense the horizontal acceleration on the vertical struts sustaining each magnet, at the intersections with the horizontal plane passing through the axis of a magnet. The imbalance of the magnet is arbitrarily chosen to be located on the external surface of the magnet along two circumferences, 72 cm apart, where four threaded holes are present to host the eye bolts used to lift the magnets. These holes allow the fastening of small balancing masses. The accelerations and the imbalances are represented by the complex numbers $\mathbf{A}_{1,2}$ and $\mathbf{M}_{1,2}$, respectively. The magnitude of the complex number is the value of the quantity, whereas the argument is its angular phase. A linear relation between the masses and the observed accelerations is assumed at the rotation frequency of the magnet ν_B :

$$\begin{aligned}\mathbf{A}_1 &= \mathbf{k}_{11}\cdot\mathbf{M}_1 + \mathbf{k}_{12}\cdot\mathbf{M}_2\\ \mathbf{A}_2 &= \mathbf{k}_{21}\cdot\mathbf{M}_1 + \mathbf{k}_{22}\cdot\mathbf{M}_2,\end{aligned}$$

where the symmetry relation between the complex coefficients $\mathbf{k}_{ij}$ require that $\mathbf{k}_{11} = \mathbf{k}_{22}$ and $\mathbf{k}_{12} = \mathbf{k}_{21}$. The values of the coefficients are determined by placing a unitary test mass in different positions on a magnet and measuring the accelerations:

$$\begin{aligned}&\mathbf{k}_{11} = \mathbf{A}_1(1) - \mathbf{A}_1(0), \quad \mathbf{k}_{21} = \mathbf{A}_2(1) - \mathbf{A}_2(0)\\ &\mathbf{k}_{12} = \mathbf{A}_1(2) - \mathbf{A}_1(0), \quad \mathbf{k}_{22} = \mathbf{A}_2(2) - \mathbf{A}_2(0).\end{aligned}$$

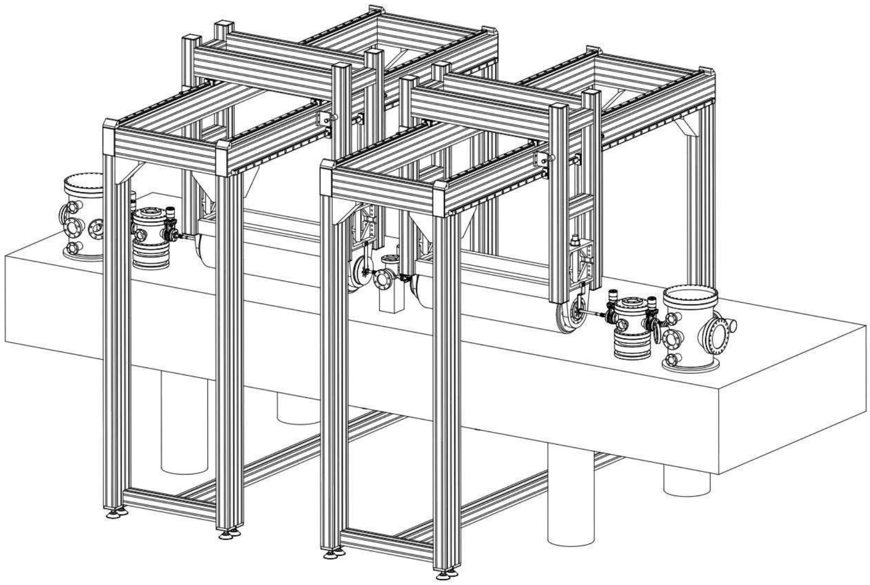

Figure 3.10: The support structure of the permanent magnets.

The argument of the accelerations indicates on which of the two circumferences a unitary test mass has been placed. The "0" argument, instead, denotes a reference measurement with no test weight. Once the values of the coefficients have been determined, the magnitude and phase of the two balancing masses $\mathbf{M}_{1,2}$ are obtained by solving the equations

$$\begin{aligned}\mathbf{A}_1(0)+\mathbf{k}_{11}\cdot\mathbf{M}_1+\mathbf{k}_{12}\cdot\mathbf{M}_2=0\\ \mathbf{A}_2(0)+\mathbf{k}_{21}\cdot\mathbf{M}_1+\mathbf{k}_{22}\cdot\mathbf{M}_2=0.\end{aligned}$$

By adding masses ~ 100 g, the balancing procedure has allowed the reduction of the imbalance below ~ 10 g, with a residual acceleration signal on the structure of $\sim 10^{-4}$ m/s^2 @ $\nu_B = 4$ Hz. The imbalance of ~ 10 g corresponds to a centrifugal force of about ~ 22 N acting on the structure with the magnets rotating at 20 Hz. The balancing limit is due to the integration time, that has been kept below 100 s, and to the fact that the magnet is fastened to the rigid structure of the cart that exhibits several mechanical resonances, resulting in an acceleration signal having periodical low-frequency amplitude oscillations. To improve the balancing of the magnets, one should work at a higher rotation frequency, at the same time integrating the acceleration signal for longer times. This improvement will be done in the next future.

Three-phase brushless motors	
Triplets of coils	10
Number of poles	20
Maximum speed	10 Hz
Maximum torque	7 kNm
Transmission	
Cog step on belt and pulleys	8 mm
Number of cogs on belt	180
Tension on belt	$\lesssim$ 100 kg
Number of V-shaped cogs on driving pulley	80
Number of V-shaped cogs on magnet pulley	18

Table 3.3: Characteristics of motors and transmission.

Motors and transmissions

An electrical motor is mounted in each of the two carts hosting the magnets to allow independent rotations of the two magnets. The movement is transmitted using a pair of pulleys and a toothed belt. The characteristics of the motors and of the transmissions are in table 3.3. The ratio of the number of teeth on the two pulleys is chosen in such a way to keep the frequencies of at least the first few harmonics of the motors and the magnets separated. This ratio was 45/42 during the first runs and has been changed to 80/18 to boost the rotation frequency of the magnets.

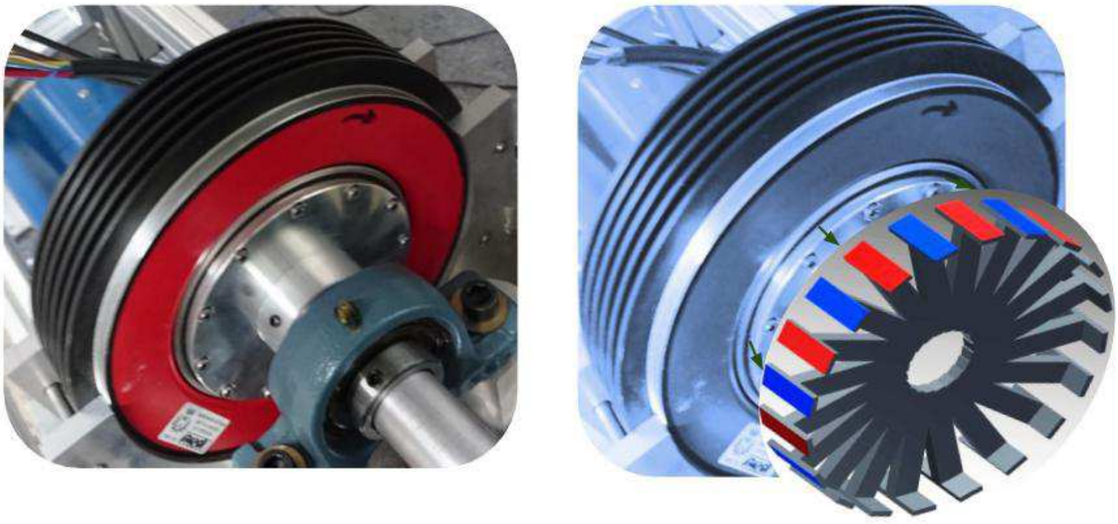

Figure 3.11: Left: a photo of the torque brushless synchronous motor mounted on the support structure of the magnet. Right: a scheme of the rotor with ten couples of dipoles distributed in a circular pattern.

The motors are brushless torque synchronous motors in which the coils are on the stator and the rotor is equipped with permanent dipole magnets. The motors are TK series by Phase Motion Control, Genova, Italy, featuring high-speed (10 Hz) and high torque (7 kNm). They consist of a stator and a rotor provided separately, planned for direct assembly in the structure. The three-phase stator has ten triplets of coils. The configuration of the coils is in groups of three for a three-phase power supply. The rotor has 10 North-South magnetic pole pairs distributed along a circular ring (see Figure 3.11). This configuration implies that the frequency of the rotor is ten times smaller than the frequency of the current in the coils of the stator.

The factory drive for this type of motor is designed to exploit its high torque: an encoder applied to the shaft of the motor allows the power supply to maintain a 90° phase advance between the current in the coils and the nearest equilibrium position of stator and rotor. In this operating condition, the rotational speed can be chosen only approximately. However, in our application, there is no need for high torque. We thus chose a different way of driving the motors: three sinusoidal signal generators are phase-locked at the same frequency at 120° one from the other. The signals from the three generators are sent to three current audio amplifiers whose output is given directly to the three phases of the motor. The frequency of the generators is slowly increased to reach the planned rotation frequency. During operation, the current in the coils of the stator is close to $\sim 0^\circ$ from the equilibrium position of the rotor. In this way, the torque delivered by the motor is quite low, with the benefit that any trouble in the rotation of the magnets ends with the magnet losing synchrony with the drive and slowing down due to friction. The big advantage of this way of operating is that the two rotating magnets represent two phase locked master clocks for the experiment, its angular phase being the time variable. That phase is a crucial feature for data acquisition and analysis.

3.4 The vacuum system

The whole polarimeter of the PVLAS experiment, from polariser to analyser, is kept under vacuum. In Figure 3.12, is shown a layout of the vacuum system, which features of five vacuum chambers and two 130 cm long dielectric tubes aligned along the path of the light beam. The inner volume of the system is less than 50 L, with 20 L for each of the input and the output chambers, 3 L for each of the mirror chambers, and about 1 L for the central vacuum chamber. Short bellows between adjacent elements compensate for small misalignments. All of the vacuum components except the tubes are realised in AISI 316 stainless steel, titanium, and aluminum, which are all nonmagnetic. Conflat flanges sealed with copper gaskets are used for all the standard connections.

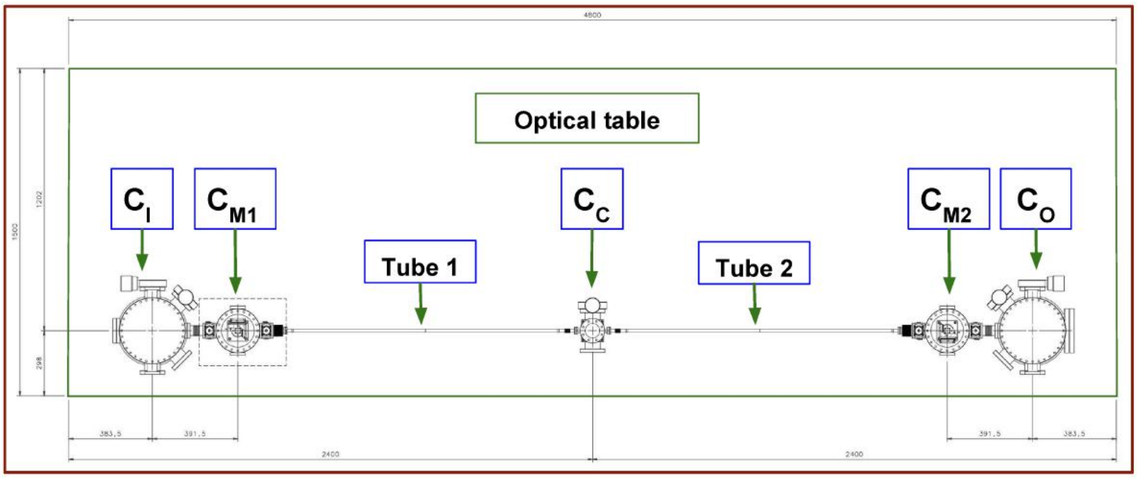

Figure 3.12: Layout of the vacuum enclosure mounted on the optical table: input vacuum chamber (C_I), first mirror vacuum chamber (C_{M1}), central vacuum chamber C_C, second mirror vacuum chamber (C_{M2}), output vacuum chamber (C_O). Mirror chambers are connected to the central one by diamagnetic tubes.

The dielectric tubes are connected to the chambers in a special way. In a first phase of the experiment, before this thesis work, the tubes were in pyrex, soldered *in situ*, after insertion in the magnet bores, to commercial glass-to-metal junctions with CF40 flanges. This had several disadvantages: the tubes could not be extracted from the magnet bores; testing tubes of a different diameter required glass blowing capability that the Physics Department does not have; testing tubes made of a different material was impossible; moreover, when disconnected from the vacuum system, the flanges weighed on the glass, risking to break it.

At the beginning of this thesis work, it was decided to resort to a different sealing system employing Viton o-rings sitting in a groove of the CF40 flanges at the extremities of the tube and compressed against its external surface. This fitting, schematically shown in Figure 3.13 allows to mount and dismount the tubes easily. Thanks to this mount, glass tubes of various diameters have been tested, all with a 1.5 mm wall thickness. In the beginning, two carbon fiber sleeves held by the supports of the magnets surrounded the glass tubes; they were intended to shield the tubes from air turbulence and periodic light coming from the rotating inner surface of the magnet's bore, which could give origin to synchronous noise. In a second phase, the carbon fiber tubes were removed, and the external wall of the glass tubes was painted black. Presently, thick and sturdy silicon nitride ceramics tubes are employed, with outer diameter 18 mm and wall thickness 3.75 mm.

The cavity mirrors are hosted in two vacuum chambers (C_{M1} and C_{M2}) each of which can be isolated from the rest of the system through two gate valves; this avoids contamination of the mirrors when air has to be put into the other chambers. The light beam enters the

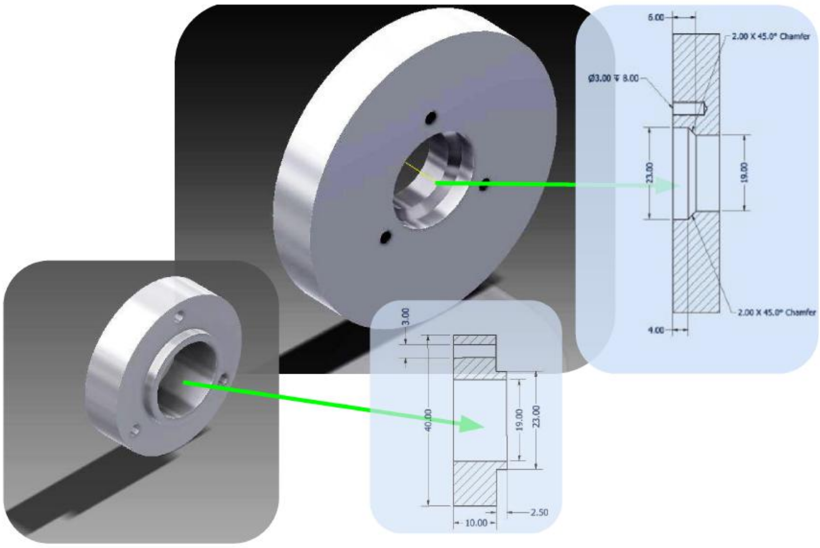

Figure 3.13: The design of the home-made seal of the dielectric tubes: a Viton o-ring compressed against the external surface of the tubes ensures sealing for vacuum.

vacuum through an AR-coated optical window of chamber C_I, which host the polariser and a compensation wave plate which can be inserted and extracted from the beam. In the exit chamber C_O a quarter-wave plate, the photo-elastic modulator (PEM) and the analyser are installed. The central chamber C_C serves as a pumping station, and contains a 5 mm diameter diaphragm, carved out from a slab of absorbing glass with antireflecting coating for 1064 nm, which can be manually centred on the beam or retracted completely. The fine positioning of most optical elements installed inside the vacuum enclosure is ensured by vacuum-compatible piezoelectric-actuated non-magnetic nanopositioners by SmarAct GmbH, Germany. The polariser and analyser can be rotated by up to 360° around the beam axis but cannot be translated. All the wave plates can be rotated by 360° and can be fully retracted from the beam. The mirrors are held by three-rotator gimbal mounts which enable the two tilts and an azimuthal 360° rotation [see Figure 3.14]; the photo-elastic modulator (PEM) can be rotated by about 90° (mechanical constraints limit a larger rotation) and translated for optimisation. The PEM can also be retracted completely from the beam. Large slabs of Schott KG5 absorbing glass with 10 mm diaphragms centred on the beam are used to absorb diffused light in the entrance and the exit chambers.

The vacuum enclosure is pumped by three oil-free pumping systems installed on the input, central and output chambers. Three scroll primary pumps bring the pressure down to $\sim 10^{-1}$ mbar, starting from atmospheric pressure; a pressure $< 10^{-7}$ mbar is reached by the use of three secondary turbo-molecular pumps and three Non-Evaporable Getter (NEG) pumps. Turbo pumps are fastened to the chambers, while scroll pumps, which generate

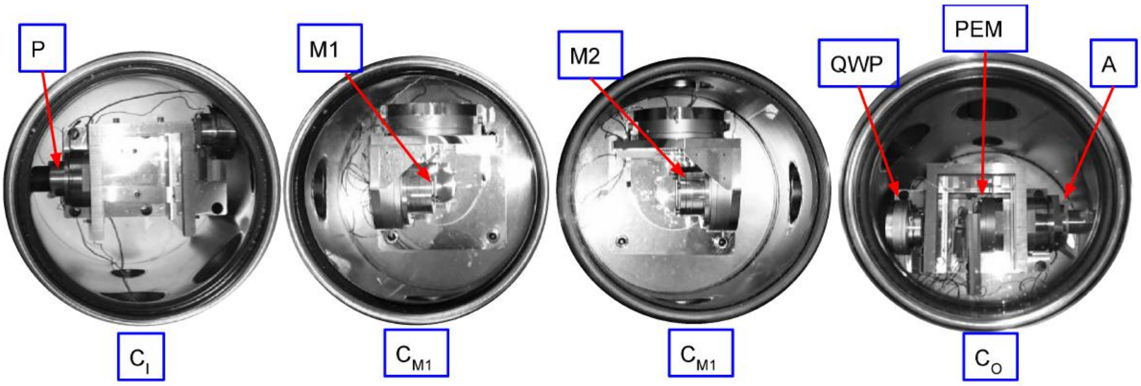

Figure 3.14: Top view pictures of the inside of the vacuum chambers. The input vacuum chamber C_I that hosts the polariser (P). The C_{M1} and C_{M1} are the two mirror vacuum chambers. The output vacuum chamber C_O hosts the quarter-wave plate (QWP) and the ellipticity modulator (PEM), the analyser (A).

intense mechanical vibrations, are positioned on a separate platform above the optical bench. When the turbo pumps have brought the system to a pressure below 10^{-6} mbar, three CapaciTorr D1000 Non-Evaporable Getter (NEG) pumps by SAES Getters, Milano, Italy, come into play through the opening of their gate valves, the gate valves on the two turbo pumps on the input and output chambers are closed and the turbo pumps are turned off. The central turbo pump is left running. Figure 3.15 shows a NEG pump and its performance, which is based on the adsorption of gas molecules from the atmosphere onto a microporous reactive surface. NEG pumping performances depend on the interaction with the getter material. Gases like Hydrogen are physically sorbed; gases such as CO, CO_2, O_2 and N_2 are sorbed irreversibly; a few species, among which water vapour and hydrocarbons, are sorbed in both ways; noble gases do not interact with the getter. These pumps have several advantages: they are quiet; they pump all gases except noble ones; given their high capacity, at pressures $\sim 10^{-7}$ they stay active for months without any power supply; they are non magnetic. When the surface of the getter material is saturated, the material can be regenerated with a baking procedure by means of an electrical heater integrated in the pump body; heating cleans the surface of the getter material by diffusing chemically sorbed molecules into the bulk and by making the physically adsorbed ones desorb; this operation can be repeated dozens of times before the cartridge of the pump has to be replaced. The only drawback of this pump is the fact that the getter material releases a small flux of Methane and, to a lesser extent, Helium. In a sealed vacuum system, the partial pressure of Methane gas grows up to an equilibrium pressure $< 10^{-7}$ mbar. Helium partial pressure, instead, grows beyond 10^{-6} mbar. This degassing of the pumps does not allow to rely uniquely on these pumps for

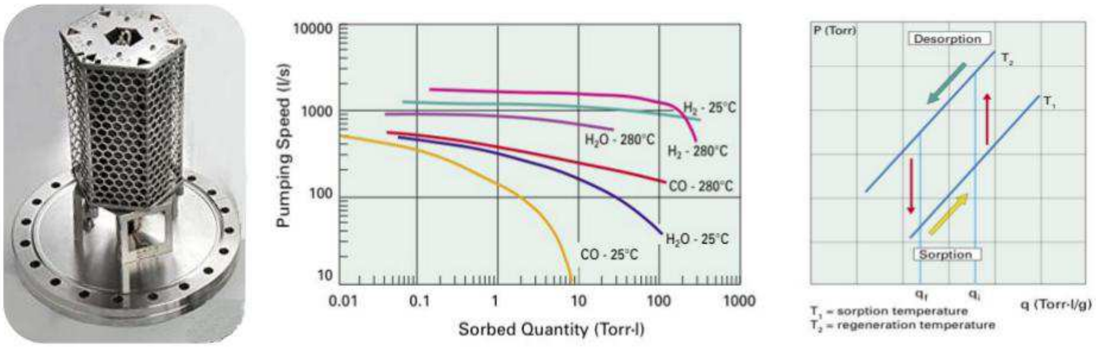

Figure 3.15: Left: picture of a NEG pump. Centre: pumping speed for a few molecular species. Right: regeneration principle: q_f is the final quantity of H_2 in the getter material in Torr·l/g, q_i is the initial amount of H_2 in the getter material in Torr·l/g.

vacuum. The turbo pump on the central chamber, which sits far from the mirrors, is kept running permanently to get rid of the Methane and Helium gases. As mentioned above, since their mechanical vibrations disturb the frequency locking of the Fabry-Perot cavity, the other two turbo pumps are usually isolated from the system using gate valves and switched off. A small valve also isolates the exhaust of the turbo pumps when they are switched off to limit water absorption in the pump body and prevent the entrance of the dust coming from the scroll pumps.

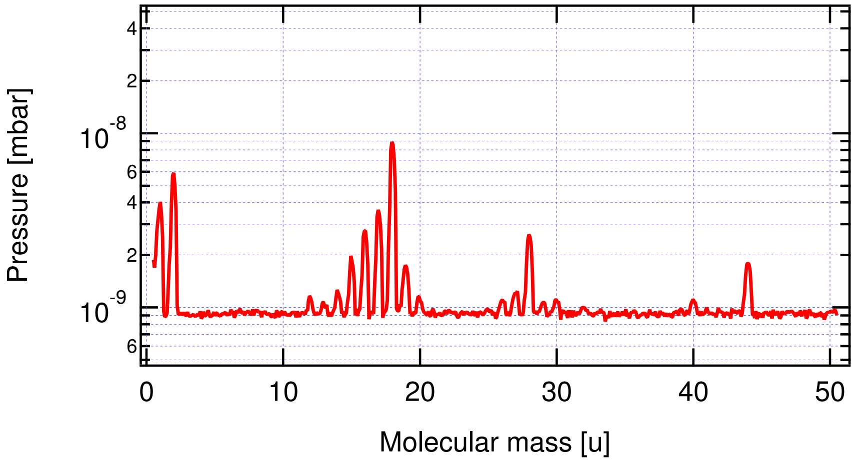

Figure 3.16: Typical RGA mass spectrum for a total pressure of 5×10^{-8} mbar. Main contaminants are Hydrogen and water.

The total pressure is measured by three pairs of Pirani and Bayard-Alpert gauges. Ultimate pressures in the low 10^{-8} mbar range are achieved. Two Residual Gas Analysers monitor the quality of the vacuum in the central and output chambers. Since gases exhibit magnetic birefringence (Cotton-Mouton effect), knowing the composition of the residual atmosphere in the vacuum system is essential to be sure that the residual gases have a birefringence much smaller than the one due to the magnetic birefringence of vacuum. A typical mass spectrum of the residual atmosphere is shown in Figure 3.16. The main residual gases are Hydrogen and water vapor (the vacuum system cannot be baked). Their contribution to the magnetic birefringence is estimated using the values listed in Chap. 2, Table 2.2. From that table, one finds that a Cotton-Mouton birefringence having the same value as vacuum magnetic birefringence is obtained with a partial pressure of 5×10^{-7} mbar of H_2 or 6×10^{-7} mbar of H_2O. From the spectra reported in the Figure 3.16, one can see that the actual contribution of each of these two species is less than 1% of the effect due to the vacuum.

Non magnetic UHV chambers	
Polarisers chambers	CF250, h 400 mm, AISI304 steel
Mirrors chambers	CF150, h 160 mm, AISI304 steel, Ti bases h 120 mm
Central chamber	5-ways standard CF40 cross
Pyrex tubes	$\oslash_{\text{ext}}$ $(15-18)$ mm, $\oslash_{\text{i}}$ $(12-15)$ mm
Si_3N_4 tubes	$\oslash_{\text{ext}}$ 17 mm, $\oslash_{\text{i}}$ 10.5 mm
Pumps	
3 turbo Pumps	Agilent V 70LP, V 81, ultimate pressure $\approx 10^{-9}$ mbar
3 NEG pumps	SAES Getters, 2 CapaciTorr D1000, 1 Sorb-AC 100 MK5
3 primary pumps	Agilent IDP-3 dry scroll, ultimate pressure 3.3×10^{-1} mbar
Gauges	
Pressure gauges	3 Bayard-Alpert + Pirani
Capacitive gauge	MKS Baratron 622A, range: 0.1 μbar – 1 mbar
2 Residual Gas Analysers	1 Balzers Prisma QMS200M, 1 Extorr XT100M, range: $(10^{-3} - 10^{-14})$ mbar

Table 3.4: Characteristics of the vacuum system.

The characteristics of the vacuum chambers, the pumps and the gauges are listed in Table 3.4. The capacitive gauge is used to monitor the gas pressure during the calibrations.

3.5 Laser

The measurements presented in this thesis have been taken with a solid state NPRO (Non-Planar Ring Oscillator) tuneable Mephisto 2000NE laser by Innolight GmbH, Hannover, Germany, with $\lambda = 1064$ nm and maximum emitted power 2.14 W. Its main characteristics are summarised in Tab. 3.5. The laser cavity is a single crystal of Nd:YAG (Yttrium-Aluminium-Garnet) within which the light describes a non-planar optical path by total internal reflection on three surfaces of the crystal (see Figure 3.17). The beam comes out through a dielectric film that serves as an output coupler for the laser and allows the longitudinal pump radiation

Wavelength	1064 nm
Fast control	range ±100 V, bandwidth 100 kHz
Fast control tuning coefficient	≈ 1 MHz/V
Slow control	range 30 GHz, bandwidth 1 Hz
Thermal tuning coefficient	-3 GHz/K
Frequency interval between mode-hops	≈ 8 GHz
Max power	2.14 W
Beam quality M^2	1.02
Beam waist	123 μm
Free laser line width	< 1 kHz
Temperature drift frequency	$\Delta\nu < 15$ MHz/h

Table 3.5: Mephisto Innolight NPRO laser characteristics.

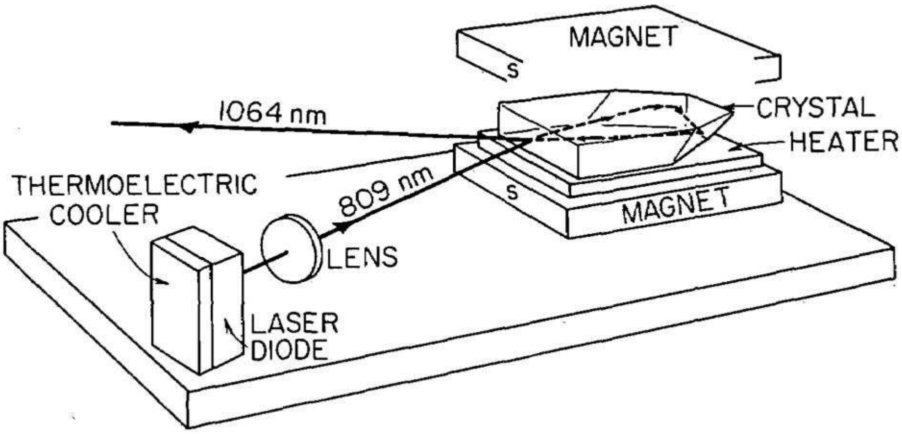

Figure 3.17: Typical NPRO cavity of the of tunable 1064 nm laser light.

from two laser diodes to enter the crystal. The power supply stabilises the temperature and the current of the two pump diodes. The presence in the laser cavity of a small magnetic field favours the excitement of a single mode propagating in only one direction and reduces the sensitivity to back reflected light. The beam quality is quantified by the M^2 factor (also called beam quality factor or beam propagation factor). Mathematically, it is the ratio of the square of the actual beam waist to the ideal Gaussian beam waist. For a theoretical Gaussian beam waist, $M^2 = 1$; for a real laser beam, $M^2 > 1$. The manufacturer quotes a value $M^2 = 1.02$.

Our measurements of the beam waist as a function of the propagation coordinate are shown in Figure 3.18. From these measurements, the beam waist is estimated to be $w_0 = 123$ μm, located at -17 cm behind the exit window of the laser. Knowledge of these values is necessary for mode matching the laser beam to the cavity. The measurements were made by measuring the laser power as a function of the distance through a pin hole

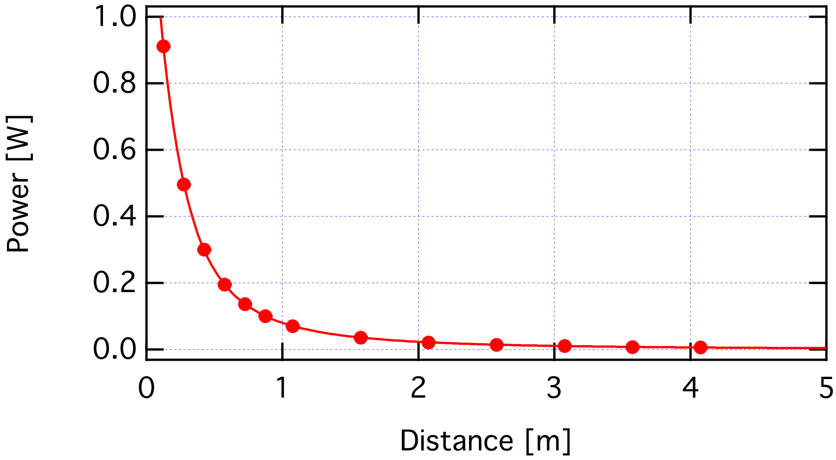

Figure 3.18: The data measures of the waist of the laser. Fitting the data we obtain the waist and its position from the head of the laser: waist $w_0 = (123 \pm 1)$ μm, located (-17±0.3) cm behind the exit window of the laser

of diameter 958 μm. The plot also shows the fit with the integrated Gaussian beam power exiting from the pin hole [see Eq. (43)].

The laser is elliptically polarised with an intensity ratio $I_s/I_p \cong 5/1$ and the main axis oriented perpendicularly to the mounting plane (s-pol). As this polarisation state represents an eigenmode of the monolithic ring laser cavity, it can be transformed without loss into any linear polarisation state using a suitable combination of a quarter-wave plate and a half-wave plate. Using the combination of such two wave plates we obtained an extinction ratio $\sigma^2_{\text{laser}} \approx \frac{1}{300}$.

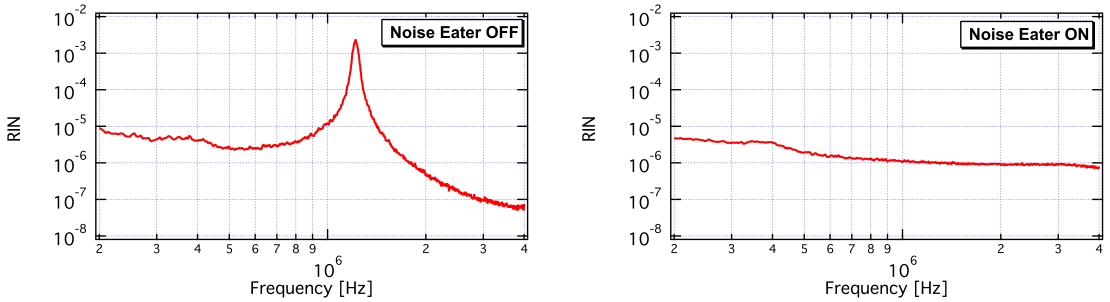

Figure 3.19: Intensity noise of the free running Mephisto 2000NE Innolight laser. The plot on the left shows the relative intensity noise as a function of the frequency with the “Noise Eater” deactivated. The plot on the right shows the same measurement with the noise eater activated.

The laser is characterised by a low amplitude relative intensity noise (RIN) -140 dB/Hz, a high-frequency stability and a wide range of frequency tuneability (over 30 GHz). The laser also has an extraordinarily narrow line-width of 1 kHz, characteristics which derive from the optical diode laser pumping and the monolithic cavity. The measured spectrum of the intensity noise of the laser is shown in Figure 3.19 in a range 0.2 MHz to 4 MHz. The spectrum shows the laser crystal resonance around 1.1 MHz. We can eliminate this disturbance by activating a feedback system provided by the manufacturer called "Noise Eater" which is integrated in the laser controller.

The frequency variation of the free running laser over a period of three hours is $\Delta\nu <$ 45 MHz. The wavelength of the Nd:YAG laser light strongly depends on the crystal temperature; as mentioned above, Nd:YAG laser crystal is therefore temperature stabilised. The typical drifts allowed by the temperature controller are only a few 100 μK/min, corresponding to a variation of the laser frequency of less than 1 MHz/min. The laser features two different systems allowing the user to control the frequency of the light. The first system (the so-called "slow" control) is a thermistor (heater) in contact with the base of the NPRO crystal (see Figure 3.17). The variation of the frequency is obtained by changing the temperature and therefore the length of the laser cavity. The laser temperature can be freely chosen (either manually, with a potentiometer, or with a voltage signal) as long as it is higher than the ambient temperature. This control system has a bandwidth of about 1 Hz over a tuning interval of about 30 GHz. The second control system ("fast control") is a piezoelectric (PZT) glued to the top surface of the monolithic laser cavity (see Figure 3.17), which exerts a mechanical pressure, thus varying the dimensions of the resonant cavity. The dynamic range of the PZT tuning system is ± 100 MHz with a 100 kHz linear response bandwidth. These controls are the basis of the feedback loop used to maintain the frequency of the emitted radiation in resonance with the Fabry-Perot cavity, described in detail in Section 3.6.2.

A key feature of the frequency locking of the laser to the cavity, is the generation of two side-bands in the emitted frequency. In the original Pound-Drever-Hall scheme, an external phase modulator is used for this task. In the PVLAS experiment, this is instead obtained by modulating at a single frequency the PZT of the "fast" frequency control of the laser outside its linearity range [48]. The choice of the optimal modulation frequency is made by studying the Residual Amplitude Modulation (RAM) induced by the modulation. We made a series of measurements modulating the laser in a range from 490 kHz to 1.1 MHz with a span of 20 kHz. We reach a minimum RAM at 502 kHz. The corresponding frequency spectrum of the parameter RAM/β (β is the amplitude of the modulation) is shown in Figure 3.20.

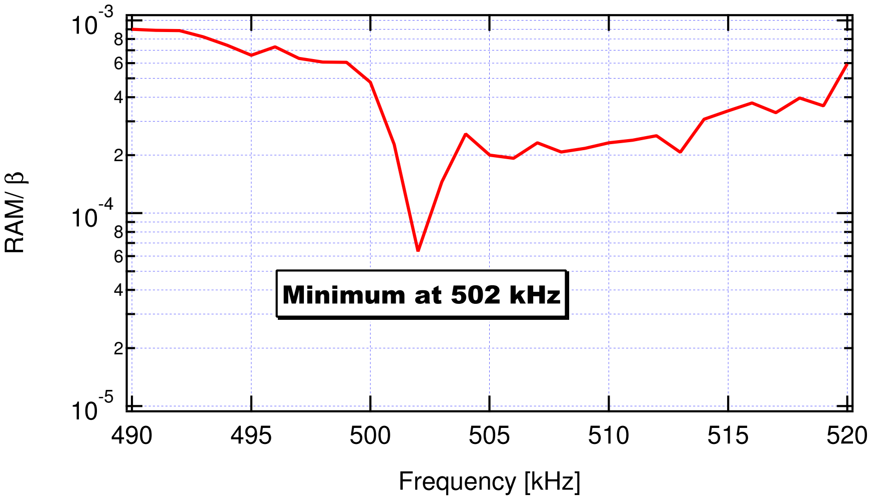

Figure 3.20: A study of the Residual Amplitude Modulation (RAM) of the Mephisto 2000NE laser as a function of frequency ν. The PZT of the "fast" frequency control of the laser is modulated with a signal $V_0 \sin(2\pi\nu t)$, where V_0 is kept constant. The quantity RAM/β is plotted against the frequency ν, where β is the amplitude of the generated side-bands.

3.6 Feedback loop

The laser is frequency tuned by a feedback circuit called "servo". A simplified diagram of the servo circuit is shown in Figure 3.21. Essentially it is a four stage integrating circuit providing, at low frequencies, the high gain G necessary for locking. For the locking to be stable, it is necessary that, at the frequency where the gain (including the frequency response of the cavity, see below) is unitary, the open loop gain slope be less than 12 dB/octave [45]. The unity gain frequency of the servo ($\approx$ 30 kHz) is much above the frequency cut-off of the cavity itself ($\frac{\nu_c}{2} \approx$ 30 Hz). To guarantee the stability of the feedback loop, the gains of all the integrators flatten out above $f_2 \approx 20$ kHz. It is the cavity itself that ensures the $1/f$ slope of the gain at the unity gain frequency.

As discussed in Section 2.3, the light reflected from the cavity is collected and demodulated at the frequency of the modulation, thus generating the error signal V_E (Eq. 2.37), which is the input of the servo (IN). The signal is first amplified by a stage of pure amplification G0. Subsequently, there are the three cascaded integrators I1, I2, and I3, that can be enabled or bypassed through the use of switches controlled manually or automatically. The signal is then sent to the inputs of two more integrators, one, IS, connected to the slow frequency control of the laser, and the second, IF, driving the fast frequency control of the laser. After the integrator IF, the RF frequency modulation signal necessary for generating the side bands of the laser frequency is added to the IF output. At this same stage, a calibration signal can be

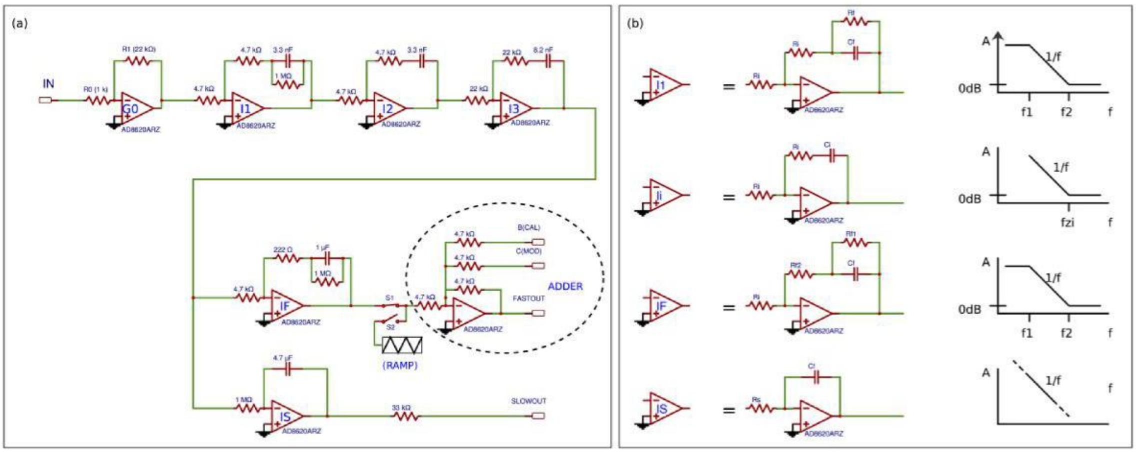

Figure 3.21: Left diagram: simplified diagram of the amplification circuit (servo). The two signals FASTOUT and SLOWOUT are directly sent to the laser. The inputs B and C are for a calibration signal and for modulating the phase of the laser, respectively. A triangular wave signal through the S2 switch generates a frequency scan of the laser light during the alignment of the cavity. Right diagram: schematic transfer functions of the integrators.

added to FASTOUT for studying the gain of the servo and for modulating the locking point to study various properties of the cavity. Before being sent to the laser, the FASTOUT signal is amplified by a factor 4, to better exploit the dynamic range of the piezo on the laser head. The SLOWOUT signal is instead attenuated by a factor 10. During cavity alignment, the switch S2 allows replacing the integrated signal of IF with a triangular wave signal scanning the laser frequency.

The frequency locking of the laser to the cavity is achieved firstly by using only the IF and I1 stages. Once a locking is obtained, the other two integrators I2 and I3 are switched on together with the slow control. With its limited frequency band of 0.01 Hz and its wide dynamic range, the slow thermal control takes on all the unbalance of the fast frequency control, which has wide frequency band but a limited dynamic range.

3.6.1 Transfer function of the feedback circuit

According to ref. [41], the piezoelectric actuator can be schematised as an RC circuit with a cut-off frequency $f_p = 100$ kHz, and a time constant $\tau_p = 1/(2\pi f_p)$. Then one can write the response of the actuator (including the ×4 amplifier) as

$$A_p(\omega) = \frac{4K_p}{1 + i\omega\tau_p} \tag{3.2}$$

with $K_p = 1$ MHz/V.

The system that uses the thermistor as an actuator has a linear response up to 1 Hz. Above 1 Hz we can assume that this actuator also behaves like an RC electronic circuit having a cutoff frequency $f_s = 1$ Hz and a time constant $\tau_s = 1/(2\pi f_s)$. We can therefore write its response function (including the ×1/10 amplifier) as

$$A_s(\omega) = \frac{K_s/10}{1+i\omega\tau_s} \tag{3.3}$$

with $K_s = 3$ GHz/V.

Two circuits act in parallel so the gain loop of the locking circuit is given by the vector sum of the open circuit functions of the Fast circuit and the Slow circuit, which we indicate with $\mathrm{G_F}$ and $\mathrm{G_S}$. Figure 3.21 is the simplified electrical diagram of the servo circuit. Referring to figure 3.21 the first amplification stage G0 has a flat transfer function

$$S_0 = \frac{\mathrm{R_1}}{\mathrm{R_0}}.$$

The first integrator stage has a transfer function given by

$$S_1(\omega) = \frac{\mathrm{R_i}}{\mathrm{R_i}} + \frac{\mathrm{R_f}}{\mathrm{R_i}}\frac{1}{(1+i\omega\mathrm{C_f R_f})}$$

where the resistance R_i indicates the input resistance and the first of the two feedback resistances. The fact that these two resistances are equal ensures that the gain at high frequency is unitary. The second feedback resistance R_f is necessary to avoid saturation during initial locking. This stage has a pole at $f_1 = \frac{1}{2\pi\mathrm{R_f C_f}} = 48$ Hz and a zero at $f_2 = \frac{1}{2\pi\mathrm{R_i C_f}} = 10$ kHz.

The next two integration stages have the following transfer functions

$$S_\mathrm{i}(\omega) = \frac{\mathrm{R_i}}{\mathrm{R_i}} + \frac{1}{i\omega\mathrm{C_i R_i}}$$

where R_i indicates both the input and feedback resistances of each integrator. Both integrators have a pole at zero frequency. The zeroes of the two stages are $f_{z2} \approx 10$ kHz and $f_{z3} \approx 882$ Hz, respectively.

Finally, the last integration stage IF has the transfer function

$$S_\mathrm{f}(\omega) = \frac{\mathrm{R_{f2}}}{\mathrm{R_i}} + \frac{\mathrm{R_{f1}}}{\mathrm{R_i}}\frac{1}{(1+i\omega\mathrm{C_f R_{f1}})}$$

where the subscripts f1,2 indicate the feedback resistances shown in Figure 3.21 (b). As for stage I1, the resistance $\mathrm{R_{f1}}$ has the function of unloading the integrated voltage at low frequencies at the input of the piezoelectric actuator, to avoid saturation and to therefore allow the search for the resonance of the cavity. The frequency of the pole of this stage is $f_1 \approx 0.16$ Hz whereas the frequency of the zero is $f_2 \approx 717$ Hz.

The transfer function for the Slow stage IS is,

$$S_\mathrm{s}(\omega) = \frac{1}{i\omega \mathrm{C_s R_s}}$$

with a pole at zero frequency.

Servo			
Integration stages	*Abbreviation*	*Elements*	*Values*
Gain	G0	$\mathrm{R_0}$ $\mathrm{R_1}$	1 kΩ 22 kΩ
First stage	I1	$\mathrm{R_i}$ R_f $\mathrm{C_1}$	4.7 kΩ 1 MΩ 3.3 nF
Second stage	I2	$\mathrm{R_2}$ $\mathrm{C_2}$	4.7 kΩ 3.3 nF
Third stage	I3	$\mathrm{R_3}$ $\mathrm{C_3}$	22 kΩ 8.2 nF
Fast stage	IF	$\mathrm{R_i}$ $\mathrm{R_{f2}}$ $\mathrm{R_{f1}}$ $\mathrm{C_f}$	4.7 kΩ 220 Ω 1 MΩ 1 μF
Slow stage	IS	$\mathrm{R_S}$ $\mathrm{C_S}$	1 MΩ 4.7 μF

Table 3.6: Values of the electric components of the Servo circuit labeled in the figure 3.21.

All the values of the circuital components are reported in the table 3.6.

The complete transfer function of the Fast channel of the circuit (without considering the laser actuator) is,

$$S_\mathrm{F}(\omega) = S_0 \cdot S_1(\omega) \cdot S_2(\omega) \cdot S_3(\omega) \cdot S_\mathrm{f}(\omega)$$

whereas for the thermistor Slow output we have:

$$S_\mathrm{S}(\omega) = S_0 \cdot S_1(\omega) \cdot S_2(\omega) \cdot S_3(\omega) \cdot S_\mathrm{s}(\omega)$$

In Figure 3.22 are shown the calculated frequency response of all the integrators and of the Fast and Slow loops with the corresponding phases. When the integrators I2 and I3 are enabled, the slope of the overall gain G increases for frequencies below the zeros of the

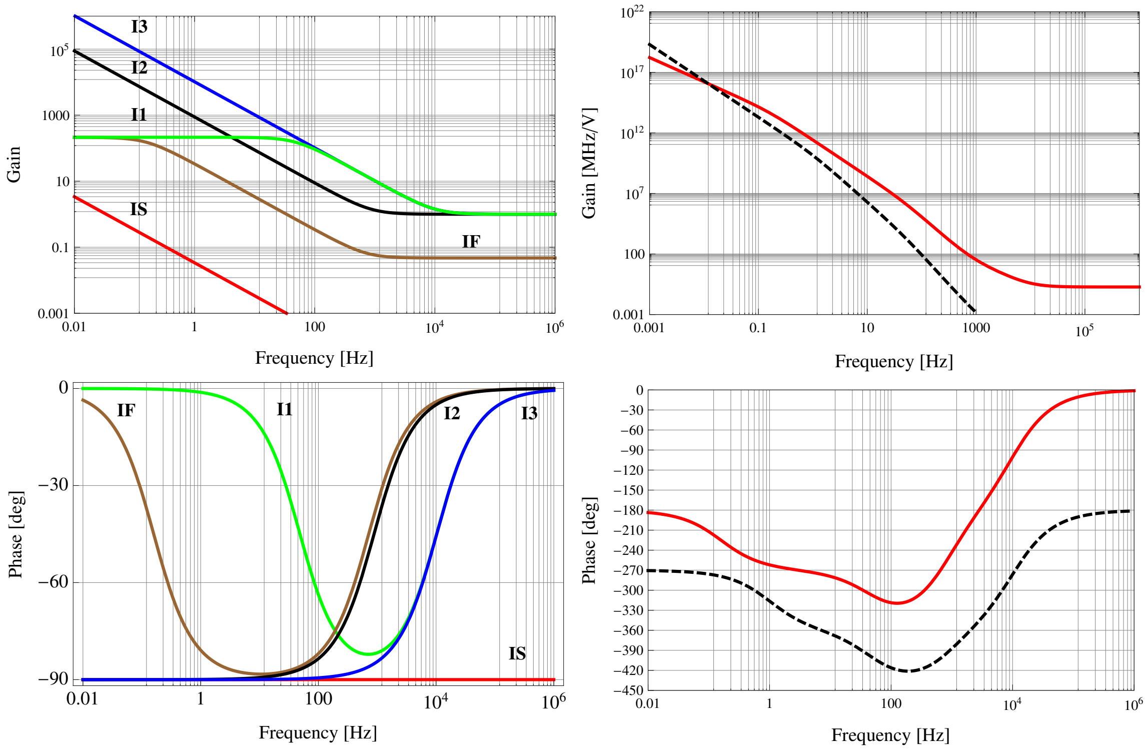

Figure 3.22: Left column: gain and phase for each integration stage as a function of frequency. Right column: gain and phase of the FAST (solid) and SLOW (dashed) branch of the servo as a function of frequency.

integrators I1 and IF. This corresponds to frequencies below ≈ 1 kHz. At low frequencies the gain G is very high to suppress the $\approx 1/f$ noise component of the laser and typical acoustic noises: in particular at 1 Hz we have $G \approx 10^{14}$.

3.6.2 Automatic laser locking

The automatic frequency locking of the laser to the cavity was designed and realised at the same time with the redesign of the electronic components of the feedback system. A picture of the compact unit is shown in Figure 3.23. The scheme is essentially the same described in figure 3.21, the main difference being that the feedback resistance of the stage G0 is programmable. The detailed scheme with the complete electronic component of the circuit is found in the appendix .1.

The new circuit has the following characteristics with respect to the previous version: OpAmps with lower noise, ultra low offset voltage and drifts, very low input voltage and current noise, very low input bias current, a signal input for the study of the Fabry-Perot

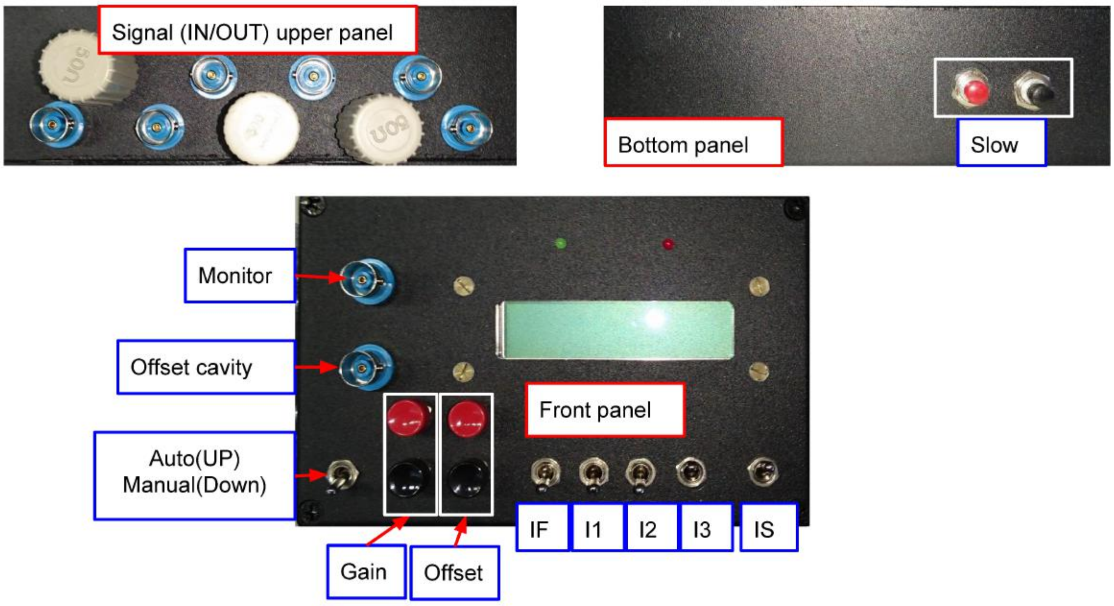

Figure 3.23: Top, bottom and front pictures of the feedback unit. On the front, two BNC connectors are found: one is the "monitor" output which is the signal error, the second is the cavity offset input used for the study of the cavity out of resonance. In the front panel it is also hosted the switch automatic/manual. In the upper panel one can see the connectors for input and output necessary for the feedback. The bottom panel has two manual buttons which change the temperature of laser crystal.

cavity through the modulation of locking point, monitor visualisation of the gain and offset values. The redesigned circuit is controlled by a microprocessor that manages the automatic locking to the cavity.

By using the automatic/manual switch, one can choose to lock the laser manually or automatically. The procedure for locking, both in the manual as well as in the automatic mode is as follows. In the automatic mode the switches of the integrators are controlled by the microprocessor. In both configurations the resonance of the cavity is searched for by scanning the frequency of the laser through the Slow control with only the integrators I1 and IF enabled. Two different gain values are preset for the G0 stage, the first, higher, is used for resonance search, and the second, lower, for laser locking. During the search for a resonance, the evidence that a rough locking has been reached is that the reflected intensity decreases. If the decrease is significant (in the automatic locking it must be at least 10%), the integrator I3 is enabled, the gain is lowered, and finally the I2 and IS integrators are enabled as well. In the automatic mode, the microprocessor continuously monitors the reflected intensity to check for unlocks, in which case the procedure starts over.

3.7 The Fabry-Perot cavity

In the PVLAS apparatus, a high-finesse Fabry-Perot cavity is employed, with length $d = 3.303 \pm 0.005$ m. The length defines the free spectral range of the interferometer

$$\nu_{\rm fsr} = \frac{c}{2d} = 45.38 \pm 0.07 \text{ MHz}. \tag{3.4}$$

The dielectric mirrors belong to a batch of seven, manufactured by ATFilms (Boulder, CO, USA), with super-polished fused silica substrates. The reflecting concave surface has been designed for the highest finesse, with a stack of 40 layers each having a thickness of $\lambda/4$; the other surface is plane and has a 1064 nm anti-reflective coating. The mirrors have 25.4 mm diameter and are 6 mm thick; the radius of curvature of the concave mirrors used in the present thesis is $R = 2$ m. In general a cavity is stable if

$$0 \leq g_1 g_2 \leq 1 \tag{3.5}$$

where $g_{1,2} = 1 - \frac{d}{R_{1,2}}$. The PVLAS cavity has $R_1 = R_2 = R$. For this value, the cavity is stable because $d/R = 1.65$ and, therefore

$$g_1 g_2 = g^2 = \left(1 - \frac{d}{R}\right)^2 = 0.42. \tag{3.6}$$

The minimum w_0 waist is in the centre of the cavity with value

$$w_0 = \sqrt{\frac{\lambda d}{2\pi}\sqrt{\frac{1+g}{1-g}}} = 0.507 \text{ mm} \tag{3.7}$$

with a Rayleigh range z_0 given by

$$z_0 = \frac{\pi w_0^2}{\lambda} = 0.759 \text{ m}. \tag{3.8}$$

The waist w on the mirrors is

$$w = \sqrt{\frac{\lambda d}{\pi}\sqrt{\frac{1}{1-g^2}}} = 1.21 \text{ mm}. \tag{3.9}$$

The separation of the transverse modes for our symmetric cavity is given by

$$\Delta\nu = \frac{\nu_{\mathrm{fsr}}}{\pi} \arccos\sqrt{g^2} = 12.44 \text{ MHz} \tag{3.10}$$

which guarantees a good separation of the lowest index transverse modes.

To mode-match the cavity to the laser beam, a single lens is employed. The distance between the minimum waists of the laser and of the Fabry-Perot cavity is $D = 4.7$ m. The focal length f of the matching lens and its position x with respect to the laser are given by the equations of Chap. 2:

$$\frac{x-f}{D-x-f} = \frac{w_0^2}{w_{\mathrm{las}}^2} \qquad (x-f)(D-x-f) = \frac{\pi w_0 w_{\mathrm{las}}}{\lambda} \tag{3.11}$$

that give $x = 0.94$ m and $f = 0.76$ m. A standard $f = 75$ cm lens is placed on a xyz lens holder allowing a fine position adjustment.

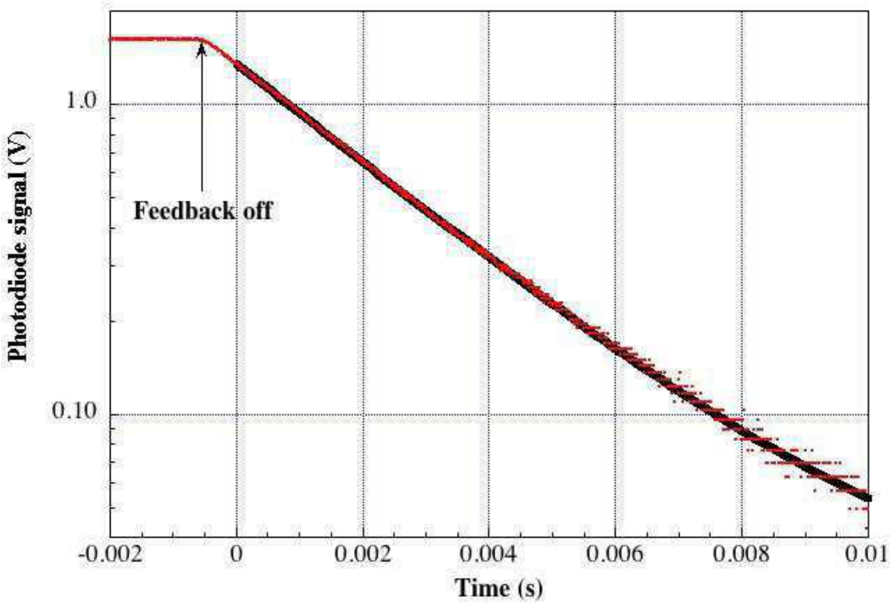

Figure 3.24: Decay of the light transmitted by the FP cavity following an abrupt unlocking of laser and the cavity. The data are fitted with an exponential function $a + be^{-t/\tau}$, giving a decay time $\tau = 2.70 \pm 0.02$ ms. The offset parameter a is compatible with zero. The response time of the electronics is less than 4 μs.

The finesse of the cavity is determined by measuring the decay time τ of the intensity exiting the cavity after switching off of the locking circuit:

$$\tau = \frac{\mathcal{F} d}{\pi c} \tag{3.12}$$

The finesse of the cavity dramatically depends on the state of cleanliness of the surface of the two mirrors. The mirrors employed have been installed in the vacuum chambers straight from the manufacturer's box without any selection or cleaning. Thanks to the valves that isolate the mirrors' vacuum chambers, we could verify that the mirror surface did not change in vacuum or low pressure pure gases on the time scale of years. Nevertheless, as the surface of the mirror can be inspected through a window by the aid of an infrared viewer while the cavity is in resonance, on each mirror we observe a few bright spots due to dust particles or surface imperfections which act as diffusing and absorbing centers. The finesse of the cavity is maximised when, by adjusting the cavity mirrors and the alignment mirrors, one obtains the condition where most of the bright spots are confined to the periphery of the beam spot.

The longest decay time ever found has been $\tau = 2.70 \pm 0.02$ ms, corresponding to a finesse $\mathcal{F} = 770,000 \pm 6,000$ as can be seen in Figure 3.24. This corresponds to a line width at FWHM

$$\nu_c = \frac{1}{2\pi\tau} = 58.9 \pm 0.4 \text{ Hz}. \tag{3.13}$$

The value of the finesse in most of the measurements presented in this thesis work is however about 10% lower, namely $\mathcal{F} = 700,000$, corresponding to $\nu_c = 65$ Hz. With this value the enhancement factor is

$$N = \frac{2\mathcal{F}}{\pi} = 446,000. \tag{3.14}$$

From the value of the finesse, a value of the reflectance of the mirrors can be determined assuming them to be identical. Considering that $R+T+A=1$ where R, T and A are respectively the reflectance, transmittance and losses of each of the two mirrors:

$$\frac{\pi}{\mathcal{F}} = 1 - R = A + T \approx 4.1 \text{ ppm} \tag{3.15}$$

To completely characterise the mirrors with the values of A and T, a few more measurements are needed. The manufacturer provides a value for the transmittance $T = 2.9 \pm 0.2$ ppm, and an estimate that the losses in the reflecting layers are as low as $A = 1$ ppm. The values of A and T determine the transmittance H_{T} and the reflectance H_{R} of the resonating Fabry-Perot as a whole. According to the formulas of Chap. 2,

$$H_{\mathrm{T}} \equiv \frac{I_{\mathrm{T}}}{I_{\mathrm{in}} - I_{\mathrm{nc}}} = \left(\frac{T}{A+T}\right)^2 \qquad H_{\mathrm{R}} \equiv \frac{I_{\mathrm{R}} - I_{\mathrm{nc}}}{I_{\mathrm{in}} - I_{\mathrm{nc}}} = \left(\frac{A}{A+T}\right)^2 . \tag{3.16}$$

where I_{nc} is the intensity reflected by the cavity that does not couple to the Fabry-Perot due to a not perfect spatial match.With the laser locked to the cavity we have measured the two quantities:

$$\frac{I_{\mathrm{T}}}{I_{\mathrm{in}}} = 0.31 \pm 0.02 \qquad \text{and} \qquad \frac{\mathrm{I_R}}{\mathrm{I_{in}}} = 0.25 \pm 0.02 \tag{3.17}$$

With these values, equations (3.15) and (3.16) give

$$T = (2.4 \pm 0.2)\ \text{ppm}; \qquad A = (1.7 \pm 0.2)\ \text{ppm}; \qquad I_{\mathrm{nc}}/I_{\mathrm{in}} = 0.09 \pm 0.04 \tag{3.18}$$

We interpret the parameter T as an intrinsic property of the mirrors, and we therefore attribute the current slightly lower finesse to an increased loss coefficient: $A_{\mathrm{actual}} = 2.1$ ppm.

The values above have been obtained with an input power of $I_{\mathrm{in}} = 0.55$ W. In fact, when working at maximum power, the output intensity from the cavity is slightly less stable, with a higher uncoupled intensity. We interpret this as caused by mirror lensing due to the large power density on the mirrors. In fact, with a maximum input power of 1.2 W, the power circulating in the cavity is about 130 kW, corresponding to a power density on the mirrors of about 3 MW/cm^2. For an absorption ~ 1 ppm this gives an absorbed power of ~ 3 W/cm^2. This absorbed power density evidently is high enough to locally deform the surface of the mirrors with consequent thermal lensing thereby reducing the mode matching. Note that the power density on the mirrors is well below the damage threshold of the mirrors as declared by the manufacturer.

The characteristic of the Fabry-Perot cavity and of the mirrors are summarised in table 3.7.

3.8 Optical layout

As mentioned before, the optical bench supports the vacuum chambers, all the optical elements, the instruments of beam manipulation and signal detection. A scheme of the optical elements is shown in Figure 3.25.

Three optical components, placed near the laser head, are used to condition the beam polarisation, adjust the power, and isolate the laser from the optical system. The polarisation of the light generated by the laser has small ellipticity with an extinction ratio of 5/1. A

Fabry-Perot cavity (λ = 1064 nm)	
Length	$d = (3303 \pm 5)$ mm
Free spectral range	$\nu_{\rm fsr} = (45.38 \pm 0.07)$ MHz
Curvature radius of the mirrors	$R = 2$ m
Transverse mode separation	$\Delta\nu = 12.4$ MHz
Minimun cavity waist	$w_0 = 0.507$ mm
Waist on mirrors	$w = 1.21$ mm
Rayleigh range	$z_0 = 0.759$ m
Best measured finesse	$\mathscr{F} = (7.7 \pm 0.06) \times 10^5$
Typical operating finesse	$\mathscr{F} \approx 7 \times 10^5$
Dielectric plano-concave mirrors	
Mirrors diameter	25.4 mm
Thickness	6 mm
Number of dielectric layers	40
Best mirrors reflectance	$R = 99.99959\%$
Typical mirrors reflectance	$R = 99.99955\%$
Mirrors transmittance	$T = (2.4 \pm 0.2)$ ppm
Minimum mirrors losses	$A = (1.7 \pm 0.2)$ ppm
Typical mirrors losses	$A \approx 2.1$ ppm

Table 3.7: Fabry-Perot specification.

quarter-wave plate (QWP) properly oriented compensates the ellipticity of the laser light. The optical isolator consists of two polarisers with a Faraday cell between them. The light passes through the first polariser and is rotated by 45° in the Faraday cell. The second polariser is oriented at 45° with respect to the first. Light reflected back by the following optical elements is further rotated by 45° by the Faraday cell and is extinguished by the first polariser. In the PVLAS setup, we have installed a dual stage Faraday isolator ($\approx$ 60 dB). The polarisation of the beam exiting the last polariser is vertical to impinge on the steering mirrors as a s-wave. A half-wave plate (HWP), placed before the isolator, adjusts the beam power by rotating the polarisation with respect to the input polariser of the isolator.

A plano-convex lens after the optical isolator focuses the light at the center of the Fabry-Perot cavity. The lens has an N-BK7 substrate and a broadband anti-reflection coating for the 1050 – 1700 nm range with a focal length $f = 750$ mm.

After the lens, the light is steered by two deflection mirrors allowing the alignment of the laser light to the Fabry-Perot cavity. The light passes then through a 10/90 beam splitter. The 10% beam is used for the measurement of the input beam intensity. The 90% beam passes through a second HWP which aligns the polarisation with the input polariser.

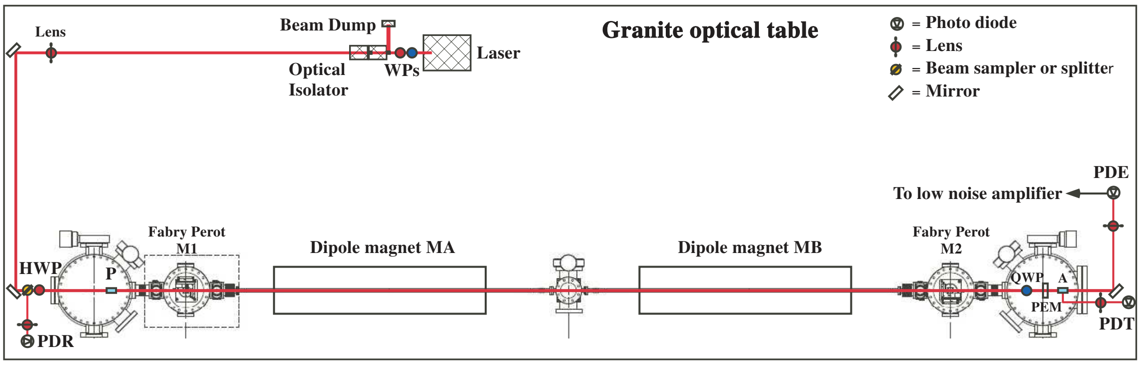

Figure 3.25: Top view scheme of the optical bench with the PVLAS apparatus. The scheme shows the optical components, the five vacuum chambers, and the two magnets. HWP= Half-wave plate; P = Polariser; A = Analyser; QWP = Quarter-wave plate; TR = transmission; EXT = extinction.

The light enters into the vacuum enclosure via an anti-reflecting window and passes then through a Glan-Thompson polariser. The polariser has a high extinction ratio $10^8 : 1$ and operates in the broadband range 350 nm – 2.3 μm. The two halves of the prism of the polariser are joined with optical cement (Canada balsam). This polariser has replaced a proper air-spaced vacuum-compatible polariser, whose many reflecting surfaces seemed to contribute to the wide-band noise.

After crossing the polariser, the light enters into the Fabry-Perot cavity. The light reflected by the cavity impinges back on the beam splitter. The diode PDR detects the 10% fraction of the light reflected by the beam splitter; its signal is used for the Pound-Drever-Hall locking.

After exiting the FP cavity, the light is modulated in ellipticity by the resonant photo-elastic modulator (PEM) which introduces a known variable ellipticity $\eta(t)$ at a frequency of about 50 kHz.

The light emerging from the PEM goes through the analyser oriented for maximum extinction. The ordinary ray exits the analyser through a side port. It is collected outside the vacuum enclosure by the transmission photodiode PDT. The extraordinary beam also emerges from the vacuum system and is detected by the photodiode in extinction PDE which is connected to a low noise amplifier typically set to a gain of 10^6 V/A with a band width of 200 kHz. The signal from the low noise amplifier contains the signal linearised in ψ: $I_e(t) \propto \eta(t)\psi(t)$. A line filter is placed before of extinction photodiode centred at $\lambda = 1064$ nm with a 10 nm FWHM; its transmittance is $F = 0.83$.

The attenuation coefficients k_x of all the optical elements shown in Fig. 3.26 have been measured. The values are reported in Tab 3.8.

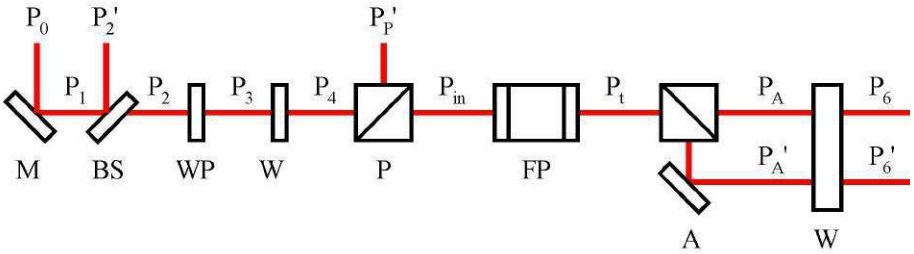

Figure 3.26: Scheme for the measurement of the attenuations of the optical components. M: steering mirror; BS: 10-90 beam splitter; WP: wave plate; W: vacuum window; P: polariser; FP: Fabry-Perot cavity; A: analyser.

$k_{\mathrm{M}} = \frac{\mathrm{P}_1}{\mathrm{P}_0}$	$k_{\mathrm{BS}} = \frac{\mathrm{P}_2}{\mathrm{P}_1}$	$k_{\mathrm{WP}} = \frac{\mathrm{P}_3}{\mathrm{P}_2}$	$k_{\mathrm{W}} = \frac{\mathrm{P}_4}{\mathrm{P}_3}$	$k_{\mathrm{P}} = \max\left[\frac{\mathrm{P}_{\mathrm{in}}}{\mathrm{P}_4}\right]$	$k_{\mathrm{FP}} = \frac{\mathrm{P}_{\mathrm{t}}}{\mathrm{P}_{\mathrm{in}}}$	$k_{\mathrm{A}} = \max\left[\frac{\mathrm{P}_{\mathrm{A}}}{\mathrm{P}_{\mathrm{t}}}\right]$
1.00	0.90	0.99	0.98	0.90	0.31	0.90

Table 3.8: Measured attenuation coefficients of the optical elements of figure 3.26.

3.9 Instrumentation and electronics

The experimental apparatus described above is inside the clean room, whereas most of the electronic equipment is installed outside the clean room to reduce mechanical and acoustic noise and the presence of operators inside the clean room during data taking. In the following we summarise the main characteristics of the instrumentation employed by the PVLAS experiment.

3.9.1 Logistics and instrumentation inside the clean room

The specifications of the electronic components and photodetectors are summarised in Table 3.9 and a scheme of their connections coming in and out the clean room are shown in Fig. 3.27.

The reflected, transmitted and extinguished intensities I_1, I_2 and I_{R} are detected by three fast photodiodes. The laser intensity I_{in} and again the transmitted one I_{R} are measured by two power meters. A three axis accelerometers is attached to each tube to measure the components $\mathrm{A}_{i\alpha,\beta}$ of their accelerations. The distance sensors $\mathrm{D}_{i\alpha,\beta}$ monitor the relative position of the optical bench with respect to the structures supporting the magnets in two points roughly coinciding with the outer (namely, near the mirrors) ends of the two tubes. By monitoring the tube acceleration we can position the tubes ends in such a way that the average force of the magnetic field at $2\nu_B$ is a minimum. This is done using four piezoelectric motors which position each tube with a precision of 30 nm. Two magnetometers B_α and B_β

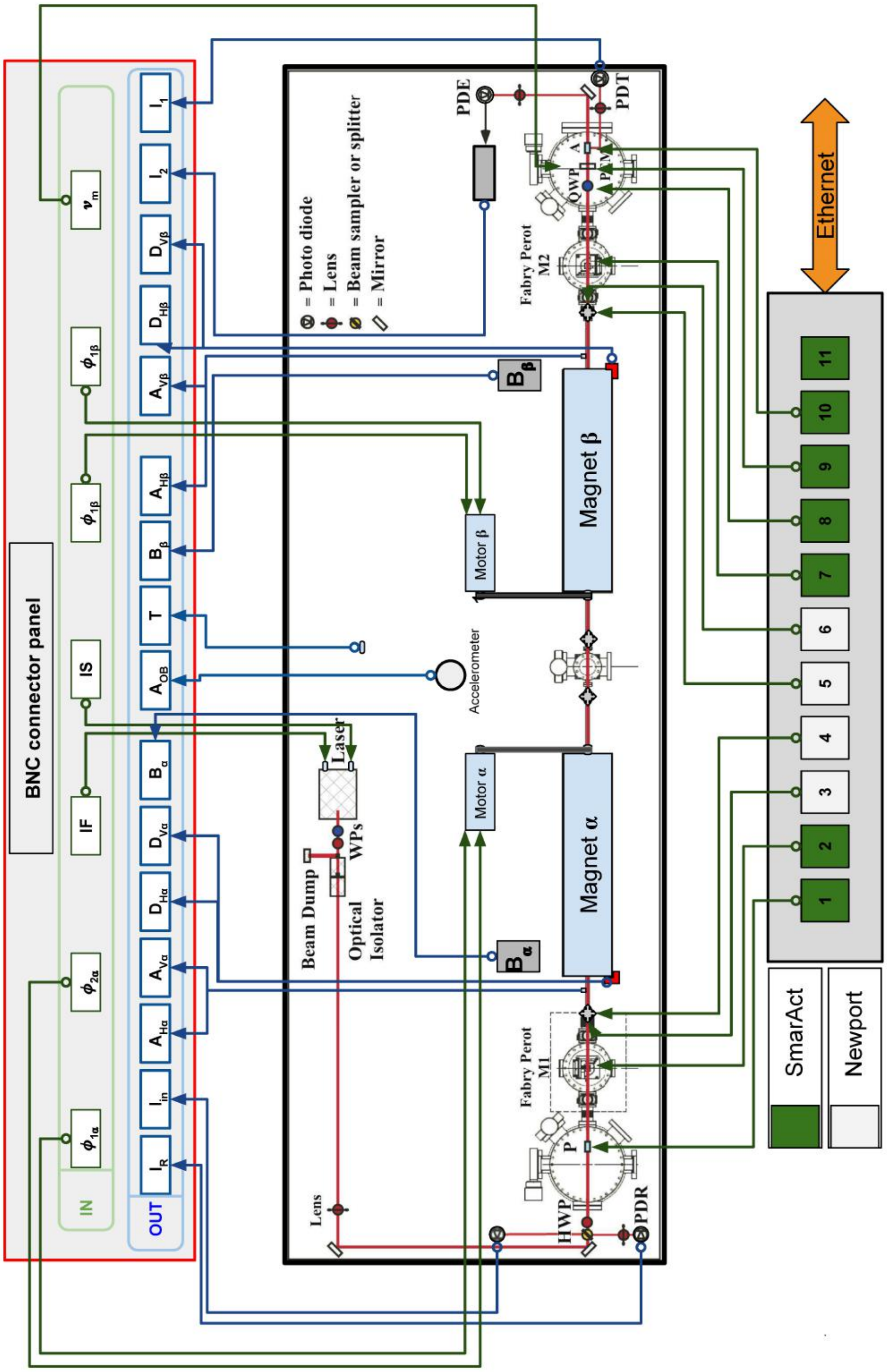

Figure 3.27: Scheme of the connections from/to instrumentation on the optical bench. The BNC panel collects the analog signals to be transferred outside the clean room over 15 m long BNC cables. The panel Smaract/Newport describes schematically the signals from/to the micropositioning devices.

Instrument	*Type*	*Characteristics*
Power meter, laser side	Thorlabs S145C	integrating sphere InGaAs photodiode, 3 W
Power meter, output side	Thorlabs S121C	Si photodiode, diam. 9.5 mm, 0.5 W
Reflection photodiode	Hamamatsu, G8376-05	1 mm^2, efficiency $q = 0.7$ A/W
Reflection current amplifier	Femto DHPCA-100	DC to 200 MHz, $(10^2 - 10^8)$ V/A
Transmission photodiode	Thorlabs PDA400	$\oslash$ 1 mm amplified InGaAs, 10 MHz BW
Extinction photodiode	Hamamatsu G8376-05	1 mm^2, efficiency $q = 0.7$ A/W
Extinction current amplifier	Femto DHPCA-200	DC to 500 kHz, $(10^3 - 10^{11})$ V/A
Stray field magnetometers	Stefan Mayer Fluxmaster	0.1 nT $-$ 200 μT, DC to 1 kHz
One-axis accelerometer	Wilcoxon 731A/P31	1000 V/g, $(0.05-450)$ Hz, 0.03 $\mu g/\sqrt{\text{Hz}}$
Triaxial accelerometers	PCB 356A17	500 mV/g, $(0.5-3000)$ Hz, 60 $\mu g/\sqrt{\text{Hz}}$
Piezoelectric step motors	Newport PZA12	50 N, resolution 30 nm
Distance sensors	Panasonic HG-C1030	repeatability 10 μm
Contrast sensor	Baumer CH-8501	response time < 50 μs
Temperature sensor	Texas Instruments LM35	$(-55 - +150)$°C, 10 mV/°C

Table 3.9: Characteristics of the instruments inside the clean room.

are used to track the phase of the rotating magnetic fields. We also use a contrast sensor to generate a trigger signal in correspondence of a mark drawn on the external surface of the rotating magnets in correspondence of the direction of the inner magnetic field. This signal is an absolute zero for the magnetometers signals.

Inside the vacuum chamber the rotators and the translators of the optical components are installed. These are all compatible with high vacuum and non magnetic. They include: the angular rotators of the polariser and the analyser; two three-degrees of freedom positioning mounts for the mirrors; a rotator for the wave plates and a translator for insertion/extraction in/from the light path; a translator and a rotator for the photo-elastic modulator PEM. All the signals from the instruments are sent outside the clean room, as shown in Fig. 3.27.

A service structure, shown in Fig. 3.28, is used for the support of instrumentation (electronics, primary pumps, etc.) above the optical bench.

3.9.2 Logistic and instrumentation outside the clean room

Most of the instrumentation of the experiment is hosted in a control area outside the clean room; a list is given in Tab. 3.10. Three uninterruptible power supplies (UPS) feed all the electrical equipment inside and outside the clean room. A first UPS feeds the motors, the pumps and the vacuum equipment; a second UPS provides the power for all the rest of the electronics, including the data acquisition; the third UPS is dedicated to the positioning system of the optical bench. In figure 3.29 the connections of the instruments in the control area are presented starting from the BNC connector panel. Most of the signals are filtered (Kemo CardMaster 255G) except the reflected signal. Then they are directly connected

Figure 3.28: A picture showing the service structure for the optical bench.

to the acquisition board NI-USB 6259 from which the signals are sampled and stored on the hard drive of the PC-DAQ. A TTL signal from a two-channels signal generator Agilent 33500B defines the sampling acquisition frequency ν_S. The second channel of the same signal generator gives a second TTL start trigger at a frequency ν_T submultiple of ν_S such that its rising edge is synchronised with fixed angular positions of both magnets and with a rising edge of the other channel. Two signal generators Agilent 33120A generate two TTL signals at ten times the frequencies $\nu_{B\alpha}$ and $\nu_{B\beta}$ of the rotation of the magnets α and β. As explained above, the factor ten comes from the structure of the coils of the motors driving the magnets. The two signal generators are synchronised with the acquisition and between them by means of a 10 MHz signal. Each TTL signal is sent to a three phase generator (TPG) designed and realised in house which generates three sine waves at the same frequency and at 120° from each other. Two of the three outputs from each TPG are sent to a Techron LCV 2016 dual channel current linear amplifier. Each pair of output signals from the two current amplifiers, $\{\phi_{1i}, \phi_{2i}\}$, is directly sent to two phases of one of the motor.

The reflected signal I_R is sent directly to two different filtering channels of a Krohn-Hite 3364. In the first channel, the signal is band-pass filtered between 100 kHz and 2 MHz and then sent to a MiniCircuits ZP-10514 mixer for demodulation. In the second filtering channel the reflected signal is filtered at 10 kHz and amplified by a factor three and then sent to the Servo to provide a value for the laser reflected intensity. A second two-channels signal generator Agilent 33500B generates the sine signal at $\nu_\mathrm{PDH} = 503$ kHz that is sent to the Servo unit to modulate the laser head and generate sidebands of the laser line. The signal

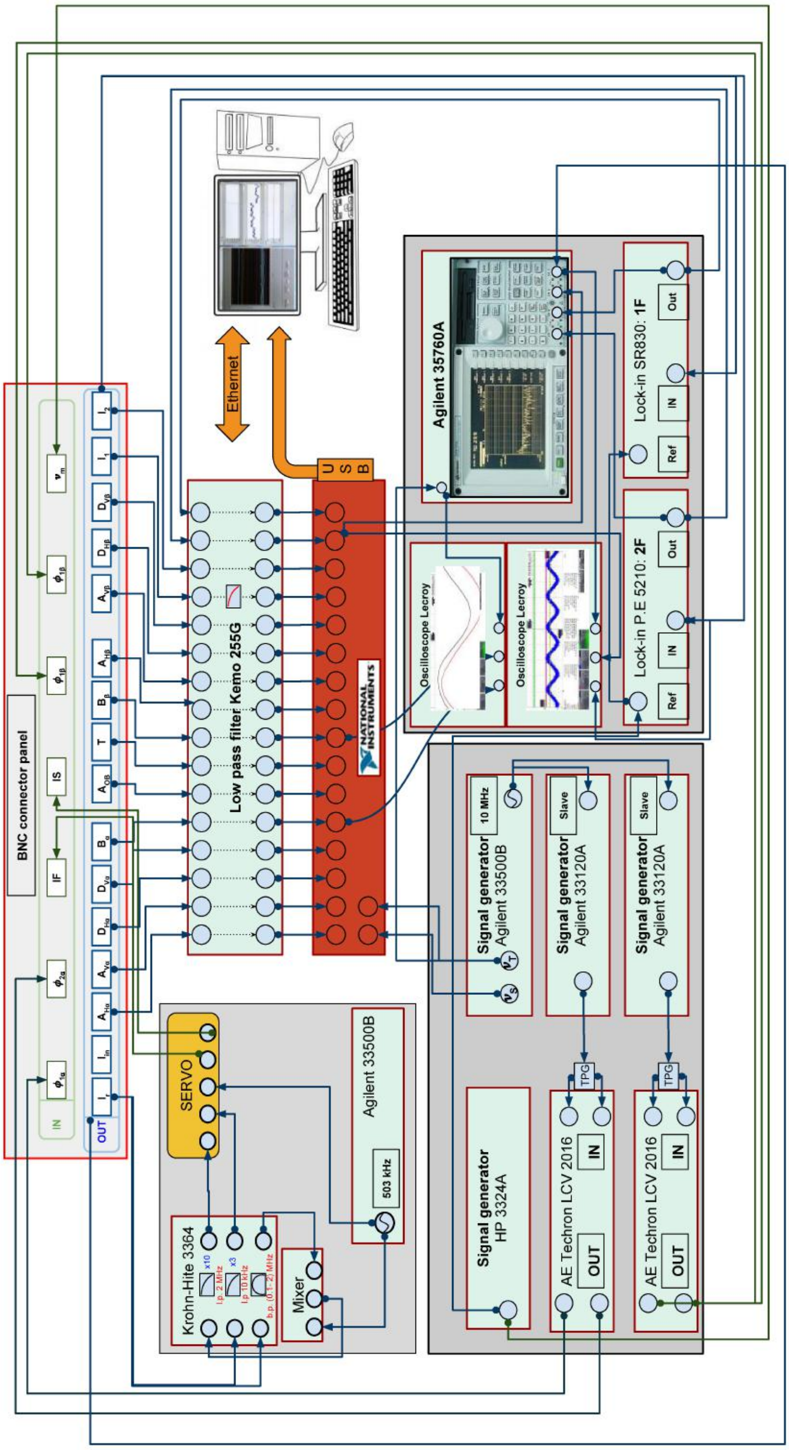

Figure 3.29: Scheme of the connection of the electronic signals in the control area. The output signals from the clean room are drawn in dark green, those entering the clean room in dark blue.

Instrument	*Type*	*Characteristics*
2 Signal generators	Agilent 33500B	2 chs, resolution 1 μHz, range 30 MHz, 1 mV$_{\mathrm{pp}}$
2 Signal generators	Agilent 33120A	10 μHz resolution, range 15 MHz, 50 mV$_{\mathrm{pp}}$
Signal generator	HP 3325A	1 μHz resolution, range 30 MHz, 1 mV$_{\mathrm{pp}}$
2 Current amplifiers	AE Techron LCV2016	2 chs, range DC to 20 kHz
Lock-in amplifier	PerkinElmer 5210	ranges: 0.5 Hz to 120 kHz, 1 nV to 1 V, time constant 1 ms to 300 ks
Lock-in amplifier	SRS SR830	ranges: 1 mHz to 104.2 kHz, 2 nV to 1 V, time constant 10 μs to 30 ks
Programmable filter	Krohn-Hite 3364	4 chs, 4 poles, range 0.1 Hz to 200 kHz
Low-pass filter	Kemo Mastercard 21.255G	16 chs, 8 poles, range 0.1 Hz to 127 kHz
Acquisition board	NI USB-6259 BNC	16 bits, 16 differential chs, sampling rate 1 MHz
Signal analyser	Agilent 35670A	4 chs, DC to 102.4, resolution 61 μHz
Signal analyser	HP 35665A	2 chs, DC to 102.4, resolution 122 μHz

Table 3.10: Specifications of the electronic instrumentation outside the clean room.

from the second channel, at the same frequency and with the proper phase, is sent to the mixer for the demodulation of the sidebands present in the reflected intensity. The output of the mixer is low-pass filtered at 2 MHz and amplified by a factor ten; it enters then the Servo unit as an error signal for the locking of laser and cavity.

A sine signal at $\nu_{\mathrm{m}} \approx 50$ kHz, generated from an HP3324A signal generator, is sent to the ellipticity modulator and to the reference inputs of two lock-in amplifiers (PerkinElmer 5210 and SRS SR830). The first one demodulates the extinguished signal I_2 at $2\nu_{\mathrm{m}}$; from the amplitude of the lock-in output we obtain the modulation amplitude η_0 of the ellipticity modulator; the phase of the Fourier component of I_2 at frequency $2\nu_{\mathrm{m}}$ represents a monitor of the resonance inside the crystal of the ellipticity modulator. The SR830 demodulates the extinguished signal I_2 at ν_{m}. We are interested in the components at $2\nu_{Bi}$ of the FFT of the demodulated signal, which are related to the phase and the amplitude of the induced ellipticity.

The computer managing the acquisition is also connected via ethernet to a hub communicating with all the rotators and translators of the optical elements under vacuum and to the four piezoelectric step motors defining the position of the outer tube ends. The user interface are LabVIEW programs. The transverse acceleration of the two tubes, $\{\mathrm{A}_{\mathrm{H}\alpha}, \mathrm{A}_{\mathrm{V}\alpha}, \mathrm{A}_{\mathrm{H}\beta}, \mathrm{A}_{\mathrm{V}\beta}\}$ are acquired and then analysed for correlations between the acceleration and the spurious ellipticity signals. The relative distances $\{\mathrm{D}_{\mathrm{H}\alpha}, \mathrm{D}_{\mathrm{V}\alpha}, \mathrm{D}_{\mathrm{H}\beta}, \mathrm{D}_{\mathrm{V}\beta}\}$ between the magnet and the optical bench are monitored by four laser distance sensors.

An oscilloscope is dedicated to the trigger signals of the acquisition system. A second oscilloscope displays online the signals of the transmitted intensity I_1, of the reflected intensity I_{R}, of the Fast signal IF and of the extinguished intensity I_2.

In parallel with the acquisition board, a four-channels spectrum analyser Agilent 35760A acquires the demodulated extinguished signal and calculates the ellipticity. To provide the correct phases, it uses the same start trigger at frequency ν_T as the acquisition board. The channels used to calculate the ellipticity are I_1 and the demodulated signal demodulated signal at $2\nu_{\rm m}$, which gives the modulation amplitude η_0 of the PEM ellipticity modulator. The reflected signal is used as a trigger when the laser gets unlocked from the cavity.

3.10 Data acquisition and data analysis

All the signals coming from the clean room are acquired by two different instruments: the first instrument is a spectrum analyser Agilent 35670A which provides a fast analysis in real time. The second instrument is a NI USB-6259 acquisition board that samples and stores the data on the hard drive of the PC-DAQ.

Channel	*Signal*
1	Extinguished intensity I_2, demodulated at $\nu_{\rm m}$
2	Extinguished intensity I_2, demodulated at $2\nu_{\rm m}$
3	Transmitted intensity $I_{\rm t}$
4	Reflected intensity $I_{\rm R}$

Table 3.11: Voltage signals acquired by the spectrum analyser Agilent 35670A. The analyser inputs are floating and DC coupled.

The spectrum analyser Agilent 35670A performs a simplified analysis based on the signals listed in Table 3.11. The first three channels are the signals necessary to calculate the values of ellipticity and rotation. We use the fourth channel as an enable signal to pause the analyser when the laser unlocks.

The second instrument is a digital data acquisition board from National Instruments which records the sampled data on the hard drive of the PC-DAQ for a detailed analysis. A list of the channels acquired is in Table 3.12.

3.10.1 Data acquisition

The two magnets rotate at frequencies ν_α and ν_β. Normally $\nu_\alpha \neq \nu_\beta$, so that the measurements taken with one magnet are a counter check for the results of the other. The two frequencies are chosen so to have no common low-order harmonics. The acquisition is started by a trigger of frequency ν_T equal to a common submultiple of ν_α and ν_β. In practice,

Channel	*Signal*
1	Extinguished intensity I_2, demodulated at ν_{m}
2	Extinguished intensity I_2, demodulated at $2\nu_{\mathrm{m}}$
3	Transmitted intensity I_1
4	Extinguished intensity I_2
5	Magnetometer B_α
6	Magnetometer B_β
7	“Slow” feedback signal IS
8	Temperature of the clean room
9	Horizontal relative distance $\mathrm{D}_{\mathrm{H}\alpha}$ of tube and magnet α
10	Vertical relative distance $\mathrm{D}_{\mathrm{V}\alpha}$ of tube and magnet α
11	Horizontal relative distance $\mathrm{D}_{\mathrm{H}\beta}$ of tube and magnet β
12	Vertical relative distance $\mathrm{D}_{\mathrm{V}\beta}$ of tube and magnet β
13	Horizontal tube acceleration $\mathrm{A}_{\mathrm{H}\alpha}$
14	Vertical tube acceleration $\mathrm{A}_{\mathrm{V}\alpha}$
15	Horizontal tube acceleration tube $\mathrm{A}_{\mathrm{H}\beta}$
16	Vertical tube acceleration $\mathrm{A}_{\mathrm{V}\beta}$

Table 3.12: Voltage signals acquired through the NI USB-6259 acquisition board, whose inputs are configured DC. The board has two more input for the sampling trigger with frequency ν_S and for the start trigger, with frequency ν_T.

$\nu_T = |\nu_\alpha - \nu_\beta|$. When the acquisition starts, the magnetic fields inside the two magnets have the same direction.

The sampling is different for the spectrum analyser and the acquisition board. In the spectrum analyser, the sampling depends on the frequency span and number of bins. To take full advantage of the measurement time of the spectrum analyser by using a uniform window, the frequencies of the two magnets are limited to the central frequency values of the bins. For example: with a frequency span of 50 Hz and 800 frequency bins in the spectrum, the frequency resolution is $50/800$ Hz $= 62.5$ mHz: the allowed rotation frequencies of the magnets are the multiples of 62.5 mHz.

Coming to the acquisition board, the numbers of samples per magnet turn, N_α and N_β, are both integers; the smaller one is usually equal to sixteen. The values of N_α and N_β are related to the rate of sampling ν_S as

$$N_\alpha \nu_\alpha = N_\beta \nu_\beta = \nu_S.$$

A practical example: if $\nu_\alpha = 8.5$ Hz and the sampling rate is $\nu_S = 8.5 \times 16 = 136$ Hz, the magnet β can have either $N_\beta = 17$ and $\nu_\beta = 8$ Hz, or $N_\beta = 20$ and $\nu_\beta = 6.8$ Hz. In the first case $\nu_T = 0.5$ Hz, in the second $\nu_T = 1.7$ Hz.

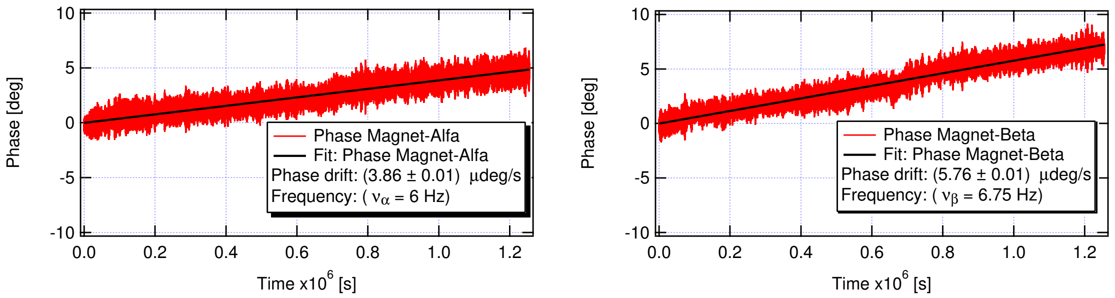

Figure 3.30: Phase drift of the magnetic field of the two magnets as a function of time. Left panel: magnet α rotates at 6 Hz with a drift of (3.86 ± 0.01) μdegrees/second. Right panel: magnet β rotates at 6.75 Hz with a drift of (5.76 ± 0.01) μdegrees/second.

As said before, all the generators are synchronised by a common 10 MHz master clock. We have verified that the phase relations between all the generators and the rotation of the magnet are maintained during each run. For very long runs, a small drift is observed, compatible with the frequency resolution of the generators. In Fig. 3.30 an example of such a drift is given. In any case every few days we adjust this phase drift.

3.10.2 Control program and feedbacks utilised during the acquisition

A series of LabVIEW control programs necessary for feedbacks and for acquiring and saving the data on a hard drive has been realised on our PC-DAQ. The acquisition is divided in subfiles of given length. The data are continuously acquired in segments of size equal to a common multiple of N_α and N_β; a user defined number of segments compose a subfile. The start trigger guarantees that all the segments start with the same phase of the magnetic fields. A filled subfile is ready for analysis while the acquisition program opens a new subfile. A practical example: with $\nu_\alpha = 8$ Hz, $\nu_\beta = 8.5$ Hz and a sampling frequency of $\nu_S = 136$, a segment can be made of 1360 samples, a subfile of 2048 segments.

Another LabVIEW program communicates with the signal generators feeding the Three Phase Generators which drive the magnets. The frequency of the generators is linearly increased, normally at 10 mHz/s, to reach the planned rotation frequency. The phase of the magnetic fields is then manually aligned to a rising edge of the start trigger.

Feedback programs

We have implemented two low-frequency control feedbacks: one for keeping the PEM at maximum resonance and the other to compensate for the slow drifting static birefringence of the polarimeter.

The first program keeps stable the phase of the extinguished intensity I_2 demodulated at the frequency $2\nu_{\mathrm{m}}$ by adjusting the frequency ν_{m}. The sign of the phase change gives the sign of the required frequency change. Typically, the program checks the phase every three seconds; a typical step for frequency change is 1 mHz.

The second program minimises the amplitude of the extinguished intensity I_2 demodulated at the frequency ν_{m}, due to a static birefringence of the polarimeter, by acting on the angular position of the polariser. The sign of the required rotation is given by the phase (positive or negative) of the demodulated signal. A typical value of static ellipticity requiring correction is $\sim 10^{-4}$; the program typically moves the polariser in steps of the order of a millidegree. The analyser is then rotated to maintain maximum extinction. One must note, however, that this procedure minimises the total static ellipticity acquired by the light beam between the two polarisers. This includes the ellipticity due to the PEM and, in the case of the rotation measurements, the contribution of the quarter-wave plate. A manual intervention is required from time to time to better adjust the situation, in particular during the rotation measurements. In these case we extract the PEM and the quarter-wave plate from the beam path and we extinguish the intensity I_2, thus minimising only the static birefringence due to the cavity. After re-insertion of PEM and quarter-wave plate, the best extinction is reached aligning only these two optical components.

3.10.3 Offline data analysis

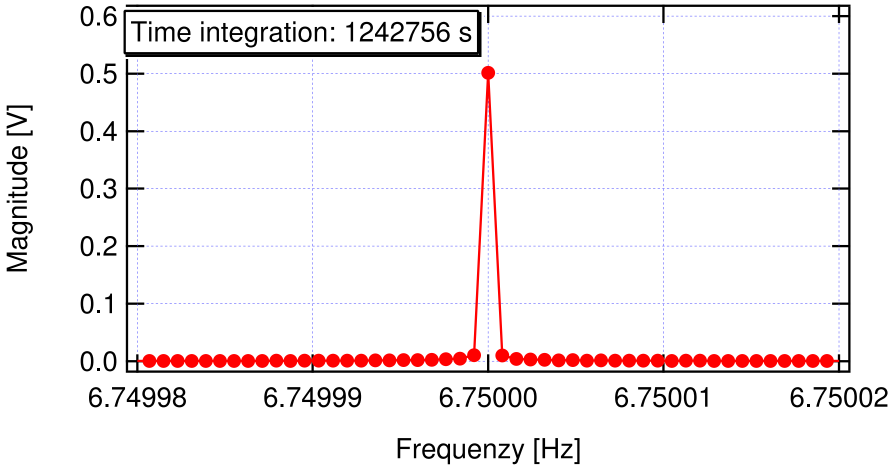

Figure 3.31: FFT of the signal from the magnetometer B_β in a 40 μHz window around $\nu_\beta = 6.75$ Hz. The integration time $T = 1.24 \times 10^6$ s corresponds to a frequency resolution of 0.82 μHz.

To analyse the data I wrote a C program. During the three years of the thesis, the program has grown with internal functions and macros which automatically import and analyse the data. After importing the data, the program performs a series of checks. The first check is on the phases of the stray magnetic fields (see Fig. 3.30), to look for a possible loss of samples. The next step is the data selection, discarding the time intervals in which any anomaly appears (laser unlocked, lock-ins saturation, etc.). In doing this, one must always cut from the file an integer number of turns of both magnets. After data selection, the phases of the magnetic fields are checked again. The residual data from all the subfiles are collected into a single file, to reach the best frequency resolution in the Fast Fourier transform. Moreover, files taken with the same rotation frequencies and the same sampling rate are normally analysed as a single file; we name this file a “block”. The frequency resolution is given by the width of the ν_B component of the Fourier transform of the signal from the magnetometers. Even for the longest runs, this line is found to occupy a single bin. An example is shown in Fig. 3.31 where the data set had an integration time $T = 1.24 \times 10^6$ s with a bin width $\Delta\nu = 1/T = 0.82$ μHz

.

We then calculate an ellipticity file through Eq. 2.5. The i-th element of the block is obtained as

$$\Psi^{(i)} = \frac{1}{4}\sqrt{\frac{2\sqrt{2}\,I^{(i)}_{2\nu_m}S_{2\nu_m}}{qGFI^{(i)}_1}\,\frac{I^{(i)}_{\nu_m}S_{\nu_m}}{I^{(i)}_{2\nu_m}S_{2\nu_m}}}$$

where I_1 is the intensity transmitted by the Fabry-Perot and I_{ν_m} and $I_{2\nu_m}$ are the extinguished intensity I_2 demodulated at the frequencies ν_m and $2\nu_\mathrm{m}$. The S’s are the sensitivities of the lock-ins used for the demodulations, q is the quantum efficiency of the extinction photodiode, G its transimpedance, and $F = 0.83$ is the transmission of the optical filter placed before the extinction photodiode.

The ellipticity is Fourier transformed to obtain the amplitude and the phase of the components at $2\nu_{B\alpha}$ and $2\nu_{B\beta}$ and to obtain a value for the noise around these two frequencies. The noise is extracted performing an FFT of the data array. A histogram of the ellipticity values of the 10 000 bins around each of the two frequencies $2\nu_{B\alpha}$ and $2\nu_{B\beta}$ is fitted with a Rayleigh distribution

$$f(x;\sigma) = A\frac{x}{\sigma^2}e^{-\frac{x^2}{2\sigma^2}}$$

where A is a normalisation parameter. The noise value corresponds to the value of σ. The values of the ellipticity at $2\nu_{B\alpha}$ and $2\nu_{B\beta}$ are calculated also with Discrete Fourier Transforms (DFTs). Comparing the ellipticity values at $2\nu_B$ with the position of their bins in the histograms defines the probability of their compatibility with zero. We note that, as we have seen before, a true ellipticity signal must have a well defined phase corresponding to the one measured in the calibration obtained with the Cotton-Mouton effect. The values of $\Psi_{2\nu_{B\alpha}}$ and $\Psi_{2\nu_{B\beta}}$ are then projected along the physical and non-physical axes. The results obtained in the analysis of the block are then quoted as the components on the physical axis, with uncertainty given by σ:

$$\Psi_{2\nu_{B\alpha}} \cos\left(\phi_{2\nu_{B\alpha}} - \phi_{\mathrm{CM}}\right) \pm \sigma \qquad \text{and} \qquad \Psi_{2\nu_{B\beta}} \cos\left(\phi_{2\nu_{B\beta}} - \phi_{\mathrm{CM}}\right) \pm \sigma$$

where ϕ_{CM} is the phase of the calibration.

We perform the same analysis also as a function of the time, by considering short intervals usually of 1024 s. In this way we can study how the ellipticity evolves and how it is correlated with other signals, what indicates the presence of a spurious effect. As we will see in the next chapter, the acceleration of the tube and the acceleration of the optical bench generate spurious signals; their correlations can be put in evidence by means of a time analysis. We observe also that, if the static ellipticity grows beyond a certain value, a correlation with the sensitivity appears. A detailed discussion of all these phenomena is found in the next chapter.

An important strength of our analysis is the resolution in frequency we reach in the long runs. As will be seen in Chapter 5, we have observed that mechanical vibrations modulate the diffused light inside the tube generating unwanted signals. In the FFT spectra of a long run, these signals are often found to occupy more than one bin around $2\nu_B$, with some structure.

Finally, to put everything together, the results obtained from blocks with different rotation frequencies of the magnets are averaged by using a weighted vector average procedure.

.1 Appendix 3.I: Automatic locking circuit scheme

.1.1 Scheme of the analogic circuit

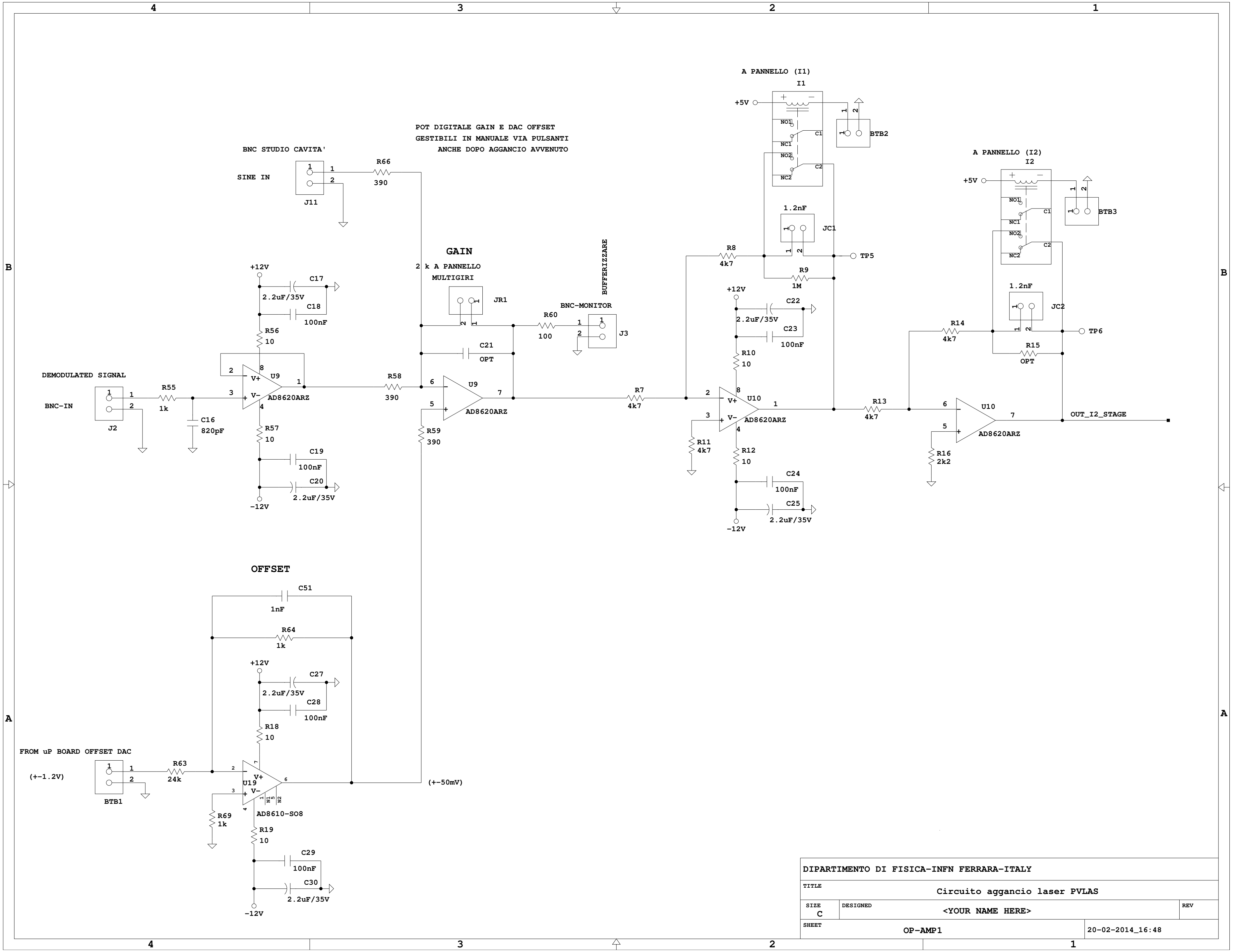

DIPARTIMENTO DI FISICA-INFN FERRARA-ITALY

TITLE Circuito aggancio laser PVLAS

SIZE C DESIGNED <YOUR NAME HERE> REV

SHEET OP-AMP1 20-02-2014_16:48

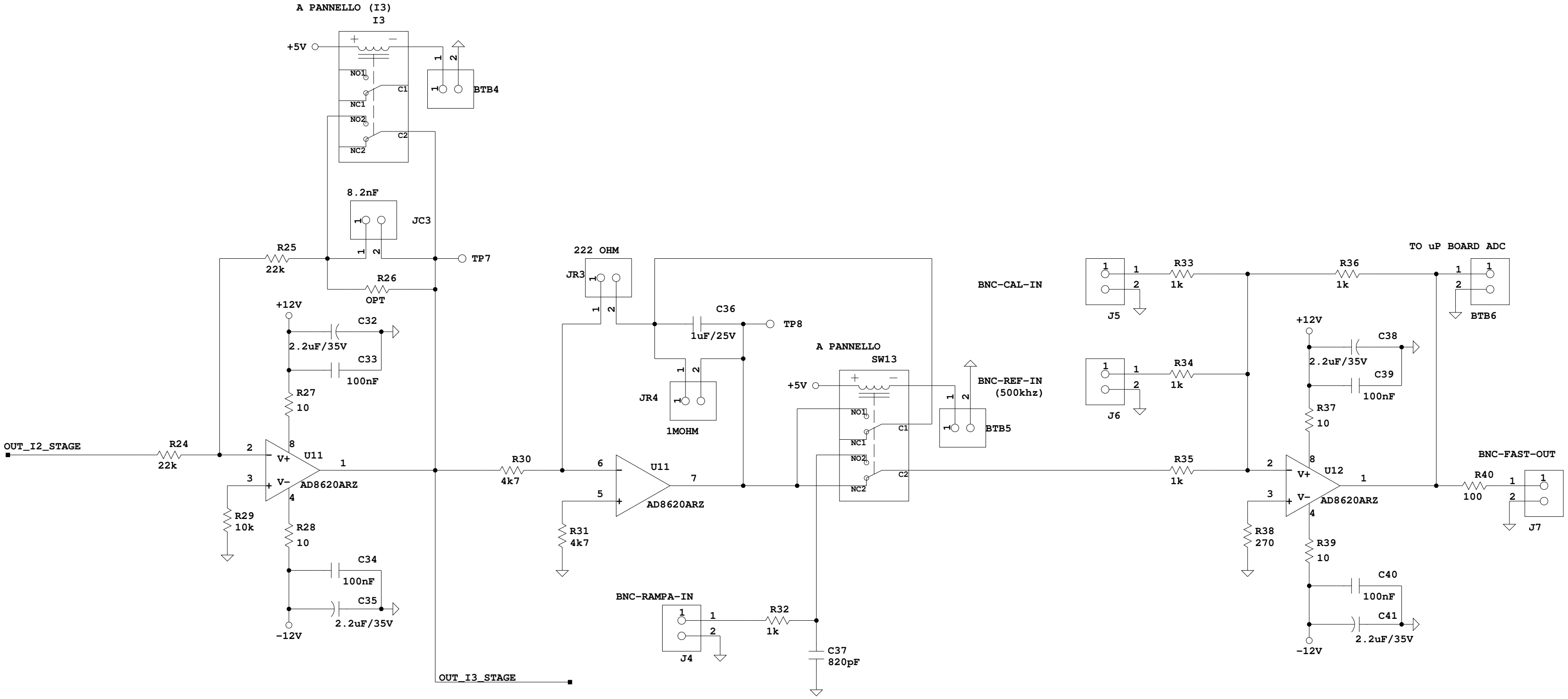

DIPARTIMENTO DI FISICA-INFN FERRARA-ITALY

TITLE
Circuito aggancio laser PVLAS

SIZE
C

DESIGNED
<YOUR NAME HERE>

REV

SHEET
OP-AMP2

31-01-2014_12:22

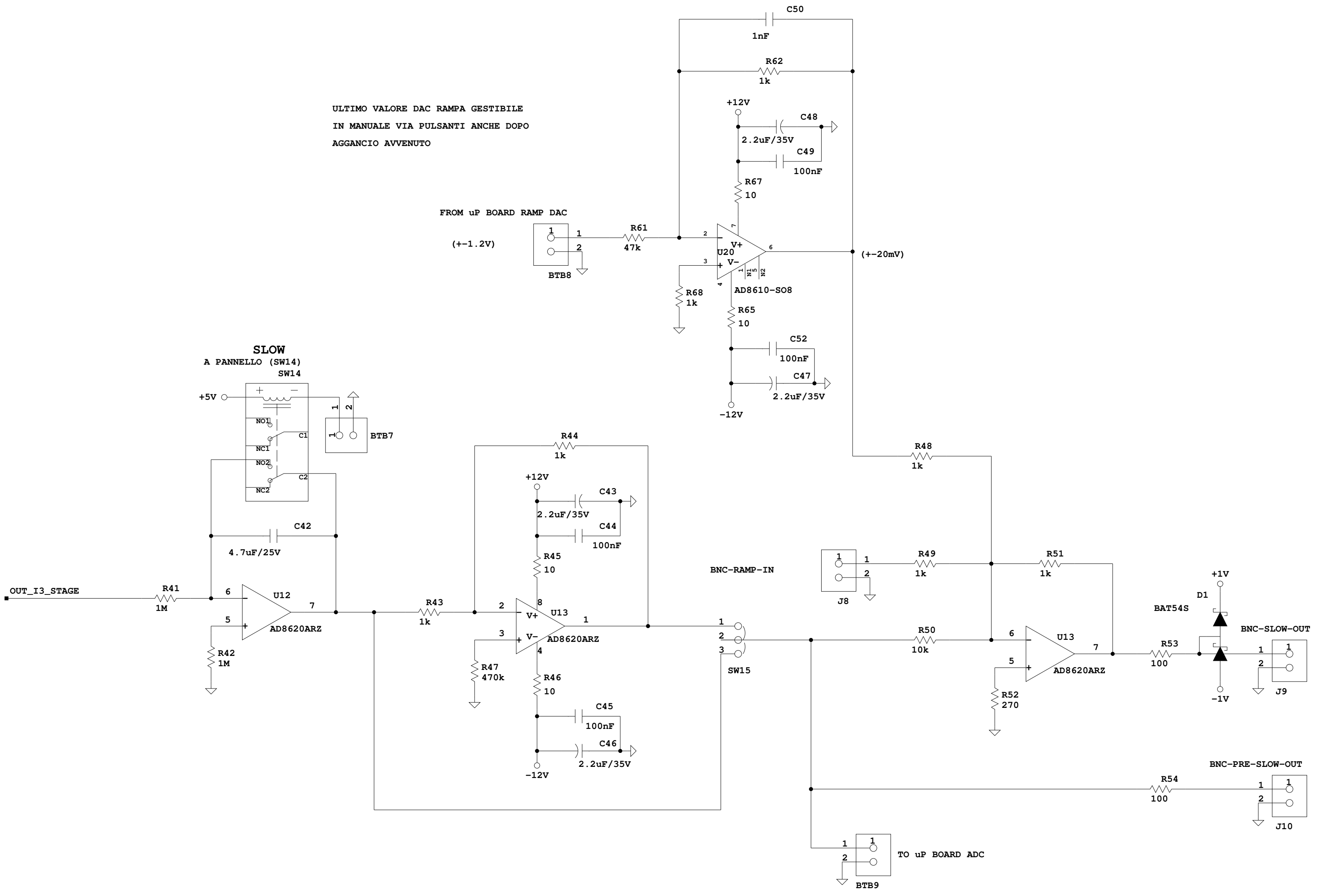

DIPARTIMENTO DI FISICA-INFN FERRARA-ITALY

TITLE
Circuito aggancio laser PVLAS

SIZE C
DESIGNED
<YOUR NAME HERE>
REV

SHEET
OP-AMP3
20-02-2014_16:49

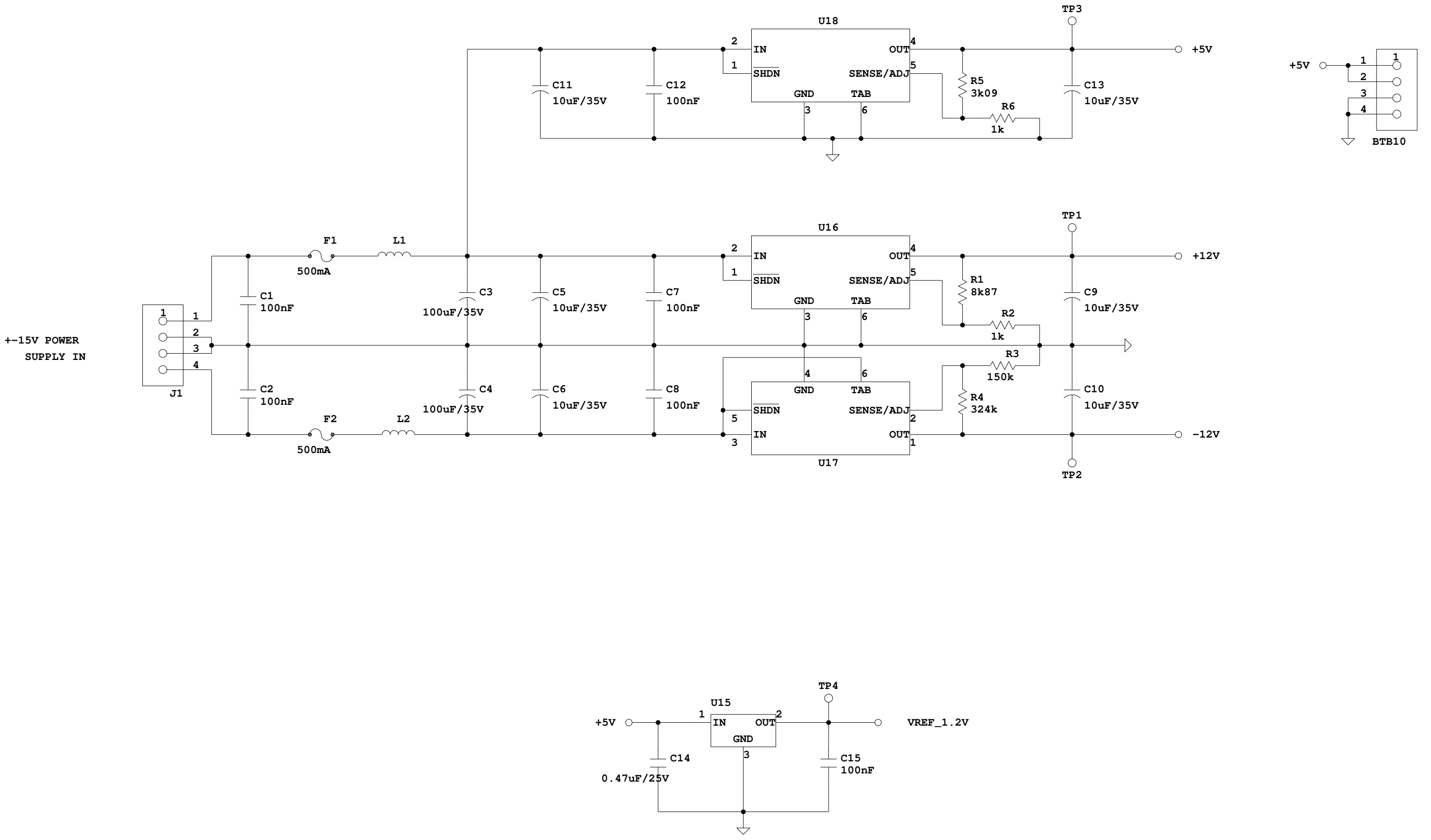

DIPARTIMENTO DI FISICA-INFN FERRARA-ITALY

TITLE	Circuito aggancio laser PVLAS	
SIZE C	DESIGNED <YOUR NAME HERE>	REV
SHEET	Power-supply	31-01-2014_12:24

.1.2 Scheme of the digital circuit

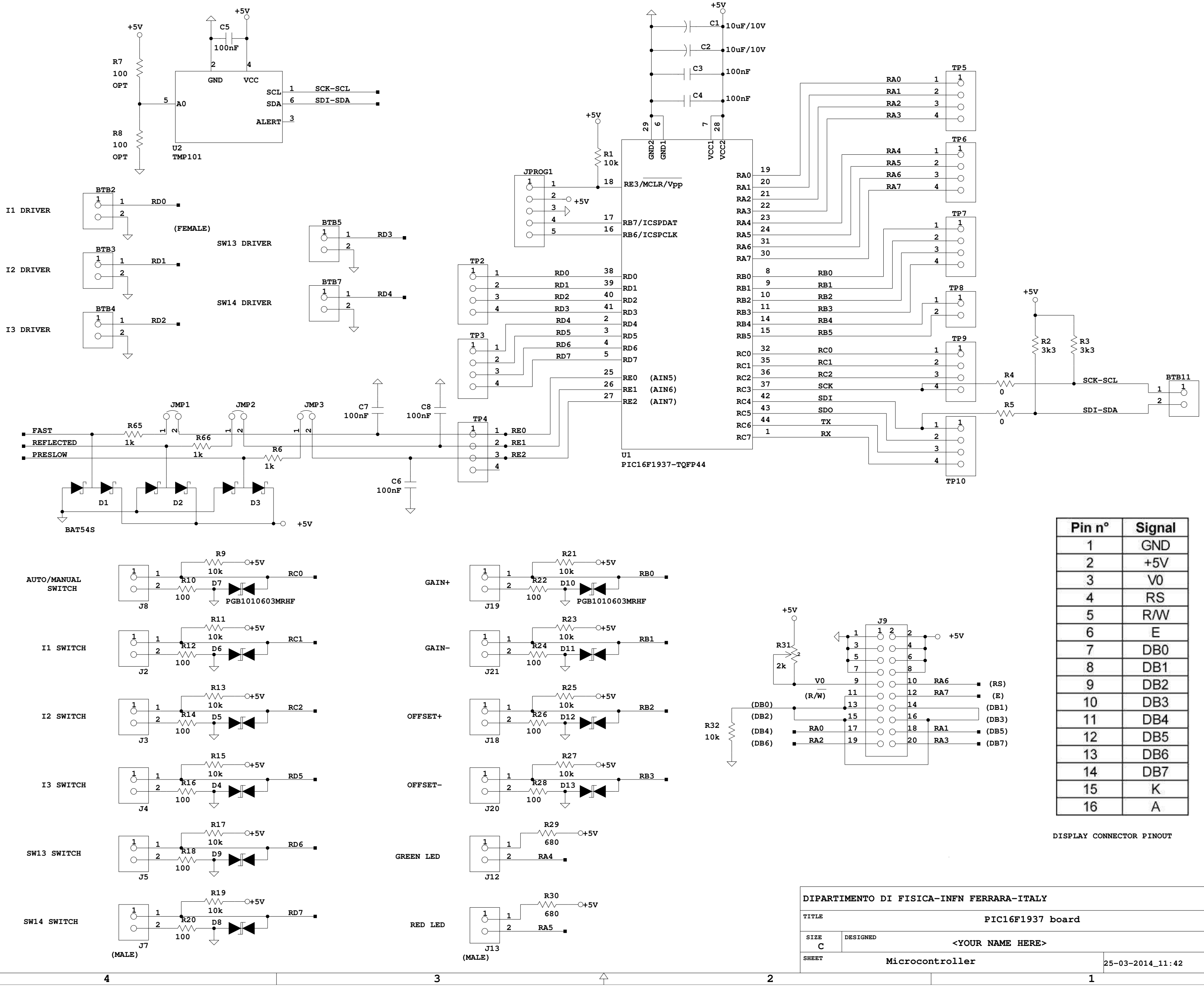

Pin n°	Signal
1	GND
2	+5V
3	V0
4	RS
5	R/W
6	E
7	DB0
8	DB1
9	DB2
10	DB3
11	DB4
12	DB5
13	DB6
14	DB7
15	K
16	A

DISPLAY CONNECTOR PINOUT

DIPARTIMENTO DI FISICA-INFN FERRARA-ITALY

TITLE PIC16F1937 board

SIZE C DESIGNED <YOUR NAME HERE> REV

SHEET Microcontroller 25-03-2014_11:42

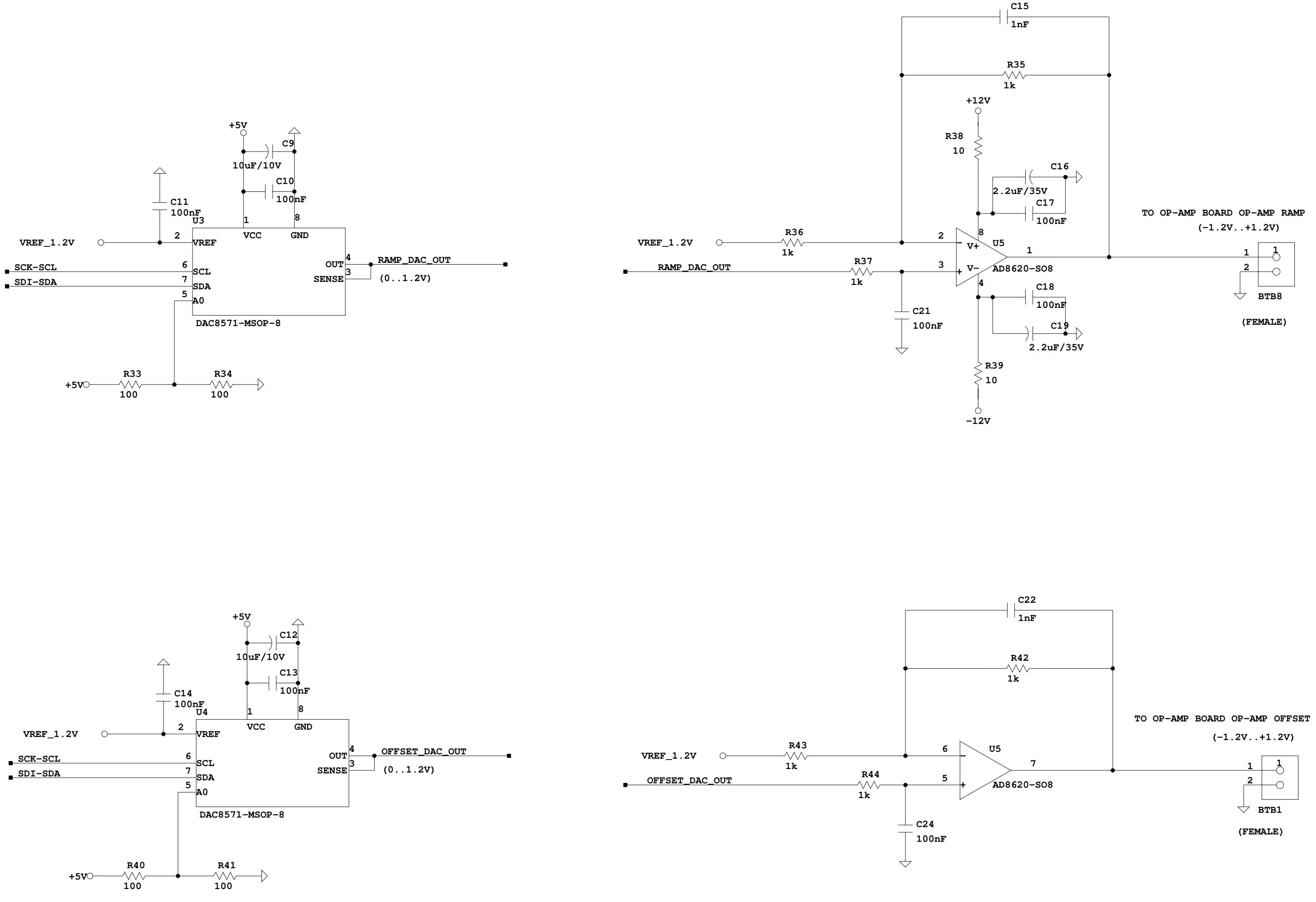

DIPARTIMENTO DI FISICA-INFN FERRARA-ITALY

TITLE	PIC16F1937 board	
SIZE C	DESIGNED <YOUR NAME HERE>	REV
SHEET	DAC	26-03-2014_11:23

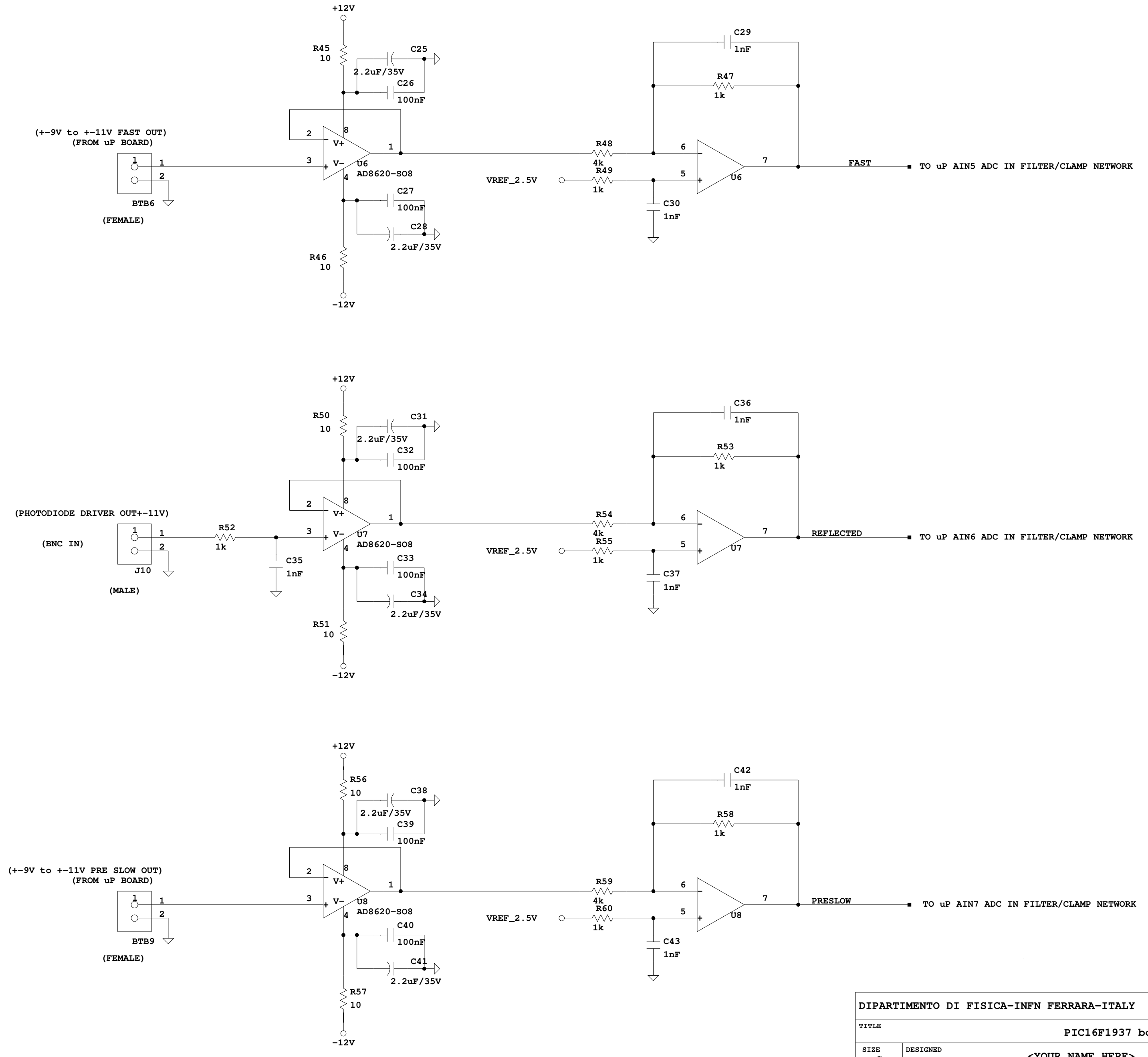

DIPARTIMENTO DI FISICA-INFN FERRARA-ITALY

TITLE
PIC16F1937 board

SIZE C
DESIGNED <YOUR NAME HERE>
REV

SHEET ADC conditioning
26-03-2014_11:17

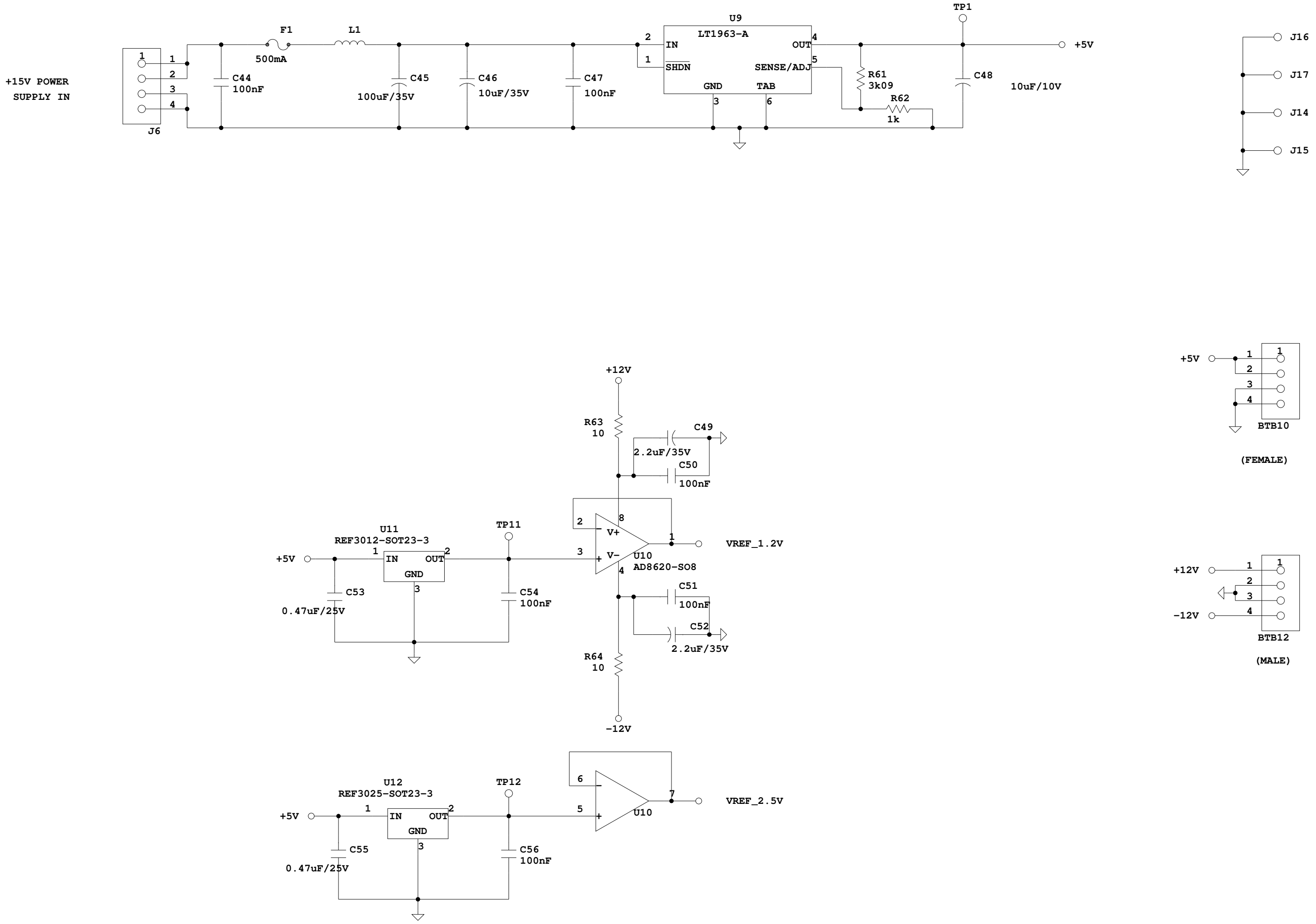

DIPARTIMENTO DI FISICA-INFN FERRARA-ITALY

TITLE
PIC16F1937 board

SIZE C
DESIGNED <YOUR NAME HERE>
REV

SHEET
Power supply
10-04-2014_11:30

Chapter 4

Systematics, spurious signals and wide-band noise

In fall 2013, we were finishing the mounting of the essential components of the PVLAS apparatus. In that year, the Cotton-Mouton effect of water vapour had been measured [57] with a low finesse cavity. The main task of my thesis work has been to set-up and tune the PVLAS apparatus for the measurement of the vacuum magnetic birefringence. This chapter presents most of my experimental work performed in the last three years. My activities included the study of the systematics affecting the experiment, the identification of spurious signals and the characterisation of the polarimeter.

4.1 Systematic effects: birefringence of the mirrors

4.1.1 Polarimetry with a birefringent cavity

In chapter 2 the polarimetry with a Fabry-Perot cavity has been treated from a principle point of view. In this section, we describe the modifications brought in by the anisotropy of the mirrors. The mirrors, in fact, behave as birefringent wave-plates with small phase differences: a linearly polarised light becomes slightly elliptical after reflection. The cavity amplifies this small ellipticity by the factor N, and this causes a substantial change in the performances of the polarimeter. Mirror birefringence has been the subject of many studies (see for example refs. [89, 90]) and it is attributed to the stress generated during the deposition of the dielectric films onto the mirror substrate and to the stress associated with the mirror mount. Here the mirror birefringence is considered as a characteristic of the FP cavity: the two mirrors act as an equivalent wave-plate.

The features of a birefringent cavity have been treated in ref. [91]. We call α_1 and α_2 the small phase differences acquired by light after each reflection from the mirrors M1 and M2. This introduces in the calculations the wave-plates

$$\mathbf{M}_{1,2} = \begin{pmatrix} e^{i\alpha_{1,2}/2} & 0 \\ 0 & e^{-i\alpha_{1,2}/2} \end{pmatrix}, \tag{4.1}$$

where one can consider the α's as positive quantities without loss of generality. If the slow axes of the mirror wave-plates are both aligned to the input polarisation, the polarisation auto-states of the Fabry-Perot cavity are given by

$$\begin{pmatrix} \left[1 - Re^{i[\delta+(\alpha_1+\alpha_2)/2]}\right]^{-1} \\ 0 \end{pmatrix} \quad \text{and} \quad \begin{pmatrix} 0 \\ \left[1 - Re^{i[\delta-(\alpha_1+\alpha_2)/2]}\right]^{-1} \end{pmatrix}.$$

This means that the resonance curves of the two orthogonal polarisations are no longer centred at $\delta = 0$, but are separated by the quantity

$$\alpha = \alpha_1 + \alpha_2.$$

In other words, if we lock the laser to the first polarisation component, the other polarisation is not in resonance. Namely, if the input light is at the top of the resonance curve ($\delta = -\alpha/2$), the orthogonal component is out of phase of the quantity α. Accordingly, the extinguished beam and the ellipticity signal may be filtered significantly. Hence, in calculating the ellipticity signal in the presence of mirror birefringence it is necessary to take into account the fact that the extinguished intensity is reduced by the factor

$$k(\alpha) = \frac{1}{1 + N^2 \sin^2(\alpha/2)} \leq 1 \tag{4.2}$$

with respect to the other polarisation.

With the same formalism of Chap. 2, the electric field at the exit of a birefringent cavity, taking into account the matrices $\mathbf{M}_{1,2}$, is

$$\mathbf{E}_{\,\mathrm{out}}(\phi,\delta) = E_0 \left[\mathbf{I} - Re^{i\delta}\mathbf{X}\cdot\mathbf{M}_1\cdot\mathbf{X}\cdot\mathbf{M}_2\right]^{-1} \cdot Te^{i\delta/2}\mathbf{X}\cdot \begin{pmatrix} 1 \\ 0 \end{pmatrix}.$$

The electric field after the analyser is given by

$$\mathbf{E}(\delta,\phi) = \mathbf{A}\cdot\mathbf{H}\cdot\mathbf{Q}\cdot\mathbf{E}_{\mathrm{out}}(\delta,\phi). \tag{4.3}$$

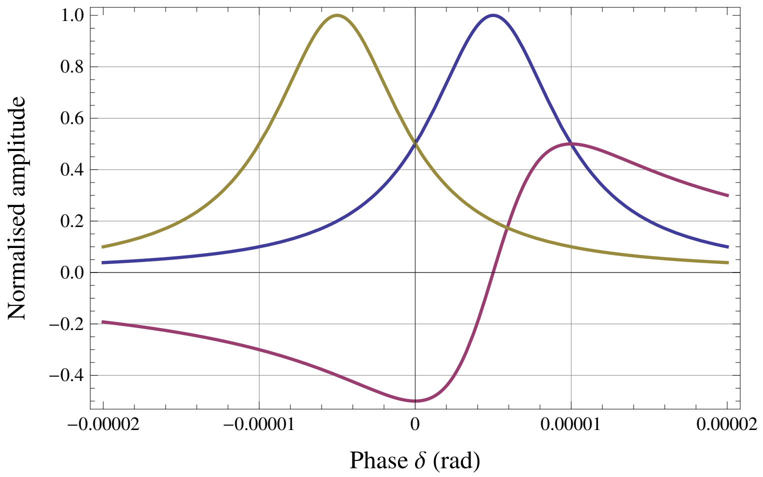

Figure 4.1: Transmitted intensity (yellow curve) I_1, amplitudes of the ellipticity signal $I_2^{\text{ell}}(\phi)$ (blue curve) and of the rotation signal $I_2^{\text{rot}}(\phi)$ (red curve) given by Equations (4.4) and (4.5) in the case of the measurement of a pure birefringence ($\theta = 0$), as functions of the Fabry-Perot cavity phase δ, for $\alpha = 10^{-5}$ and $N = 4 \times 10^5$. The Airy curves are normalised to unity; the rotation signal bears the same normalisation coefficient as the ellipticity.

One has to note that small static ellipticities or rotations acquired by the beam before or after the cavity do not interfere with the signal at $2\nu_B$, and can thus be neglected. The intensities, considering that the phase delay α induced by one passage is small and $R \approx 1$, are given by

$$I_2^{\text{ell}}(\phi) = I_1 \left[\eta^2 + \eta \frac{2N\psi - N^2\theta \sin\left(\delta - \frac{\alpha}{2}\right)}{1 + N^2 \sin^2\left(\frac{\delta}{2} - \frac{\alpha}{4}\right)} \sin 2\phi \right] \tag{4.4}$$

for the measurements of ellipticity, and

$$I_2^{\text{rot}}(\phi) = I_1 \left[\eta^2 + \eta \frac{2N\theta + N^2\psi \sin\left(\delta - \frac{\alpha}{2}\right)}{1 + N^2 \sin^2\left(\frac{\delta}{2} - \frac{\alpha}{4}\right)} \sin 2\phi \right] \tag{4.5}$$

for rotation measurements. Here the transmitted intensity I_1 is

$$I_1 = \varepsilon_0 c \frac{E_0^2}{2} \frac{T^2N^2/4}{1 + N^2 \sin^2\left(\frac{\delta}{2} + \frac{\alpha}{4}\right)}. \tag{4.6}$$

From equations (4.4) and (4.5), one can see that there is a cross-talk between the ellipticity and the rotation signals as can be determined by Equation (2.5): with $\psi \neq 0$ a rotation is measured even in the case $\theta = 0$. Conversely, in the case, $\psi = 0$ and $\theta \neq 0$, an ellipticity is observed. In Figure 4.1, we plot the last three equations as functions of δ for the case $\theta = 0$ (pure birefringence), for $N = 4\times10^5$ and $\alpha = 10^{-5}$. The transmitted intensity is centered at $\delta = -\alpha/2$, the other two curves, which refer to the other polarisation, at $\delta = \alpha/2$. It should be noted that the amplitudes of the ellipticity and rotation signals, which are normalised to unity in the figure, are in reality a factor $k(\alpha) = 0.2$ smaller than the maximum.

Note in passing that the same mixing of ellipticity and rotation appears also in a non birefringent cavity if the cavity is not locked on top of the resonance curve. In fact, in this case ($\alpha = 0$) the equations (4.4) and (4.5) become

$$I_2^{\rm ell}(\phi,\delta) \simeq I_0\left[\eta^2 + \eta\,\frac{2N\psi - N^2\theta\sin\delta}{1+N^2\sin^2(\delta/2)}\,\sin 2\phi\right] \tag{4.7}$$

and

$$I_2^{\rm rot}(\phi,\delta) \simeq I_0\left[\eta^2 + \eta\,\frac{2N\theta + N^2\psi\sin\delta}{1+N^2\sin^2(\delta/2)}\,\sin 2\phi\right]. \tag{4.8}$$

In all these cases, measuring the ellipticity and rotation signals is not enough to determine the birefringence and the dichroism of the medium under study. In fact, to this end, information about the degree of mixing of the two quantities is needed.

When the laser is locked on top of the resonance curve at $\delta = -\alpha/2$, by using the factor $k(\alpha)$ defined by Eq. (4.2), Equation (4.4) for an ellipticity measurement becomes

$$I_2^{\rm ell}(\phi) = I_1\left[\eta^2 + \eta k(\alpha)\,(2N\psi + N^2\theta\alpha)\,\sin 2\phi\right], \tag{4.9}$$

while for a rotation measurement, Equation (4.5) reads

$$I_2^{\rm rot}(\phi) = I_1\left[\eta^2 + \eta k(\alpha)\,(2N\theta - N^2\psi\alpha)\,\sin 2\phi\right]. \tag{4.10}$$

With respect to equations (2.20) and (2.21), in which the birefringence of the mirrors is not taken into account, the expected signals of ellipticity and rotation are attenuated by the factor $k(\alpha)$. Moreover, a cross talk between the two measurement channels appears. In fact, even with $\theta = 0$, a rotation $-kN^2\alpha\psi$ is observed: the ratio R_0 of the “spurious” rotation over the “true” ellipticity is

$$R_0 = -\frac{N}{2}\alpha. \tag{4.11}$$

Since $N/2$ is the number of passes of the light beam through the equivalent wave-plate, R_0 is precisely the total phase difference experienced by the light beam. The measurement of the ratio between the rotation and the ellipticity signals provides thus a direct measurement of α.

The case of pure dichroism ($\psi = 0$) is entirely analogous: an ellipticity $kN^2\alpha\theta$ appears.

4.1.2 Measurement of the birefringence of the mirrors

In this section we discuss the experimental work done to minimise the phase difference of the equivalent wave-plate $\Delta\alpha = \alpha_1 - \alpha_2$ by aligning the slow axis of one mirror with the fast axis of the other. This configuration ensures that the peak of the $I_2^{\mathrm{ell}}(\phi)$ approaches the peak of I_1 as much as possible; in this case the value of $\alpha = \alpha_1 + \alpha_2$, of the formulas (4.4) and (4.5) is given by $\Delta\alpha = |\alpha_2| - |\alpha_1|$. In general, the phase difference of the equivalent wave-plate depends on the angular orientation of one mirror with respect to the other [92]. Let us suppose that one mirror is placed with its axis of birefringence at an azimuthal angle ϕ_{WP} with respect to the other. The composition of the two birefringent wave plates is equivalent to a single wave-plate [92] with a phase difference α_{EQ} given by

$$\alpha_{\mathrm{EQ}} = \sqrt{(\alpha_1 - \alpha_2)^2 + 4\alpha_1\alpha_2\cos^2\phi_{\mathrm{WP}}} \tag{4.12}$$

and placed at the angle ϕ_{EQ} with respect to the slow axis of the first mirror, where

$$\cos 2\phi_{\mathrm{EQ}} = \frac{\alpha_1/\alpha_2 + \cos 2\phi_{\mathrm{WP}}}{\sqrt{(\alpha_1/\alpha_2 - 1)^2 + 4(\alpha_1/\alpha_2)\cos^2\phi_{\mathrm{WP}}}}. \tag{4.13}$$

The equivalent wave plate could be neutralised if α_1 were equal to α_2 and $\phi_{\mathrm{WP}} = 90^\circ$. In this case, the resonance curves of the two polarisation auto-states would appear superimposed on a plot like that of Figure 4.1. If $\alpha_1 \neq \alpha_2$, the effect of the equivalent wave plate can only be minimised but never extinguished. In the previous section, we always supposed that the laser polarisation was aligned to the axes of the equivalent wave-plate. If this is not the case, a large ellipticity is observed in the polarisation of the extinguished beam, at the frequency ν_{m} of the ellipticity modulator (PEM) without affecting the signal at $2\nu_{\mathrm{m}}$. In Chapter 3 we have shown that the Fourier component at ν_{m} is maintained at zero by rotating the polariser. This procedure means that the input polarisation is aligned to the sum of all the static birefringences existing in the polarimeter in the path from the polariser to the analyser, an amount that does not coincide exactly with the birefringence of the cavity. Nevertheless, we assume alignment to occur in a first approximation, namely that the laser polarisation is aligned with the axis of the equivalent wave plate of the mirrors.

In order to study the equivalent wave-plate of the cavity, we have performed the measurement of the ellipticity and of the rotation generated by the Cotton-Mouton effect in a gas as a function of the relative azimuthal position of the two mirrors. In this experimental condition there is no dichroism ($\theta = 0$). In the measurements, the magnets rotated at $\nu_B = 4$ Hz; this corresponds to a negligible correction factor due to the cavity first order filtering [see

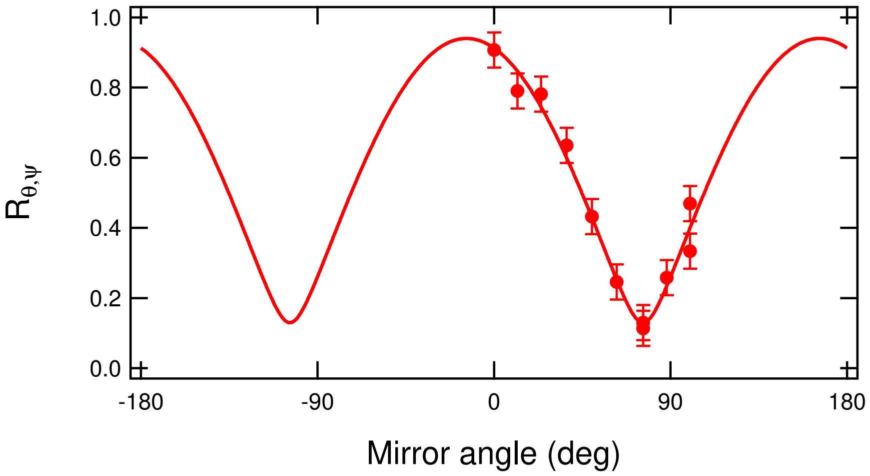

Figure 4.2: Rotation-to-ellipticity signals ratio plotted as a function of the azimuthal angle ϕ_{WP} of the input mirror for a Cotton-Mouton effect of 230 μbar of Ar gas. The fit line corresponds to $N\alpha_{\mathrm{EQ}}/2$ phase difference of the amplified equivalent wave-plate of the mirrors given by Equation (4.12).

Eq. (2.7)]:

$$h_{\mathrm{T}} \equiv \frac{E_{\mathrm{T}}(\nu)}{E_0} = \frac{T}{\sqrt{1+R^2-2R\cos\delta}} = 0.97 \tag{4.14}$$

for the signals at $\nu = 8$ Hz. In each measurement, the laser polarisation direction has been adjusted to minimise the ellipticity at frequency ν_{m} in the extinguished beam. In Figure 4.2, we show the ratio R_0 plotted as a function of the azimuthal angle ϕ_{WP} of the first mirror (the second mirror was never moved). Each rotation step, of about 15°, has been followed by cavity realignment through the adjustment of the two tilt stages of the mirror, by optimisation and measurement of the extinction ratio, and by a measurement of the finesse. The experimental points are fitted with Equation (4.11), where α is given by α_{EQ} of Equation (4.12). The best fit produces values for the quantities $N\alpha_1/2$, $N\alpha_2/2$, and for the angular position of the maxima with respect to the initial angular position of the input mirror ($\phi_{\mathrm{WP}} = 0$). With $N/2 \approx 2.2 \times 10^5$, the phase differences of the two mirrors are calculated to be

$$\alpha_{1,2} = (2.4 \pm 0.1)\ \mu\text{rad} \qquad \text{and} \qquad \alpha_{2,1} = (1.9 \pm 0.1)\ \mu\text{rad} \tag{4.15}$$

but it is not possible to associate α_1 and α_2 unequivocally to M1 or M2 with this single measurement. According to the relative angular position of the two mirrors, the value of α_{EQ} can be found between 0.6 μrad and 4.3 μrad, which is equivalent to saying that the Airy curve of the ellipticity resonance is 5 Hz to 31 Hz away from the resonance of the input polarisation. Correspondingly, the $k(\alpha)$ parameter can be found between ≈ 1 and

≈ 0.5. By substituting one of the mirrors with a third one, it is likely that the new one would exhibit a different value of phase shift, thus allowing to tag each of the three mirrors with a unique value. Moreover, having at one's disposal a number of mirrors, and by repeating the procedure, one could select the pair of mirrors giving the smallest minimum value of $\Delta\alpha$.

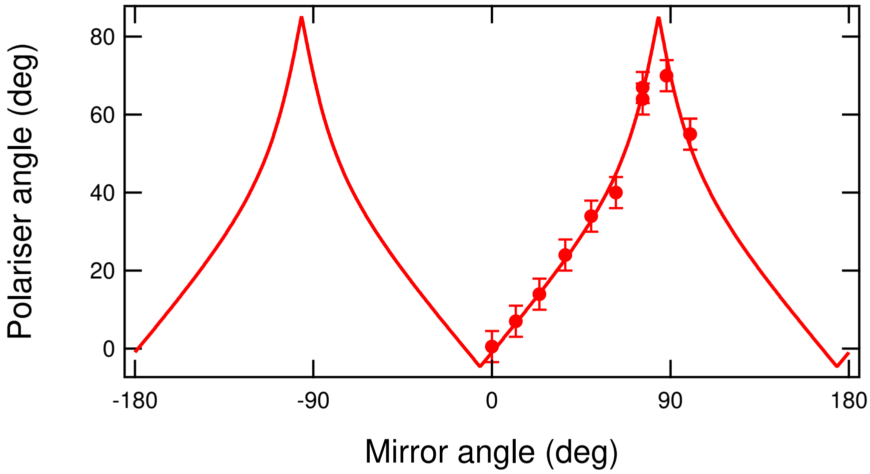

Figure 4.3: Polariser angle as a function of the azimuthal angle ϕ_{WP} of the mirror in a Cotton-Mouton measurement of 230 μbar of Ar. Data are fitted with ϕ_{EQ} as given by Eq. (4.13).

As said before, for each rotation step of the entrance mirror M1, the best extinction ratio is obtained by rotating the polariser. This condition ensures the alignment of the polarisation with the axis of the equivalent wave-plate. Figure 4.3 shows the azimuthal angle ϕ_{EQ} of the polariser for which the best extinction ratio is obtained, as a function of the mirror rotation angle ϕ_{WP}. These points are fitted with Equation (4.13). The best fit gives a value of $\alpha_1/\alpha_2 = 0.62 \pm 0.08$, allowing the assignment of the phase delay of each mirror. This value is slightly different from the one obtained by the fit in Figure 4.2, but is compatible within the fit uncertainties. However, the zero references of ϕ_{WP} in the two fits appear to be different by about 10°, well beyond the fit uncertainty. This can be interpreted as evidence of the contribution of other birefringent elements (mirror substrates and PEM) between the two crossed polarisers. The apparent discrepancy of the two measurements is due to their different character: the positioning of the polariser in the measurement of the extinction ratio is made following the indications of the ν_{m} signal in the Fourier transform of the extinguished beam, which is the DC component of the demodulated intensity, whereas the measurement of the CM effect is performed at twice the rotation frequency ν_B of the magnet.

A unique feature of our apparatus is the possibility to modify the set point of the electronic feedback which locks the frequency of the laser to the resonance frequency of the cavity. This

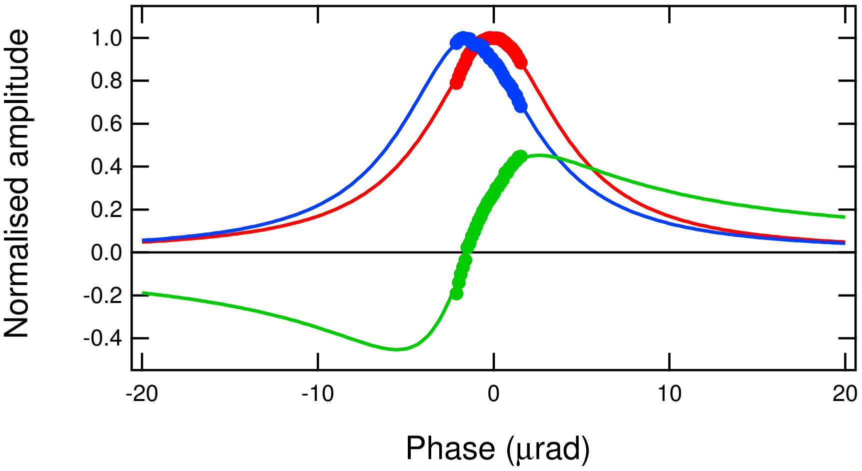

Figure 4.4: From left to right: ellipticity, transmitted intensity, and rotation, measured in the Cotton-Mouton effect of 230 μbar of Ar gas, plotted as functions of the set point of the laser locking feedback circuit. The continuous lines are the fits obtained with formulas (4.9), (4.6), and (4.10). For a comparison with the theory, see Fig. 4.1.

allows for polarimetric measurements with arbitrary values of δ, opening the possibility for testing experimentally the mathematics presented in Section 4.1.1. In these measurements, the azimuthal coordinate of the first mirror are kept fixed and δ is changed. Figure 4.4 shows the experimental data that correspond to the model of Figure 4.1. The solid lines are the fits obtained with the formulas (4.6), (4.9), and (4.10). In the three fits, a common value has been used for the resonance width. The ellipticity and rotation data are forced to have the same resonance frequency. From the fits, one determines the scale factor between the feedback set point and the phase δ. The distance between the two Airy curves correspond to a phase delay of the two orthogonal polarisations, $\alpha = 1.5$ μrad (with negative sign). This corresponds to a difference in the resonance frequencies of the two orthogonal polarisation of about $\Delta\nu = 11$ Hz.

4.2 Systematic effects: frequency response of a birefringent Fabry-Perot cavity

As we will see, the wide-band noise decreases with a certain power law as a function of the frequency. As a consequence, and in principle, the higher the working frequency, namely the rotation frequency of the magnets, the better the signal to noise ratio (SRN) of the measurement (see section 4.4). One has to note, however, that the Fabry-Perot cavity is a low-pass filter. Well before $2\nu_B$ approaches the cutoff frequency of the cavity, the calibration discussed in Section 2.4 depends on the frequency response of the cavity.

4.2.1 Polarisation dynamics: theory

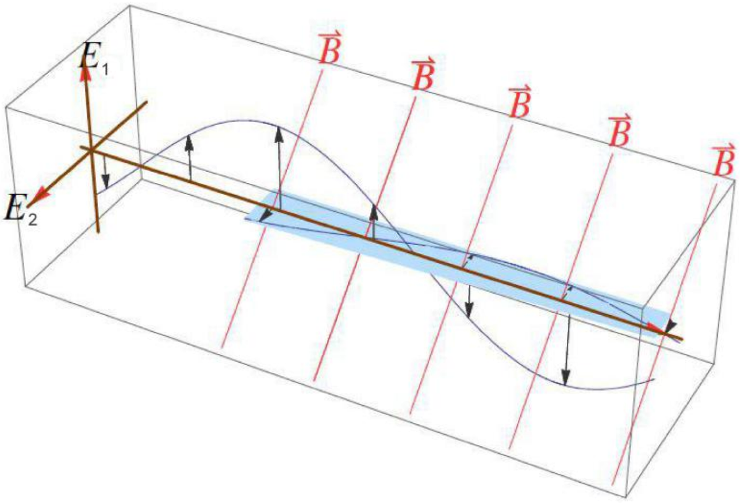

Figure 4.5: Electric fields in a birefringent FP cavity immersed in a transverse rotating magnetic field, corresponding to a rotating birefringent medium. The input light has polarisation direction indicated by the index 1.

In this section we derive the frequency response of a model birefringent cavity. Actually one has to deal with two different cavities, corresponding to the two polarisation auto-states of the cavity. The two cavities coincide spatially, but do not interfere (see Fig. 4.5). We suppose that the input polarisation, indicated with the index 1 is aligned with one of the axes of the cavity, and that the laser is frequency-locked to the cavity. This means that between the two orthogonal components of the electric field of Fig. 4.5 there is a spatial phase delay. The rotating transverse magnetic field can be schematised as a rotating birefringent medium of length L. The mathematical treatment is made with reference to the same configuration as the one presented in chapter 2 [see Fig. 2.3], but in the time dependent context of the rotating magnetic field.

To perform the calculations, we choose a time step equal to the time of flight of the light in the cavity $\tau = 2d/c = 22$ ns. During this time the azimuthal angle of the magnetic field changes by $\Delta\phi = \phi(t+\tau) - \phi(t) = \omega_B\tau$. At the highest rotation frequency employed $\nu_B = 23$ Hz, the maximum value of $\Delta\phi$ is less than 0.0002°.

As the laser light is frequency locked to the cavity, the electric field E_1 is on top of the resonance defined by Eq. (2.7) of Chapter 2:

$$E_{\text{out},1} = E_0 \frac{t_1 t_2}{1 - r_1 r_2} \tag{4.16}$$

We explicitly note that this electric field is not time dependent. This is a consequence of assuming that the feedback system that locks the frequencies of the laser and the cavity is able to maintain in resonance the polarisation component parallel to the input field in spite of the periodic change of the optical path given by the rotation of the magnet. This is true since the bandwidth of the feedback system is much larger than the maximum possible value of $2\nu_B$. In doing this, the feedback system imposes a periodic change to the laser frequency.

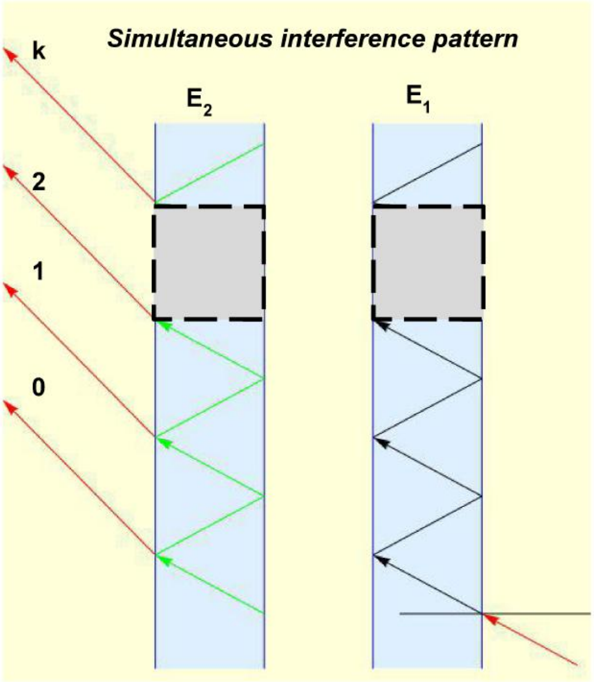

Figure 4.6: Conceptual view of the k-th components of the polarised electric field in the cavity. On the right is shown the simultaneous multiple reflection of the electric field parallel to the polarisation E_1. Left, a generation of simultaneous orthogonal components along the axis E_2 is shown.

The electric field component E_2 has no external input beam, but is pumped by the magnetic birefringence. Let us consider the pattern of reflections of the electric field E_1 depicted on the right in Fig. 4.6. Due to the presence of the birefringent medium, during each passage of the light in the first cavity, a small electric field is generated in the second cavity, whose amplitude is obtained by multiplying the parent amplitude by $i\psi_0 \sin 2\phi$, where

$$\psi_0 = \pi \frac{\Delta n L}{\lambda}$$

is the maximum ellipticity per passage through the magnetic field and $\phi(t) = \omega_B t + \phi_0$ is the angle between the input electric field and the magnetic field. Grouping the passages in the first cavity two by two one obtains the following scheme for the relation between the two orthogonal inner fields:

$$\begin{array}{lcl}
E_1^0 = E_0 t_1 & \Longrightarrow & E_2^0 = E_0 t_1 i \psi_0 \sin 2\phi \\
E_1^1 \approx E_0 t_1 (r_1 r_2) & \Longrightarrow & E_2^1 = E_0 t_1 (r_1 r_2)\, i2\psi_0 \sin 2\phi \\
E_1^2 \approx E_0 t_1 (r_1 r_2)^2 & \Longrightarrow & E_2^2 = E_0 t_1 (r_1 r_2)^2\, i2\psi_0 \sin 2\phi \\
\dots & & \dots \\
E_1^k \approx E_0 t_1 (r_1 r_2)^k & \Longrightarrow & E_2^k = E_0 t_1 (r_1 r_2)^k\, i2\psi_0 \sin 2\phi
\end{array} \tag{4.17}$$

The above relations are all written at the same time t. In fact, as already said, the reflection pattern in the first cavity is not time dependent, but stationary. We want now to calculate the electric field at the exit of the cavity with orthogonal polarisation at time t. This is done taking into account all the multiple reflections of the radiation generated by the magnetic birefringence in the second cavity during a time interval τ at time t: at each reflection a fraction t_2 filters out of the cavity. In doing this, however, since the radiation in this second cavity is not stationary but time dependent, one has to pay attention to synchronising all the output. This is done by taking, at each reflection, the radiation generated at a *previous* time:

$$\begin{array}{lcl}
E_2^0 = E_0 t_1\, i\psi_0 \sin 2\phi & \Longrightarrow & E_{\text{out},2}^{0j} = E_0 t_1 t_2 \sum_{j=0}^{\infty} \left(r_1 r_2 e^{i\alpha}\right)^j i\psi_0 \sin 2\phi_j \\
E_2^1 = E_0 t_1\, (r_1 r_2)\, i2\psi_0 \sin 2\phi & \Longrightarrow & E_{\text{out},2}^{1j} = E_0 t_1 t_2 \,(r_1 r_2) \sum_{j=0}^{\infty} \left(r_1 r_2 e^{i\alpha}\right)^j i2\psi_0 \sin 2\phi_j \\
E_2^1 = E_0 t_1\, (r_1 r_2)^2\, i2\psi_0 \sin 2\phi & \Longrightarrow & E_{\text{out},2}^{2j} = E_0 t_1 t_2 \,(r_1 r_2)^2 \sum_{j=0}^{\infty} \left(r_1 r_2 e^{i\alpha}\right)^j i2\psi_0 \sin 2\phi_j \\
\dots & & \dots \\
E_2^1 = E_0 t_1\, (r_1 r_2)^k\, i2\psi_0 \sin 2\phi & \Longrightarrow & E_{\text{out},2}^{kj} = E_0 t_1 t_2 \,(r_1 r_2)^k \sum_{j=0}^{\infty} \left(r_1 r_2 e^{i\alpha}\right)^j i2\psi_0 \sin 2\phi_j
\end{array} \tag{4.18}$$

where ϕ_j is $\phi - j\omega_B \tau$ and α is the phase due to the birefringence of the mirrors acquired by the light in a round trip in the cavity with orthogonal polarisation. Taking into account all the transmitted components in the E_2 cavity, the transmitted electric field is:

$$\begin{aligned} E_{\text{out},2} &= E_0 t_1 t_2 \sum_{j=0}^{\infty} \left[i\psi_0 \sin 2\phi_j \left(r_1 r_2 e^{i\alpha} \right)^j \right] + \\ &\quad + E_0 t_1 t_2 \sum_{k=1}^{\infty} (r_1 r_2)^k \sum_{j=0}^{\infty} \left[i2\psi_0 \sin 2\phi_j \left(r_1 r_2 e^{i\alpha} \right)^j \right]. \end{aligned} \tag{4.19}$$

The first term in this equation, differing from the other terms for lacking a factor two, is simply the first line of the Equations (4.18) and corresponds to the radiation generated in the single first passage in the primary cavity. In the following we will use an approximation of the radiation coming out of the second cavity written as:

$$E_{\text{out},2} \approx E_0 t_1 t_2 \sum_{k=0}^{\infty} (r_1 r_2)^k \sum_{j=0}^{\infty} \left[i2\psi_0 \sin 2\phi_j \left(r_1 r_2 e^{i\alpha} \right)^j \right]. \tag{4.20}$$

We obtain the final expression for the transmitted electric field as:

$$E_{\text{out},2} = E_0 \frac{\psi_0 t_1 t_2}{1 - r_1 r_2} \left[\frac{e^{2i\phi}}{1 - r_1 r_2 e^{i(\alpha - 2\omega_B \tau)}} + \frac{e^{-2i\phi}}{1 - r_1 r_2 e^{i(\alpha + 2\omega_B \tau)}} \right]. \tag{4.21}$$

The Jones matrix for the transmitted electric field is:

$$\mathbf{E}_{\text{out}} = \begin{pmatrix} E_{\text{out},1} \\ E_{\text{out},2} \end{pmatrix}$$

with $E_{\text{out},1}$ given by Eq. (4.16). Following the optical scheme of Chapter 2 we introduce the ellipticity modulator **H**, the analyser prism **A**, and the quarter wave plate **Q**, inserted before the ellipticity modulator for rotation measurements:

$$\mathbf{H} = \begin{pmatrix} 1 & i\eta \\ i\eta & 1 \end{pmatrix}, \qquad \mathbf{A} = \begin{pmatrix} 0 & 0 \\ 0 & 1 \end{pmatrix}, \qquad \mathbf{Q} = \frac{1}{\sqrt{2}} \begin{pmatrix} (1+i) & 0 \\ 0 & (1-i) \end{pmatrix}$$

where $\eta = \eta_0 \cos \omega_{\text{m}} t$. We treat now separately the cases of the ellipticity and rotation measurements.

Ellipticity measurements

The orthogonal electric field after the analyser **A** is:

$$E_2^{\text{ell}} = (\mathbf{A} \cdot \mathbf{H} \cdot \mathbf{E}_{\text{out}})_2 = i\eta E_{\text{out},1} + E_{\text{out},2}. \tag{4.22}$$

The intensity I_2^{ell} associated to E_2^{ell} is demodulated at the frequency of the ellipticity modulator ν_{m}. We consider only the term linear in the product $\eta_0\psi_0$. With $r_1r_2 = R$ and $t_1t_2 = T$, one has

$$\begin{aligned} I_{2\nu_B}^{\mathrm{ell}} &\approx 4I_0\eta_0\psi_0\sin2\phi\,\frac{1+R^2\left(1+\cos2\alpha+\cos4\omega_B\tau\right)-R\left(R^2+3\right)\cos\alpha\cos2\omega_B\tau}{\left[1+R^2-2R\cos(\alpha-2\omega_B\tau)\right]\left[1+R^2-2R\cos(\alpha+2\omega_B\tau)\right]}+ \\ &+ 4I_0\eta_0\psi_0\cos2\phi\,\frac{R^2\sin4\omega_B\tau-\left(R^3+R\right)\cos\alpha\sin2\omega_B\tau}{\left[1+R^2-2R\cos(\alpha-2\omega_B\tau)\right]\left[1+R^2-2R\cos(\alpha+2\omega_B\tau)\right]}. \end{aligned} \tag{4.23}$$

Substituting $2\omega_B$ with a generic signal angular frequency $2\pi\nu$, the phase of the ellipticity signal is

$$\Phi^{\mathrm{ell}} = \tan^{-1}\left[\frac{R^2\sin2\delta_\nu-\left(R^3+R\right)\cos\alpha\sin\delta_\nu}{1+R^2\left(1+\cos2\alpha+\cos2\delta_\nu\right)-R\left(R^2+3\right)\cos\alpha\cos\delta_\nu}\right] \tag{4.24}$$

where $\delta_\nu = 2\pi\nu\tau$. The amplitude of the ellipticity signal is:

$$|A^{\mathrm{ell}}| = I_0\sqrt{\frac{8\psi_0^2\left[2-4R\cos\alpha\cos\delta_\nu+R^2(1+\cos2\alpha)\right]}{\left[1+R^2-2R\cos(\alpha-\delta_\nu)\right]\left[1+R^2-2R\cos(\alpha+\delta_\nu)\right]}}. \tag{4.25}$$

Rotation measurements

To detect rotations, a quarter wave plate is inserted before the ellipticity modulator, thus transforming rotations into ellipticities. The orthogonal electric field after the analyser is:

$$E_2^{\mathrm{rot}} = (\mathbf{A}\cdot\mathbf{H}\cdot\mathbf{Q}\cdot\mathbf{E}_{\mathrm{out}})_2 = \frac{1+i}{\sqrt{2}}\eta E_{\mathrm{out},1}+\frac{1-i}{\sqrt{2}}E_{\mathrm{out},2}. \tag{4.26}$$

The linear term in the demodulated intensity is then

$$\begin{aligned} I_{2\nu_B}^{\mathrm{rot}} &\approx 4I_0\eta_0\psi_0\sin2\phi\left[\frac{R\sin\alpha\left[\left(1+R^2\right)\cos2\omega_B\tau-2R\cos\alpha\right]}{\left[1+R^2-2R\cos(\alpha-2\omega_B\tau)\right]\left[1+R^2-2R\cos(\alpha+2\omega_B\tau)\right]}\right] \\ &+ 4I_0\eta_0\psi_0\cos2\phi\left[\frac{R\sin\alpha(1+R)\sin2\omega_B\tau}{\left[1+R^2-2R\cos(\alpha-2\omega_B\tau)\right]\left[1+R^2-2R\cos(\alpha+\omega_B\tau)\right]}\right]. \end{aligned} \tag{4.27}$$

The phase of the rotation signal is

$$\Phi^{\mathrm{rot}} = \tan^{-1}\left[\frac{\left(1-R^2\right)\sin\delta_\nu}{(1+R^2)\cos\delta_\nu-2R\cos\alpha}\right] \tag{4.28}$$

and the amplitude of the rotation signal is:

$$|A^{\rm rot}| = I_0\sqrt{\frac{16\psi_0^2R^2\sin^2\alpha}{[1+R^2-2R\cos(\alpha-\delta_\nu)]\,[1+R^2-2R\cos(\alpha+\delta_\nu)]}}. \tag{4.29}$$

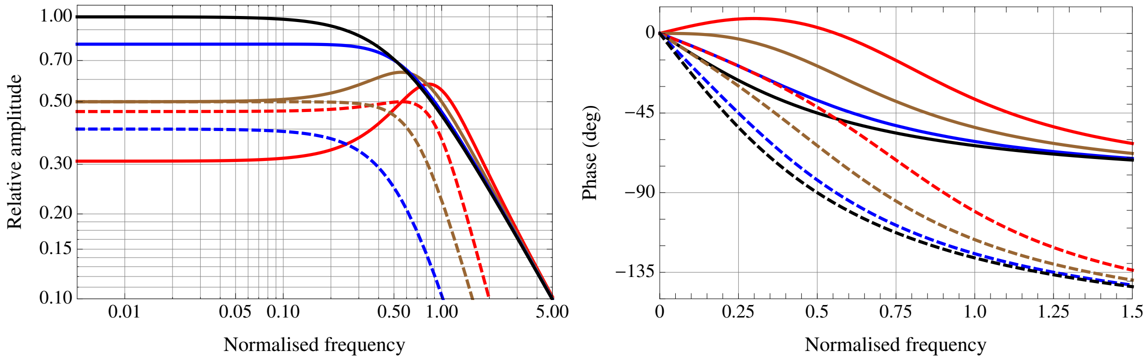

Figure 4.7: Left: Calculated frequency response of the amplitude of the ellipticity (continuous curves) and of the rotation (dashed curves) generated by magnetic birefringence in gas in the PVLAS polarimeter, for $\mathscr{F} = 662\times10^3$. The frequency scale is expressed in units of the cavity line-width ν_c; the vertical scale is normalised to the low-frequency amplitude of the $R_0 = 0$ filter [Eq. (4.30)]. The ellipticity curves are drawn for the values of the low-frequency ratio of rotation to ellipticity [Eq. (4.11)] $R_0 = 0$ (black), 0.5 (blue), 1.0 (brown) and 1.5 (red); the rotation curves have $R_0 = 0.5$, 1.0 and 1.5. Right: Calculated frequency response of the phase of the ellipticity (continuous curves) and of the rotation (dashed curves), drawn for the values of $R_0 = 0$, 0.5, 1.0 and 1.5. The curves have been arbitrarily chosen to start at zero phase and have negative trend.

In Figure 4.7 the amplitude and phase of the equations (4.24), (4.25), (4.29) and (4.28) for several values of the parameter R_0 of Eq. (4.11) are shown.

In the limit $\alpha\to0$, the phase and amplitude of the ellipticity become:

$$\begin{aligned}\lim_{\alpha\to0}\Phi^{\rm ell} &= \tan^{-1}\left[\frac{R\sin\delta_\nu}{1-R\cos\delta_\nu}\right] \equiv \Phi_{\rm I}(\nu)\\ \lim_{\alpha\to0}A^{\rm ell} &\sim \sqrt{\frac{1}{1+R^2-2R\cos\delta_\nu}} \equiv H_{\rm I}(\nu).\end{aligned} \tag{4.30}$$

Phase and amplitude of the ellipticity have thus the same frequency dependence as the transmitted electric field derived in Chapter 2: the ellipicity is subject to a first order filter. On the contrary, the rotation amplitude disappears for $\alpha = 0$ (no rotation is generated in a non birefringent cavity). Nevertheless, in the same limit, the phase of the rotation $\Phi^{\rm rot}$ reduces to the phase of a second order filter. We remind that the frequency response of a second order filter is

$$H_{\mathrm{II}} = H_{\mathrm{I}}^2 \qquad \text{and} \qquad \Phi_{\mathrm{II}} = 2\Phi_{\mathrm{I}}. \tag{4.31}$$

In the limit $\nu \to 0$ the static case of the previous section is found:

$$\lim_{\delta_\nu \to 0} \Phi^{\mathrm{ell}} = 0 \tag{4.32}$$

$$\lim_{\delta_\nu \to 0} |A^{\mathrm{ell}}| = 4I_0\eta_0\psi_0 \frac{1 - R\cos\alpha}{1 - 2R\cos\alpha + R^2} \approx 2I_0 k(\alpha) N \psi_0 \tag{4.33}$$

where the last passage holds for small α. For the rotation signal we have:

$$\begin{aligned} \lim_{\delta_\nu \to 0} \Phi^{\mathrm{rot}} &= 0 \\ \lim_{\delta_\nu \to 0} |A^{\mathrm{rot}}| &= 4I_0\eta_0\psi_0 \frac{R\sin\alpha}{1 - 2R\cos\alpha + R^2} \approx I_0 k(\alpha) N^2 \psi_0 \alpha. \end{aligned} \tag{4.34}$$

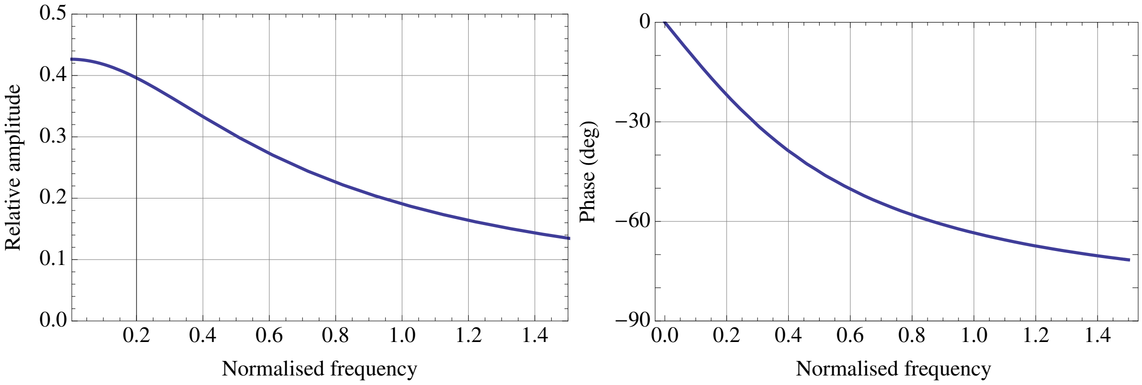

Figure 4.8: Left: ratio of rotation and ellipticity in a dynamic FP. The frequency is expressed in units of the cavity line-width $\nu_c = \nu_{\mathrm{fsr}}/\mathscr{F}$ for $\mathscr{F} = 660 \times 10^3$ and a value of $\alpha = 2 \times 10^{-6}$ rad. Right: phase difference between the signals of rotation and ellipticity.

Also the ratio R_0 of rotation and ellipticity [see Eq. (4.11)] is now a function of frequency:

$$\frac{|A^{\mathrm{rot}}|}{|A^{\mathrm{ell}}|} = \sqrt{\frac{2R^2\sin^2\alpha}{2 + R^2\cos 2\alpha + R^2 - 4R\cos\alpha\cos\delta_\nu}}. \tag{4.35}$$

A plot of the frequency dependence of R_0 is shown in Fig. 4.8 for the cavity of the PVLAS experiment. The static value holds only up to ∼ 5 Hz ($\nu_B = 2.5$ Hz). At higher frequency the ratio is filtered as a first order filter.

This mathematics was developed for the case of a pure birefringence, but equally well applies to the case of a pure dichroism. The formulas are easily obtained from the ones already shown with the substitution of ψ_0 with θ_0 and of the exchange of the superscripts "ell" and "rot":

$$|A^{\rm rot}| = I_0\sqrt{\frac{8\theta_0^2\,[2-4R\cos\alpha\cos\delta_\nu+R^2(1+\cos 2\alpha)]}{[1+R^2-2R\cos(\alpha-\delta_\nu)]\,[1+R^2-2R\cos(\alpha+\delta_\nu)]}}, \qquad (4.36)$$

$$\Phi^{\rm rot} = \tan^{-1}\left[\frac{R^2\sin 2\delta_\nu-\left(R^3+R\right)\cos\alpha\sin\delta_\nu}{1+R^2\left(1+\cos 2\alpha+\cos 2\delta_\nu\right)-R\left(R^2+3\right)\cos\alpha\cos\delta_\nu}\right], \qquad (4.37)$$

$$|A^{\rm ell}| = I_0\sqrt{\frac{16\theta_0^2R^2\sin^2\alpha}{[1+R^2-2R\cos(\alpha-\delta_\nu)]\,[1+R^2-2R\cos(\alpha+\delta_\nu)]}}, \qquad (4.38)$$

$$\Phi^{\rm ell} = \tan^{-1}\left[\frac{\left(1-R^2\right)\sin\delta_\nu}{(1+R^2)\cos\delta_\nu-2R\cos\alpha}\right]. \qquad (4.39)$$

4.2.2 Polarisation dynamics: experiment

We have confirmed the frequency dependences presented above with two different measurements. The first one is the Cotton-Mouton effect in 880 μbar of Ar gas, measured as a function of frequency between $\nu_B = 0.5$ Hz and $\nu_B = 23$ Hz with a measurement every 0.5 Hz. Each ellipticity and rotation point has been integrated for a time of 256 s. For this measurement, a single magnet was employed. The phase of the magnet was measured with respect to a trigger signal generated by a contrast sensor in correspondence of the passage of a mark drawn on the external surface of the rotating magnet. The response time of the sensor is < 50 μs; this leads to a maximum phase uncertainty $< 0.8^\circ$ at $2\nu_B = 46$ Hz.

As we are not aware of the existence of any magnetic dichroism in the optical range, we have used a solenoid coil to place a magnetic field on the reflecting surface of one of the cavity mirrors, thus generating a Faraday effect (FE) [93]. Since in this second experiment the vacuum vessel is kept in vacuum, no gas birefringence is generated and the above formulas apply. The effect appears at the first harmonic of the oscillating magnetic field and is linear in the magnitude of the magnetic field. In Fig. 4.9 a scheme of this measurement is shown; the two permanent magnets are not represented. The coil roughly aims at the center of the mirror, thus generating an alternating magnetic field on its surface, with a significant component orthogonal to the surface of the mirror. Precise values of the magnitude and of the orientation of the magnetic field at the position where the light beam impinges on the mirror are unknown, but on the other hand unnecessary. The position and the orientation of the coil has been chosen so as to maximise the observed effect.

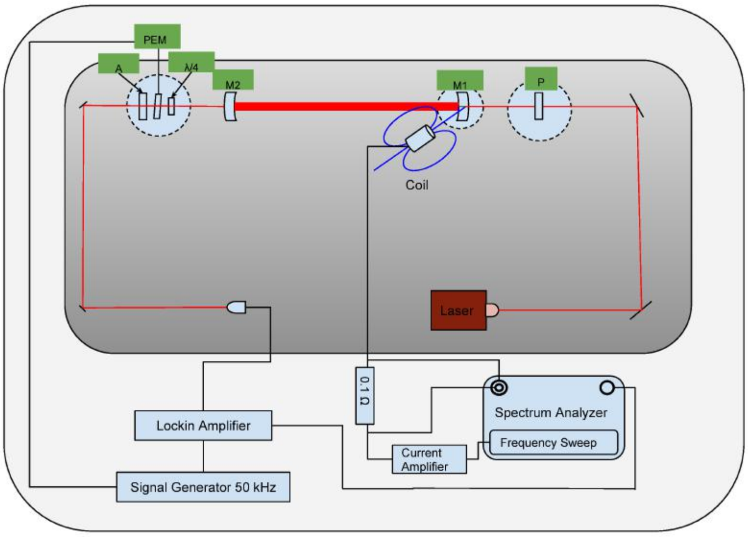

Figure 4.9: Scheme of the measurement of the frequency response due to the cavity of the Faraday effect. The coil is located outside the vacuum chamber hosting the M_1 mirror; the distance from the mouth of the coil to the mirror is about 15 cm. P is the polariser, A the analyser, PEM the photoelastic modulator and $\lambda/4$ the quarter wave plate.

Fig. 4.10 shows the scheme of the solenoid employed and the measured field generated along its axis as a function of the distance z from the centre of the coil. The magnetic field along the axis z of a coil of length L_F and internal and external radii ρ_1 and ρ_2, with N_t turns of wire traversed by a current I [41]

$$B(z) = \frac{\mu_0}{2} \frac{N_t I}{L_F(\rho_2 - \rho_1)} \left[|z^+| \ln \left(\frac{\sqrt{1+x_1^2} - x_1}{\sqrt{1+x_2^2} - x_2} \right) + |z^-| \ln \left(\frac{\sqrt{1+y_1^2} - y_1}{\sqrt{1+y_2^2} - y_2} \right) \right] \tag{4.40}$$

is superimposed to the experimental data for comparison, where

$$z^{+,-} = L_F \pm z, \qquad x_{1,2} = \rho_{1,2}/z^+ \qquad \text{and} \qquad y_{1,2} = \rho_{1,2}/z^- .$$

The solenoid was traversed by an alternating current with amplitude $I \sim 1$ A at an adjustable frequency ν_F. With such a current, the coil produces a magnetic field ≈ 1 G at a distance of 15 cm from the mouth of the coil (distance to the mirror).

To perform the Faraday effect measurements, the Frequency Response function of an Agilent 35670A Dynamic Signal Analyzer has been employed. The voltage signal from a small resistance in series with the solenoid has been used as a phase reference and to normalise the amplitude of the observed rotation. We explored the frequency range from

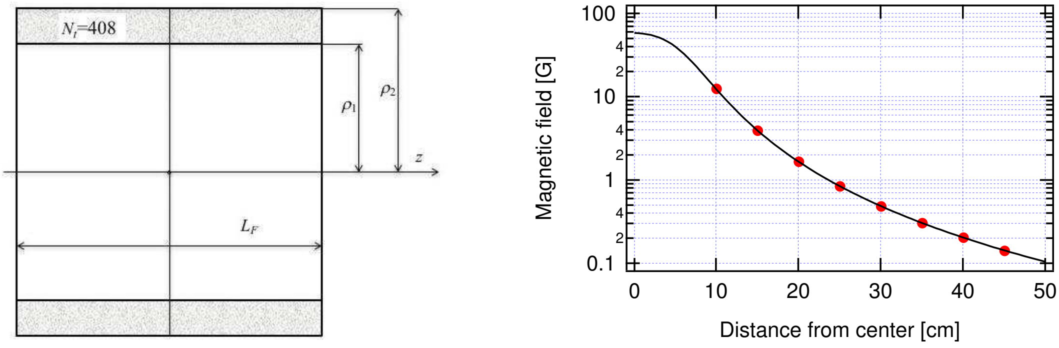

Figure 4.10: Left: Scheme of the solenoid used in the tests, $L_F = 112$ mm, $\rho_1 = 47$ mm and $\rho_2 = 60$ mm. The coil has $N_t = 408$ turns. Right: magnetic field on the axis of the solenoid traversed by a current $I = 1$ A. Red dots represent the experimental points.

0 to 50 Hz with 400 frequency bins and a sweep time of 8 s. For the rotation signal, the integration time was ≈ 2 hours, which corresponds to an integration time of 18 s per bin. The ellipticity signal, which was approximately three times smaller, was integrated for a total time of ≈ 5.5 hours, corresponding to an integration time of 50 s per bin.

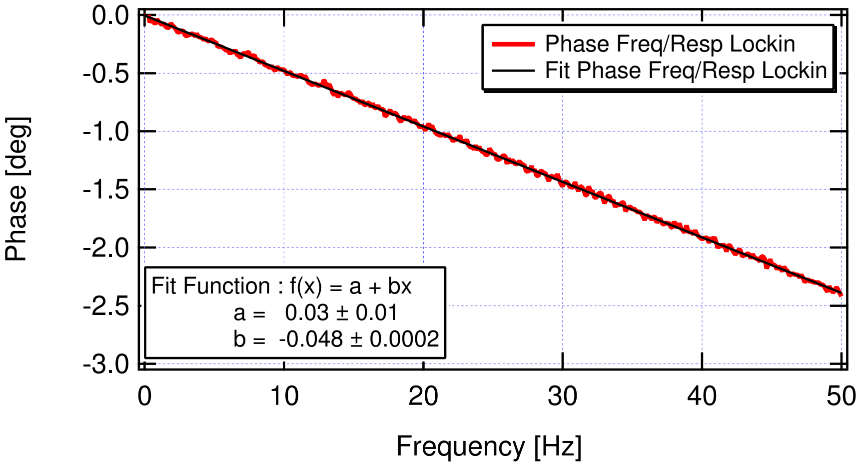

Figure 4.11: Phase of the signal from the lock-in amplifier SRS830 demodulating at $\nu_{\mathrm{m}} = 50$ kHz the extinguished intensity, measured as a function of the frequency. The lock-in had a time constant of 30 μs and a sensitivity of 50 mV.

A small correction (see Fig. 4.11) has been subtracted from the measured phase of both the Cotton-Mouton effect and the Faraday effect, due to the frequency response of the lock-in amplifier used to demodulate the signal from the diode PDE collecting the extinguished intensity. This frequency response as been obtained by demodulating an amplitude modulated signal at $\nu = 50$ kHz. The frequency response of the current amplifier Femto DLPCA-200 that follows the diode PDE was instead neglected. In fact, given its nominal 200 kHz bandwidth, one expects that, in a 100 Hz band around 50 kHz, the amplitude should be constant and the phase should change by less than 0.1° (first order filter).

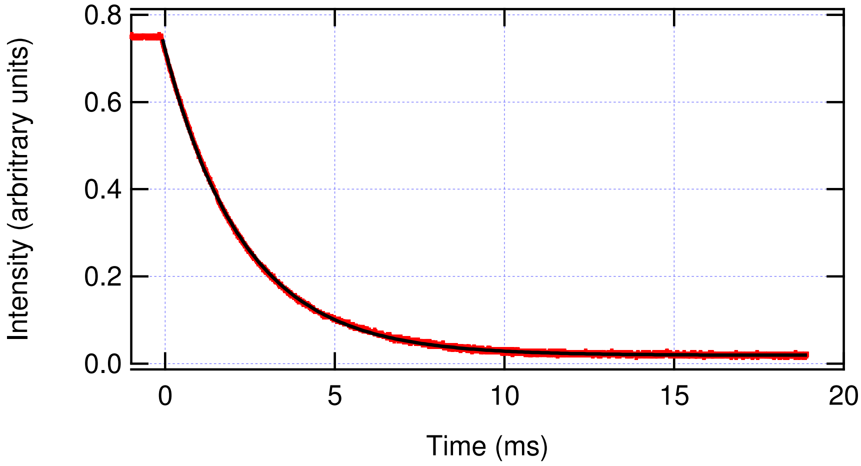

Figure 4.12: Decay of the intensity I_1 transmitted by the Fabry-Perot cavity after having switched off the system that locks the frequency of the laser to the cavity. The experimental curve is fitted with an exponential function $Ae^{-t/\tau_I}+C$ with $\tau_I = 2.32$ ms, corresponding to a finesse $\mathscr{F} = 662\times10^3$.

During the Cotton-Mouton and the Faraday measurements, the finesse of the cavity has been measured by observing the decay of the intensity I_1 recorded by photodiode PDT. No difference was found between the measurements taken with and without gas in the cavity. A typical datum is shown in Fig. 4.12, fitted with an exponential function. From the fit we obtain the decay time τ_I and the corresponding finesse $\mathscr{F}$ as

$$\tau_I = (2.32\pm0.02)\ \text{ms} \qquad \text{and} \qquad \mathscr{F} = (662\pm6)\times10^3.$$

Cotton-Mouton measurements

The data of the frequency response of the CME are presented in Fig. 4.13. A constant phase, measuring the zero-frequency relative position of the signals and the trigger, has been subtracted from the phase data, so as to have both curves starting at zero phase. The data are fitted simultaneously with the four functions given in Eqs. (4.24), (4.25), (4.29) and (4.28), and the values of the reflectance R (and hence the finesse $\mathscr{F}$ of the mirrors) and the phase difference α of their equivalent wave-plate have been obtained:

$$\mathscr{F} = (640\pm4)\times10^3 \qquad \text{and} \qquad \alpha = (1.78\pm0.01)\ \mu\text{rad}.$$

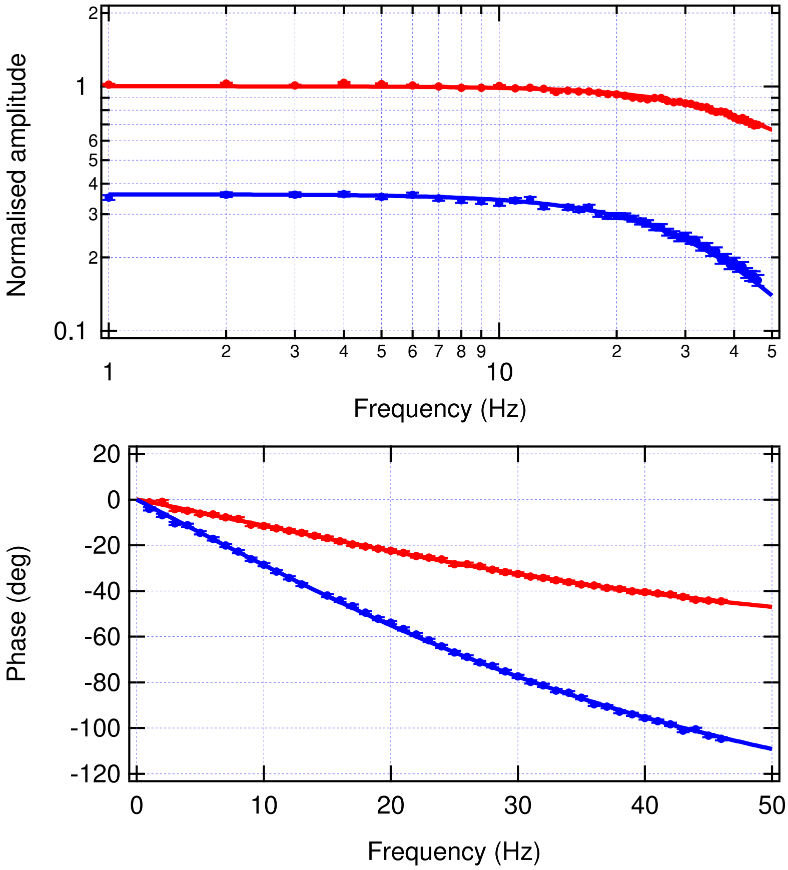

Figure 4.13: Measured frequency response of the CME of 880 μbar of Ar gas, as a function of the frequency. Top: amplitude of the ellipticity (upper curve) and the rotation (lower curve) signals. Bottom: phase of the ellipticity (upper curve) and the rotation (lower curve) signals. The amplitude and phase data are simultaneously fitted with Eqs. (4.24), (4.25), (4.29) and (4.28). The values of the finesse $\mathscr{F}$ and the phase difference α are obtained as $\mathscr{F} = 640 \times 10^3$ and $\alpha = 1.78$ μrad.

with a normalised $\chi^2_{\text{o.d.f.}} = 181/174$. The value of the finesse is 4% smaller than the one obtained recording the decay of the intensity (see Fig. 4.12). The uncertainties used in the fit are the piecewise standard deviations of the residuals obtained by fitting the four curves separately. In a first tentative of a global fit, the residuals of the phase data exhibited a marked linear behaviour of a few degrees over the whole frequency interval. This behaviour can be attributed to the fact that, during the measurements, the polarisation direction of the light entering the Fabry-Perot cavity is varied by small quantities to compensate for the slow drift of the static birefringence of the cavity. We have then added two linear functions to the two phase fit functions. The values of the slopes obtained through the fit are $(0.1^\circ \pm 0.01^\circ)$ Hz^{-1} for the phase of the ellipticity, and $(0.05^\circ \pm 0.01^\circ)$ Hz^{-1} for the phase of the rotation. Note that the duration of the ellipticity and rotation measurements were, respectively, eight hours and four hours, leading to an identical drift of 160 μdeg/s in the two measurements. This strongly supports the suggested interpretation. It is worth noting that the value of α is small enough that fitting simultaneously the four data sets with the expressions of the first and second order filters (4.30) and (4.31) still produces a reasonable fit, with a similar χ^2 probability, but at the expenses of an unreasonable 20% reduction of the value of $\mathscr{F}$ and of completely incompatible drifts of the ellipticity and rotation phases.

Faraday effect measurements

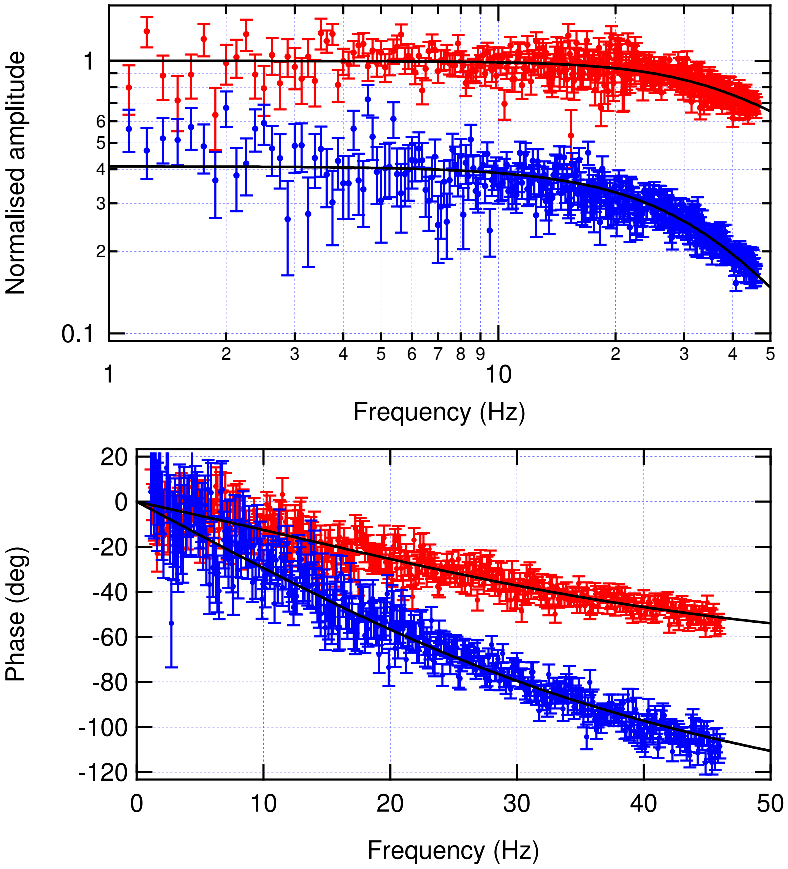

Figure 4.14: Top panel: relative amplitude of the rotation signal (upper curve) and of the ellipticity signal (lower curve) measured as a function of frequency for the Faraday effect on the reflecting surface of a mirror of the FP cavity. Bottom panel: phases of the rotation signal (upper curve) and of the ellipticity signal (lower curve). The continuous lines are the global fit obtained with Eqs. (4.36), (4.37), (4.38) and (4.39).

The data of the frequency response of the Faraday effect are shown in Fig. 4.14. A constant phase, measuring the zero-frequency relative position of the signals and the trigger, has been subtracted from the phase data, so as to have both curves starting at zero phase. The data are fitted simultaneously with the four fit functions (4.36), (4.24), (4.38) and (4.39). The fit gives a unique value for the mirror reflectance R and the phase delay α:

$$\mathscr{F} = (691 \pm 0.08) \times 10^3 \qquad \text{and} \qquad \alpha = (1.87 \pm 0.02)\ \mu\text{rad}$$

with a normalised $\chi^2_{\text{o.d.f.}} = 1472/1434$. The value obtained for the finesse is about 4% larger than the value obtained from the analysis of the decay of the transmitted intensity (see Fig. 4.12). The value of α is 5% larger than the one found in the Cotton-Mouton experiment. This small difference could be accounted for by the fact that the two data sets were taken in different days and that we know that α is subject to small drifts. As in the case of the Cotton-Mouton measurement, the uncertainties used in the fit are the piecewise standard deviations of the residuals obtained by fitting the four curves separately. Differently from the Cotton-Mouton case, no linear addition to the phase fit function was necessary. This is consistent with the interpretation of the feature observed in the Cotton-Mouton effect: in fact, in the case of the Faraday measurements, the phase is electronically defined. By fitting the four curves with the expressions of the first and second order filters (4.30) and (4.31) we obtained $\mathscr{F} = 594 \times 10^3$, with a χ^2 probability of 5×10^{-3}, justifying the necessity of introducing the parameter α.

4.3 Spurious signals

This section concerns the spurious ellipticity signals at several harmonics of the rotation frequency of the magnets that were plaguing the PVLAS experiment during the first period after installation and that showed up already after a few thousands seconds of integration. Spurious signals in ellipticity and rotation have been observed in all the past experimental PVLAS setups since the Legnaro one, with similar characteristics of apparent randomness as in the present apparatus. Their sources were not identified. We have explored several possible phenomena from which spurious signals could originate, dealing with one hypothesis at a time. As mentioned before, one of the main strengths of the experiment is the possibility of obtaining the Fourier transform of very long data runs; disturbances not exactly at $2\nu_B$, for example due to a beat, are likely to show up in a nearby but different bin. Nevertheless, mechanical disturbances have broad frequency responses, thus bypassing the exceptional resolution. In the following we discuss some of the possible causes of spurious peaks, and describe the tests done, the successes and the questions still open.

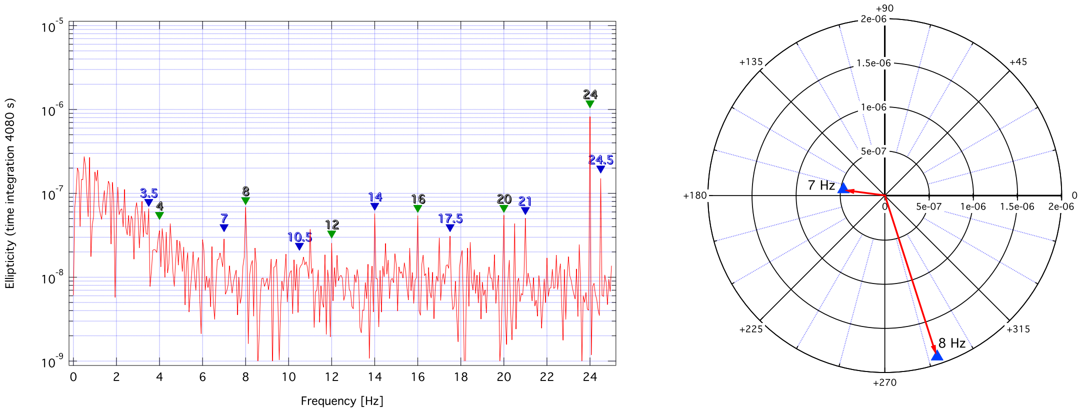

Figure 4.15: Left: Fourier transform of the ellipticity in vacuum, integrated for a time of 4080 s. The magnets rotate at frequencies $\nu_{B\alpha} = 3.5$ Hz and $\nu_{B\beta} = 4$ Hz. Several harmonics of the rotating magnets are observed. Right: Polar plot showing the components $2\nu_{B\alpha}$ and $2\nu_{B\beta}$.

4.3.1 Spurious signals: residual gases

In the presence of a rotating magnetic field, residual gases generate in the Fourier ellipticity spectrum a signal at the second harmonic of the rotation frequency with a well defined amplitude and phase. Indeed we use the CME to calibrate the apparatus by introducing a controlled amount of a pure gas in the vacuum vessel. The amplitude and phase of the CM signal can be predicted by knowing the partial pressures of the residual gas composition. By monitoring the residual pressure, one can be sure to be in a situation in which the CM signal from the residual gas species is much smaller than the signal expected from the magnetic birefringence of vacuum. In the current condition, no observed signal could be attributed to an effect of the residual gas.

As already said before (see the calibration section in Chap. 3), a general method to identify a signal in the PVLAS apparatus as due to a true magnetic birefringence effect is to compare the signals obtained by running the two magnets at two different frequencies: true birefringence signals should have, after correction for the dynamical response of the Fabry-Perot, the same amplitude and phase; moreover, each phase should coincide with the "zero frequency" phase determined in the CM calibration measurements with gases.

Figure 4.15 shows a typical spectrum featuring spurious signals. The rotation frequencies of the two magnets were $\nu_{B\alpha} = 3.5$ Hz and $\nu_{B\beta} = 4$ Hz and peaks appeared at several harmonic frequencies. The amplitudes and phases at the second harmonics of the two magnets are different from each other and the phases do not correspond to signals observed in the CM calibration with gases. These spurious signals cannot be attributed to the residual gas in the vacuum system.

4.3.2 Aliases and ground loops

As a second point, we checked that the observed signals were real and not generated by ground loops in the electric circuits or by aliases in the acquisition boards. The rotation frequency of the magnets enters explicitly in the electronic chain only through the signals from the two magnetometers that pick-up the stray field of the magnets and that we use to track the phase of the rotation. As these instruments are not essential, the polarimeter was run without them, essentially with no modification in the spurious peaks.

The coincidence of the observed signals in the spectra recorded by independent systems such as the signal analysers and the acquisition board, excludes the possibility that they might be due to some sort of alias generated inside the acquisition boards. Since we plan to acquire data for long times with the two magnets running at different frequencies, the acquisition system has a limited number of optimal configurations, but it enjoys of maximum flexibility in the case of short tests. None of the different configurations employed has ever had effect on spurious peaks.

Finally, an extensive series of test has been performed modifying the ground connection of several instruments, in particular of the circuit which locks the laser frequency to the resonance frequency of the cavity. In fact, if the spurious signal would enter this device and modulate the laser frequency, this would be equivalent to a modulation of the phase δ of the FP cavity. Modulation of δ generates ellipticity and rotation signals, most likely with all the harmonics. This tests brought us to modify a few of the ground connections of the electronics. However, a complete separation of the various sections of the electronics has never been necessary.

4.3.3 Stray fields and pick-ups

Another possible origin for spurious signals could be the stray field of the rotating magnets. The magnetic stray field is $\lesssim 1$ G along the magnet axis at a distance ≈ 40 cm outside the magnet extremity, which is about the distance of the magnets from the mirrors. The oscillating stray fields could also act on some piece of optics, thus modulating directly the light, or could be picked-up by one or more electric circuits. From there, the signal could end up in the ellipticity signal directly, or via ground loops, or by means of some other mechanism. Notice, however, that harmful spurious signals which may be confused with an ellipticity signal are only at the second harmonic of the frequency of oscillation of the magnetic field.

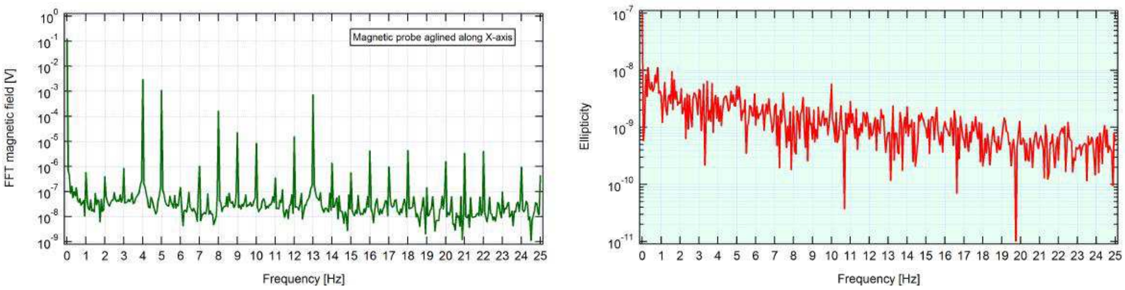

Figure 4.16: Left: Fourier Transform of the magnetic field at the position of the laser. The rotation frequencies of the two magnets, 4 Hz and 5 Hz, are visible together with the oscillation frequency of the current in the Faraday coil at 13 Hz. Note that the stray fields of the rotating magnets also have second and third harmonics. A small non linearity of the magnetic field sensor causes a slight mixing. Right: Corresponding ellipticity spectrum in vacuum showing only the spurious signal at $2\nu_{B\beta}$.

In a first series of tests we tried to identify possible targets of the stray field. To this end the coil of Fig. 4.10 was employed to place a magnetic field on the various components of the experiment. The coil was positioned in proximity of a piece of optics (first suspect the laser itself) or of an electronic instrument, and peaks at the frequencies ν_F and $2\nu_F$ were searched for in the ellipticity spectrum. The integration time of the spectra was such that the integrated noise value at $2\nu_F$ was less than the observed height of the spurious peak under study. In Fig. 4.16 we show the result of one of the tests performed. In this case, the laser was investigated. The left graph is the Fourier spectrum of the magnetic field at the position of the laser. In the spectrum, the rotating frequencies of the two magnets $\nu_{B\alpha} = 4$ Hz and $\nu_{B\beta} = 5$ Hz can be seen together with the oscillation frequency of the current in the solenoid $\nu_F = 13$ Hz. Note that the stray fields of the rotating magnets also have second and third harmonics. A small non linearity of the magnetic field sensor causes a slight mixing.The Faraday coil was positioned right by the laser. The sensor head of the magnetometer was aligned in the horizontal direction transverse with respect to the light path; quite similar spectra have been recorded for the other two directions of the sensor. The corresponding ellipticity spectrum shows a single peak at 10 Hz $= 2\nu_{B\beta}$, allowing to exclude a direct sensitivity of the laser to magnetic fields.

The search has given a negative result for all the elements investigated except when the solenoid aimed at the mirrors of the cavity. This, however, is nothing new for the PVLAS set-up, since in the ellipticity spectra we have always observed small rotation and ellipticity signals at the frequency ν_B (see Fig. 4.17). We explain them as due to a Faraday effect on the

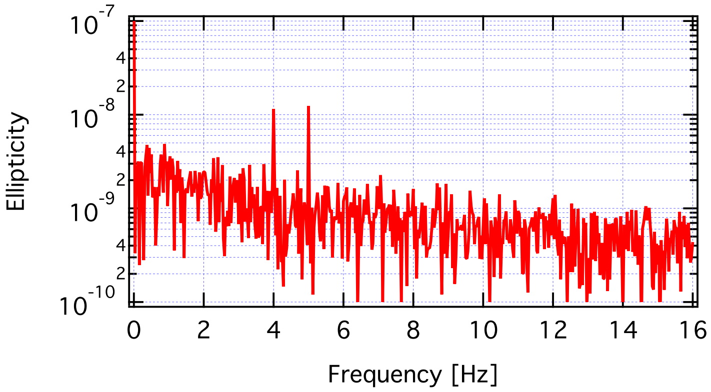

Figure 4.17: Ellipticity and rotation spectra showing peaks at $\nu_{B\alpha} = 5$ Hz and at $\nu_{B\beta} = 4$ Hz. Integration time $T \approx 9 \times 10^5$ s.

dielectric layers of the mirrors producing a rotation that the birefringent cavity transforms into ellipticity. To generate a Faraday effect inside the dielectric layers of the mirrors, the stray field must have a small longitudinal component. Moreover, since the magnetic field is rotating with the magnet, one needs that the rotation axis does not coincide with the beam. However, it is not difficult to imagine that all these conditions are met; one can also suppose that the magnetic field inside the mirror vacuum chambers might be somewhat distorted. Let us try an order of magnitude estimation for the observed rotation. The rotation signal should have an amplitude

$$\theta = NB\theta_0$$

where N is the amplification factor of the Fabry-Perot. The Verdet constants of the materials composing the dielectric layers of the mirrors was measured by Iacopini et al. in 1983 [93]; they found a value for the induced rotation per reflection of $\theta_0 = 0.37 \times 10^{-9}$ nrad/G. The estimated longitudinal component of the stray magnetic field at the position of the mirror is of the order of 2×10^{-4} G. This results in a calculated rotation of $\theta = 3 \times 10^{-8}$ rad. This value is in good agreement with the measured rotation shown in Fig. 4.17. Remember rotations are transformed into ellipticities with a conversion factor $R_0 \approx 0.3$.

4.3.4 Mechanical coupling and spurious signals

Mechanical noise from the rotating magnets

As another possible source of noise and spurious signals, we have investigated the mechanical vibrations transmitted by the rotating magnets to the optical components through the ground and the seismic isolation of the optical bench. The PVLAS experiment was designed with the

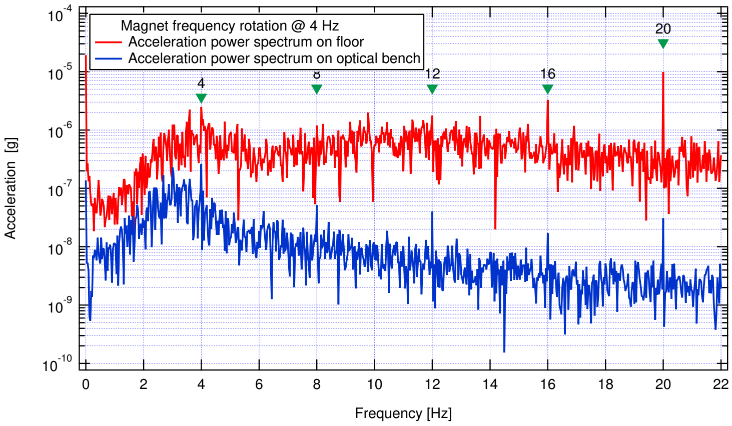

Figure 4.18: Vertical component of the acceleration on the floor and on the optical bench. Harmonics of the rotating magnet (4 Hz) are also present on the optical bench.

structure supporting the magnets separated from the optical bench, but both systems stand on the same concrete ground plate. The vibrations excited by a small unbalancing of the magnets are transmitted to the ground plate and filtered by the pneumatic air springs of the optical bench. This mechanism may play a significant role in the generation of the spurious peaks, in particular now that the rotation frequency of the magnets is being increased. In Fig. 4.18 we show the vertical component of the acceleration of the optical bench and of the ground, measured with the magnets rotating at 4 Hz. The magnets had been balanced in 2013, and I tried to improve the balancing, with the same method described in Chap. 3. The results were quite ambiguous: in the measured acceleration of the bench, the amplitude of the first harmonic of the magnet rotation decreased below the noise, while the second harmonic seemed not to be affected by the procedure.

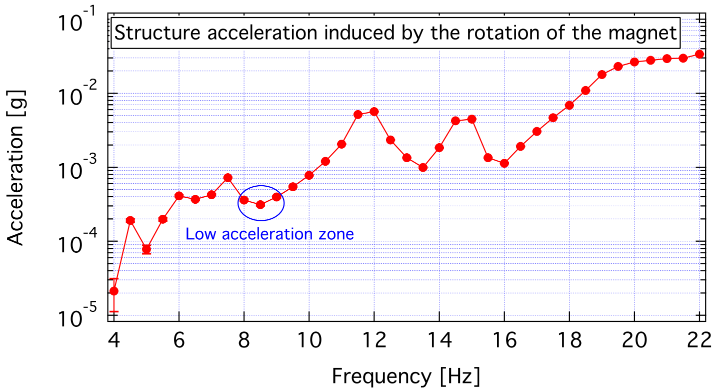

Figure 4.19: First harmonic of the horizontal component of the acceleration of the structure measured as a function of the rotation frequency of one of the magnets after balancing the magnets at 4 Hz.

We observed also the resonances of the structures supporting the magnets. In Fig. 4.19, we show the horizontal acceleration measured on one of the two structures as a function of the frequency of rotation of the magnets. It is evident that, as a general trend, the acceleration increases with frequency. As we will see in the next chapter, the measurements of the vacuum birefringence have been taken initially with the rotation frequency of the magnets ranging from 3 Hz to 5 Hz, and only in 2016 the frequency ν_B has been increased to 8 Hz to exploit the relative minimum of the noise around 16 Hz.

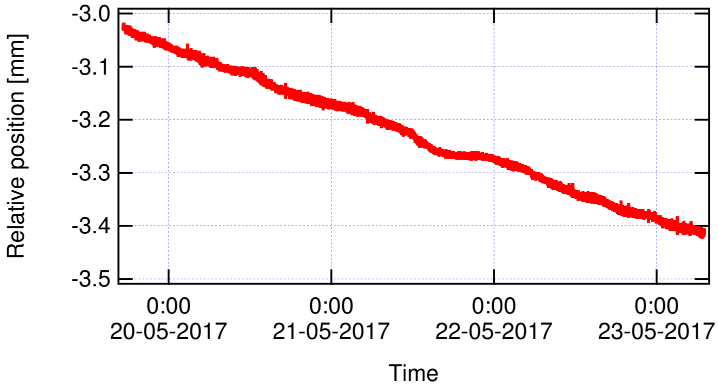

Figure 4.20: Position of the support structure of the magnets with respect to the optical bench as a function of time. The support structure is slowly drifting.

Quite recently, as a last attempt to reduce the mechanical noise associated with the rotation of the magnets, we have devised to lift the structures supporting the magnets on anti-vibration feet. This should reduce the vibrations transmitted to the ground. We have identified the FAEBI® Rubber Air Springs by Bilz as possible candidates. To do this operation, we had first to surmount a general problem concerning the mechanical stability of the structures: the centre of mass of each support structure is too high compared to the width of the structure to guarantee stability on the FAEBI springs. The solution we found to this problem has been to connect the two structures with two girders placed down near the floor. We obtained a single 1.6 ton structure which fullfills the stability requirements, and the structure has been lifted on four pneumatic feet. The new mechanical system is presently under study; preliminary measurements seem to indicate that the acceleration measured on the bench at the frequency of rotation of the magnets are significantly reduced, but not at $2\nu_B$. Another problem is the long stabilisation time that required by the pneumatic feet, causing drifts in the position of the structure (see Fig. 4.20). Air pressure should be controlled by a feedback.

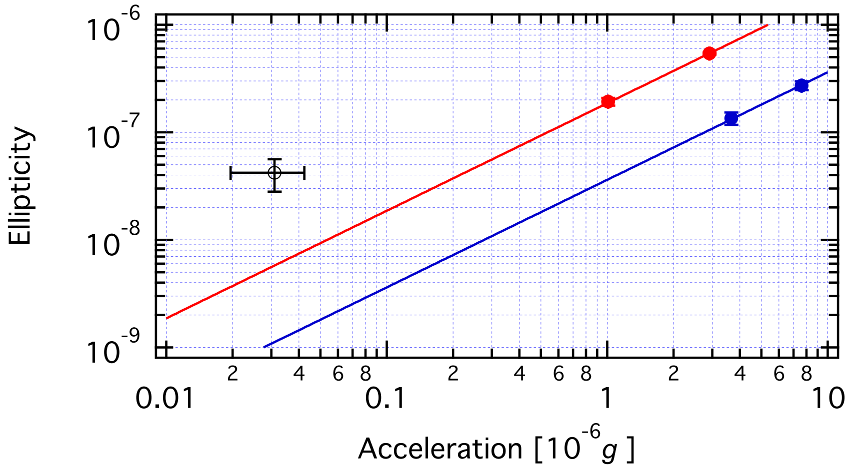

Figure 4.21: Ellipticity as a function of the acceleration of the optical bench due to the mass oscillation at 11 Hz and to the magnet rotation at $\nu_B = 4$ Hz. Points on the two linear curves are the 11 Hz components due to the parallel (top) and perpendicular (bottom) oscillation of the mass. The isolated point is the 8 Hz component.

Acceleration of the optical bench

Here we investigate the connection between the acceleration of the optical bench and the spurious ellipticity signals. For this study, we have placed a mass of 10 kg on a linear translator mounted horizontally on the optical bench. By substituting the fine thread screw with a piezoelectric ceramics, the mass could be put in oscillation at a chosen frequency in the directions parallel or orthogonal with respect to the light propagation in the FP cavity. While the mass was oscillating, we measured the acceleration of the optical bench in the direction of the oscillation and the spurious ellipticity signals at the frequency of oscillation. The observed ellipticity signals are linear in the acceleration, with a linearity coefficient $(3.6 \pm 0.3) \times 10^{-3}$ s^2/m for the direction perpendicular to the light path, and $(17.6 \pm 0.4) \times 10^{-3}$ s^2/m for the parallel direction as shown in Fig. 4.21. From the figure one can see that the 8 Hz spurious signal associated with the rotation of the magnet is at least one order of magnitude too intense to fit in the linear relations, suggesting the existence of a different mechanism of coupling between the rotation of the magnets and the ellipticity.

The oscillation of the 10 kg mass generates a modulation at the same frequency also in the correction signal of the feedback system locking the laser frequency to the cavity. This modulation indicates that there is a phase modulation of the electric field reflected by the cavity with respect to the incident beam. From equation (4.4), one can see that a modulation of the phase δ, with the laser locked to the cavity, is a direct modulation of the ellipticity.

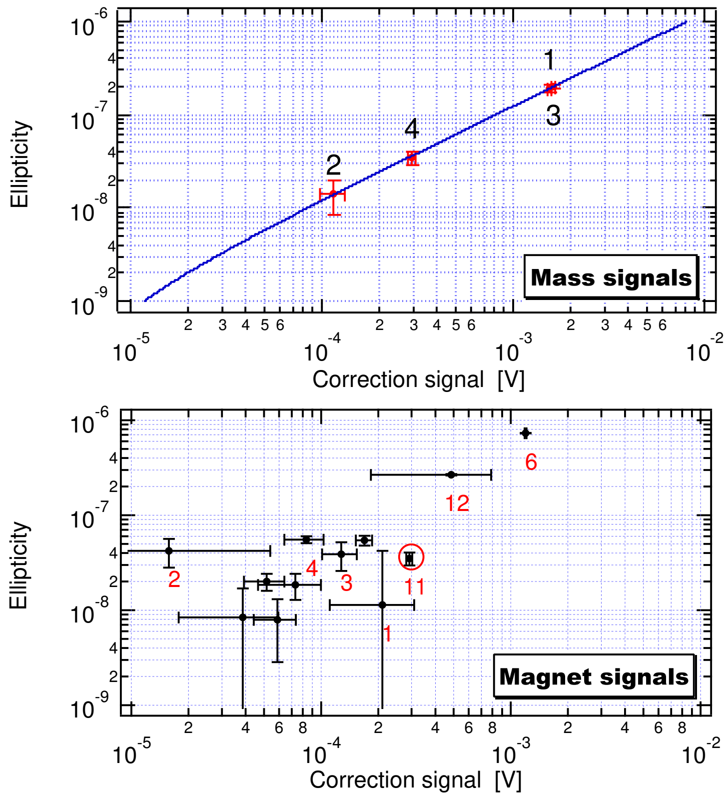

Figure 4.22: Correlations between the ellipticity and the correction signal. Integration time was 1600 s for the ellipticity and 160 s for the correction signal. Top graph: the experimental points are the amplitudes of the first four harmonics of the mass oscillation frequency (11 Hz). The numbers above each data point indicate the corresponding harmonic. The straight line is the best fit with slope 1.24×10^{-4}/V. Bottom graph: the experimental points are the amplitudes of the harmonics of the rotation frequency of the magnet (4 Hz). Note that the eleventh harmonic indicated by the red circle is common to the two graphs.

In Fig. 4.22 we show the correlation of the ellipticity and the correction signal of the feedback system locking the laser to the cavity. The measurement is taken while the mass oscillates at 11 Hz along the cavity direction and both magnets rotate at 4 Hz. The top panel plots the amplitude of the harmonics of the mass oscillation; the bottom panel plots the amplitude of the harmonics of the magnets rotation. While the correlation of the first graph is clear, the correlation shown in the second graph is fuzzy, again indicating that the two noise sources, the oscillating mass and the rotating magnets, have different mechanisms of coupling with the ellipticity.

4.3.5 Diffused light and spurious peaks

A real breakthrough with the spurious signals came when we started paying attention to diffused light. As seen from the centre of the mirror, the incidence angle on the inner surface of the glass tube ranges from $\geq 88^\circ$ to $\approx 89.8^\circ$. This corresponds to an average reflective power of the inner surface of the tube ranging from 0.82 to 1. Since diffused light is a source of noise in a Fabry-Perot cavity [94], its modulation might generate spurious signals. Diffused light is essentially unpolarised light that can traverse both the polariser and the analyser. Its intensity may be modulated if the tube vibrates synchronously with the rotation of the magnets. As a matter of fact, by monitoring the infrared radiation coming out laterally from the accessible portion of the glass tube just outside the magnets, we found an intensity modulation at harmonics of the rotating magnets. On the other hand, the ellipticity and rotation signals in the extinguished beam are extracted through a demodulation process that is insensitive, to first order, to intensity modulation. The same is true for the reflected beam and the error signal for the laser frequency-locking system. The diffused light could also be modulated in phase.

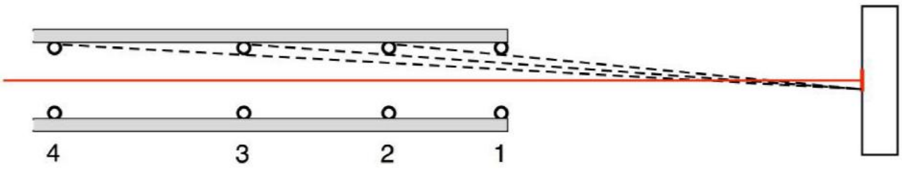

Figure 4.23: Positioning of the baffles inside the tube. The baffles prevent light from a blind spot on the mirror from reaching the tube.

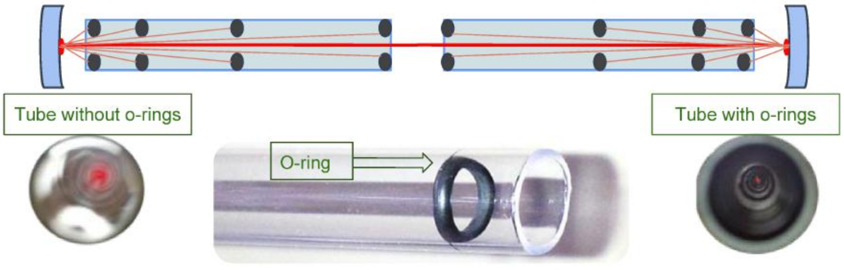

Figure 4.24: Above: schematic view of the baffles inserted inside the tubes. Below: looking through the tube before and after the insertion of the o-rings; a net attenuation of the diffused light is observed.

The first action we took was to place inside the tube (at that time a 12.5 mm internal diameter glass tube) a system of baffles to absorb the diffused light. The irises where Viton o-rings with external diameter equal to the internal diameter of the tube and chord thickness ~ 1 mm. The sequence of the positions of the o-rings inside the tube was such that the internal surface of the glass tube could not be seen from any position inside a round spot in the centre of the mirror (see Fig. 4.23). The first o-ring is placed just at the end of the tube near the mirror; the second o-ring intercepts the light that grazes the edge of the first o-ring coming from the periphery of the blind spot; the position of the third o-ring is further away, chosen with the same criterion, and so on. The improvement obtained can be appreciated already by looking through the tube with the naked eye (see figure 4.24). The diameter of the blind spot grows with the number of baffles, in principle allowing to screen the whole surface of the mirror; however, as the edges of the o-rings themselves are reflective in grazing incidence, we never used more than 20 o-rings per tube, with blind spot dimensions of the order of twice the waist of the laser light on the mirrors.

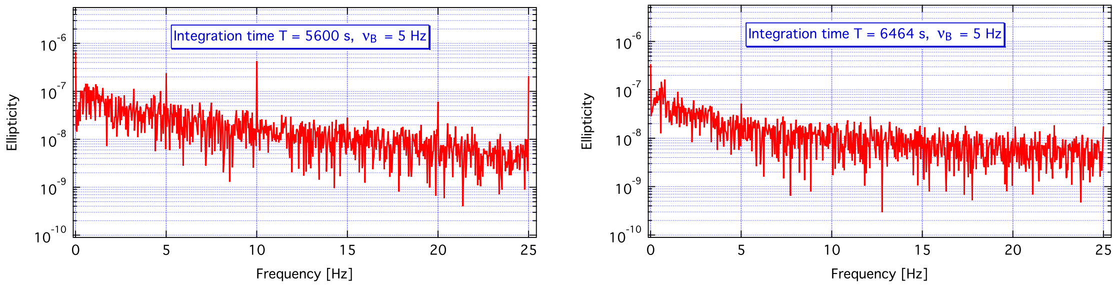

Figure 4.25: Left: ellipticity spectrum before the insertion of the o-rings inside the tubes; signals are observed at harmonics of the magnet rotation frequency $\nu_B = 5$ Hz. Right: ellipticity spectrum after installation of the baffles.

The effect of the installation of the o-rings was a sudden reduction of the spurious signals. The spectra reported in Fig. 4.25 prove this beyond any doubt: the signal at $2\nu_B$ disappears, being reduced by a factor at least 10. We note that the peak at ν_B, which is due to a Faraday effect on the mirrors, is reduced but does not disappear, unlike the other harmonics. The remedy we found to the problem of the spurious signals was quite effective, indicating that the spurious signals are actually generated by a modulation of the diffused light (amplitude or phase). The nature of this modulation is still unclear. In the next section we will show that the movement of the tube induces ellipticity signals, thus suggesting that the movement of the tube might modulate the diffused light.

4.3.6 Magnetic forces on the tube

Fig. 4.26 shows that the acceleration of the tube is correlated to the measured ellipticity. The acceleration is measured with a three-axes accelerometer fastened at the outer (namely, near

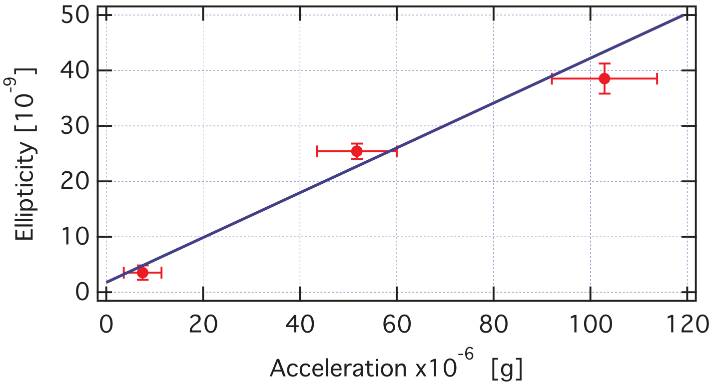

Figure 4.26: Correlation of measured ellipticity and tube acceleration. The spectra are obtained forcing the movement of the tube with a piezo at $\nu_{\mathrm{piezo}} = 7.5$ Hz. In the acceleration spectrum three harmonics were observed. The three points shown correspond to the harmonics at 7.5, 15.0 and 22.5 Hz.

the mirror) end of the tube. In the data presented here, a piezoelectric crystal is used to induce an oscillation of the (glass) tube in the horizontal direction with a nominal amplitude of 1 μm. The piezoelectric crystal applies a force between the optical bench and the tube (also supported by the optical bench); given the difference of masses, the results are interpreted here in terms of the movement of the tube (not the bench) with respect to the magnets (we point this out because we have seen that the oscillations of the bench play a role in generating spurious signals). We conclude that the movement of the tube generates spurious ellipticity signals.

Figure 4.27 shows one component of the acceleration of the tube compared to the position of the tube relative to the rotating magnet, recorded for a time of a few days during which the pneumatic positioning systems of the optical bench (top graph) or of the support structure of the magnets (bottom graph) were misbehaving. For the acceleration in the two plots, the amplitude of the second harmonic of the rotating magnet integrated for a time of 1024 s is reported. The two graphs bear the clear evidence of a correlation between acceleration and relative position of the tube with respect to the magnet.

The data presented in Fig. 4.28 refer to the same situation as the bottom graph of Fig. 4.27: the structure supporting the magnets had been lifted on new pneumatic support feet which were settling down after installation and were therefore drifting. The direction of drift was mainly in the vertical direction, with a displacement of 0.9 mm, but also in the transverse direction (~ 0.35 mm). In the figure the two components of the acceleration signal at $2\nu_B$ are shown on a polar plot. They both describe in the polar plane straight lines that do not intercept the origin.

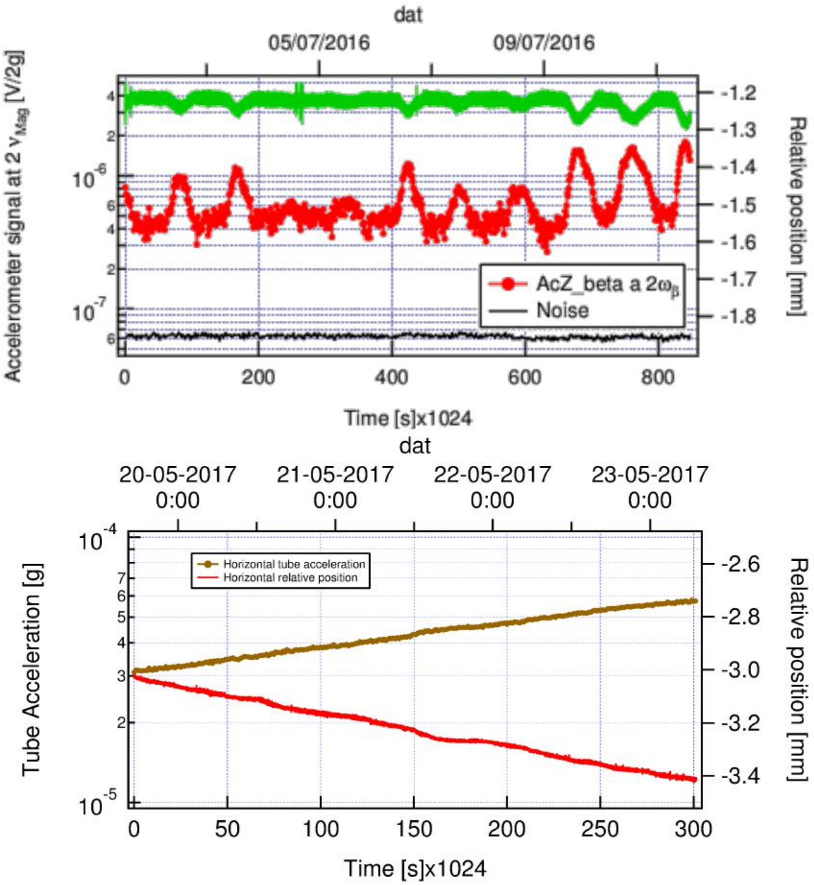

Figure 4.27: Both graphs represent the second harmonic of the acceleration of the tube (coordinate axis on the left) and the relative position of tube (right coordinate axis) with respect to the magnet, monitored for a few days. The position data in the bottom graph are those of Fig. 4.20.

The last two figures demonstrate a correlation between the position of the tube relative to the magnet and the acceleration measured on the tube. We explain these data with the existence of magnetic forces on the tube. Both the glass and the ceramic tubes are diamagnetic materials inserted in a magnetic field. The magnetic force on a magnetic body is given by

$$\vec{F} = \frac{1}{2\mu_0}\frac{\mu_r - 1}{\mu_r^2}\int \vec{\nabla} B^2 \, dV \tag{4.41}$$

where the integral extends over the volume of the body and the magnetic susceptibility $\chi = \mu_r - 1$ is in the present case small and negative ($\chi \sim -10^{-6}$). Due to the Halbach configuration, the magnetic field is relatively uniform in the center with small gradients on the edge of the bore. If the geometry of the magnets and the positioning of the tubes were

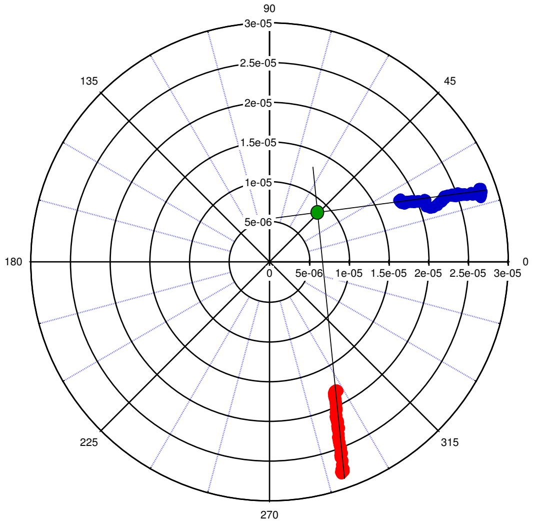

Figure 4.28: Polar plot of the tube acceleration at twice the frequency ν_B. The two acceleration components in a plane perpendicular to the tube are shown separately. During this measurement, lasted a few days, the relative position of magnet and tube was drifting in a straight line about 1 mm long.

ideal, the net force on the tube would be zero. The magnet, however, is made of several layers of magnetic materials, which produce the somewhat irregular field map reported in Fig. 3.9; moreover, the position of the tube coincides only approximately with the axis of the magnet. The asymmetry of the magnetic field with respect to the tube position results in a net transverse force on the tube. This force rotates with the magnet; since the force field described by Eq. (4.41) has rotational symmetry of order two, the principal Fourier component of the force appears at $2\nu_B$ as is experimentally observed.

In a first attempt to solve this problem, we tried to compensate for the diamagnetism of the glass by lining the tube with a paramagnetic material [95]. The operation proved to be too difficult, and we were led, as a tentative solution, to a fine positioning of the tube inside the magnet. To this end, I have designed and realised a fine *xy* positioning system for the two ends of each tube (see Fig. 4.29). On the inner side of the tubes, the position is defined by two 100-threads-per-inch screws. On the outer ends, NanoPZ$^{\text{TM}}$ piezoelectric actuators by Newport with minimum step-size of 30 nm are employed. Accelerations are measured with three-axes accelerometers fastened at the outer extremity of each tube. For each accelerometer, the signals of the two transverse axes are sent to two lock-in amplifiers referenced to the signal of the magnetometer. The lock-in amplifiers demodulate the acceleration at the second harmonic of the reference frequency; a long integration time of hundreds of seconds is employed to extract the average value of the acceleration at $2\nu_B$.

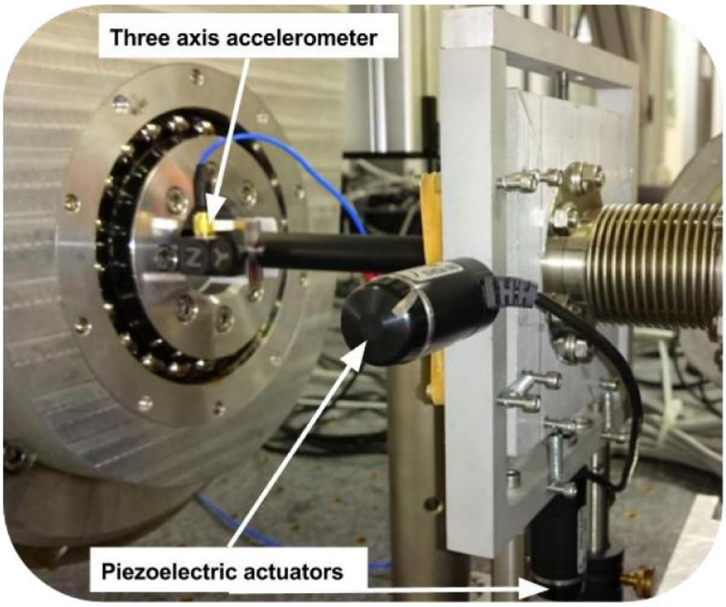

Figure 4.29: A picture of the outer end of one tube. The two piezoelectric actuators define the transverse position of the tube according to two orthogonal directions. In the figure, the accelerometer fastened to the tube is also shown.

From the above reported observations, considering that the ellipticity signal must be integrated for a very long time, we conclude that an automatic feedback system, finely positioning the tube in order to continuously minimise the acceleration components, is needed. Given the smallness of the acceleration signals, the system will require long integration time.

4.3.7 Conclusions on the topic of spurious signals

The origin of the spurious signals in the PVLAS experiment is far to be completely clarified. I would tentatively distinguish between the low frequency regime used until 2016 and the high frequencies that the experiment plans to employ in the future.

At low frequency, the spurious signals seem to be mainly generated by the diffused light, by means of the movement of the tube excited by the magnetic forces on the tube. The machinery deployed up to now, with the o-rings installed inside the tube and the fine positioning of the tube relative to the bore of the magnet, has guaranteed the possibility to integrate the ellipticity signal for several millions of seconds. The planned automatic positioning of the tube controlled by the $2\nu_B$ component of the magnetic force promises to further improve the situation.

A different argument applies to the high frequency range, where the mechanical noise originates from the rotation of the magnets and is transmitted to the structure supporting the magnets and at same time to the ground and the optical bench. As a matter of fact, at high frequency, the noise is still too high to allow for a measurement free from systematics. This topic has to be tackled in the near future.

4.4 Wide band noise

In this section we discuss the wide band noise of the experiment, or better the noise which is not in phase with the rotating magnets. The mechanism that produces wide band noise is still not completely understood. As seen in Chapter 2, the estimated intrinsic ellipticity wide band noise at frequencies around 10-20 Hz, considering the budget of all known noise contributions, is $8 \times 10^{-9}\ 1/\sqrt{\text{Hz}}$. On the contrary, the measured ellipticity noise during data acquisition is $4 \times 10^{-7}\ 1/\sqrt{\text{Hz}}$ @ 12 Hz and depends on frequency. The experimental evidence is about a factor ≈ 50 worse than the expected sensitivity.

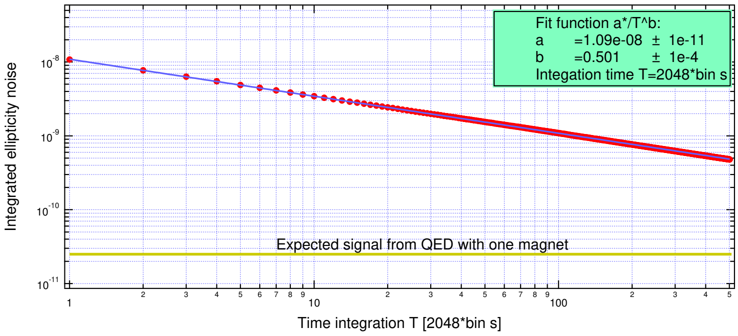

Figure 4.30: Integrated ellipticity noise as a function of integration time T at 10 Hz with one magnet in rotation at 5 Hz. The time separation between two consecutive points in the graph is 2048 s. The fit shows a decrease of the integrated noise as $1/\sqrt{T}$. The signal in ellipticity expected from the vacuum magnetic birefringence with one magnet in rotation is also shown.

One important feature of the PVLAS apparatus is the capability of integrating data for long periods with duty cycle almost 100%. The integrated noise in the PVLAS polarimeter decreases as function of time precisely as $1/\sqrt{T}$ as can be seen in figure Fig. 4.30, as expected for uncorrelated noise. As will be reported in Chapter 5, the total integration time of the PVLAS apparatus is a few millions of seconds and it is not thinkable to integrate 100 times longer to improve the present noise floor by another factor 10. Experience gained during these three years of PhD activity have shown that a reasonable integration time of about $T = 10^6$ s is a maximum, in practical terms, because longer integration times would make systematic studies and checks too time consuming.

4.4.1 Diffused light and wide band noise

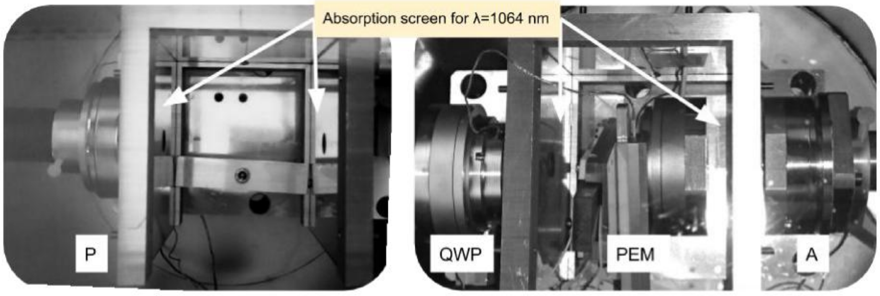

Figure 4.31: Left: input vacuum chamber C1 hosting the polariser (P); Right: output vacuum chamber C2 hosting the analyser (A), the photoelastic modulator (PEM) and the quarter wave plate (QWP). In the photographs, the frames supporting the absorbing screens can be seen.

After having understood the connection between spurious signals and diffused light in the cavity, we performed studies to search for an analogous connection between diffused light and wide band noise. The ellipticity data acquired after the implementation of the baffles in the cavity as described above and shown in Figure 4.25 excluded a change in sensitivity. Our attention was therefore moved to the other optical elements from which the light is scattered. A system of absorbing glass screens was installed in both the polariser chamber and the analyser chamber, as shown in Figure 4.31. The glass screens perpendicular to the beam direction have a small hole of 1 cm diameter to allow the passage of the laser beam. By observing with an infrared viewer the inside of the vacuum chambers before and after the installation of the absorbing glasses, one could clearly see that the amount of scattered light was greatly reduced. Unfortunately, the installation of the screens did not have any effect on the ellipticity noise.

In Figure 4.32 two photographs of the surface of the two mirrors taken with an infrared camera while the laser is locked to the cavity are shown. On the mirror surfaces, the diffused light allows one to see the Gaussian beam with a few more brilliant dots distributed around the main spots. These dots could be due either to dust or to local defects of the mirror surface. Hence we still had to exclude the diffused light generated in the vacuum chambers hosting the mirrors. Nevertheless, we decided not to put any screen in the chambers where the mirrors of the cavity are mounted, to avoid the exposition of the mirrors to air. As a matter of fact, in the last three years the vacuum chambers hosting the mirrors have never been opened. The experience gained with the tests described in this subsection brought us to consider not worth to risk the degradation of the mirror surfaces. Two different tests were performed instead: in

Figure 4.32: Infrared photographs of the reflecting surface of the mirrors with the laser locked to the cavity.

the first we increased the light diffused in the mirror chambers, while in the other we studied the diffused light exiting the system.

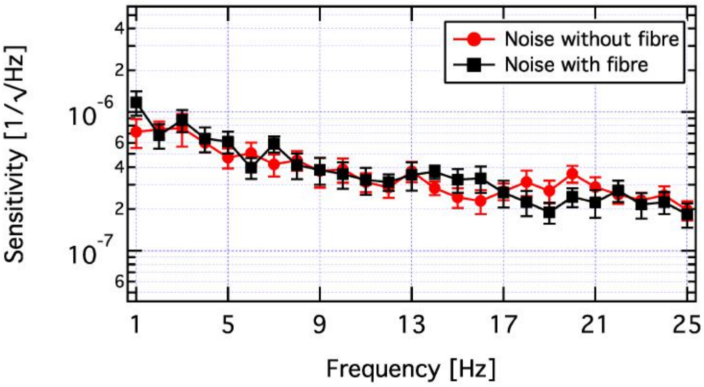

Figure 4.33: Ellipticity sensitivity with (black points) and without (red points) the extra scattered light in the M1 vacuum chamber. Each point in the two graphs is the average over 32 bins in a 1 Hz frequency interval. Integration time is $T = 10^3$ s.

To increase the scattered light in the mirror chambers, we collected with an optical fibre the light coming out of the Faraday isolator and injected it into the mirror chambers. Since the laser is locked to the cavity, this light has the correct frequency to resonate inside the cavity. The total power at the output of the fibre was 180 mW whereas the power at the input of the Fabry-Perot cavity was approximately 40 mW. In Figure 4.33 we show two measurements of the sensitivity in ellipticity as a function of frequency with and without the extra scattered light. No significant effect of the introduction of the diffused light can be seen in the graphs. We must mention that, with the diffused light in the mirror chambers, the static ellipticity showed marked but slow drifts which have remained unexplained. We have also introduced extra light in all the other vacuum chambers, again without any variation of the sensitivity. We conclude that the excess wide band noise present in the apparatus is not due to scattered light in the chambers.

What cannot be investigated directly is the diffused light having a direction very close to the propagation of the laser beam. To try to verify this contribution we made the following assumption: the diffused light exiting the cavity should diverge much more rapidly than the Gaussian laser beam exiting from the cavity. If this is true, we sought for changes in sensitivity moving the photodiodes away from the cavity. No change in the ellipticity sensitivity was observed.

Another way to seek for the same effect is to study the shape of the beam at the photodiode PDE in different conditions. One would expect that the presence of diffused light would change the beam profile at maximum extinction with respect to the beam profile slightly out of extinction. We therefore analysed the beam shape, along one direction, at different intensities of the extinguished beam. Firstly we examined the beam shape at maximum extinction without the PEM in the light path. Then we inserted the PEM and used it at various modulation depths to add controlled amounts of light to the extinction condition; from this study a reference beam profile was measured. The data without and with PEM were acquired keeping the polariser and analyser at maximum extinction.

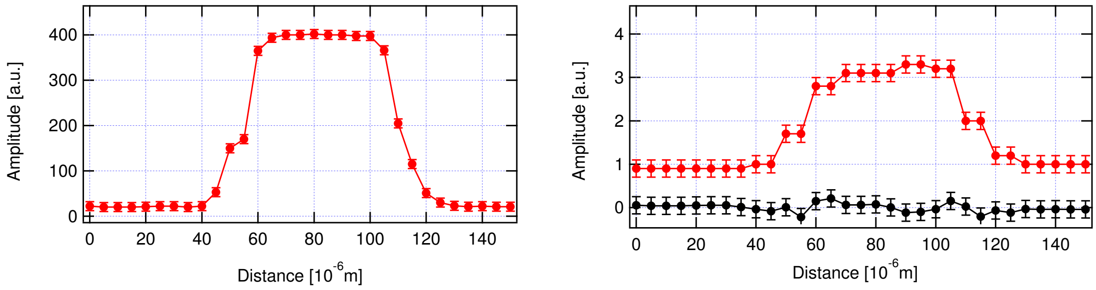

Figure 4.34: Intensity profiles of the extinguished beam scanned in the horizontal direction. Left: reference profile with the PEM turned on. Right in red: beam profile with the PEM out of the light path. Extinction ratio was $\sigma^2 = 5 \times 10^{-8}$. Right in black: difference between the extinction profile and the reference profile, having taken into account the relative amplitudes and having subtracted the background values.

Figure 4.34 shows the two profiles taken by translating sideways a plano convex lens with a focal length $f = 100$ mm focusing the beam on the sensitive surface of the photodiode PDE. The lens was moved in the horizontal direction in steps of 5 μm. The measured extinction of the beam was $\sigma^2 = 5 \times 10^{-8}$ and the corresponding profile is shown in red in the right panel of Figure 4.34. In the left panel of the same figure the profile of the beam with the

PEM turned on is reported; this is the reference profile. The curve shown in black in the right panel of Figure 4.34 is the difference of the two profiles, the one with the PEM on and the one obtained with the PEM off. To make the difference, the two amplitudes have been normalised after having subtracted the backgrounds. As can be seen, there is no significant deformation of the beam profile as would be expected from the hypothesis of diffused light travelling along with the Gaussian beam.

4.4.2 Ambient noise

Previous experiments showed a clear evidence that seismic insulation reduced the noise in ellipticity [79]. They concluded that a seismic isolation system supporting the optical bench was necessary to reduce noise and for stable laser locking. One could suppose that the residual mechanical noise present on the optical bench might be the source of the observed ellipticity noise. In fact, the mirrors have of a birefringence pattern and each surface point corresponds to a different phase delay [89]. Mechanical noise moves the mirror and therefore the beam spot scans different points on the surface of the mirror, possibly inducing a phase modulation in a wide frequency range. As already said in a previous section, one of the tests for the spurious peaks implied putting the whole optical bench in oscillation at various frequencies. In that experiment, a linear relation was found between the oscillation amplitude of the bench and the ellipticity. The same linear relation applied to the observed mechanical noise measured by an accelerometer mounted on the optical bench would imply a level of ellipticity noise much lower than the one observed. In fact, the observed acceleration noise density measured on the optical table is about $5 \times 10^{-7} g/\sqrt{\text{Hz}}$, corresponding to an ellipticity noise $8 \times 10^{-8}/\sqrt{\text{Hz}}$ or lower (see Fig. 4.21). We conclude that mechanical vibrations of the bench cannot account for the observed sensitivity of the polarimeter. What remains to be explored is the acoustic noise and the ventilation in the clean room. The air flow generates turbulences which affect the propagation of the laser. We performed a study of the influence of ambient noise on light intensity noise and on the noise in ellipticity.

A comparison of the amplitude noise of the incident beam with the air flow on and off was performed. We measured the relative intensity noise (RIN) of the beam in two points: 0.5 m from the laser and after a further distance of about 2 m. In Figure 4.35 the intensity noise of the laser beam in the two positions with the air flow on and off are shown. Let us consider the two spectra with the air flow off (black graphs in the two panels). They have different slopes at low frequencies up to about 50 Hz; the worse RIN is found in the light that has travelled a longer distance. The data with the air flow on are plotted in red in the two graphs; the second graph presents structured noise in the frequency ranges {(95-99), (114-133), (168-172)} Hz. We have identified this noise as due to resonances of various optical mounts excited by the

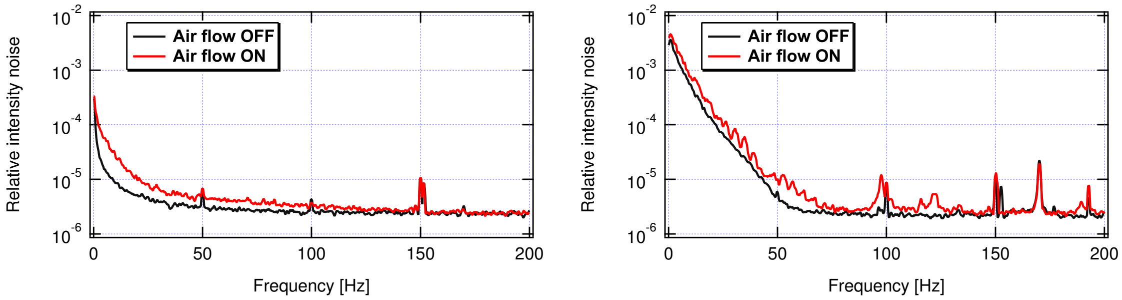

Figure 4.35: Comparison of the relative intensity noise (RIN) of the laser with air conditioning on and off. Left: measurements taken 0.5 m from the laser head. Right: measurements taken at a distance of 2.5 m from the laser head.

air flow. The same structures can be seen in ellipticity measurements, but they are outside the frequency region of interest.

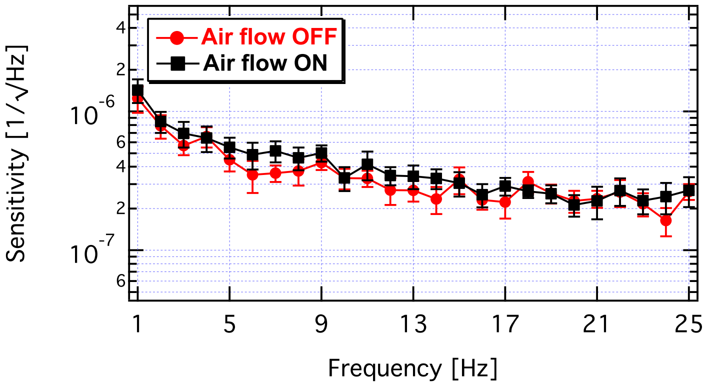

Figure 4.36: Ellipticity sensitivity with air flow on (black points) and off (red points). Each point in the two graphs is the average over the 32 bins in a 1 Hz frequency interval. Integration time for the two graphs is $T = 4.1 \times 10^3$ s and $T = 5.6 \times 10^3$ s, respectively.

In Figure 4.36 we show two measurements of the sensitivity in ellipticity as a function of frequency with the air flow off and on. As can be seen, differently from the case of RIN, the air flow has little or no influence on the sensitivity in ellipticity. This indicates that intensity noise is not a limiting noise source. The dominant ellipticity noise seems to be of a different nature. To complete this series of test, we have also performed measurements with all the other sources of acoustic and vibrational noise, such as the turbo and scroll vacuum pumps, switched off. Again, the sensitivity did not change.

Furthermore, the electronics used to lock the laser to the cavity has been completely redesigned implementing OpAmps with lower noise and, more importantly, lower offset drifts. None of the above operations resulted in an improvement in ellipticity sensitivity.

4.4.3 The role of the finesse

The design of the PVLAS experiment was fundamentally based on the following considerations:

1. With a Fabry-Perot cavity, the total acquired ellipticity is $\Psi = N\psi$, where ψ is the ellipticity acquired for a single pass in the birefringent medium. With $\int B^2\,dL \approx 10\,\mathrm{T^2m}$ and a finesse $\mathscr{F} = 7\times10^5$ this gives $\Psi = 5\times10^{-11}$. In order to reach a unitary signal to noise ratio in an integration time $T = 10^6$ s, a sensitivity of $5\cdot10^{-8}\frac{1}{\sqrt{\mathrm{Hz}}}$ is needed.

2. In principle, at a modulation $\eta_0 = 0.01$, near shot-noise sensitivity of $6\cdot10^{-9}\frac{1}{\sqrt{\mathrm{Hz}}}$ should be possible. Since shot noise is always very difficult to achieve, the PVLAS apparatus was designed with a contingency factor about ten.

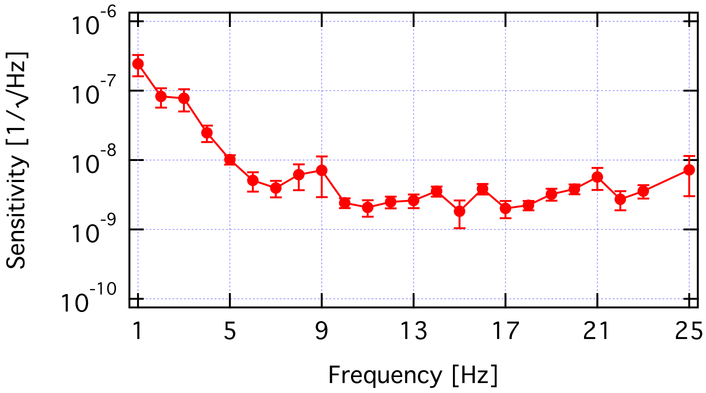

Figure 4.37: Ellipticity sensitivity measured as a function of the frequency in the optical scheme of the PVLAS experiment but without the FP cavity. At lower frequency, the noise is dominated by the pointing stability of the laser. Instead, in the frequency region from 6 up to 25 Hz the sensitivity is flat and reaches the expected value from the known noise budget.

As can be seen in Figure Fig. 4.37, in the case of a polarimeter without a Fabry-Perot cavity, the ellipticity sensitivity is indeed limited by the expected noise budget above about 7 Hz. It is clear that the measured sensitivity from 6 to 25 Hz has a flat distribution over the frequency range and is compatible with the theoretical known noise value discussed in section 2.2.3. At lower frequencies the sensitivity is worsened due to the pointing instability of the laser beam. What we observe is that the introduction of the very high finesse Fabry-Perot cavity changes the wide band noise distribution as a function of the frequency in an unexpected way. The fundamental role of the Fabry-Perot cavity is the amplification of the signal to noise ratio by the number of the passages N. This is the case for relatively low finesses, but it might be possible that for very high finesses the signal to noise ratio reaches a plateau, if both the noise and the signal increase together. We have not yet systematically studied the noise introduced by the cavity as a function of the finesse of the cavity. Such a study should allow to choose the optimal cavity finesse for the experiment.

4.4.4 Ellipticity modulation

In this section we discuss the ellipticity modulator PEM as a source of ellipticity noise. A theoretical plot of the noise contribution as a function of the modulation η_0 is shown in Chapter 2, Fig. 2.5. In that figure, the total intrinsic noise density has a minimum at $\eta_0 \approx 10^{-2}$. Since the noise is a function of the modulation amplitude, a series of measurements of the ellipticity sensitivity was performed to study the discrepancy between the measured data and the calculated sensitivity.

We made a series of measurements of the sensitivity in ellipticity at frequencies ranging from 2 to 25 Hz, as a function of the amplitude modulation η_0. Each of the first four panels of Figure 4.38 presents the data relative to a 6 Hz frequency interval. In the first frequency range from 2 to 7 Hz, the noise is almost independent from the modulation amplitude and is far from the calculated noise of the polarimeter. Passing on to the higher frequency regions, the noise distribution as a function of the modulation amplitude changes. In the interval from 8 to 13 Hz the sensitivity is slightly better and at small modulation amplitudes of $\eta_0 \approx 3.8 \times 10^{-5}$ the measured noise densities seem to have the same slope as the calculated one but with a slightly higher value. At higher frequencies, the ellipticity noise becomes almost frequency independent, whereas, as a function of η_0, it flattens off earlier than the calculated curve. The measured minimum is reached at values of $\eta_0 \approx 10^{-3}$ in contrast to the minimum reached at about $\eta_0 \approx 10^{-2}$ for the calculated curve.

The 24 sensitivity curves are fitted using the function of Eq. (2.24) to which a constant, uncorrelated, frequency-dependent noise A_ν is added:

$$S'_{\text{tot}}(\nu) = \sqrt{S_{\text{tot}}^2 + A_\nu^2}.$$

Free parameters are $N_{\text{RIN}}(\nu_{\text{m}})$ [see Eq. (2.23)], which is common for all the curves, and A_ν. A value $N_{\text{RIN}} = (1.6 \pm 0.3) \times 10^{-5} \frac{1}{\sqrt{\text{Hz}}}$ is obtained. An example of the fits is shown for the

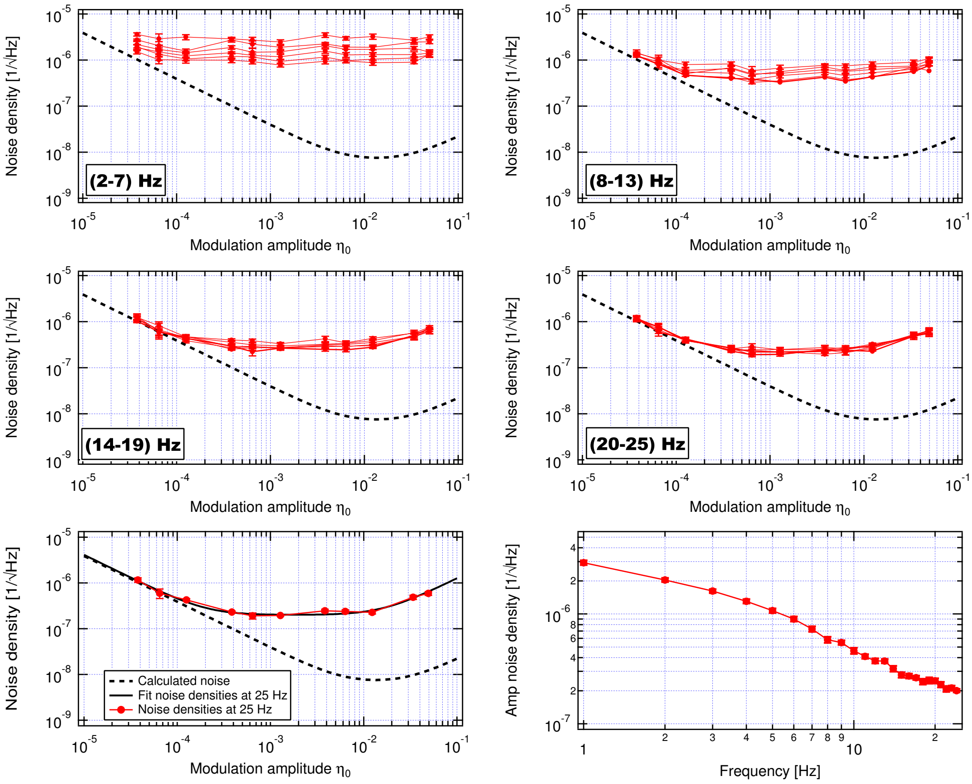

Figure 4.38: First four panels: measured ellipticity noise density (red dots) compared to the theoretical intrinsic noise density S_{tot} (dashed line) of Eq. (2.24), plotted as a function of the modulation amplitude η_0. Each of the panels presents measurements at six different frequencies, up to 25 Hz, in steps of 1 Hz. The twenty-four data sets are fitted with the theoretical noise of Eq. (2.24) plus a frequency dependent uncorrelated noise A_ν, with N_{RIN} left as a free parameter common to all the curves. In the fifth panel, the fit of the 25 Hz points is shown. The sixth and last panel shows the 24 values of A_ν.

25 Hz case in the fifth panel of Figure 4.38, for which $A_{25\ \mathrm{Hz}} = (1.99 \pm 0.05) \times 10^{-7} \frac{1}{\sqrt{\mathrm{Hz}}}$. The values of A_ν are plotted as a function of frequency in the sixth panel of the same figure.

The value obtained for the RIN from the fit is about a factor 50 greater than the value measured at 50 kHz: $N_{\mathrm{RIN}}(50\,\mathrm{kHz}) \approx 3 \times 10^{-7} \frac{1}{\sqrt{\mathrm{Hz}}}$. It seems as if there exists another contribution to the sensitivity that is proportional to the modulation η_0: $S_\psi = k\eta_0$ with $k \approx (1.6 \pm 0.3) \times 10^{-5} \frac{1}{\sqrt{\mathrm{Hz}}}$. This hypothetical contribution, though, remains unexplained.

4.4.5 Cavity frequency difference for the two polarisation states

An important property of the PVLAS locking scheme is the possibility to scan the laser frequency in a small interval around the resonance. In our case, the FWHM of the resonance

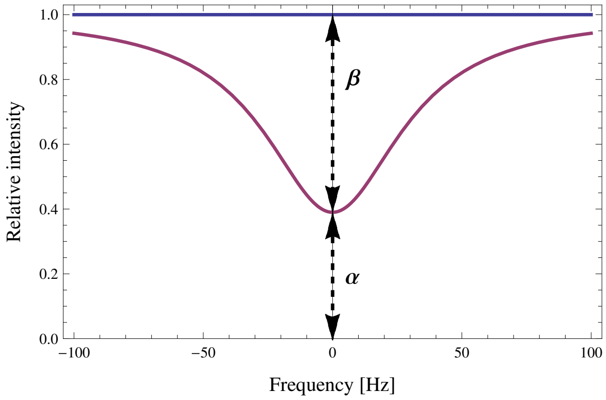

Figure 4.39: Schematics of the reflected intensity as function of the frequency. The quantities α and β are respectively the fractions of the intensity not locked and locked to the cavity.

is about 65 Hz, with the possibility of adjusting the laser away from the resonance of about ±5 Hz; we term this shift as an "offset". Due to the birefringence of the cavity mirrors [59], we observe that modulating the laser frequency around the resonance, there is an induced ellipticity proportional to the amplitude of the modulation. We modulated the offset with the laser locked to the cavity. We used this modulation to determine the slope coefficient $\frac{\partial \mathrm{V_E}}{\partial(\Delta\nu)} = D_\nu$ of the error signal near resonance [see Eq. (2.38)]. The quantity D_ν is the discriminator as discussed in Chapter 2 [Sec 2.3]. A direct measurement of the coefficient D_ν by observing the error signal at the Monitor output of the locking circuit while scanning the frequency of the input light is extremely difficult due to the narrowness of the resonance. For its determination we recall the expression of the light intensity reflected from the cavity [Eq. (2.16)]

$$H_\mathrm{R} \equiv \frac{I_\mathrm{R}(\delta)}{I_0} = \frac{R\left[1-2(1-A)\cos\delta+(1-A)^2\right]}{1-2R\cos\delta+R^2}.$$

When the laser is locked to the cavity ($\delta = 2m\pi$) the reflected intensity is

$$I_\mathrm{R}(\delta) = I_0\left(\frac{A}{1-R}\right)^2.$$

In practice, the reflected intensity is slightly higher due to imperfect mode matching [44]. From last equation, the quantities α and β defined in Figure 4.39 are obtained as $\alpha = A^2/(1-R)^2$ and $\beta = T(T+2A)/(1-R)^2$ since $\alpha+\beta = 1$. For the voltage signal from the reflection photodiode for small values of δ, the following relation can be written starting from $H_\mathrm{R}(\delta)$:

$$\frac{V_\mathrm{R}(\delta)}{V_\mathrm{ref}} \approx \beta\frac{\delta^2}{(1-R)^2}+\alpha \tag{4.42}$$

where $V_{\mathrm{R}}(\delta)$ is the intensity reflected by the cavity near resonance and V_{ref} is the reference signal when the laser is unlocked. Modulating the offset is equivalent to modulating δ

$$\delta = \frac{4\pi d \Delta\nu}{c} = \frac{4\pi d}{c}\frac{(\Delta V + V_0)}{D_\nu}$$

where $\Delta\nu$ is the amplitude of the frequency modulation, ΔV the voltage modulation sent to the locking system and V_0 is a DC voltage shift from the top of resonance. The introduction of of the parameter V_0 is necessary to allow for the laser to be locked slightly off the resonance due to some small electronic offset. The signal sent to the feedback system is a sinusoidal signal expressed as $\Delta V = A\cos(\omega_{\mathrm{off}}t)$, where A is the amplitude of the modulation signal and ω_{off} is its angular frequency. By substituting the expressions of δ and ΔV into equation (4.42) one has two frequency components: one at ω_{off} and the other at $2\omega_{\mathrm{off}}$.

$$\frac{V_{\mathrm{R}}(\delta)}{V_{\mathrm{ref}}} \approx \alpha + 2\beta\left(\frac{\mathscr{F}}{D_\nu \nu_{\mathrm{fsr}}}\right)^2\left(A^2 + 2V_0^2 + 4AV_0\cos\omega_{\mathrm{off}}t + A^2\cos 2\omega_{\mathrm{off}}t\right) \tag{4.43}$$

The measured parameters are A, α, β, $\mathscr{F}$ and ν_{fsr}, whereas the unknown ones are D_ν and V_0. The coefficient D_ν can be extracted from the amplitude of the component at $2\omega_{\mathrm{off}}$ whereas the value of V_0 is obtained from the amplitude of the component at ω_{off}.

The following parameters correspond to our Fabry-Perot cavity: $\nu_{\mathrm{fsr}} = 45.4$ MHz, $\mathscr{F} = 6.7 \times 10^5$, $\beta = 0.61 \pm 0.01$. We set an amplitude modulation $A = 9.9$ mV measured at the output of the monitor channel of the feedback circuit shown in Figure 3.23, corresponding to the same point in the feedback loop where D_ν needs to be measured. In this situation the amplitude of the reflected voltage signal at $V_R(\delta)|_{2\omega_{\mathrm{off}}}$ was 54 μV. One finds for D_ν

$$\frac{1}{D_\nu} = \sqrt{\left.\frac{V_{\mathrm{R}}(\delta)}{V_{\mathrm{ref}}}\right|_{2\omega_{\mathrm{off}}} \frac{\nu_{\mathrm{fsr}}^2}{2\beta A^2 \mathscr{F}^2}} = 190\ \mathrm{Hz/V}.$$

The offset modulation corresponds to a frequency modulation $\Delta\nu = A/D_\nu = 1.9$ Hz.

From this value we can determine two interesting quantities: the approximate frequency noise of the laser with respect to the cavity and the ellipticity induced noise due to the frequency noise. The relative frequency noise of the laser with respect to the cavity can be obtained by measuring the voltage noise spectrum at the monitor output of the locking circuit with the laser unlocked. This represents the limit in the relative frequency noise between the laser and the cavity, that can be reached if, as in our case, the locking circuit has a sufficiently high gain. The voltage noise is transferred to the laser as frequency noise with a coefficient D_ν. The resulting noise at the monitor output with the laser unlocked is

$\Delta V_{\mathrm{unlock}} = 3.5\ \mu\mathrm{V}/\sqrt{\mathrm{Hz}}$ and has a flat spectrum, resulting in a relative laser-cavity frequency noise of $S_\nu = 6.6 \times 10^{-4}\ \mathrm{Hz}/\sqrt{\mathrm{Hz}}$.

With the modulation active, peaks are present at ω_{off} and $2\omega_{\mathrm{off}}$ in both the ellipticity spectrum and in the reflected signal spectrum. The peaks at ω_{off} depend on V_0. To cancel the effect of V_0 we set the static offset of the locking circuit so that in the reflected signal there is no signal at ω_{off}, indicating that the laser is locked at the top of the resonance. The residual ellipticity peak at ω_{off} was $\psi = 2.0 \times 10^{-4}$. Since the induced ellipticity is proportional to the offset amplitude modulation, we determined a coefficient:

$$\frac{\partial \psi}{\partial(\Delta\nu)} = \frac{2.0 \times 10^{-4}}{1.9\ \mathrm{Hz}} \approx 1 \times 10^{-4}\ \frac{1}{\mathrm{Hz}} \tag{4.44}$$

To evaluate if this effect can justify the measured ellipticity sensitivity one can estimate its contribution as

$$S_{\mathrm{feedback}} = \frac{\partial \psi}{\partial(\Delta\nu)} \frac{\Delta V_{\mathrm{unlock}}}{D_\nu} = 6.6 \times 10^{-8}\ 1/\sqrt{\mathrm{Hz}}$$

This value cannot account for the measured noise at least up to 25 Hz, as can be seen in Figure 4.38 bottom right, thereby excluding the locking system as the wide band noise source.

We now take into consideration the normal functioning of the interferemeter without modulations. The ellipticity noise at 10 Hz $S_\psi = 5 \times 10^{-7}\ 1/\sqrt{\mathrm{Hz}}$ can also be interpreted as a noise in the frequency difference between the two orthogonal polarisations. One cannot compute this noise using the conversion factor obtained above with equation (4.44) because what was determined there is the phase difference between the two polarisation states due to the simultaneous scanning of the two resonances. In this case we are interested in, the laser is locked to the resonance of one polarisation while the orthogonal resonance frequency is shifting back and forth due to the mirrors birefringence noise while being slightly off resonance due to the static component of the birefringence of the mirrors. The phase difference between the two polarisation states is

$$\tan\phi = \frac{(1+R)\sin\frac{\alpha}{2}}{(1-R)\cos\frac{\alpha}{2}} \approx \frac{\alpha}{1-R} = \frac{2\pi}{1-R}\frac{\Delta\nu}{\nu_{\mathrm{fsr}}} = \pi N \frac{\Delta\nu}{\nu_{\mathrm{fsr}}} \tag{4.45}$$

Given that $\tan\phi \approx \phi$ and that $S_\psi = S_\phi/2$ one finds a relative frequency noise between the two polarisation states

$$S_{\Delta\nu} = \frac{2 S_\psi \nu_{\mathrm{fsr}}}{\pi N} = 3.2 \times 10^{-5}\ \frac{\mathrm{Hz}}{\sqrt{\mathrm{Hz}}} \tag{4.46}$$

This frequency noise corresponds to a noise in optical path difference $S_{\Delta\ell}$ of

$$S_{\Delta\ell} = d\frac{S_{\Delta\nu}}{\nu_{\rm laser}} = \frac{S_\psi \lambda}{\pi N} = 3.8\times 10^{-19}\ \frac{\rm m}{\sqrt{\rm Hz}} \tag{4.47}$$

One can estimate the relative frequency noise of Eq (4.46) as due to a variation of the cavity length. A fluctuation $S_{\Delta\nu}$ of the relative frequency shift between the two polarisation states is related to a fluctuation of the inverse of the cavity length as

$$S_{\Delta\nu} = \nu_{\rm laser}\,\Delta\ell\,\Delta\left(\frac{1}{d}\right) = \nu_{\rm laser}\,\Delta\ell\,\frac{\Delta d}{d^2} = \Delta\nu\frac{\Delta d}{d}.$$

From this one obtains

$$\Delta d = d\frac{S_{\Delta\nu}}{\Delta\nu} = 6.6\ \frac{\mu\rm m}{\sqrt{\rm Hz}} \tag{4.48}$$

The cavity length stability is far better than this value, excluding this effect too as a source of wide band noise: again, the vibrational noise of the mirrors of the cavity cannot account for the observed ellipticity noise.

4.4.6 Final discussion on wide band noise

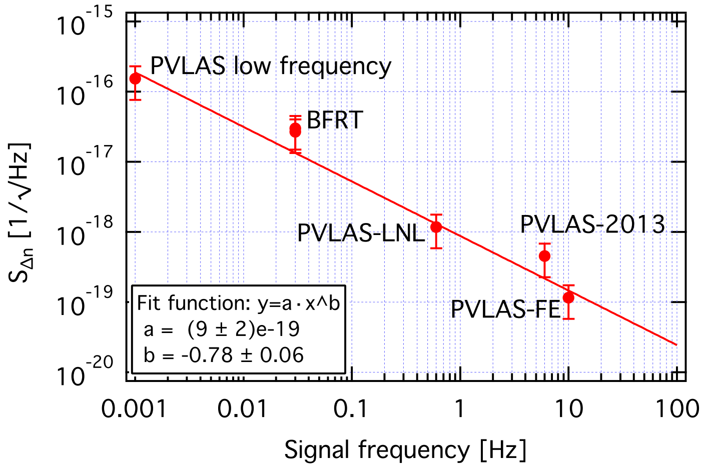

Figure 4.40: Birefringence noise densities measured in polarimeters set up to measure the magnetic vacuum birefringence plotted as a function of their working frequency. Data from the experiments BFRT [35], PVLAS-LNL [76, 77], PVLAS-2013 [78], PVLAS-FE [59] are normalised to the length of the optical cavities, to the number of passes and to the wavelength. The leftmost point has been measured during the 2015 data taking campaign of the PVLAS experiment. The two almost equivalent points from BFRT were measured with two different cavities, one having 34 passes and the other 578 passes. The error bars are an estimated 50%.

At present we have no explanation for the origin of the wide band noise which is limiting the sensitivity of the PVLAS experiment. It is interesting to note, though, that by plotting the sensitivity in birefringence $S_{\Delta n}$ as a function of the working frequency for PVLAS and for other past efforts to measure vacuum magnetic birefringence, one finds the plot shown in Figure 4.40. As can be seen, the sensitivities seem to follow on a power law. The experiments are very different in size, in the number of passes through the magnetic field region (Fabry-Perot and multi-pass cavities) ranging from 34 to 4.5×10^5, type of modulator and the use of homodyne versus heterodyne detection.

One point seems to be clear: the noise is due to the presence of the cavity. One common aspect to all the experiments is the use of dielectric interferential mirrors for the cavity. It is known that these are birefringent but their stability in birefringence is not known. The excess noise seems to be a real ellipticity generated in the cavity proportional to the number of passes. It is a noise which is multiplied in the same way as the signal induced by the magnetic field.

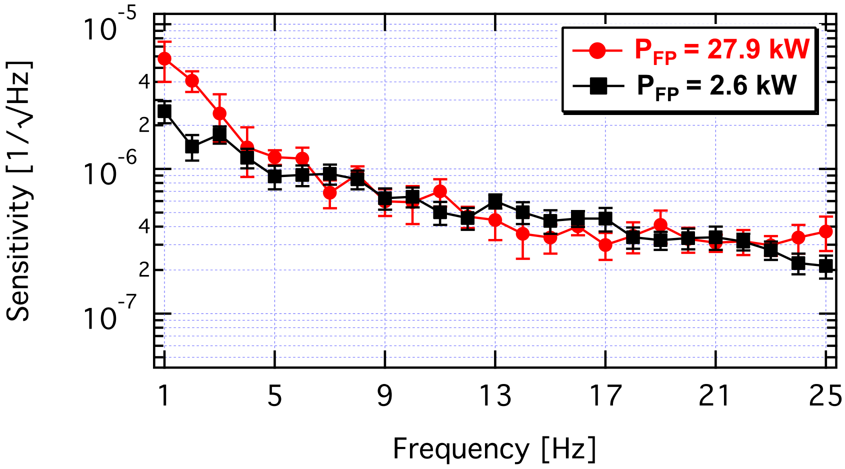

Figure 4.41: Ellipticity sensitivity measured as a function of frequency at two different values of the circulating power in the Fabry-Perot cavity. Integration time is $T = 7\times10^3$ s for the 2.6 kW spectrum and $T = 2.6\times10^3$ s for the 27.9 kW spectrum.

We believe that the source of this noise is thermal but the thermal noise we are thinking of is not due to the presence of the power inside the cavity because the sensitivity at frequencies above about 5 Hz is unaffected by changing the input power by a factor 10. This is shown in Figure 4.41. The two sensitivity curves correspond to circulating powers of 27.9 kW and 2.6 kW. With the higher power, instabilities in the static birefringence are seen but at very slow frequencies. We are thinking instead of an intrinsic thermal noise generating stress in the coating which fluctuates and generates birefringence noise through the stress-optic coefficient. One way to verify such a hypothesis is to cool the mirrors to see whether the sensitivity improves or not.

Chapter 5

Measurements of the optical properties of vacuum

5.1 Data analysis procedure

In this section we present the polarimetric vacuum measurements performed in the attempt to test its optical magnetic properties. Every year, after an optimisation of the apparatus, we dedicated time to performing long measurements. For the purpose of this presentation I divide the data into three groups, corresponding to the three solar years: I have labeled them Run2014, Run2015, Run2016. For each run presented in this thesis the alignment of the FP cavity and the rotation of the mirrors was optimised. Each run has thus a different value of the parameter α describing the mixing of ellipticity and rotation. The runs are subdivided into blocks, each block being characterised by the rotation frequency of the magnets and hence the sampling frequency of the signals; each block has a different sensitivity $S_{\Delta n}$.

The procedure of the data analysis of each block was the same for all the runs and took the following steps:

- A verification that there are no lost data points. This is performed by verifying that the sampled magnetic stray field has a regular sinusoidal oscillation without phase jumps, in particular before and after data taking interruptions, e.g. laser unlocks, magnets unlock from the trigger, saturation of signals voltage or other anomalies occurring during the run. After data selection, we calculate the ellipticity according to equation 2.5. The amplitude $\psi_{2\nu_B}$ and the phase $\phi_{2\nu_B}$ corresponding to the bin at the frequency $2\nu_B$ are obtained by a discrete Fourier transform (DFT) of the ellipticity data array (this is done because the FFT needs a number of point that are a power of 2). The noise frequency amplitude spectrum is obtained by a Fast Fourier Transform (FFT) of the ellipticity data. All the transformed values are divided for the $k(\alpha)$ coefficient [see Eqs. (4.9) and (4.10)].

- The ellipticity noise amplitude around $2\nu_B$, $\sigma_{2\nu_B}$, is extracted by making a histogram of 10 000 bins centred at $2\nu_B$ of the FFT. The ellipticity histogram follows a Rayleigh distribution $P(\rho) = (\rho/\sigma^2)e^{-\frac{\rho^2}{2\sigma^2}}$, in which the parameter σ represents the standard deviation of two identical independent Gaussian distributions for the two variables x and y and $\rho = \sqrt{x^2+y^2}$. In our case, x and y represent the projections of the ellipticity value at $2\nu_B$ along the physical and the non-physical axes as determined from a Cotton-Mouton calibration. The average of $P(\rho)$ is related to σ by $\langle P\rangle = \sigma\sqrt{\pi/2}$ allowing a determination of $\sigma_{2\nu_B}$ around $2\nu_B$ for each data block. This value is used in the next step as the uncertainty for the ellipticity value at $2\nu_B$.

- The unprojected values of Δn and $\sigma_{\Delta n}$ are determined for each block as:

  $$(\Delta n \pm \sigma_{\Delta n}) = \frac{\lambda}{\pi N L}\left(\psi_{2\nu_B} \pm \sigma_{2\nu_B}\right).$$

  The birefringence Δn is then projected onto the physical as well as the non-physical axes.

- The mixing of ellipticities and rotations due to the cavity birefringence permits also to derive, from the ellipticity data, the rotation of the electric field and *vice-versa*. From the birefringence noise measurements we can thus determine also a value for the dichroism $\Delta\kappa$.

- Finally we determine the weighted average of the values of Δn and $\Delta\kappa$ for the various blocks to get a value of Δn and $\Delta\kappa$ for the Run. In doing this one is assuming a linear dependence of the ellipticity and the rotation with the length of the field region. As we will see, when putting limits on ALPs with different magnet lengths, this is not the case.

To correctly determine the phase and amplitude calibration of an ellipticity signal, we performed calibration measurements for each configuration of magnet length and rotation frequency by using the Cotton-Mouton effect (CME) in gases. The actual phase of the ellipticity directly depends on the angle θ_0 of the polariser and on the angular position of the magnets at the starting time of a measurement. These parameters do not necessarily always have the same values but may be adjusted from block to block. Furthermore, electronic components (lock-ins, filters, etc.) introduce a phase which depends on the signal frequency. Therefore, for a correct phase calibration, the Cotton-Mouton signal is used, defining what we call the physical axis of the measurements; we expect that the signal of the vacuum magnetic birefringence comes with the same phase as that of the corresponding Cotton-Mouton signal of the noble gases [62]. The CME measurements provide two more fundamental parameters, namely the amplitude of an ellipticity signal and the value of the mixing parameter α. To determine this last parameter one has to measure also the rotation spectrum and to analyse the data taking into account the frequency dependence of the signals as discussed in Sect. 4.2.1. The values obtained for the amplitude are compared with theoretical calculations as well as with the experimental data in the literature [62]. In this way we calibrate the apparatus in amplitude and phase. Signals in quadrature to the physical phase are considered spurious and, if present, indicate a problem. The Cotton-Mouton measurements at various pressures of the gas employed permit also to check the linear response of the polarimeter.

5.2 Run 2014

5.2.1 Characteristics of the 2014 run

In this run, Viton o-rings were installed inside the glass tubes. The analog locking circuit was still the first generation version and when the laser unlocked from the cavity resonance, locking had to be performed manually. The power of the light at the output of the cavity was $I_0 = 70$ mW corresponding to a power stored inside the FP cavity of $I_{\rm FP} \approx 30$ kW. The runs consisted of three data blocks:

1) acquisition trigger 96 Hz and frequency of both magnets $\nu_\alpha = \nu_\beta = 3$ Hz, sampling rate 32 samples/turn and acquisition time $T = 370\,000$ s;

2) acquisition trigger 80 Hz and frequency of both magnets $\nu_\alpha = \nu_\beta = 2.5$ Hz, sampling rate 32 samples/turn and the acquisition time $T = 240\,000$ s;

3) acquisition trigger 96 Hz and frequencies of the magnets $\nu_\alpha = 2.4$ Hz and $\nu_\beta = 3$ Hz, sampling rate for magnet α was 40 samples/turn and for magnet β was 32 samples/turn. The acquisition time was $T = 287\,000$ s.

The ellipticity modulation amplitude of the PEM was $\eta_0 = 6 \times 10^{-3}$ and the finesse was $\mathscr{F} = 670\,000$.

Of the Cotton-Mouton calibrations performed, we report here only the one at $\nu_\alpha = \nu_\beta = 3$ Hz. We filled the vacuum chamber with 0.98 mbar of Helium gas with a purity of 1 ppm. In Figure 5.1 two spectra are shown: on the left the ellipticity and on the right the rotation, for an integration time $T = 640$ s. The signal at $2\nu_B$ is present in both the rotation and ellipticity

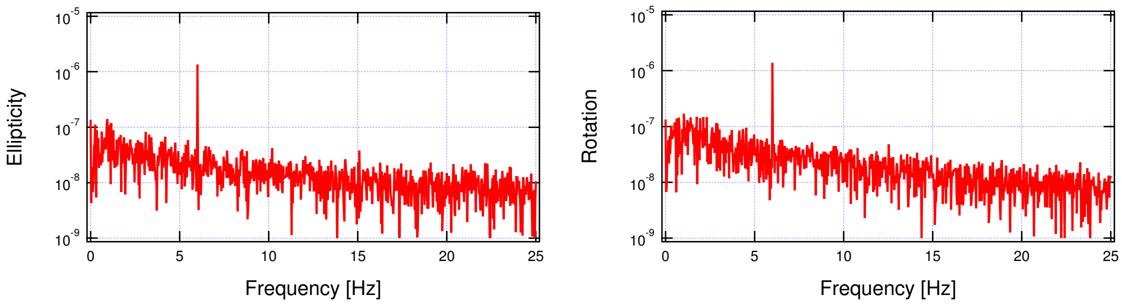

Figure 5.1: Cotton-Mouton effect measurements for 0.98 mbar of He gas: Fourier spectra of the extinguished intensity demodulated at the modulator frequency ν_{m}. The two magnets were rotating at $\nu_\alpha = \nu_\beta = 3$ Hz. Left panel: ellipticity measurement. Right panel: rotation measurement ($\lambda/4$ plate inserted). Integration time $T = 640$ s for both spectra.

spectra. From the ratio of the amplitudes of the two peaks [see Equations (4.9) and (4.10)] one finds a value $\alpha = 4.5$ μrad, corresponding to an attenuation factor $k(\alpha) = 0.50$. This value is used to extract the real ellipticity generated in the cavity. The corresponding unitary birefringence of Helium at room temperature is:

$$\Delta n_u^{(\mathrm{He})} = (2.2 \pm 0.1) \times 10^{-16}\ \mathrm{T}^{-2}\ \mathrm{atm}^{-1}.$$

This value agrees well with the experimental values present in the literature.

5.2.2 2014 vacuum magneto-optical measurements

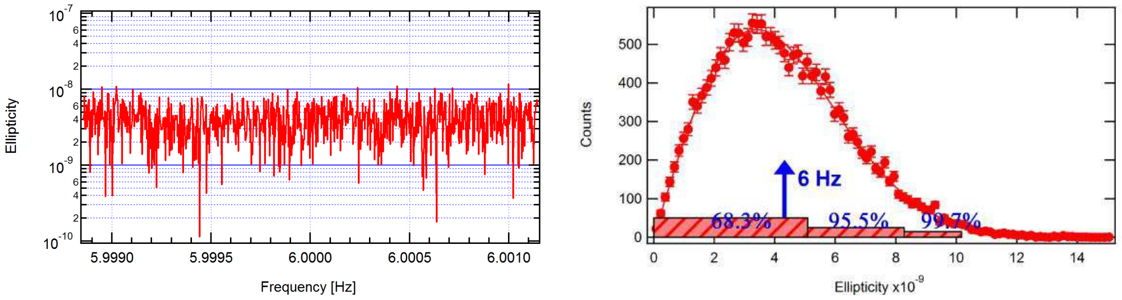

Figure 5.2: Vacuum ellipticity data with integration time $T = 370\,000$ s. Left: the amplitude of the Fourier transform of the ellipticity in a window centered at twice the frequency of the rotating magnets $\nu_\alpha = \nu_\beta = 3$ Hz. Right: histogram of the data points of the left panel fitted with a Rayleigh distribution. The vertical arrow indicates the value of the bin at 6 Hz; the strips at the bottom of the plot correspond to the 68.3%, 95.5%, and 99.7% integrated probabilities.

Block	$\nu_\alpha,\ \nu_\beta$ (Hz)	Quantity	In-phase	Quadrature	Noise floor σ	$S^{\rm meas}_{2\nu_B}$ $\left(1/\sqrt{\rm Hz}\right)$	$k(\alpha)$
1	3.0, 3.0	Δn	$+1.8\times10^{-21}$	-0.05×10^{-21}	1.8×10^{-21}	1.0×10^{-18}	0.50
2	2.5, 2.5	Δn	-0.63×10^{-21}	-2.0×10^{-21}	2.0×10^{-21}	1.3×10^{-18}	0.50
3	2.4, 3.0	Δn	-2.3×10^{-21}	8.8×10^{-21}	3.4×10^{-21}	2.5×10^{-18}	0.50
1	3.0, 3.0	$\Delta\kappa'$	$+1.8\times10^{-21}$		1.8×10^{-21}	1.0×10^{-18}	
2	2.5, 2.5	$\Delta\kappa'$	-0.63×10^{-21}		2.0×10^{-21}	1.3×10^{-18}	
3	2.4, 3.0	$\Delta\kappa'$	-2.3×10^{-21}		3.4×10^{-21}	2.5×10^{-18}	

Table 5.1: 2014 measured values of the magnetic birefringence and the magnetic dichroism of vacuum for $B = 2.5$ T corrected for the factor $k(\alpha)$. The primed quantities are obtained through the use of Equations (4.9) and (4.10). The parameter σ represents the ellipticity standard deviation of the integrated noise along the physical axis obtained by fitting the Rayleigh distributions for each block. The $S^{\rm meas}_{2\nu_{\rm B}}$ is the sensitivity of each data block.

In Figure 5.2 the ellipticity spectrum measured under vacuum conditions (with residual pressure $p \lesssim 10^{-7}$ mbar) is shown with both magnets rotating at the same frequency $\nu_\alpha = \nu_\beta = 3$ Hz (first block of 2014). The integration time was 370 000 s. The noise histogram around the second harmonic and a fit with the Rayleigh distribution are also shown. The birefringence Δn obtained from the three data blocks are given in the first half of table 5.1. Due to the mixing of ellipticities and rotations and due to the absence of signals, each line can also be interpreted in terms of the reciprocal quantity. The second half of the same table, with primed $\Delta\kappa'$, presents the values of this quantity obtained by applying Equations (4.9) and (4.10).

The limits on the magnetic birefringence and the vacuum magnetic dichroism obtained by the weighted averages of the in-phase values of Table 5.1, expressed at 68% c.l, are:

$$\Delta n^{(2014)} = (3 \pm 13) \times 10^{-22} \qquad @\ B = 2.5\ \mathrm{T}, \tag{5.1}$$

$$\Delta\kappa^{(2014)} = (3 \pm 13) \times 10^{-22} \qquad @\ B = 2.5\ \mathrm{T}. \tag{5.2}$$

The quadrature value of Δn results to be $(4 \pm 13) \times 10^{-22}$. All the numbers found are compatible with zero. These results were published in the Physical Review D journal [58].

5.3 Run 2015

5.3.1 Characteristics of the 2015 run

The vacuum measurements of 2015 were preceded by a study of the cavity birefringence performed by rotating one of the two mirrors of the cavity while keeping the other one fixed (see Chapter 4) whereby the cavity took different equivalent wave-plate values. Furthermore, the analog locking circuit was substituted with an improved automatic locking circuit. A fundamental property of the automatic locking is the increase in duty cycle to $\approx 24/24$ hr. Another important advantage is that the polarimeter's stability shows an improvement due to the reduced unlocked time. The power of the light stored inside the FP cavity was reduced by a factor ≈ 8 ($I_0 = 9$ mW, $I_{\rm FP} = 3.7$ kW) with respect to the Run2014 again to improve the stability. This reduction in power did not affect the sensitivity of the polarimeter. This run featured three different data blocks, two in ellipticity and one in rotation:

1) ellipticity: acquisition trigger 160 Hz; frequency of the magnets $\nu_\alpha = 4$ Hz and $\nu_\beta = 5$ Hz; sampling rate 40 and 32 samples/turn respectively. The acquisition time was $T = 1\,000\,000$ s;

2) ellipticity: acquisition trigger 100 Hz with $\nu_\alpha = 5$ Hz and $\nu_\beta = 6.25$ Hz resulting in a sampling rate of 20 samples/turn for magnet α and 16 samples/turn for magnet β. The acquisition time was $T = 890\,000$ s;

3) rotation: acquisition trigger 160 Hz with $\nu_\alpha = \nu_\beta = 5$ Hz, resulting in a sampling rate for both magnets of 32 samples/turn. The acquisition time was $T = 140\,000$ s.

The ellipticity modulation amplitude of the PEM was $\eta_0 = 4 \times 10^{-3}$ and the finesse was $\mathscr{F} = 700\,000$.

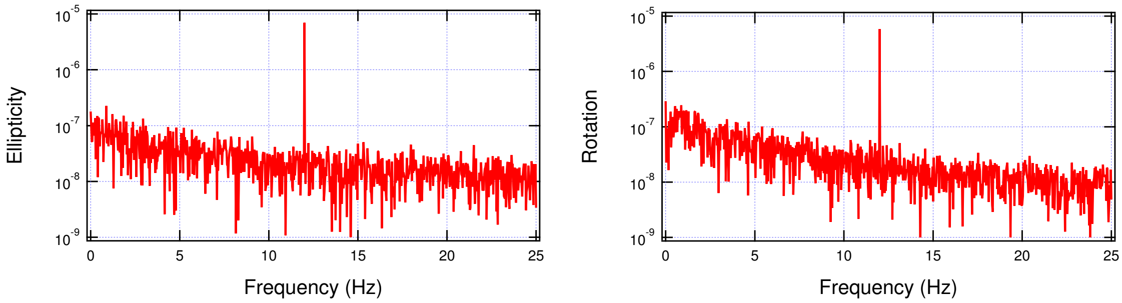

Figure 5.3: Cotton-Mouton effect measurements for 230 μbar of Ar gas: Fourier spectra of the extinguished intensity demodulated at the modulator frequency $\nu_{\rm m}$. A single magnet was rotating at $\nu_B = 6$ Hz. Left: ellipticity spectrum. Right: rotation spectrum. Integration time is $T = 640$ s for both spectra.

Again here we present only one of the calibrations of this run. This calibration was made by filling the vacuum chamber with 0.230 mbar of Argon gas with a purity of 1 ppm and then measuring the CME. Figure 5.3 shows the two spectra for the ellipticity and the rotation. Taking the ratio of the amplitudes of the two peaks [see Equations (4.9) and (4.10)] one finds a value $\alpha = 3.7$ μrad, corresponding to an attenuation factor $k(\alpha) = 0.59$. The frequency distance between the two Airy curves is 27 Hz. From these data one can extract a value for the unitary birefringence of Ar gas at room temperature:

$$\Delta n_u^{(\mathrm{Ar})} = (7.5 \pm 0.5) \times 10^{-15}\ \mathrm{T}^{-2}\ \mathrm{atm}^{-1}.$$

This value is in agreement with published data [62].

5.3.2 2015 vacuum magneto-optical measurements

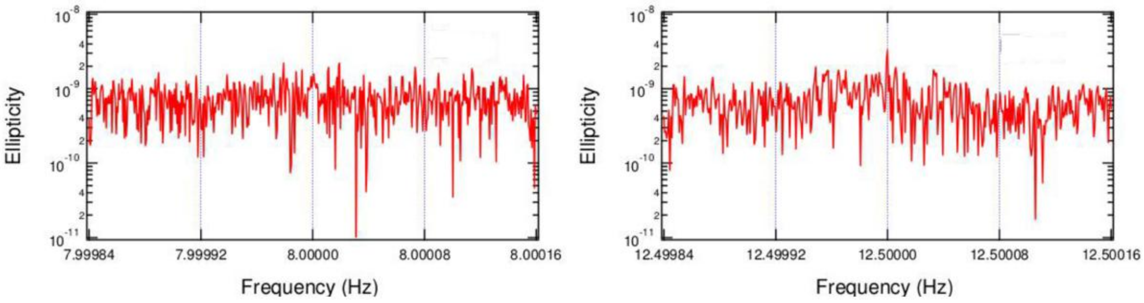

Figure 5.4: Fourier transform of the ellipticity signals of data from block 1, magnet β, and from block 2, magnet α. In both cases, a structure is present around $2\nu_B$. These data do not contribute to the results presented in this work.

In the Fourier spectra of both the data blocks 1 and 2, there were spurious ellipticity structures several bins wide around the $2\nu_B$ frequencies: in data block 1 at the frequency $2\nu_\alpha = 8$ Hz and in data block 2 at the frequency $2\nu_\beta = 12.5$ Hz. The corresponding spectra can be seen in Figure 5.4. Spurious ellipticity signals were not present at $2\nu_\beta = 10$ Hz of block 1 and $2\nu_\alpha = 10$ Hz of block 2. A physical ellipticity signal should occupy a single bin in the Fourier spectra at $2\nu_B$, the two magnets should give the same amplitude with phase corresponding to the physical axis. Not fulfilling these conditions, the data of Fig. 5.4 have been discarded. The spurious effects are plausibly due to the magnetic coupling between the rotating magnetic gradients and the glass tubes. As already discussed in Chapter 4, this coupling modulates the diffused light and generates spurious structures. We concluded that, in long runs, active positioning of the two tubes, based on the monitoring of the tubes accelerations, is needed.

The left column of graphs in Figure 5.5 shows the FFT's of the accepted data in blocks 1, 2 and 3 in a small frequency interval around $2\nu_B$; in the right column the corresponding histograms are shown. The first two rows refer to ellipticity measurements and the third one

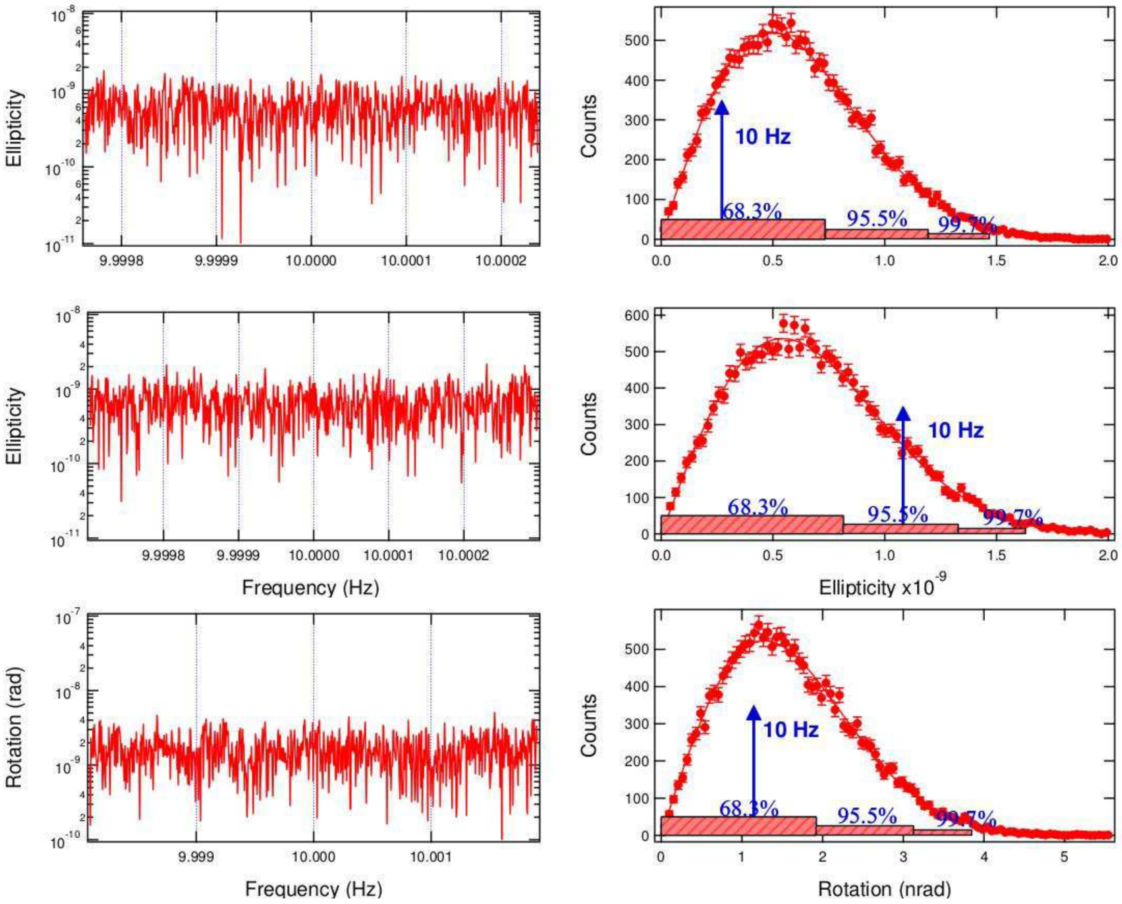

Figure 5.5: Results for Run2015. Left column: Fourier spectra of the signals in a narrow interval around $2\nu_B$. The values are corrected for the attenuation factor $k(\alpha)$. Right column: histograms of the corresponding spectra plotted in the left panel; the data are fitted with the Rayleigh distribution; the vertical arrows mark the amplitude values at $2\nu_B$. The strips at the bottom of the plots correspond to the 68.3%, 95.5%, and 99.7% integrated probabilities. Top row: magnet β rotating at $\nu_\beta = 5$ Hz, with integration time $T = 10^6$ s. Middle row: magnet α rotating at frequency $\nu_\alpha = 5$ Hz, $T = 8.9 \times 10^5$ s. Bottom row: two magnets rotating at the same frequency $\nu_\alpha = \nu_\beta = 5$ Hz.

to the measurement of the rotation. The histograms are fitted with the Rayleigh distribution; a blue arrow indicates the value of the bin at $2\nu_B$.

Block	Magnet frequency	Quantity	In-phase	Quadrature	Noise floor σ	$S_{2\nu_B}^{\text{meas}}$ $(1/\sqrt{\text{Hz}})$	$k(\alpha)$
1	$\nu_\beta =$ 5 Hz	Δn	-0.6×10^{-22}	$+2.4\times10^{-22}$	4.5×10^{-22}	4.5×10^{-19}	0.65
2	$\nu_\alpha =$ 5 Hz	Δn	-3.8×10^{-22}	$+9.3\times10^{-22}$	5.0×10^{-22}	4.7×10^{-19}	0.65
3	$(\nu_\alpha, \nu_\beta) = (5, 5)$ Hz	$\Delta n'$	$+0.4\times10^{-22}$		8.2×10^{-22}	3.0×10^{-19}	0.65
1	$\nu_\beta =$ 5 Hz	$\Delta\kappa'$	-0.9×10^{-22}		6.2×10^{-22}	6.2×10^{-19}	
2	$\nu_\alpha =$ 5 Hz	$\Delta\kappa'$	-5.2×10^{-22}		6.8×10^{-22}	6.4×10^{-19}	
3	$(\nu_\alpha, \nu_\beta) = (5, 5)$ Hz	$\Delta\kappa$	-0.3×10^{-22}	-8.8×10^{-22}	6.0×10^{-22}	2.2×10^{-19}	

Table 5.2: Results of the 2015 measurements, corrected for $k(\alpha)$, of the magnetic birefringence and dichroism of vacuum for $B = 2.5$ T. The primed measurements are obtained through the use of Equations (4.9) and (4.10).

The values obtained for σ define the noise floor level of each measurement achieved after the integration time T. A summary is presented in Table 5.2 in terms of Δn and $\Delta\kappa$. In the first half of Table 5.2, we summarise the results of all the measurements in vacuum. Due to the mixing of ellipticities and rotations and due to the absence of signals, each line can also be interpreted in terms of the reciprocal quantity. The second half of the same table, with primed $\Delta n'$ and $\Delta\kappa'$, presents the values obtained by applying Equations (4.9) and (4.10).

The weighted averages are

$$\Delta n^{(2015)} = (-1.7 \pm 3.1) \times 10^{-22} \qquad @\ B = 2.5\ \text{T}, \tag{5.3}$$

$$\Delta\kappa^{(2015)} = (-1.9 \pm 3.6) \times 10^{-22} \qquad @\ B = 2.5\ \text{T}. \tag{5.4}$$

The quadrature value of Δn results to be $(+5.5 \pm 3.3) \times 10^{-22}$. All the values found for Δn and $\Delta\kappa$ are compatible with zero.

5.4 Run 2016

5.4.1 Characteristics of the 2016 run

Before run 2016 some improvements were introduced. We substituted the glass vacuum tubes with more rigid ceramic material (silicon nitride). The interior of the ceramic tubes is rough, and we found that this roughness does not permit the insertion of o-rings without generating dust and thereby creating serious problems to the cavity stability when the magnets rotate. All the attempts of inserting the o-ring baffles in the ceramic tubes (as in the glass tubes) failed.

The observed noise level of the polarimeter has a frequency dependence and therefore one should work at the highest possibile frequency of rotation of the magnets to have a better sensitivity. By upgrading the transmission system, we were able to reach a rotating frequency of the magnets of 23 Hz with the polarimeter working. However, the vibrations induced by the rotating magnets excited resonances of the structure sustaining the magnets and of the vacuum tubes which rendered the measurements unfeasible. In fact, at high rotation frequencies, spurious peaks were present in the ellipticity spectrum at $2\nu_B$. At a rotation frequency of 8 Hz it was possible to integrate for long times with low accelerations of the tubes and of the bench. We set the frequencies of the magnets at $\nu_\alpha = 8$ Hz and $\nu_\beta = 8.5$ Hz. We also reduced the power circulating inside the FP cavity to $I_{\rm FP} = 1$ kW corresponding to an output intensity $I_0 = 2.5$ mW.

The 2016 run features only one ellipticity data block:

1) ellipticity: acquisition trigger 136 Hz, frequency of the magnets $\nu_\alpha = 8$ Hz and $\nu_\beta = 8.5$ Hz, sampling rate is 17 samples/turn for the magnet α and 16 samples/turn for the magnet β and acquisition time $T = 2\,000\,000$ s.

The ellipticity modulation amplitude of the PEM was set to $\eta_0 = 4 \times 10^{-3}$ and the measured finesse was $\mathscr{F} = 700\,000$.

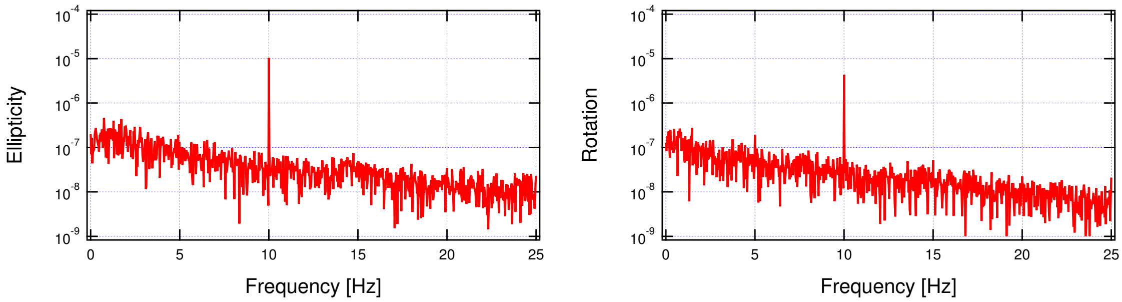

Figure 5.6: Cotton-Mouton effect measurements for 228 μbar of Ar gas: Fourier spectra of the extinguished intensity demodulated at the modulator frequency ν_m. Only magnet Alpha was rotating at $\nu_\alpha = 5$ Hz. Left panel: ellipticity measurement. Right panel: rotation measurement. Integration time is $T = 128$ s for both spectra.

By filling the vacuum chamber with 0.228 mbar of Argon gas with a purity of 1 ppm, we made the Cotton-Mouton calibration. Figure 5.6 shows two spectra of the extinguished intensity after the analyzer, demodulated at the frequency $\nu_{\rm m}$: the left panel shows the Cotton-Mouton ellipticity signal at 10 Hz. The right panel shows the observed rotation signal. Taking the ratio of the amplitudes of the two peaks [see Equations (4.9) and (4.10)] one finds a value $\alpha = 1.9$ μrad, corresponding to an attenuation factor $k(\alpha) = 0.85$. The frequency distance between the two Airy curves for the two orthogonal polarisation states corresponds to 14 Hz. From these data one can extract a value for the unitary birefringence of Ar gas at room temperature:

$$\Delta n_u^{(\mathrm{Ar})} = (7.6 \pm 0.5) \times 10^{-15}\ \mathrm{T}^{-2}\ \mathrm{atm}^{-1}$$

in agrement with value obtained during Run2015. It must be noted that during this calibration the magnet used was rotating at $\nu_B = 5$ Hz rather than at one of the frequencies used during the vacuum measurements. The correct physical axis was determined from this calibration by using the phase dependence on frequency as determined in Chapter 4.

5.4.2 2016 vacuum magneto-optical measurements

Some data segments that featured an excess wideband noise were discarded reducing the useful integration time to $T = 1\,600\,000$ s. Furthermore we continuously monitored the acceleration of the ceramic tubes keeping it at a minimum.

In Figure 5.7, top and middle rows, an FFT of the data blocks for the two magnets and relative histograms are shown. These refer to ellipticity measurements. In the top row, the amplitudes of the complex Fourier transform of the signal in a narrow interval around $2\nu_B$ confirm the absence of structures due to spurious signals. In the middle row, the histograms of the values of the ellipticity noise amplitudes plotted in the top row, are shown, and are fitted with the Rayleigh distribution. The arrow in blue indicates the value of the bin at $2\nu_B$.

The bottom row shows the Fourier transforms of the magnetic field probes used to monitor the rotation of the magnets. These refer to the whole data set lasting 2×10^6 s. As can be seen, each Fourier spectrum has a single bin above the noise in correspondence of the rotation frequency of the magnet. The small pedestal is due to very slow drifts of the phase locked frequency generators which have their intrinsic frequency resolution. Every few days we corrected for this slight drift causing a small phase mismatch and hence the small pedestal. It is important to note that a birefringence signal, if present, must occupy a single bin in the Fourier spectrum just as the magnetic field probes.

Magnet frequency	Quantity	In-phase	Quadrature	Noise floor σ	$S_{2\nu_B}^{\mathrm{meas}}\ \left(1/\sqrt{\mathrm{Hz}}\right)$	$k(\alpha)$
$(\nu_\alpha) = 8.0$ Hz	Δn	6.0×10^{-22}	2.1×10^{-22}	3.0×10^{-22}	3.8×10^{-19}	0.85
$(\nu_\beta) = 8.5$ Hz	Δn	-0.7×10^{-22}	-5.4×10^{-22}	2.8×10^{-22}	3.7×10^{-19}	0.85
$(\nu_\alpha) = 8.0$ Hz	$\Delta\kappa'$	14×10^{-22}		7.1×10^{-22}	8.8×10^{-19}	
$(\nu_\beta) = 8.5$ Hz	$\Delta\kappa'$	-1.7×10^{-22}		6.7×10^{-22}	8.6×10^{-19}	

Table 5.3: 2016 values of the magnetic birefringence and dichroism of vacuum for $B = 2.5$ T. The primed measurements are obtained through the use of Equations (4.9) and (4.10).

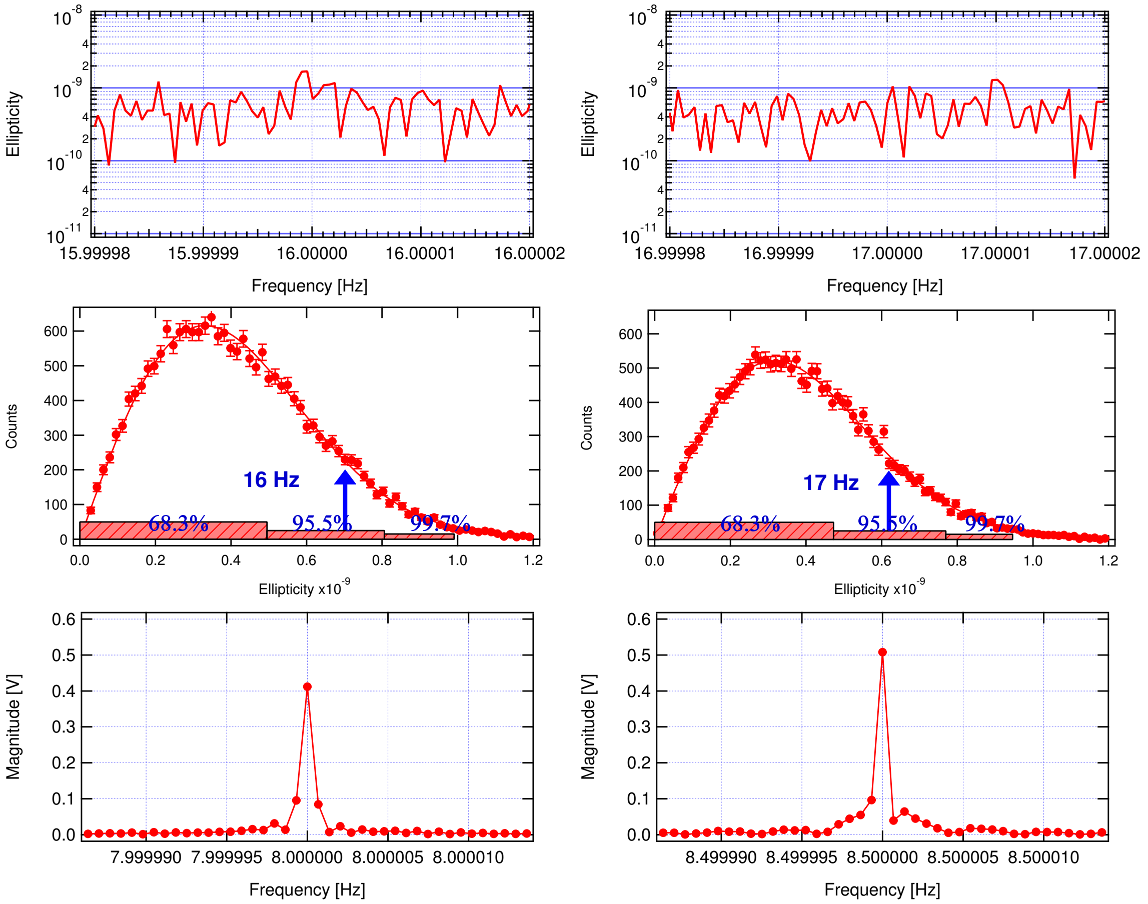

Figure 5.7: Ellipticity data blocks for Run2016: Top row: the amplitude of the complex Fourier transforms of the signal in a narrow interval around $2\nu_B$. The values are corrected for the factor $k(\alpha)$. Middle row: histograms of the values plotted in the top row; we fit the data with the Rayleigh distribution; the vertical arrows mark the unprojected values at $2\nu_B$ for each magnet. The strips at the bottom of the plots correspond to the 68.3%, 95.5%, and 99.7% integrated probabilities. Left colum: magnet α rotating at $\nu_\alpha = 8$ Hz, with integration time $T = 1.6 \times 10^6$ s. Right column: magnet β rotating at $\nu_\alpha = 8.5$ Hz, $T = 1.6 \times 10^6$ s. Bottom row: Fourier spectra, in a narrow frequency band around ν_B, of the magnetic field monitors for each of the two magnets. As can be seen the signal occupies a single bin at exactly the right rotation frequency. The slight pedestal is due to small phase adjustments during the run (see text).

The summarised data and the complete data analysis are reported in Table 5.3. Due to the mixing between ellipticities and rotations we also interpret each line in terms of the reciprocal quantity. The second half of the same table, with primed $\Delta\kappa'$, presents the values obtained by applying Equations (4.9) and (4.10). The weighted averages of the numbers listed in the "In-phase" column of Table 5.3 are:

$$\Delta n^{(2016)} = (2.4 \pm 2.0) \times 10^{-22} \qquad @\ B = 2.5\ \mathrm{T}, \tag{5.5}$$

$$\Delta\kappa^{(2016)} = (5.7 \pm 4.8) \times 10^{-22} \qquad @\ B = 2.5\ \mathrm{T}. \tag{5.6}$$

The quadrature value of Δn results to be $(-1.9 \pm 2.0) \times 10^{-22}$. All the values found are compatible with zero within 95% c.l..

5.5 Vacuum measurement summary and time evolution

The summary of the vacuum magnetic birefringence measurements for runs Run2014, Run2015, Run2016 are:

$$\begin{cases} \Delta n^{(2014)} = (+3.0 \pm 13) \times 10^{-22} & @\ B = 2.5\ \mathrm{T}, \\ \Delta n^{(2015)} = (-1.7 \pm 3.1) \times 10^{-22} & @\ B = 2.5\ \mathrm{T}, \\ \Delta n^{(2016)} = (+2.4 \pm 2.0) \times 10^{-22} & @\ B = 2.5\ \mathrm{T}. \end{cases}$$

where the errors indicate the 68 % c.l.. The weighted average of all values gives:

$$\Delta n^{(\mathrm{PVLAS})} = (12 \pm 17) \times 10^{-23} \qquad @\ B = 2.5\ \mathrm{T}. \tag{5.7}$$

We must note that the magnetic birefringence predicted by Euler and Heisenberg is $\Delta n^{(\mathrm{EH})} = 2.5 \times 10^{-23}$ at $B = 2.5$ T, i.e. the noise level is a factor seven larger than the predicted signal at 68 % c.l.

Figure 5.8 shows the historical evolution of the limits on the absolute value of the magnetic birefringence of vacuum for PVLAS and other experimental efforts. All values have been normalised to B^2_{ext}. As can be seen, the PVLAS experiment has reached the best limit. A detection of the signal predicted by QED will be possible only if the sensitivity of the polarimeter is improved by an order of magnitude.

As far as dichroism is concerned, and again assuming a linear dependence of the measured rotation on the length of the magnetic region, we obtain the following limits from the measurement of ellipticity and rotation expressed at 68% c.l..

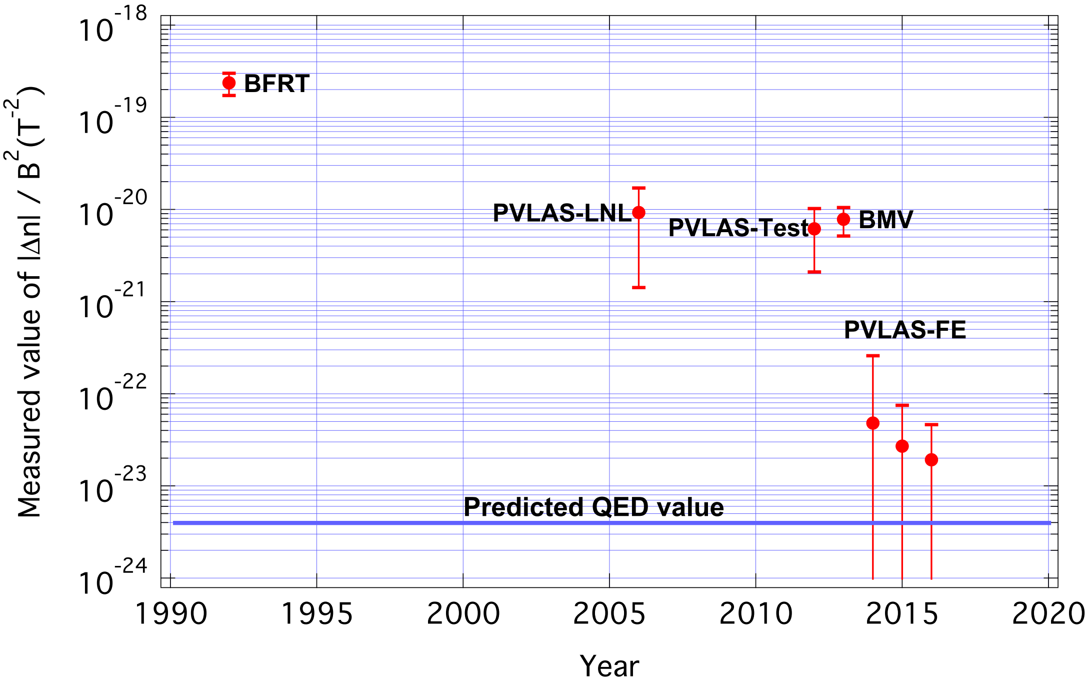

Figure 5.8: Time evolution of the measurement of vacuum magnetic birefringence normalised to B^2_{ext}. Error bars correspond to one σ. The values derives from the following references: BFRT [35]; Legnaro [76, 77], Ferrara Test [78], BMV [82].

$$\begin{cases} \Delta\kappa^{(2014)} = (+3.0 \pm 13) \times 10^{-22} & @\ B = 2.5\ \text{T}, \\ \Delta\kappa^{(2015)} = (-1.9 \pm 3.6) \times 10^{-22} & @\ B = 2.5\ \text{T}, \\ \Delta\kappa^{(2016)} = (+5.7 \pm 4.8) \times 10^{-22} & @\ B = 2.5\ \text{T}. \end{cases}$$

By computing the weighted average one obtaines:

$$\Delta\kappa^{(\text{PVLAS})} = (9 \pm 28) \times 10^{-23} \qquad @\ B = 2.5\ \text{T} \tag{5.8}$$

5.6 Limits on hypothetical particles

5.6.1 Axion Like Particles

The ellipticity and rotation measurements can be used to draw exclusion plots in the plane (m, g) for Axion-like particles. However, it is not possible to use the birefringence and dichroism results presented above since they are obtained with different magnet lengths. In fact the dichroism due to ALPs has an L^2 dependence [cf. Equations (1.48)]. In the ellipticity measurement, the best limits for (m, g) are obtained considering each magnet separately at

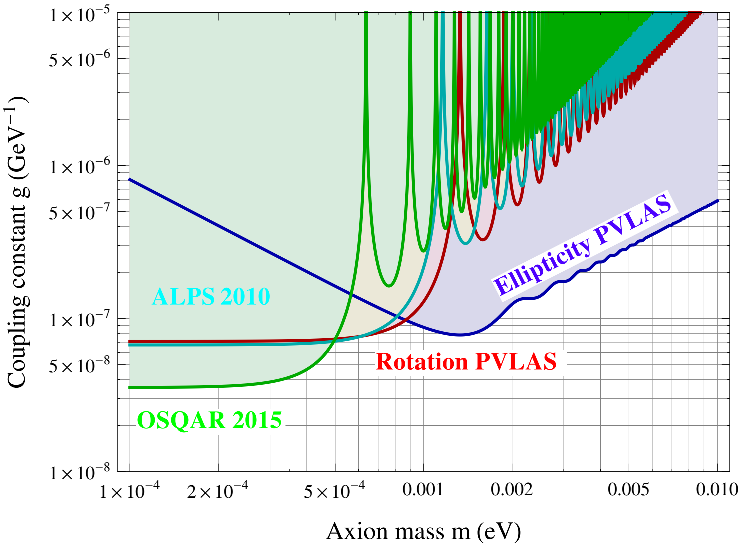

Figure 5.9: Comparison of laboratory experiments which put limits on the existence of ALPs particles at 95% c.l. The shaded regions of the graph are excluded. The limits obtained by PVLAS are for both scalar and pseudoscalar ALPs. The figure also shows the measurements by the OSQAR [81] and the ALPS [96] collaborations.

different rotation frequencies, while for the rotation measurements the best limit is obtained with both magnets rotating at the same frequency and in phase. The results are shown in Figure 5.9. The limits exist for both scalar and pseudoscalar ALPs. Below 0.5 meV for the model independent laboratory experiments the most stringent limits are given by the OSQAR experiment [81], whereas the exclusion plot obtained using the PVLAS ellipticity measurement dominates the $m \geq 1$ meV region. Between these two values, our rotation limit almost coincides with the 2010 ALPS result [96]. One must remind the reader that the CAST solar helioscope has already excluded the whole region down to the level $g \sim 10^{-10}$ GeV^{-1} [97, 98]. However, the CAST results depend on the model assumed for the axion production and emission by the sun.

In the low mass limit with $m \ll \sqrt{\frac{4\omega}{L}} = 10^{-3}$ eV, where the coupling constant does not depend on the mass of the ALP, one can do slightly better by taking the weighted average of $\frac{\Delta\kappa}{L}$ for the single and double magnet configurations. In fact in the limit above,

$$g \approx \sqrt{\frac{\pi\Delta\kappa}{\lambda L}\frac{4}{B_{\text{ext}}}} \tag{5.9}$$

By averaging lines 4 and 5 of Table 5.2, lines 3 and 4 of Table 5.3, all divided by L, and line 6 of Table 5.2 divided by $2L$ and inserting it in the expression (5.9) one finds

$$\left\langle \frac{\Delta\kappa}{L} \right\rangle = (1.3 \pm 2.7) \times 10^{-22}\ \mathrm{m}^{-1} \tag{5.10}$$

having used $L = 0.82$ m corresponding to the length of one magnet. The resulting 95% c.l. limit on g is therefore ($1\ \mathrm{T} = \sqrt{\frac{\hbar^3 c^3}{e^4 \mu_0}} = 195\ \mathrm{eV}^2$ and $1\ \mathrm{m} = \frac{e}{\hbar c} = 5.06 \times 10^6\ \mathrm{eV}^{-1}$)

$$g = \sqrt{\left\langle \frac{\Delta\kappa}{L} \right\rangle \frac{\pi}{\lambda} \frac{4}{B_{\mathrm{ext}}}} < 6.5 \times 10^{-8}\ \mathrm{GeV}^{-1}. \tag{5.11}$$

5.6.2 Millicharged Particles

Figure 5.10 shows the PVLAS exclusion plots on the existence of millicharged particles. Two independent limits are derived from the birefringence and the dichroism values of Equations (5.7) and (5.8), the latter being more stringent in the low-mass range ($m_\varepsilon \leq 0.1$ eV), whereas the former is dominating the high-mass range. We explicitly note that the Fermion exclusion plot also applies to all types of neutrinos, limiting their charge to be less than $\approx 3 \times 10^{-8} e$ for masses smaller than 10 meV.

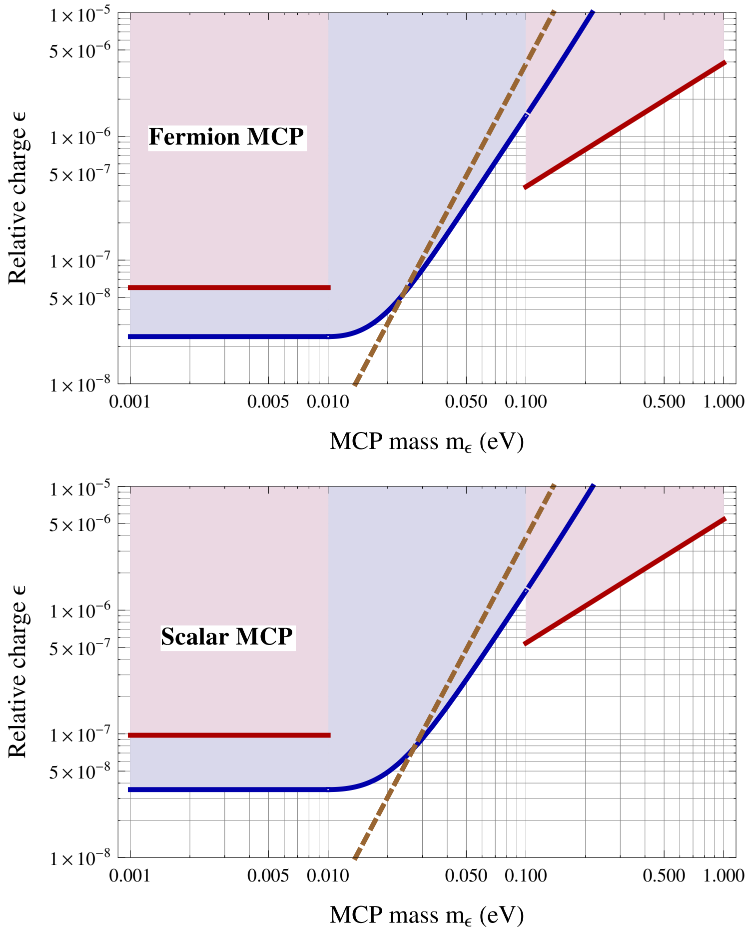

Figure 5.10: Exclusion plots for MCP particles at 95% c.l. derived from the dichroism and birefringence values of Equations (5.7) and (5.8). The top panel shows the Fermion MCP, and the bottom panel shows the scalar MCP. The excluded regions are above the curves. The limit derived from rotation dominates at small masses, whereas the birefringence limit is effective at large masses. The two branches of the birefringence curve are not connected in the mass range around $\chi = 1$ (dashed line), where Δn changes sign. A cubic spline joins the two branches of the dichroism curve.

Chapter 6

Conclusions

The work described in this thesis was carried out as part of the experiment PVLAS, developed at the INFN of Ferrara (Italy) and at the Department of Physics of the Ferrara University. Heisenberg's Uncertainty Principle together with the existence of the positron lead to corrections of Maxwell's equations in vacuum, giving rise to new effects including the interaction between photons. These corrections show that vacuum, in the presence of a magnetic field, becomes birefringent. The aim of the PVLAS experiment is to perform a first measurement of the magnetic birefringence of vacuum (MBV). Experimentally this is done by measuring the ellipticity acquired by a linearly polarised laser beam that propagates in a direction orthogonal to a magnetic field which fills a vacuum region. In this configuration, a rotating magnetic field will induce a modulated ellipticity on the laser beam at twice the rotation frequency. An ellipticity and a rotation (due to a dichroism) of the polarised beam in a transverse magnetic field can also be generated due to a coupling of two photons with an axion like particle or a millicharged particle.

The activities during the three years of PhD studies were centered on a characterisation of the two main issues for the detection of MBV: systematics and wide band noise. The first part was dedicated to systematic effects or, better, the noise in phase with the rotation of the magnetic field. We have identified two types of systematic signals: one is due to the coupling between the diffused light and the vacuum tubes passing through the magnets and the second to the mechanical acceleration of the optical bench induced by the rotating magnets. As a consequence of the magnetic gradients inside the magnets, a coupling force between the vacuum tube and the magnets pushes laterally the diamagnetic tube during rotation. This displacement modulates the diffused light inside the cavity and generates both spurious ellipticity and rotation signals. Similarly to the effect of a birefringence, this systematic effect is present at twice the frequency of the rotation of the magnets. The acceleration of the optical bench also generates fake signals. Although the optical bench is seismically isolated by means of air springs, it presents small components of acceleration in phase with the rotating magnets. This acceleration is transmitted to the optical bench by an unbalance of the magnets. This residual acceleration, reaching the elements of the optical bench, modulates the phase of the locking system and generates spurious signals in ellipticity and rotation. After a detailed study of these two phenomena, we concluded that the systematics due to the tube and diffused light dominates in the low-frequency range (0-16 Hz). Instead, the systematics due to the optical bench dominates in the high-frequency range and both phenomena generate spurious signals in ellipticity and rotation measurements.

We also identified a cross talk between ellipticities and rotations in a birefringent Fabry-Perot cavity by measuring the Cotton-Mouton effect in gases. To correctly measure these signals in a high frequency range one must first determine the frequency dependence of the signal. A characterisation of a birefringent cavity by analytical calculations, followed by a measurement of the birefringence of the mirrors, was then performed. Furthermore, the dynamic behaviour of the cavity is also explained showing how the measured signal is filtered. This analytical study and experimental measurements show how the birefringence of the mirrors modify the frequency response of the cavity from a standard first order filter. This effect must also be taken into account for a correct interpretation of the signal of ellipticity or rotation. Since the birefringence of a mirrors is never zero, this characterisation of the dynamical behaviour of a cavity will be useful for other similar experimental setups. Up to now only a simple first order linear filter correction was considered in the literature.

The wide band noise has also been investigated experimentally and is the only obstacle limiting the present apparatus from reaching of the final goal. We have done tests by changing a number of parameters of the apparatus: different modulation amplitudes of the ellipticity modulator, different circulating power in the Fabry-Perot cavity, redesign of the electronics of the locking system, further reduction of the diffused light and possible correlations between the wide band noise level and mechanical and environmental noise. The results of these tests always brought us to conclude that these are not limiting the present wide band noise.

The comprehension of the systematic effects has allowed long integration times limited by the present wide band noise. In fact, after curing the diffused light, by mounting a series of baffles inside the vacuum tube between the two mirrors of the Fabry-Perot cavity, it was possible to integrate for a long time T with the noise scaling as $1/\sqrt{T}$. The automatic laser locking circuit played an important role for 24/24 hrs data taking, and a total time of $T \approx 5 \times 10^6$ s was obtained. We measured at rotation frequencies of the magnets up to 8.5 Hz (signal at 17 Hz). A further increment of the frequency was not been possible due to resonances of the vacuum glass tube and to the vibrations of the structures supporting the magnets.

Although the present sensitivity of the PVLAS experiment has not yet reached the level that would guarantee the capability of measuring MBV in a reasonable time, it is the best sensitivity $S_{\Delta n/B^2}$ in the unitary birefringence ever realised:

$$S^{\mathrm{meas}}_{\Delta n/B^2} = 4.1 \times 10^{-20} \frac{1}{\mathrm{T}^2\sqrt{\mathrm{Hz}}}.$$

This sensitivity would require an integration time $T \approx 10^8$ s to reach the predicted QED birefringence signal with a signal to noise ratio of 1. By comparing the different MBV detection experiments, at present the PVLAS apparatus has reached the lowest noise level in the measurement of magnetic birefringence of vacuum:

$$\Delta n^{\,(\mathrm{PVLAS})} = (12 \pm 17) \times 10^{-23} \qquad @\ B = 2.5\ \mathrm{T}.$$

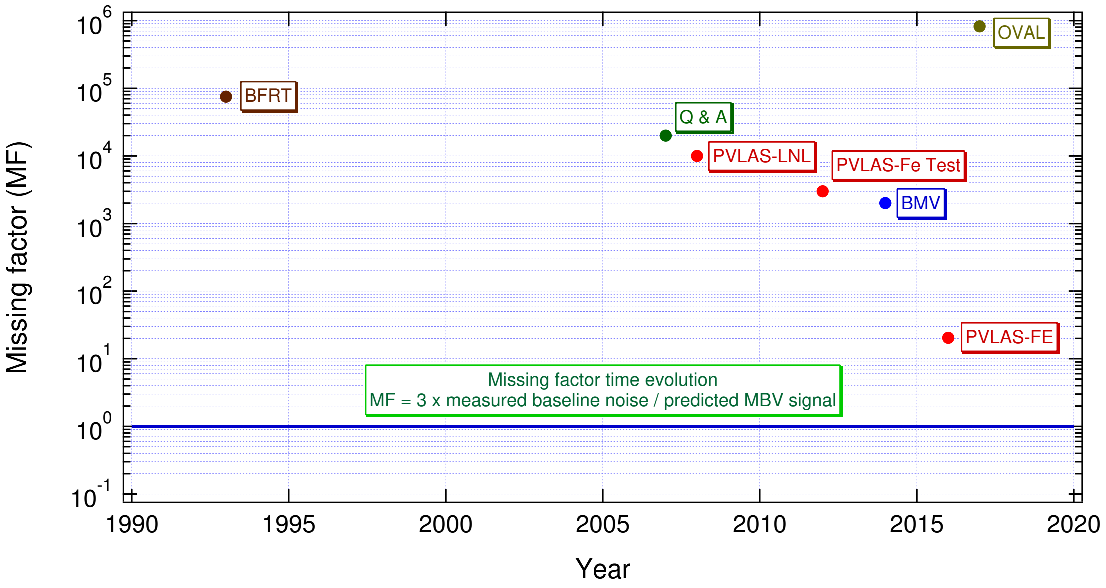

Figure 6.1: Plot of the missing factor of the baseline noise at 3σ c.l. to reach the predicted QED value for different experimental efforts.

In Fig. 6.1 we report the missing factor, at a 3 σ level, to reach the first detection of MBV. The significant improvement of the last PVLAS-FE data was made possible due to the extensive search and determination of systematic sources of spurious signals. This allowed long integration time leading to a noise floor without signals at $2\nu_B$ at a 1 σ level.

The result for the dichroism is:

$$\Delta\kappa^{(\mathrm{PVLAS})} = (9 \pm 28) \times 10^{-23} \qquad @\, B = 2.5\ \mathrm{T}$$

The new results on the magnetically induced dichroism and birefringence have also set new limits on the existence of hypothetical particles which couple to two photons, both axion-like and milli-charged.

Regarding our current limiting noise, i.e. the wide band noise, a hint on the origin of the excess wide band noise may come from the fact that this noise seems to be present in all experiments that want to measure the MBV. In fact the sensitivities in birefringence of all the experiments at their working frequency follow a common law approximately given by $1/f^{\alpha}$ law with α between 0.5 and 1. Without the presence of a Fabry-Perot cavity, the noise measured is compatible to the predicted one (usually shot-noise). This experimental fact is a hinting that this noise may be due to a fundamental intrinsic noise which may have a thermal origin. A attempt to cool the mirrors may clarify this hypothesis. An analytical estimation of this hypothesis is needed. This will be a future project of the experiment.

In any case there are two possible ways to increase the signal-to-noise ratio. The first method is to increase the $\int B^2 dl$ for example resorting to superconductor high-field magnets. The second is to increase the frequency of the effect on the basis the $1/f^{\alpha}$ law. These two possibilities are correlated because typically intense magnetic fields may be modulated at relatively low frequencies. In the case of weak magnetic fields of the order of $\approx 2-3$ T higher rotation frequencies are possible at the cost of a smaller effect due to the filtering by the cavity. A possibility to uncouple the two methods, which still has to be verified experimentally, is the rotation of the polarisation inside the magnetic field but keeping its direction fixed on the mirrors. This modulation can be realised by inserting two rotating half wave plates inside the cavity. This proposal is described in detail in ref. [99].

As for the cooling of the mirrors, some preliminary tests are underway within the PVLAS collaboration. By using a liquid nitrogen cooled, an almost 4π shield surrounding a mockup mirror, has given a temperature of ≈ 160 K through radiative cooling [100]. The system for cooling the interferometer mirrors is under realisation.

According to different possible thermal effects, the intrinsic thermal noise could have a dependence on temperature as T or $\sqrt{T}$. Even if the noise is inversely proportional to T a factor ≈ 2 gain is still not sufficient to measure the magnetic vacuum birefringence with a signal-to-noise ratio of 1 at the present rotation frequencies. However, if the noise of the experiment shows an improvement the way to reach MBV is drawn. The cooling at 160 K accompanied by an improvement of the structure supporting the magnets and of the rigidity of the vacuum tubes is a possible solution.

Bibliography

[1] A. Cotton and H. Mouton, *C. R. Acad. Sci., Paris* **141**, 317 (1905).

[2] A. Cotton and H. Mouton, *C. R. Acad. Sci., Paris* **141**, 349 (1905).

[3] J. Kerr, *Phil. Mag.* **50**, 337 (1875).

[4] J. Kerr, *Phil. Mag.* **50**, 446 (1875).

[5] Y.R. Shen, *The Principles of Nonlinear Optics*, (Wiley, New York, 1984).

[6] J.D. Jackson, *Classical electrodynamics* 3rd ed., (Wiley, New York, 1999).

[7] V.B. Berestetskii, E.M. Lifshitz, L.P. Pitaevskii, Quantum Electrodynamics 2nd ed., (Butterworth-Heinemann, Oxford, 1982).

[8] W. Heisenberg, Zeitschrift fur Physik (in German), **43**, 172 (1927).

[9] P.A.M. Dirac, Proc. R. Soc. A **117**, 610 (1928).

[10] O. Halpern, *Phys. Rev.* **44**, 855 (1933).

[11] G. Breit and J.A. Wheeler, *Phys. Rev.* **46**, 1087 (1934).

[12] H. Euler and B. Kochel, *Naturwiss.* **23**, 246 (1935).

[13] H. Euler, *Annalen der Physik* **5**, 398 (1936).

[14] W. Heisenberg and H. Euler, *Z. Phys.* **98**, 714 (1936).

[15] J. Schwinger, Phys. Rev. **82**, 664 (1951).

[16] V. Weisskopf, *Mat.-Fis. Med. Dan. Vidensk. Selsk.* **14**, 6 (1936).

[17] Z. Bialynicka-Birula and I. Bialynicki-Birula, *Phys. Rev. D* **2**, 2341 (1970).

[18] W.H. Furry, Phys. Rev. **51**, 125 (1937).

[19] S. Adler, Ann. Phys. (NY) **67**, 599 (1971).

[20] V.I. Ritus, Sov. Phys.-JETP **42**, 774 (1975).

[21] P. Castelo Ferreira and J. Dias de Deus, Eur. Phys. J. C **54**, 539 (2008).

[22] H. Gies, J. Jaeckel and A. Ringwald, Phys. Rev. Lett. **97**, 140402 (2006).

[23] M. Ahlers *et al.*, Phys. Rev. D **75**, 035011 (2007).

[24] L. Maiani, R. Petronzio and E. Zavattini, Phys. Lett. B **175**, 359 (1986).

[25] P. Sikivie, Phys. Rev. Lett. **51**, 1415 (1983).

[26] M. Gasperini, Phys. Rev. Lett. **59**, 396 (1987).

[27] S. Andriamonje *et al.* (CAST Collaboration), JCAP **0704**, 010 (2007).

[28] E. Arik *et al.* (CAST Collaboration), JCAP **0902**, (008 2009).

[29] R.D. Peccei and H.R. Quinn, Phys. Rev. Lett. **38**, 1440 (1977).

[30] R.D. Peccei and H.R. Quinn, Phys. Rev. D **16**, 1791 (1977).

[31] F. Wilczek, Phys. Rev. Lett. **40**, 279 (1978).

[32] G. Raffelt and L. Stodolsky, Phys. Rev. D **37**, 1237 (1988).

[33] H. Gies, *J. Phys. A: Math. Theor.* **41**, 164039 (2008).

[34] H. Primakoff, Phys. Rev. **81**, 899 (1951).

[35] R. Cameron *et al.* (BFRT collaboration), Phys. Rev. D **47**, 3707 (1993).

[36] W. Tsai and T. Erber, Phys. Rev D **10**, 492 (1974).

[37] W. Tsai and T. Erber, Phys. Rev D **12**, 1132 (1975).

[38] E. Iacopini and E. Zavattini, Phys. Lett. B **85**, 151 (1979).

[39] R.C. Jones, J. Opt. Soc. Am. **38**, 671 (1948) and references therein.

[40] D. Bakalov *et al.* (PVLAS collaboration), Nucl. Phys. B (Proc. Suppl.) **35**, 180 (1994).

[41] P. Pace, “Studio e realizzazione di un ellissometro basato su una cavità Fabry-Perot in aria nell’ambito dell’esperimento PVLAS”, Laurea Thesis, Università di Trieste, 1994.

[42] D. Jacob *et al.*, Appl. Phys. Lett. **66**, 3546 (1995).

[43] M. Born and E. Wolf, *Principle of Optics*, (Pergamon, New York, 1980) **73-74**.

[44] F. Della Valle *et al.*, Opt. Express **22**, 11570 (2014).

[45] J.L. Bower and P.M. Schultheiss, *Introduction to the design of servomechanims*, (Wiley, New, York, 1958).

[46] R.V. Pound, Rev. Sci. Instrum. **17**, 490, (1946).

[47] R.W.P. Drever *et al.*, Appl. Phys. B **31**, 97 (1983).

[48] G. Cantatore *et al.*, Rev. Sci. Instrum. **66**, 2785 (1995).

[49] M. Bregant *et al.*, Rev. Sci. Instrum. **73**, 4142 (2002).

[50] R.E. Bartolo, A. Tveten and C.K. Kirkendal, in *20th International Conference on Optical Fibre Sensors*, J. Jones *et al.* eds., Proc. SPIE **7503**, 750370 (2009).

[51] W. Voigt, *Lehrbuch der Magneto- und Elektro-optik*, (Teubner, Leipzig, 1908).

[52] F. Brandi *et al.* (PVLAS collaboration), J. Opt. Soc. Am. B **15**, 1278 (1998).

[53] M. Bregant *et al.* (PVLAS collaboration), Chem. Phys. Lett. **392**, 276 (2004).

[54] M. Bregant *et al.* (PVLAS collaboration), Chem. Phys. Lett. **410**, 288 (2005).

[55] M. Bregant *et al.* (PVLAS collaboration), Chem. Phys. Lett. **477**, 415 (2009).

[56] M. Bregant *et al.* (PVLAS collaboration), Chem. Phys. Lett. **471**, 322 (2009).

[57] F. Della Valle *et al.*, Chem. Phys. Lett. **592**, 288 (2014).

[58] F. Della Valle *et al.* (PVLAS collaboration), Phys. Rev. D 90, 092003 (2014).

[59] F. Della Valle *et al.* (PVLAS collaboration), Eur. Phys. J. C **76**, 24 (2016).

[60] A.D. Buckingham and J.A. Pople, Proc. Phys. Soc. B **69**, 1133 (1956).

[61] P. Langevin, Radium, Paris **7**, 249 (1910).

[62] C. Rizzo, A. Rizzo and D.M. Bishop, Int. Rev. Phys. Chem.**16**, 81 (1997).

[63] A. Cadène *et al.* (BMV collaboration), Phys. Rev. A **88**, 043815 (2013).

[64] S.-J. Chen, H.-H. Mei and W.-T. Ni, Mod. Phys. Lett. A **22**, 2815 (2007).

[65] H.-H. Mei *et al.*, Chem. Phys. Lett. **471**, 216 (2009).

[66] A. Cadène *et al.* (BMV collaboration), J. Chem. Phys. **142**, 124313 (2015).

[67] E. Iacopini *et al.*, European Organization for Nuclear Research, Proposal D2 (1980).

[68] E. Iacopini *et al.*, Nuovo Cimento B **61**, 21 (1981).

[69] S. Carusotto *et al.*, Opt. Commun. **42**, 104 (1982).

[70] S. Carusotto *et al.*, J. Opt. Soc. Am. B **1**, 635 (1984).

[71] F. Scuri *et al.*, J Chem. Phys. **85**, 1789 (1986).

[72] Y. Semertzidis *at al.*, Phys. Rev. Lett. **64**, 2988 (1990).

[73] D. Bakalov *et al.* (PVLAS collaboration), Quantum Semiclass. Opt. **10**, 239 (1998).

[74] E. Zavattini *et al.* (PVLAS Collaboration), Phys. Rev. Lett. **97**, 110406 (2006).

[75] E. Zavattini *et al.* (PVLAS Collaboration), Nucl. Phys. B **174** (Proc. Suppl.), 233-236 (2007).

[76] E. Zavattini *et al.* (PVLAS collaboration), Phys. Rev. D **77**, 032006 (2008).

[77] M. Bregant *et al.* (PVLAS collaboration), Phys. Rev. D **78**, 032006 (2008).

[78] F. Della Valle *et al.* (PVLAS collaboration), New J. Phys. **15**, 053026 (2013).

[79] F. Della Valle *et al.* (PVLAS collaboration), Opt. Commun. **283**, 4194 (2010).

[80] H.-H. Mei *et al.*, Mod. Phys. Lett. A **25**, 983 (2010).

[81] R. Ballou *et al.* (OSQAR collaboration), Phys. Rev. D **92**, 092002 (2015).

[82] A. Cadène *et al.* (BMV collaboration), Eur. Phys. J. D **68**, 16 (2014).

[83] Xing Fan *et al.* (OVAL collaboration), arXiv:1705.00495v2 (2017).

[84] J.H. Pöld, “VMB measurement @ ALPS II. Considerations for Integrating QED optics in the ALPS II setup.” Presentation at the QED vacuum birefringence workshop, DESY, Hamburg (D), 1–3 November 2015, https://indico.desy.de/contributionDisplay.py?contribId=15&sessionId=3&confId=12654

[85] Advanced Thin Films, personal communication to G. Zavattini.

[86] A.E. Siegman, *Lasers*, (University Science Books, Mill Valey, CA, 1986).

[87] O. Svelto, *Principles of Lasers* 5th ed., (Springer Science and Business Media, new York, 2010).

[88] H. Zijlstra, Philips J. Res. **40**, 259 (1985).

[89] P. Micossi *et al.*, Appl. Phys. B **57**, 95 (1993).

[90] F. Bielsa *et al.*, Appl. Phys. B **97**, 457 (2009).

[91] G. Zavattini *et al.*, Appl. Phys. B **83**, 571 (2006).

[92] F. Brandi *et al.*, Appl. Phys. B **65**, 351 (1997).

[93] E. Iacopini, G. Stefanini, and E. Zavattini, Appl. Phys. A **32**, 63 (1983).

[94] The Virgo Collaboration, *Advanced Virgo Technical Design Report*, VIR-0128A-12 (2012).

[95] G.P. Buso *et al.*, INFN-LNL Annual Report 2015, p. 176.

[96] K. Ehret *et al.* (ALPS collaboration), Phys. Lett. B. **689**, 149 (2010).

[97] K. Zioutas *et al.* (CAST collaboration), Phys. Rev. Lett. **94**, 121301 (2005);

[98] S. Andriamonje *et al.* (CAST collaboration), JCAP **0704**, 010 (2007).

[99] G. Zavattini *et al.*, Eur. Phys. J. C **76**, 294 (2016).

[100] F. Della Valle *et al.*, INFN-LNL Annual Report 2016, p. 154.